TESIS DE LA UNIVERSIDAD DE ZARAGOZA

2019 47

Jesús Carro Fernández

New Methodologies for the Development and Validation of Electrophysiological Models

Departamento

Instituto de Investigación en Ingeniería [I3A]

Director/es

RODRIGUEZ MATAS, JOSE FELIX
PUEYO PAULES, ESTHER

ISSN 2254-7606

Prensas de la Universidad Universidad Zaragoza

ISSN 2254-7606

Universidad Zaragoza
1542

Tesis Doctoral

NEW METHODOLOGIES FOR THE DEVELOPMENT AND VALIDATION OF ELECTROPHYSIOLOGICAL MODELS

Autor

Jesús Carro Fernández

Director/es

RODRIGUEZ MATAS, JOSE FELIX
PUEYO PAULES, ESTHER

UNIVERSIDAD DE ZARAGOZA

Instituto de Investigación en Ingeniería [I3A]

2019

New Methodologies for the Development and Validation of Electrophysiological Models

Author: ***Jesús Carro Fernández***

Supervisors:

Esther Pueyo Paules

José Félix Rodríguez Matas

PhD Thesis in
Biomedical Engineering

Zaragoza, September, 2018

Instituto Universitario de Investigación
de Ingeniería de Aragón
Universidad Zaragoza

New Methodologies for the Development and Validation of Electrophysiological Models

Author: ***Jesús Carro Fernández***

Supervisors:

Esther Pueyo Paules
José Félix Rodríguez Matas

PhD Thesis in
Biomedical Engineering

Zaragoza, September, 2018

Instituto Universitario de Investigación
en Ingeniería de Aragón
Universidad Zaragoza

To Débora.
To Nacho, Samuel, and Lucía.

Acknowledgment

This thesis has been a long journey and, therefore, many people have put a bit to get here. My thanks to all of you.

To Esther and José Félix. It is very difficult to summarize everything received from you in these years. How much we have done, how much remains to be done, how much to know and to understand. You have generated me more questions than answers. Thank you.

To Pablo Laguna. For your support and help, especially in the first phases of this thesis: the beginning, the search of founds, etc. Thank you.

To Juan, Pablo Vicente, David Sampedro, Carlos, Jesús Fernández and all the members of BSICoS. Every time I met with you, it did not matter how much time had passed since the last time, I was once again one more in the group. You spread your enthusiasm for research. Thank you.

To Pamela, Ana, and Arantxa. The least visible part of the group, but those that have made all the procedures easy. Thank you.

To Jorge, David, África, Jesús, Carlos, Paqui, Gabriel, Violeta, Jaime, Lorena, and all those who have been encouraging and supporting me these years at the USJ. Thank you.

To my parents-in-law. For all the help received during these years: to have time to write, to travel, etc. For everything. Thank you.

To my parents, and my brothers and sisters; especially to my father. For all the values that you have transmitted to me, for all your support, for helping me to be who I am. Thank you.

To Nacho, Samuel and Lucia. I do not know who have taken me away more sleep hours in these years: the thesis or you; but you have the ability to make me forget both things with a smile and a hug. I hope I did not steal too much of your time. Thank you.

To Débora. For your patience all these years. For getting me up in the hardest moments, and putting my feet on the ground in the best ones. For being by my side on this road. Thank you.

Thank you very much to all.

Agradecimientos

Esta tesis ha sido un viaje largo y, por ello, son muchas las personas que han puesto un granito de arena para llegar hasta aquí. Mi agradecimiento a todos vosotros.

A Esther y José Félix. Es muy difícil resumir todo lo recibido de vosotros en estos años. Cuánto hemos hecho y cuánto queda por hacer, cuánto por conocer y entender. Me habéis generado más preguntas que respuestas. Gracias.

A Pablo Laguna. Por el apoyo y la ayuda recibida, especialmente en las primeras fases de esta tesis: el arranque, la búsqueda de financiación, etc. Gracias.

A Juan, Pablo Vicente, David Sampedro, Carlos, Jesús Fernández y a todos los miembros de BSICoS. Cada vez que me juntaba con vosotros, daba igual el tiempo que hubiera pasado desde la última vez, volvía a ser uno más. Contagiáis vuestro entusiasmo por investigar. Gracias.

A Pamela, Ana, y Arantxa. La parte menos visible del grupo, pero las que han hecho que todos los trámites fueran fáciles. Gracias.

A Jorge, David, África, Jesús, Carlos, Paqui, Gabriel, Violeta, Jaime, Lorena, y todos aquellos que me habéis estado animando y apoyando estos años en la USJ. Gracias.

A mis suegros. Por toda la ayuda recibida en estos años, para escribir, para los congresos, para todo. Gracias .

A mis padres y a mis hermanos; especialmente a mi padre. Por todos los valores transmitidos, por todo el apoyo dado, por haberme ayudado a ser quien soy. Gracias.

A Nacho, Samuel y Lucía. No sé quién me habrá quitado más horas de sueño en estos años: la tesis o vosotros; pero tenéis la capacidad de hacerme olvidar ambas cosas con una sonrisa y un abrazo. Espero no haberos robado yo demasiado tiempo a vosotros. Gracias.

A Débora. Por tu paciencia todos estos años. Por levantarme en los momentos más duros, y ponerme los pies en la tierra en los mejores. Por estar a mi lado en este camino. Gracias.

Muchas gracias a todos.

Abstract

According to data from the World Health Organization (WHO), 17.7 million people were estimated to have died of cardiovascular diseases (CVDs) in 2015. That represents 31% of all global deaths, making these diseases the leading cause of death worldwide. The heart is a complex system that works due to the interaction of a large number of elements at different temporal and spatial scales. The main function of the heart is to pump blood throughout the body, with this mechanical action being triggered by electrical impulses. Issues arising in the electrical or mechanical actions of the heart at any of the involved temporal and spatial scales can lead to cardiac malfunctioning. Mathematical modeling and simulation of the heart's electrical activity (so-called cardiac electrophysiology) and signal processing of bioelectrical signals provide an ideal framework to join the information from clinical and experimental studies with the understanding of the mechanisms underlying them. Due to the high number of factors involved in the development and validation of cardiac computational electrophysiological models and the intricate interrelationships between them, novel methodologies that help control the design, update and validation of new models become of great advantage. These methodologies can target from the definition of ionic gating in the simulated cells to the propagation of the electrical impulse in multi-scale models. This thesis aims to improve the existing knowledge on heart's electrophysiology by developing novel techniques to develop and validate cardiac computational models, with evaluation of the effects of the modeled events by considering interactions between model components and by simulating a range of spatio-temporal scales.

In chapter 2, a new paradigm was introduced to develop a novel human ventricular cell model, the CRLP model, by departing from a previously published model and incorporating novel experimental measurements of potassium currents and reformulating the L-type calcium current. The introduced paradigm was based on the analysis of the model's ability to replicate a set of well-established electrophysiological markers and on a sensitivity analysis of those markers to variations in model parameters. A major advantage of the proposed paradigm was the possibility to identify model parameter values that do not directly depend on individual current measurements or concentrations and which are commonly set in an *ad hoc*

manner. The developed CRLP model was validated, and its improved capacity to investigate arrhythmia-related properties, as compared to the cell model it was based on, was corroborated.

In chapter 3, the CRLP model developed in chapter 2 was updated to introduce the formulation of intracellular potassium ($[K^+]_i$) dynamics. This is an important characteristic for investigation of ventricular arrhythmias arising under conditions of hyperkalemia, one of the components of myocardial ischemia. Direct introduction of $[K^+]_i$ dynamics into the model generated an imbalance in the potassium currents leading to a drift in $[K^+]_i$. To correct for such an imbalance, an optimization framework was proposed that allowed estimating the ionic current conductances of the CRLP model while guaranteeing physiologically plausible values of selected electrophysiological properties, some of them highly relevant for investigation of ventricular arrhythmias.

As mentioned above, when proposing a new model, or when updating an existing model, consistency between simulated and experimental data should be verified by considering all involved effects and scales. The closer the experimental conditions are reproduced in the computer simulations, the more robust the process of model development and validation can be. In chapter 4, *in silico* simulation of experimental protocols was proposed to analyze: how interactions between model components affect the development and validation of mathematical ion channel models; and how propagation affects action potential (AP)-based markers simulated in isolated cells and in tissue preparations, with identification of the ionic contributors in each case. The CRLP model, developed in chapter 2 and updated in chapter 3, presented a rather atypical shape at the end of the depolarization phase of the AP (phase 1). *In silico* simulations of experimental protocols described in chapter 4 and the optimization methodology introduced in chapter 3 were used to improve the AP shape while validating the adjusted model at ionic, cell and tissue scales.

In chapter 6 all the initial formulations and subsequent updates of the CRLP model proposed in previous chapters were integrated and the ionic conductances of the integrated model were readjusted to improve replication of experimental electrophysiological measures. All the methodologies introduced throughout the thesis were used to build a novel human ventricular AP model. For model validation, a range of available experimental data at different scales and aimed at evaluating different electrophysiological properties was considered. Conditions underlying each of the experimental studies were replicated as faithfully as possible. Results simulated with the final version of the CRLP model were in all cases compared with all available experimental evidences and with the most recent human ventricular cell models published in the literature.

Chapter 7 summarizes the main conclusions of the thesis and presents new lines of research that could be undertaken in future studies.

Resumen y conclusiones

De acuerdo a los datos de la Organización Mundial de la Salud, se estima que 17,7 millones de personas murieron de enfermedades cardiacas en 2015, lo que supone el 31% de las muertes, haciendo de estas patologías la primera causa de muerte en el mundo. El corazón es un sistema complejo que trabaja gracias a la interacción de un gran número de elementos en diferentes escalas espaciales y temporales. La función principal del corazón es bombear sangre en todo el cuerpo, siendo esta acción mecánica activada por la estimulación eléctrica. La aparición de problemas en el funcionamiento eléctrico o mecánico del corazón en cualquiera de las escalas involucradas, temporal o espacial, puede dar lugar a un mal funcionamiento cardiaco. El modelado matemático y la simulación de la actividad eléctrica del corazón (denominada electrofisiología cardiaca) y el procesado de señales bioeléctricas proporcionan un marco ideal para unir la información clínica y los estudios experimentales con la comprensión de los mecanismos que subyacen a estos problemas. Debido al gran número de factores que se deben tener en cuenta a la hora de desarrollar y validar un modelo computacional de electrofisiología cardiaca, asi como las complejas interacciones que existen entre ellos, hacen que nuevas metodologías que facilitan la concepción, la actualización y la validación de nuevos modelos sean de gran valor. Estas metodologías pueden enfocarse sea en la definición de las compuertas iónicas de los modelos, como en la propagación del impulso eléctrico en modelos multiescala. Esta tesis pretende mejorar el conocimiento existente sobre electrofisiología cardiaca proponiendo nuevas técnicas para desarrollar y validar modelos computacionales cardiacos, a través de la evaluación de los efectos de los eventos modelados mediante la consideración de las interacciones entre los diferentes componentes del modelo y la simulación de un rango de escalas espacio-temporales.

En el capítulo 2, se introdujo un nuevo paradigma para desarrollar un nuevo modelo de potencial de acción de cardiomiocito humano, el modelo CRLP, partiendo de un modelo previamente publicado e incorporando nuevas mediciones experimentales de corrientes de potasio y reformulando la corriente de calcio tipo L. El paradigma introducido se basó en el análisis de la capacidad del modelo para replicar un conjunto de marcadores electrofisiológicos bien establecidos y en un análisis de sensibilidad de esos marcadores a las variaciones en los parámetros

del modelo. Una de las ventajas del paradigma propuesto fue la posibilidad de identificar parámetros del modelo que no dependen directamente de las mediciones individuales de corrientes o concentraciones y que comúnmente se establecen *ad hoc*. El modelo CRLP se validó y se midió su rendimiento en la capacidad para predecir marcadores relacionados con la arritmia ventricular en comparación con el modelo cellular en el que se había basado.

En el capítulo 3, se actualizó el modelo CRLP desarrollado en el capítulo 2 para introducir la formulación de la dinámica de potasio intracelular ($[K^+]_i$). Esta es una característica importante para la investigación de arritmias ventriculares que surgen en condiciones de hiperpotasemia, uno de los componentes de la isquemia de miocardio. La introducción directa de la dinámica de $[K^+]_i$ en el modelo generó un desequilibrio en las corrientes de potasio que condugeron a una deriva en $[K^+]_i$. Para corregir tal desequilibrio, se propuso un algoritmo de optimización que permitía estimar las conductancias de las corrientes iónicas del modelo CRLP al tiempo que garantizaba valores fisiológicamente plausibles de una selección de propiedades electrofisiológicas, algunas de ellas muy relevantes en el estudio de arritmias ventriculares.

Como se mencionó anteriormente, al proponer un nuevo modelo o al actualizar un modelo existente, la coherencia entre los datos simulados y experimentales debe verificarse considerando todos los efectos y escalas involucradas. Cuanto mejor se reproduzcan las condiciones experimentales en las simulaciones, más robusto será el proceso de desarrollo y validación del modelo. En el capítulo 4, se propuso la simulación de protocolos experimentales *in silico* para analizar cómo las interacciones entre los componentes del modelo afectan el desarrollo y la validación de los modelos matemáticos de canales iónicos; y cómo la propagación afecta los marcadores basados en el potencial de acción cuando son simulados en células aisladas o en preparaciones tisulares, identificando cómo contribuye cada corriente iónica en cada caso.

El modelo CRLP, desarrollado en el capítulo 2 y actualizado en el capítulo 3, presentaba una forma más bien atípica al final de la fase de despolarización del potencial de acción (fase 1). La simulación *in silico* de los protocolos experimentales descritos en el capítulo 4 y la metodología de optimización presentada en el capítulo 3 se utilizaron para mejorar la forma del potencial de acción al tiempo que validaba el modelo ajustado a escalas iónicas, celulares y de tejido.

En el capítulo 6 se integraron todas las formulaciones iniciales y actualizaciones subsiguientes del modelo CRLP propuestas en los capítulos anteriores y se reajustaron las conductancias iónicas del modelo para mejorar el comportamiento del modelo con respecto a medidas electrofisiológicas experimentales. Todas las metodologías introducidas a lo largo de la tesis se utilizaron para obtener un nuevo modelo de potencial de acción ventricular humano. Para la validación del modelo, se consideró un rango de datos experimentales disponibles a diferentes escalas y destinados a evaluar diferentes propiedades electrofisiológicas. Las condiciones subyacentes a cada uno de los estudios experimentales se replicaron tan fielmente como fue posible. Los resultados simulados con la versión final del modelo CRLP se compararon en todos los casos con todas las evidencias experimentales disponibles

y con los modelos de células ventriculares humanas más recientes publicados en la literatura.

El capítulo 7 resume las principales conclusiones de la tesis y presenta nuevas líneas de investigación que podrían emprenderse en futuros estudios. En conclusión, diferentes técnicas para mejorar el desarrollo y la validación de modelos electrofisiológicos cardíacos han sido propuestos y analizados en esta tesis. Basándose en el aumento de potencia computacional, se han considerado nuevas estrategias para reducir el número de hipótesis y/o supuestos al construir un modelo de potencial de acción de cardiomiocito ventricular. La aplicación de un algoritmo de optimización junto con la simulación *in silico* de los protocolos experimentales han ayudado a encontrar un modelo que represente mejor los resultados experimentales de los marcadores electrofisiológicos de riesgo arrítmico.

Index

Contents

Acknowledgment vii

Agradecimientos ix

Abstract xi

Resumen y Conclusiones xiii

Index xvii

Contents xix

List of Figures xxv

List of Tables xxix

Dissertation 1

1 Introduction 3

1.1 Motivation . . . 3

1.2 Electrical and Mechanical Activity of the Heart . . . 4

1.2.1 Excitability of cardiac cells . . . 5

1.2.2 Electromechanical coupling . . . 6

1.2.3 Propagation of the electrical signal throughout the heart . . . 6

1.2.4 The electrocardiogram . . . 8

1.2.5 Acute myocardial ischemia . . . 8

1.3 Modeling the Electrical Activity of the Heart . . . 10

1.3.1 First electrophysiological model of an excitable cell . . . 10

1.3.2 Evolution of electrophysiological models for cardiac cells . . . 14

1.3.3 Human ventricular electrophysiological models: main ionic currents . . . 15
1.3.4 Human ventricular electrophysiological models: recent developments . . . 17
1.3.5 The *Grandi-Pasqualini-Bers* model . . . 18
1.3.6 Acute ischemia models . . . 21
1.4 Objectives and Outline of the Thesis . . . 22
1.4.1 Aim of the thesis . . . 22
1.4.2 Specific objectives . . . 22
1.4.3 Outline of the thesis . . . 23

2 A New Paradigm for Electrophysiological Model Development 27
2.1 Introduction . . . 27
2.2 Methods . . . 28
2.2.1 Selected markers . . . 28
2.2.2 Stimulation Protocols . . . 29
2.2.3 The CRLP Model . . . 31
2.2.4 Conducted Simulations . . . 37
2.3 Results . . . 38
2.3.1 Results for Control Conditions . . . 38
2.3.2 Results for Hyperkalemic Conditions . . . 45
2.4 Discussion and conclusions . . . 48
2.4.1 New model characteristics . . . 49
2.4.2 Simulation of hyperkalemic conditions . . . 49
2.4.3 Data sources . . . 50
2.4.4 Model limitations . . . 50

3 Improvement of Existing Electrophysiological Models 53
3.1 Introduction . . . 53
3.2 Materials and Methods . . . 55
3.2.1 Optimization problem . . . 55
3.2.2 Upgrade of the CRLP model . . . 60
3.2.3 Frequency-dependence behavior . . . 65
3.2.4 Simulation of changes in potassium concentration . . . 65
3.2.5 Implementation . . . 66
3.3 Results . . . 66
3.3.1 Sensitivity Analysis . . . 66
3.3.2 Non-linear optimization . . . 68
3.3.3 Model Comparison . . . 68
3.3.4 Frequency response . . . 71
3.3.5 Response to changes in extracellular potassium . . . 71
3.3.6 Computational Cost . . . 72
3.4 Discussion . . . 73
3.4.1 Response surface optimization . . . 73
3.4.2 Database generation . . . 74

3.4.3 Computational cost . . . 75
3.4.4 Definition of the optimization problem . . . 75
3.4.5 Model comparison . . . 76
3.4.6 Response to potassium concentration changes . . . 76
3.5 Conclusions . . . 77

4 Limitations in Electrophysiological Model Development and Validation 79
4.1 Introduction . . . 79
4.2 Materials and Methods . . . 82
4.2.1 L-type calcium channel gating . . . 82
4.2.2 Characterization of L-type calcium voltage-dependent inactivation . . . 83
4.2.3 Steady-state AP markers . . . 85
4.2.4 Ionic contributors to AP markers . . . 85
4.2.5 Computational simulations . . . 86
4.3 Results . . . 87
4.3.1 Characterization of L-type calcium voltage-dependent inactivation . . . 87
4.3.2 Ionic contributors to AP markers . . . 90
4.4 Discussion . . . 94
4.4.1 Effect of submodel variable interactions in the evaluation of voltage-dependent L-Type Calcium Current inactivation . . . 94
4.4.2 Effect of cell-to-cell interactions in the evaluation of ionic contributors to AP markers . . . 97
4.5 Conclusions . . . 97

5 Reformulation of Ionic Current Expression 99
5.1 Introduction . . . 99
5.2 Methods . . . 100
5.2.1 Modification of I_{CaL} voltage-dependent inactivation time constants . . . 100
5.2.2 Adjustment of I_{CaL} voltage-dependent inactivation steady-state 100
5.2.3 Numerical methods and implementation . . . 103
5.3 Results . . . 104
5.3.1 Solution to the minimization problem . . . 104
5.3.2 New definition of I_{CaL} current . . . 104
5.4 Discussion . . . 106
5.4.1 Development and validation of a new ionic current formulation 107
5.4.2 Reproducing experimental data from different laboratories . . . 107
5.5 Conclusions . . . 108

6 A Human Ventricular Electrophysiological Model with Improved Description of Experimental Behavior 109
6.1 Introduction . . . 109
6.2 Methods . . . 111

6.2.1 Adjustment of ionic conductances . . . 111
6.2.2 Model comparison . . . 120
6.2.3 Model validation . . . 120
6.3 Results . . . 121
6.3.1 Model optimization . . . 121
6.3.2 Model validation . . . 129
6.4 Discussion . . . 129
6.4.1 Model performance . . . 129
6.4.2 Optimization algorithm . . . 133
6.4.3 Validation . . . 134
6.5 Conclusions . . . 135

7 Conclusions and Future Work **137**
7.1 Conclusions . . . 137
7.1.1 Identification of major issues in electrophysiological model development and validation . . . 137
7.1.2 New techniques for improved model development and validation 138
7.2 Future work . . . 139

Appendix **143**

A Publications **145**
A.1 Publications in Journal Articles . . . 145
A.2 Publications in Conference Proceedings . . . 145
A.3 Other Conferences . . . 146

B Description of the First Model **147**
B.1 Model Parameters . . . 147
B.1.1 Physical Constants . . . 147
B.1.2 Enviromental Parameters . . . 147
B.1.3 Fractional Currents . . . 148
B.1.4 Ion Concentrations . . . 148
B.1.5 Sodium Transport . . . 148
B.1.6 Potassium Currents . . . 148
B.1.7 Chlorine currents . . . 149
B.1.8 Calcium Transport . . . 149
B.1.9 SR Calcium Fluxes . . . 149
B.1.10 Buffering . . . 150
B.2 Model Equations . . . 151
B.2.1 Nerst Potentials . . . 151
B.2.2 I_{Na}:Fast Sodium Current . . . 151
B.2.3 $I_{Na,bk}$: Background Sodium Current . . . 152
B.2.4 I_{NaK}: Na-K Pump Current . . . 153
B.2.5 I_{Kr}: Rapidly Activating Potassium Current . . . 153

B.2.6 I_{Ks}: Slowly Activating Potassium Current . . . 153
B.2.7 I_{Kp}: Plateau Potassium Current . . . 154
B.2.8 I_{to}: Transient Outward Potassium Current . . . 154
B.2.9 I_{K1}:Inward Rectifier Potassium Current . . . 155
B.2.10 I_{ClCa}: Calcium-Activated Chlorine Current . . . 155
B.2.11 $I_{Cl,bk}$: Background Chlorine Current . . . 155
B.2.12 I_{CaL}: L-type Calcium Current . . . 155
B.2.13 I_{ncx}: Na-Ca Exchanger Current . . . 158
B.2.14 I_{pCa}: Sarcolemmal Calcium Pump Current . . . 158
B.2.15 $I_{Ca,bk}$: Background Calcium Current . . . 159
B.2.16 SR Fluxes: Calcium Release, SR Calcium Pump, SR Calcium Leak . . . 159
B.2.17 Ion Homeostasis . . . 159
B.2.18 Membrane Potential . . . 161

C Description of the Final Model 163
C.1 Model Parameters . . . 163
C.1.1 Enviromental Parameters . . . 163
C.1.2 Fractional Currents . . . 163
C.1.3 Sodium Transport . . . 163
C.1.4 Potassium Currents . . . 164
C.1.5 Chlorine currents . . . 164
C.1.6 Calcium Transport . . . 164
C.1.7 SR Calcium Fluxes . . . 164
C.2 Model Equations . . . 164
C.2.1 I_{to}: Transient Outward Potassium Current . . . 164
C.2.2 I_{CaL}: L-type Calcium Current . . . 164
C.2.3 SR Fluxes: Calcium Release, SR Calcium Pump, SR Calcium Leak . . . 166
C.2.4 Ion Homeostasis . . . 166
C.2.5 Membrane Potential . . . 166

D Acronyms 167

References 169

List of Figures

1.1 The anatomy of the heart and associated vessels 5
1.2 Isochronic surfaces of the ventricular activation 7
1.3 Different waveforms for each of the specialized cells found in the heart 7
1.4 Electrode positions in the standard 12-lead ECG 8
1.5 The equivalent circuit of the Hodgkin-Huxley model. 11
1.6 Voltage dependence of the particles in the potassium channels of the HH model 13
1.7 Voltage dependence of the particles in the sodium channels of the HH model 13

2.1 Graphical description (using simulation results) of the markers of arrhythmic risk 30
2.2 Characteristics of I_{CaL} and I_{K1} in simulations and experiments 35
2.3 APs computed with the TP06, GPB and CRLP models for isolated cells and 1D tissue at CL = 1000 ms 39
2.4 markers of arrhythmic risk from TP06, GPB and CRLP models . . . 43
2.5 Effect of blocking potassium currents for the GPB and CRLP models 44
2.6 CV and APD_{90} restitution curves for the TP06, GPB and CRLP models in a simulated 1D fiber. 45
2.7 Simulated hyperkalemia in cell and tissue using the CRLP model . . 46
2.8 Behavior of the CRLP model under hyperkalemic conditions in a 1D fiber 47

3.1 Flow chart of the proposed algorithm. 58
3.2 Temporal evolution of $[K^+]_i$ in CRLP and GPB models after introducing $[K^+]_i$ dynamics 61

3.3 Results of the sensitivity analysis applied to the original CRLP model. The blue scale indicates relative sensitivity for each marker. White color indicates maximum relative sensitivity and dark blue color indicates that property and parameter are independent. Percentages in the white boxes indicate the absolute sensitivity of the property. A minus sign in a box indicates that marker and model parameter vary inversely. 'Trian' stands for Triangulation, 'Sys' stands for systolic and 'Dia' stands for diastolic. 67
3.4 Model Comparison Results 69
3.5 Model Comparison Results 70
3.6 Steady-state APD_{90} values as a function of pacing CL. 71
3.7 Results for an unstimulated cell simulated with the modified CRLP model following changes in $[K^+]_o$. a) Temporal evolution of membrane potential; b) Time to achieve 90% of the steady-state membrane potential ($t_{90\%}$). 71
3.8 $[K^+]_i$ evolution following $[K^+]_o$ changes simulated with the modified CRLP model. a) $[K^+]_i$ dependence on $[K^+]_o$ at different time instants; b) time course of $[K^+]_i$ for different $[K^+]_o$ values. 72

4.1 Paired-pulse voltage clamp protocol and measurement of the steady-state value f_{ss} of voltage-dependent inactivation. 84
4.2 Comparison between model definition (continuous and discontinuous lines), *in silico* simulations (yellow crosses) and experimental results (red circles) for f_{ss}. a) TP06 model and data from [1]. b) GPB model and data from [2]. c) ORd model and data from [3]. d) CRLP model and data from [1]. 88
4.3 Temporal evolution of the I_{CaL} gates during simulation of the paired-pulse protocol (see text for specific values of t_{pre}, t_{sep} and t_{pulse} used in the simulations): a) TP06 model. b) GPB model. c) ORd model. d) CRLP model 89
4.4 Contribution of ionic conductances to electrophysiological markers simulated in tissue and cell with the TP06 model. Dark colors (blue or brown) indicate maximum correlation between changes in a conductance and changes in a marker; white color indicates no correlation. Percentages in boxes indicate the contribution of changes in a conductance to changes in a marker. Minus signs indicate that conductances and markers vary inversely; plus signs indicate that conductances and markers vary in the same direction. 92
4.5 Contribution of ionic conductances to AP markers simulated in cell and tissue with the GPB model. The legend of the figure is the same as in see Figure 4.4. 92
4.6 Contribution of ionic conductances to AP markers simulated in cell and tissue with the ORd model. The legend of the figure is the same as in see Figure 4.4. 93

4.7 Contribution of ionic conductances to AP markers simulated in cell and tissue with the ORd_{Na} model. The legend of the figure is the same as in see Figure 4.4. 93
4.8 Contribution of ionic conductances to AP markers simulated in cell and tissue with the CRLP model. The legend of the figure is the same as in see Figure 4.4. 94

5.1 Time constants of I_{CaL} voltage-dependent inactivation in the CRLP model and following the readjustment proposed in this chapter. Comparison with experimental data [2, 4–7] is provided as well. . . . 100
5.2 Effect of varying β_{f2} in the AP shape. Red line represents control conditions. Dark grey lines correspond to reductions in β_{f2}, while light grey lines correspond to increases in β_{f2}. 101
5.3 Effect of varying β_f in the AP shape after having modified β_{f2} in the CRLP model. Red line represents control conditions. Dark grey lines correspond to reductions in β_f, while light grey lines correspond to increases in β_f. 101
5.4 Comparison between the results of the *in silico* simulations for the CRLP model and the adjusted model of this chapter and the experimental results of [1–3]. 106
5.5 Results of tissue simulations computed with the readjusted CRLP model proposed in this chapter. a) AP at a cycle length of 1000 ms. b) $[Ca^{2+}]_i$ at a cycle length of 1000 ms. c) APD adaptation to abrupt cycle length changes. 106

6.1 Action Potential of the different models under control conditions in single epicardial cells: a) optimized CRLP model; b) initial CRLP model; c) GPB model; d) ORd model; e) TP06 model. 123
6.2 APD_{90} variation with CL under the same conditions of the CLVPET dataset. 124
6.3 APD_{90} variation with CL under the same conditions of the CLVPET dataset following ionic current inhibitions: A) 15% I_{Kr} block; B) 70% I_{Kr} block; C) 95% I_{Ks} block; D) Zoomed graphic for 15% I_{Ks} block; E) 75% I_{K1} block. 125
6.4 Simulations of the experiments by Drouin *et al.* [8]: A) APD_{90} variation with CL for epicardial cells. B) Zoomed version of the figure shown in A. C) APD_{90} variation with CL for endocardial cells. D) Zoomed version of the figure shown in C. 127
6.5 Variation in $[Na^+]_i$ under the same conditions of the experiments by Piekse *et al.* [9] for endocardial cells. 128
6.6 Variation in $[Ca^{2+}]_i$ under the same conditions of the experiments by Schmidt *et al.* [10]: A) Diastolic $[Ca^{2+}]_i$ normalized by the value when the frequency is 1Hz; B) Systolic $[Ca^{2+}]_i$ normalized by the value when the the frequency is 1Hz. 128

6.7 Variation in $[Ca^{2+}]_i$ characteristics under the same conditions of the experiments by Coppini *et al.* [11]: A) Difference between systolic and diastolic $[Ca^{2+}]_i$ levels as a function of CL; B) Systolic $[Ca^{2+}]_i$ for different CLs normalized by the value when CL is 1000 ms; C) Time from $[Ca^{2+}]_i$ peak to 50% as a function of CL; D) Time from $[Ca^{2+}]_i$ peak to 90% as a function of CL. 130

List of Tables

1.1 Differences between human ventricular cell models 19

2.1 Results of the sensitivity analysis applied to the GPB model 41
2.2 markers of arrhythmic risk for the TP06, GPB and CRLP human models 42
2.3 Percentages of variation in APD_{90} caused by blocking different potassium currents 42

3.1 Electrophysiological markers evaluated in the proposed response surface approximation-based optimization. 64
3.2 Steady-state values of $[K^+]_i$ for different $[K^+]_o$ values as calculated with the optimized CRLP model. 73
3.3 Computational cost of the different protocols used for the optimization. 73

4.1 Paired-pulse test parameters in experimental protocols. 85
4.2 Comparison of electrophysiological markers simulated in single cell and 1D tissue under control conditions. 90
4.3 Absolute (Ea) and relative (Er) differences between electrophysiological markers in single cell and 1D tissue simulations. 91

5.1 Results of the minimization problem and subsequent validation. Improvement represents the error for each combination of constraints normalized by the error before the optimization. 105
5.2 Evaluation of electrophysiological markers in tissue for the initial and adjusted CRLP models (third and fourth columns). Available physiological ranges are provided in the second column [12]. 105

6.1 Evaluation of APD_{90} and V_{rest} in the TESZT dataset. 113
6.2 Evaluation of variations in APD_{90} in the CLVPET dataset. 114
6.3 Evaluation of APD_{90} in the study by Drouin *et al.* [8]. 115

6.4 Evaluation of $[Na^+]_i$ and its variations in the study by Pieske *et al.* [9]. . . . 115
6.5 Evaluation of $[Ca^{2+}]_i$ and its variations in the study by Schmidt *et al.* [10]. . . . 116
6.6 Evaluation of $[Ca^{2+}]_i$ characteristics in the study by Coppini *et al.* [11]. . . . 117
6.7 Evaluation of time for APD rate adaptation in the study by Pueyo *et al.* [13]. . . . 117
6.8 Results of steady-state AP markers for a CL of 1000 ms computed with the optimized CRLP model and other published human ventricular cell models. . . . 122
6.9 Results of steady-state $[Na^+]_i$ and $[Ca^{2+}]_i$ for a CL of 1000 ms computed with the optimized CRLP model and other published human ventricular cell models. . . . 126
6.10 Results of APD adaptation to abrupt CL changes computed with all tested human ventricular models under the same conditions as in [13]. 129
6.11 Validation results. Steady-state AP markers for a CL of 1000 ms calculated in tissue fibers simulated with the optimized and initial CRLP models. . . . 131

Dissertation

Chapter 1

Introduction

1.1 Motivation

According to data of the World Health Organization, an estimated 17.7 million people died of cardiovascular diseases (CVDs) in 2015. That represents 31% of all global deaths, making these diseases the leading cause of death worldwide. CVDs are caused by different disorders of the heart and blood vessels, which include coronary heart disease (heart attacks), cerebrovascular disease (stroke), raised blood pressure (hypertension), peripheral artery disease. It is also important to note that CVDs are the leading noncommunicable disease (NCD). In 2011, 36 million people died from an NCD, with half caused by CVDs [14]. For this reason, it is necessary to improve the current techniques to detect, diagnose, and prevent CVDs.

In particular, within the group of CVDs, one of the most important causes of sudden death is cardiac arrhythmia, when the heart beats with an abnormal rhythm: too quickly, too slowly, or erratically. Types of arrhythmia include: atrial fibrillation, bradycardia, conduction disorders, premature contraction, tachycardia, and ventricular fibrillation. Typically, a cardiac arrhythmia is caused by an abnormal behavior of the heart's natural pacemaker, a problem in the conduction system to contract the heart, or because another part of the heart starts working as the pacemaker. These pathological situations preclude the heart carrying out its main function: to pump deoxygenated blood to the lungs and oxygenated blood to the rest of the body.

The heart is a complex system that works through the interaction of different elements at different scales, in which its main function is performed by a mechanical action that is electrically controlled. Mathematical modeling and simulation of the heart's electrical activity (so-called cardiac electrophysiology) and signal processing of bioelectrical signals provide an ideal framework for joining the information from clinical and experimental studies with the understanding of the mechanisms underlying them. Tools capable of testing different hypotheses and

predicting potential abnormalities in the heart's behavior can be produced within such a framework, and, in a relatively near future, they may be used in clinical practice as complementary instruments to help in the prevention of cardiac diseases and in the improvement of their diagnosis and therapy. In particular, for the study of ventricular arrhythmias, the utilization of an *in silico* model of the heart could improve understanding of the heart function, how different pathologies are developed, and how they are expressed. Nevertheless, it remains essential to have an action potential (AP) model able to reproduce experimentally and clinically observed arrhythmic behaviors at the cell and tissue levels. This would allow simulation of the electrical activity of the heart from cell to body surface. Then, a total *in silico* reconstruction of the most well known bioelectrical signal, the electrocardiogram (ECG), could be used for investigating the mechanisms and manifestations of ventricular arrhythmias at different scales.

Due to the number of factors to be considered during the development of a model, the interrelationships between them, and the need to preserve the improvements obtained by previous models, it is necessary to develop novel methodologies that help control the design, modification, and validation of new models. These new methodologies should help control all elements of the model during its development, from the definition of the ionic gates to the combination in multiscale models, and to consider the implication of any definition or modification in the simulation of the entire heart.

In the following sections, a general introduction is presented on how the heart works (mainly from an electrical point of view), how the behavior of the heart is affected by disease or by pathological conditions and how mathematical models can be used to study the heart in physiological and pathological conditions. Subsequently, a description is provided on the electrical conduction system of the heart and on the range of involved spatio-temporal scales. Next, the evolution of cardiac electrophysiological models and the main components of a model of human ventricular cells are analyzed. Finally, the *Grandi-Pasqualini-Bers* (GPB) model of human ventricular cells [15], used as a starting point for this thesis, is studied. The chapter end with the main objectives and a short outline of the different studies described in this thesis.

1.2 Electrical and Mechanical Activity of the Heart

The heart is a volumetric pump that beats at 75 beats per minute and moves more than five liters of blood. It consists of four chambers, the left and right ventricles, and the left and right atria (see Figure 1.1). Deoxygenated blood enters the heart through the right atrium, and, from there, flows through the tricuspid valve to the right ventricle and is pumped to the lungs. Oxygenated blood returns from the lungs through the left atrium, then, flows to the left ventricle through the mitral valve. Once, the blood is in the left ventricle, it is pumped through the aortic valve to the systemic circulation. Under normal conditions, all of these phases are timed and synchronized, and this permits the blood to circulate and to transport oxygen and other nutrients throughout the body. This mechanism works because

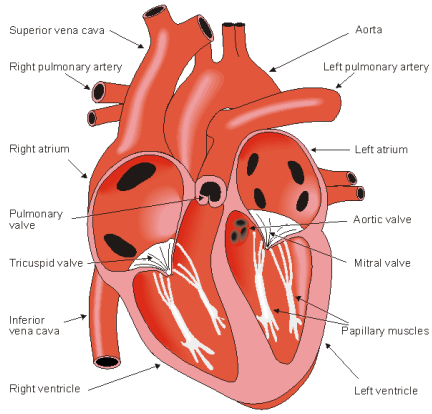

Figure 1.1: The anatomy of the heart and associated vessels, and orientation of cardiac muscle fibers. Figure from [16].

of the electromechanical coupling of the cardiac cells, and to a complex system that propagates the electrical signals to obtain a coordinated contraction of the heart.

1.2.1 Excitability of cardiac cells

Cardiac muscle cells (or cardiomyocytes) are excitable cells, that is, when a stimulation current pulse depolarizes the resting membrane of a cardiomyocyte beyond the threshold voltage, then an action potential (AP) is generated. During an AP, the membrane potential (the potential at the inner surface relative to that at the outer surface of the membrane), rises rapidly at the beginning (depolarization). This first depolarization phase is followed by a small decrease in the action potential (*dome*) to then enter the third phase (*plateau*) where the membrane potential is held at a high voltage for few milliseconds prior to enter the repolarization (the fourth phase), in which the membrane potential recovers its resting value (the fifth and last phase).

The membrane potential is caused by the difference of concentration between the ions in the intracellular and extracellular compartments. The three main ions present in the cardiomyocytes are sodium (Na^+), potassium (K^+) and calcium (Ca^{2+}). When an external stimulus is applied, an initial upstroke is generated by the inward flux of sodium ions through the corresponding sodium channels. After the first phase, the sodium channels close and the transient outward potassium current is activated and attempts to return the cell to its resting state. The outward potassium current is compensated by and inward calcium ion flux and therefore slow down the decrease in the potential during the *plateau* phase. Calcium channels begin closing while slow potassium currents begin acting until the cell recovers its initial resting state. In cardiac muscle, the activation of one cell can propagate to the neighbor cells, and, as a result, the activation generates complex wavefronts that propagate through the cardiac tissue.

1.2.2 Electromechanical coupling

When the membrane of the myocyte is depolarized, the channels that allow the passage of calcium ions through them are open. Most of these ions enter through the L-type calcium channel to a subspace called the dyadic space, which is formed by the T-tubule (an extension of the cell membrane) and the close proximity of the sarcoplasmic reticulum (the internal store for calcium). When calcium enters, the concentration in the dyadic space elevates and it triggers the opening of the ryanodine receptors in the sarcoplasmic reticulum. This launches a process known as calcium-induced calcium release, during which, the calcium input into the cell is amplified with the calcium present in the sarcoplasmic reticulum (SR). Free calcium present in the cytosol binds to troponin and calmodulin favoring myofilament contraction. The joint action of many cardiac cells contracting in an orderly way in a small period of time causes the blood to be pumped by the heart.

1.2.3 Propagation of the electrical signal throughout the heart

As explained in the previous sections, the cardiac tissue is electrically excitable and its excitation propagates through the tissue. In addition, when a cardiac tissue is excited, it contracts because of the electromechanical coupling described previously. These two phenomena are fundamental for the correct functioning of the heart, but its proper operation also depends on the regulation and synchronization of the different cardiac chambers.

The *pacemaker* of the heart is the sinoatrial (SA) node which is located in the right atrium at the superior vena cava. It consists of specialized self-excitatory muscle cells that are self-activated at the rate of about 70 beats per minute. From the sinus node, activation propagates throughout the atria, but it cannot propagate directly to the ventricle because a barrier of fibrous tissue is present. To do this, the activation propagates first through the atrioventricular (AV) node, which is located at the boundary between the atria and ventricles and which delays the excitation of the ventricular tissue due to a very low conduction velocity (CV): 2-5 cm/s (e.g. the CV of the atria is between 80 and 100 cm/s) [16]. Activation wavefront takes an estimated 75 ms to cross the AV node. Because of this, the atria contract and pump the blood to the ventricles when they are still relaxed.

Once the activation traverses the AV node, it travels through a *common bundle*, called the *bundle of His* which later separates into two bundle branches: the *right* and *left bundle branches*. Finally, these branches ramify into the *Purkinje fibers* that are connected to the ventricular walls and, through them, the activation is spread in the ventricle from many different locations. The ventricles, which have the blood coming from the atria, contract with the propagation of the electrical activation and pump the blood to the lungs and the rest of the body.

Figure 1.2 illustrates the isochronic surface of the activation in the ventricles. The image is from [16] with data from [17].

Different AP shapes can be found at the various types of cardiac cells in the heart. Figure 1.3 illustrates them with a delay similar to the one that is normally found in a healthy heart.

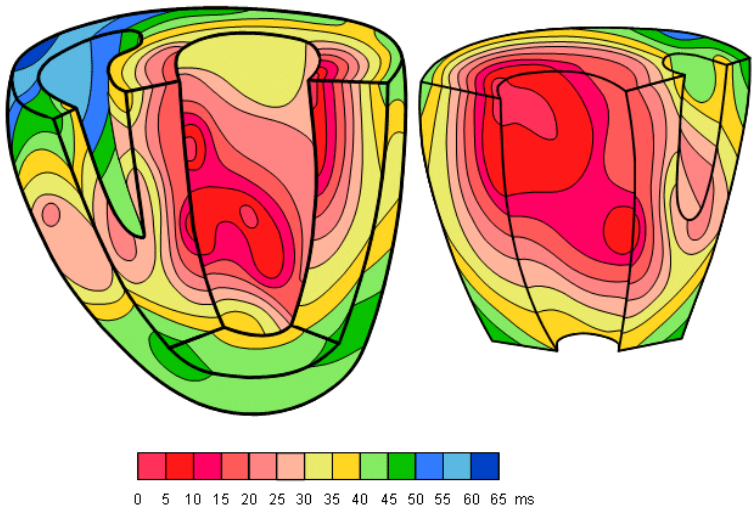

Figure 1.2: Isochronic surfaces of the ventricular activation. Image from [16] with data from [17].

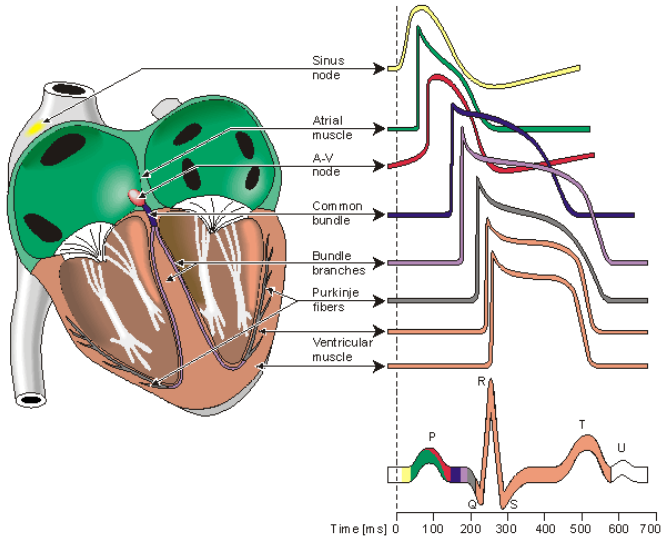

Figure 1.3: Different waveforms for each of the specialized cells found in the heart are shown. The latency shown approximates that normally found in the healthy heart. Image from [16].

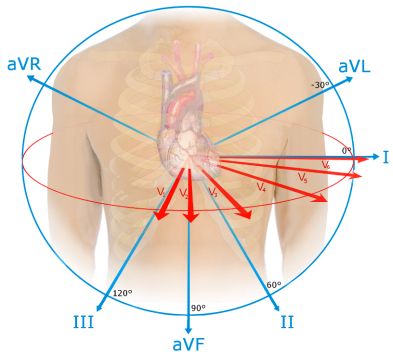

Figure 1.4: Electrode positions in the standard 12-lead ECG. Image created by Nicholas Patche, Boston Medical Center (CC BY-SA 4.0).

1.2.4 The electrocardiogram

The ECG is a tool that can be used to assess the electrical and muscular activities of the heart. It records the electric potential on the surface of the thorax that has been generated by the electrical activity of cardiac cells. To measure it, electrodes can be placed on the thorax that will record various electric signals depending on their positions. Figure 1.4 illustrates, the standard 12-lead ECG is presented.

As depicted in Figure 1.3, the depolarization and repolarization of the cardiac cells is represented in the following parts of the ECG:

- The atrial depolarization generates the P-wave.
- The ventricular depolarization corresponds to the QRS-complex that hides the atrial repolarization.
- The ventricular repolarization corresponds to the T-wave.

The use of the ECG is widespread in clinical practice because it is a non-invasive test that provides significant information about cardiac electrical events. One of the limitations of the ECG is that it offers simultaneous information in different spatio-temporal scales. The main limitation of this measurement is that, in many cases, some information could be masked by other events in the heart or by the effect of the propagation. In-silico models of the electrical activity of the heart is a powerful tool to solve this limitation, and to help in the better understanding of the ECG, because this technique permits simultaneous observation of what is happening in each of the involved scale.

1.2.5 Acute myocardial ischemia

In previous sections, heart's behavior under physiological conditions and its primary function of pumping blood to the body have been described. However, many pathologies and diseases can lead to cardiac malfunctioning. From the electrical

point of view, when an alteration of the normal conditions generates an abnormal propagation of the electrical waves from the SA node to the rest of the heart, due to the electromechanical coupling the heart would not be able to contract properly, and consequently, would not be able to pump blood to the rest of the body. The arrhythmias are among the most important causes of sudden death. They can be generated by two main mechanisms: abnormal automaticity and abnormal conduction.

Injured or damaged tissue can conduct slowly or act as an obstacle (no conducting tissue) causing an abnormal anatomical conduction. Conversely, abnormal behavior of myocardial cells associated with channelopathies or the influence of certain drugs can generate an abnormal automaticity. This could cause heart beats that originate not in the SA node (ectopic beats) but ones that can degenerate into different types of arrhythmias grouped into two large families: supra ventricular arrhythmias and ventricular arrhythmias. Supra ventricular arrhythmias are associated with arrhythmic behaviour of the upper part of the heart (the atria). On the contrary, ventricular arrhythmias are associated with the lower part of the heart, and are of two types –ventricular tachycardia or ventricular fibrillation– [18, 19]. Many pathological conditions can result in a ventricular tachycardia or fibrillation, but one of the most important perpetrators is ventricular ischemia caused by the obstruction of one of the main coronary arteries. When the flow of blood is partially interrupted by this blockage, the flow of oxygen and glucose to the muscle cells and the washout are also interrupted within the affected region [20]. This situation generates mainly three effects: a reduction in oxygen (hypoxia), an increasing of the extracellular potassium (hyperkalemia), and an acidification of the tissue (acidosis). Under these effects, the AP suffers significant alterations: the excitability of the cell and the conduction velocity in the tissue are reduced, and the effective refractive period (ERP) is increased [20, 21]. In addition, all of these changes appear with a high degree of heterogeneity which makes it an important pro-arrhythmic substrate.

Although the pro-arrhythmic mechanisms under acute ischemia have been extensively investigated, they are not yet fully understood. Many studies have attempted to shed some light on this phenomenon, primarily using animal models instead of human ventricles, as for example Janse *et al.* in porcine [22] and canine subjects [21]. Experimental studies demonstrated that, this heterogeneity (mainly in the border between the ischemic and the healthy zones) leads to the establishment of reentries around the ischemic zone [21, 23]. When these phenomena appear under ischemic conditions, they could separate the rhythm of the heart from the one marked by the SA node and cause it to beat in a disorderly fashion.

Myocardial ischemia is clinically recognized when a ST-segment depression is detected in the ECG [24, 25]. However, the mechanisms behind this depression remain under discussion and other techniques are being explored to attempt to increase the detection capacity. Due to the complexity of the problem and to the different scales involved, computer simulations of three dimensional human hearts have been used to study this pathology to better understand the mechanisms of reentry formations and maintenance under myocardial ischemia.

1.3 Modeling the Electrical Activity of the Heart

Cardiac electrophyisiological models can be used to simulate the electrical behavior of one myocyte, a fiber of cardiac cells, a tissue, or the entire heart. This wide range of possibilities enables their use in many different situations and for many purposes. The primary reasons to use these models can be summarized in the following ideas:

- *Reduce animal experimentation*: The development and validation of medical drugs require different phases. One is the experimental validation of the drug: before testing the drug in humans, it can first be tested in animal models.

- *Increase electrophyisiological cardiac knowledge*: One of the limitations of the *in vivo* or *in vitro* experiments is that only a few variables can be measured at the same time during the experiment. The *in silico* simulation of the electrical activity of the cardiac cells permits simultaneous study of all parameters of interest, improving understanding of the mechanisms behind a normal or a pathological behavior of the cell. Given that models are limited by their imperfections or the lack of knowledge of some parts of the cell, their proper use must include awareness of the model limitations, consideration during the research process, and careful use.

- *Assist the decision-making process*: Once a patient has been diagnosed, it is important to consider his specific characteristics to determine the most effective treatment. The dosage of a medical drug and the area of a tachycardic heart to be ablated are among the many example situations in which the simulation of the patient's heart could result in a more accurate treatment.

1.3.1 First electrophysiological model of an excitable cell

The first action-reaction electrophysiological model was proposed by Alan L. Hodgkin and Andrew F. Huxley and their colleagues at Cambridge [26]. This model was possible because of their measurements of the electrical activity of the squid giant fiber with the voltage clamp technique. With the results of the measurements, they proposed a model in which the cell was described as an electrical circuit in which ionic currents pass through the ionic channels that act as resistances, and the membrane work as a capacitor. The electrical activity of the squid giant fiber was described using four currents: one of sodium (I_{Na}), another of potassium (I_K), a small *leakage current* (I_l), that represents the current carried by other ions, and the capacitive current. Each of these currents uses its own path or channel in the cell, and for this reason, this model is called the *parallel conductance model* or the *chord conductance model* [27]. In the original formulation of the *Hodgkin-Huxley* (HH) model a current from the outside to the inside was represented by a positive current, but in this thesis the current notation that represents a current from the inside to the outside as a positive one is used [16] (see Figure 1.5).

Two forces move the ions into or out of the cell: diffusion and electrostatic attraction. For a type of ion, when these two forces are equals in magnitude but

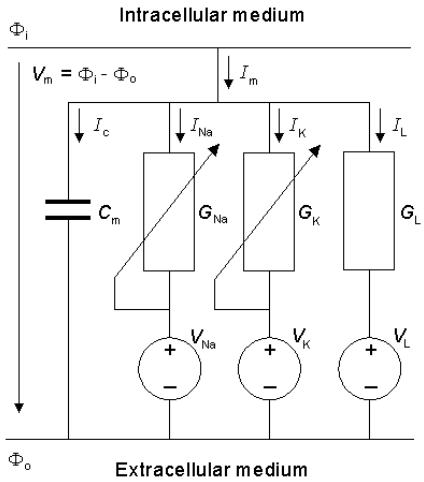

Figure 1.5: The equivalent circuit of the Hodgkin-Huxley model. The voltage sources show the polarity of the positive value. The calculated Nernst voltages of sodium, potassium, and chloride designate the value of corresponding voltage sources. Image from [16].

opposite, this ion is in equilibrium. The equilibrium voltage of an ion is called the *Nernst potential* and is defined as follows [28]:

$$V_K = -\frac{R \cdot T}{z_k \cdot F} \log\left(\frac{[k]_i}{[k]_o}\right) \tag{1.1}$$

where V_K is Nernst potential for the ion k, R is the gas constant, T is the absolute temperature, z_k is the valence of the ion k, F is the Faraday's constant, $[k]_i$ is the intracellular concentration of the ion k, and $[k]_o$ is the extracellular concentration of the ion k.

The diffusion force is modeled as a voltage source in the HH model using the Nernst potential, and the ion permeability of the membrane for the different ions is modeled with a conductance per unit area (based on Ohm's law) as follows:

$$G_K = \frac{I_k}{V_m - V_K} \tag{1.2}$$

where G_K is the membrane conductance per unit area for the ion k, I_k is the electric current carried by the ion k per unit area, V_K is the Nernst voltage for the ion k, and V_m is the membrane voltage.

Hodgkin and Huxley assumed that each type of ion passes only through a specific channel for it; they also supposed that the opening and closing of the channels are controlled by electrically charged particles. The probability that one of this particles is in an open state depends on the membrane voltage. So, they

defined the ionic conductance for each channel as the product between the maximal conductance of the channel (a constant value) and the fraction of particles in open state, but, as is explained in [16], they did not make any assumptions on the chemical or anatomical nature of these particles.

They modeled mathematically the fraction of them in an open state with ordinary differential equations as follows:

$$\frac{dg}{dt} = \alpha_g \cdot (1 - g) - \beta_g \cdot g \tag{1.3}$$

where α_g is the transfer rate coefficient for particles from closed to open state, β_g is the transfer rate coefficient for particles from open to closed state, g is the fraction of particles in the open state and $(1 - g)$ is the fraction of particles in the closed state.

Using the previous equation the steady-state values of the fraction of them in an open state and the constant time they need to reach the steady-state can be obtained:

$$g_{ss} = \frac{\alpha_g}{\alpha_g + \beta_g} \tag{1.4}$$

$$\tau_g = \frac{1}{\alpha_g + \beta_g} \tag{1.5}$$

During a voltage-clamp experiment, the fraction of particles in an open state will follow this expression:

$$g(t) = g_{ss} + (g_{ss} - g_0) \cdot e^{-\frac{t}{\tau_g}} \tag{1.6}$$

where g_0 is the fraction of particles in an open state at the beginning of the experiment.

According to the definition proposed by Hodgkin and Huxley, each channel can have more than one type of particles and can need more than one particle in open state to permit to the ions to pass through itself. For example, in the HH model, the potassium channels are formed by four particles of type n, and the sodium ones are formed by three of type m and one of type h. The potassium and sodium conductances in the HH model are defined as follows:

$$G_K = G_{K,max} \cdot n^4 \tag{1.7}$$

$$G_{Na} = G_{Na,max} \cdot m^3 \cdot h \tag{1.8}$$

where $G_{K,max}$ and $G_{Na,max}$ are the maximal conductances of the potassium and sodium channel respectively.

The particles of type n and m are particles of activation. Under the resting potential they are not in the open states and when the voltage increases, the fraction of particles in the open state increases (see Figure 1.6 and Figure 1.7). On the contrary, the h particles are deactivation ones. When the voltage tend to

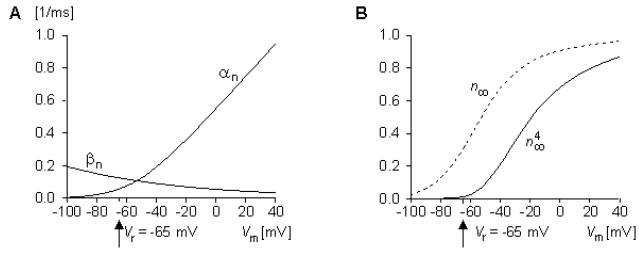

Figure 1.6: Voltage dependence of the particles in the potassium channels of the HH model. (A)Variation of transfer rate coefficients α_n and β_n, (B) Variation of n and n^4 as functions of membrane voltage. Image from [16].

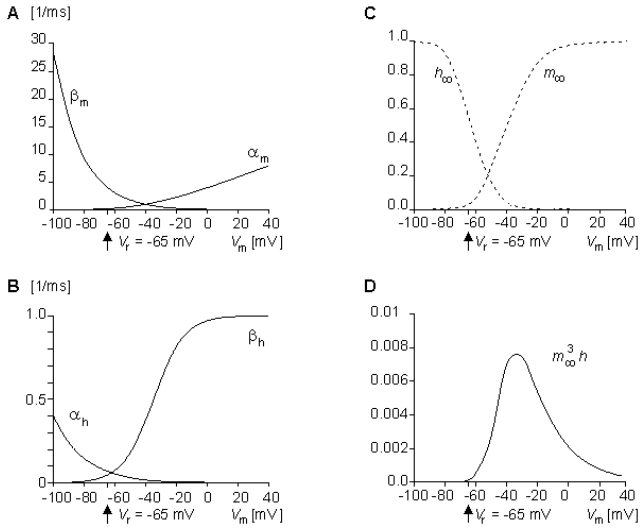

Figure 1.7: Voltage dependence of the particles in the sodium channels of the HH model. (A) α_m and β_m, (B) α_h and β_h, (C) m and h, and (D) $m^3 \cdot h$ as a function of membrane voltage. Image from [16].

minus infinity all the particles are in the open state but when the voltage increases, the fraction of particles in the open state is reduced (see Figure 1.7).

The total transmembrane current density in the HH model is the sum of the capacitive and ionic currents as follows:

$$I_m = C_m \cdot \frac{dV_m}{dt} + (V_m - V_{Na}) \cdot G_{Na} + (V_m - V_K) \cdot G_K + (V_m - V_K) \cdot G_L \qquad (1.9)$$

where I_m is the membrane current per unit area; C_m is the membrane capacitance per unit area; V_m is the membrane voltage; V_{Na}, V_K and V_K are the Nernst potential for sodium, potassium and leakage ions respectively; and G_{Na}, G_K and G_L are the sodium, potassium, and leakage conductance per unit area respectively.

When the cell is in an open circuit, there cannot be axial current since there is no potential gradient in the axial direction. Under this situation, the previous equation can be expressed as follows:

$$\frac{dV_m}{dt} = -\frac{1}{C_m} \cdot ((V_m - V_{Na}) \cdot G_{Na} + (V_m - V_K) \cdot G_K + (V_m - V_K) \cdot G_L) \qquad (1.10)$$

1.3.2 Evolution of electrophysiological models for cardiac cells

While the Hodgkin and Huxley equations were empirically derived, their formalism continues to be used, and most of the electrophysiological models developed after Hodgkin and Huxley (nerve models, cardiac models, and neuronal models, for example) follow the formalism they proposed.

Ten years after the HH model, Denis Noble proposed the first model of cardiac cell in which he adapted the HH model to represent the electrophysiological behavior of a Purkinje cell [29]. The first cardiac electrophysiological models were developed to explain the main differences between the heart cells and the nervous cells: the AP duration [30]. Soon, these models became more complex by incorporating the different ionic currents that were being discovered. Initially, the potassium current was separated into two new currents: I_{K1} and I_{K2} [31–33]. Later, Sanguinetti and Jurkiewicz discovered that the I_{K2} current was made up of two components: I_{Kr} and I_{Ks} [34]. However, it was not until 1964 that voltage-clamp experiments allowed the discovery of the calcium current [35]. Step by step, other elements were incorporated to the models as the *sodium-calcium exchanger* (I_{ncx}) and the homeostasis of the intracellular concentrations [36].

Similarly, the models were adapted to different cell types: ventricle [37], atrium [38]; and different species: rabbit [38, 39], guinea pig [40, 41], dog [42, 43], and human [44–47], for example.

One of the possibilities of cellular action potential models is that they can be incorporated into cellular network models to simulate cardiac tissue [48–51] and study the behavior of the entire organ under pathological situations or before the effect of drugs.

1.3.3 Human ventricular electrophysiological models: main ionic currents

An electrophysiological cardiac model describes the membrane potential of a cardiac cell and is composed of different currents that pass through the cell membrane. As described for the HH model, these currents are generated by the passage of ions through different channels, exchangers, and pumps that connect the intracellular and the extracellular media. Each current is formulated mathematically to represent the various effects that occur in the channels (for example, activation and inactivation of ion channels) and these models also include the balance between the intracellular and extracellular ionic concentrations, and between the different compartments of the miocyte. In the cases of the human ventricular models, the most important ions for the modeling of the AP are: sodium (Na^+), potassium (K^+), and calcium (Ca^{2+}). While there are many differences between the existing human ventricular cell models, the main currents are present in all of them. In the following subsections, the principal ones are described.

Sodium current

The fast sodium current (I_{Na}) is the main sodium current in human ventricular cells. There exists also the late sodium current (I_{NaL}) but this current plays a relevant role only under pathological conditions (for example, LQT3 or HF [52]). I_{Na} is mainly modeled following the formalism proposed by Hodgkin and Huxley, with three activation gates of type m and two inactivation gates (j and h).

Potassium currents

Four potassium currents are mostly present in the human ventricular cell models. Three correspond to voltage-gated ion channels (K_v), whereas the fourth is an inward rectifying current. K_v channels are the most diverse super-family of ion channels and have a significant impact on AP shape and duration. These differences are related to the cell type and function, but also to differences among various species [52]. These differences make it important to use data from human cardiomyocytes for the characterization of these currents.

Transient outward potassium current (I_{to}): This voltage gated current activates and inactivates rapidly during the depolarization phase of the action potential. It can be divided into two components ($I_{to,f}$ and $I_{to,s}$).Both components activate rapidly following membrane depolarization. On the contrary, $I_{to,f}$ inactivates rapidly whereas $I_{to,s}$ inactivates slowly (compared to $I_{to,f}$). While not all of the models divide the current into two components, all define it with two voltage-dependent gates (one for activation and another one for inactivation). The major difference between models lies in how they model the differences between the ventricular cell types: by varying the conductance, by modifying the proportion of the fast and the slow component, or both together.

Rapidly activation potassium current (I_{Kr}): This current activates rapidly upon depolarization [53]. The activation occurs faster than inactivation ($\tau_{act} > 100ms$, $\tau_{inact} < 20ms$) [52]. In all of the recent human ventricular cell models, this current is modeled with two voltage-dependent gates (one for activation and another for inactivation) and uses the Nernst potential following the HH formalism.

Slowly activation potassium current (I_{Ks}): This slow component of the total potassium current is much smaller than I_{Kr} and plays an less significant role in the APD [54]. When this current is blocked, and in the absence of sympathetic stimulation, the role played by I_{Ks} is quite small. However, when the ventricular muscle repolarization reserve is attenuated, the role of this current in limiting AP prolongation becomes significant [55]. This current is generally modeled using the Nernst potential and with two voltage-dependent activation gates. In most parts of the models, the two voltage-dependent gates are the same.

Inward rectifier potassium current (I_{K1}): This current is present in all ventricular and atrial myocytes and plays a major role in the action potential repolarization [56]. It is usually modeled with one voltage-dependent and time-independent gate, and the formulation used for this gate also makes use of the Nernst potential following the HH formalism.

Calcium current

The *L-type calcium current* (I_{CaL}) is the principal current for the entry of calcium in the cardiac cells and it is typically modeled using the *Goldman-Hodgkin-Katz* equation. This current plays an important role during the *plateau* phase of the action potential, in the action potential duration, and in the shape of the repolarization.

The L-type calcium channels are frequently modeled by a voltage-dependent activation gate (d), by one or more voltage-dependent inactivation gates (f, $f2$), and by calcium-dependent inactivation gates.

Pumps and exchangers

The previous currents modeled the behavior of ionic channels, through which the ions pass without needing energy expenditure. However, there are also currents in the cell caused by the movement of ions against gradient that require consuming ATP (pumps), or by using the force of ions that pass in the direction of the gradient (exchangers). Two of these types of currents are present in most human ventricular cell models: the sodium-potassium pump current and the sodium-calcium exchanger current.

Sodium-potassium pump(I_{NaK}): The sodium-potassium pump current is the principal mechanism for active ion transport across the membrane of excitable cells [57]. In addition, it plays an important role in regulating cardiac electrophysiology

under physiological and pathological conditions. Two schemes have become predominant for modeling this current: the first one proposed by Di Francesco and Noble in their seminal work [36], and the second one corresponding to it [58]. The DiFrancesco–Noble formulation is mostly present in the majority of the models for the specialized conduction system (sinoatrial node and Purkinje fiber models), and, on the contrary, the Luo–Rudy formulation results predominate in mathematical models of atrial and ventricular cardiac myocytes.

Sodium-calcium exchanger current (I_{ncx}): The sodium-calcium exchanger plays an important role in the regulation of intracellular calcium concentration ($[Ca^{2+}]_i$). This exchanger regulates muscle relaxation in cardiac myocytes [59]. This current is usually modeled following the formulation proposed by Mullins [60] and simplified by DiFrancesco and Noble [36]. In this formulation, the sodium calcium exchanger current is modeled as a time-independent current, with the value of the current being dependent on the intracellular and the extracellular concentration of Na^+ and Ca^{2+} ions, and on the membrane potential.

1.3.4 Human ventricular electrophysiological models: recent developments

In recent years a number of mathematical models of electrical and ionic homeostasis in human ventricular myocytes have been proposed. One of the most extensively used models is that proposed by *ten Tusscher-Panfilov* (TP06) [51], which is an improved version of the *ten Tusscher-Nobel-Nobel-Panfilov* (TNNP04) model [46], in which the calcium dynamics, the slow delayed rectifier potassium current (I_{Ks}) and the L-type calcium current (I_{CaL}) were reformulated. Both the TNNP04 and the TP06 models are based on experimental human data for most of the main ionic currents. One of the major advantages of the TP06 model over previous human ventricular models is that it accurately reproduces restitution of the AP duration (APD). Conversely, the TP06 model presents the major shortcomings of being insensitive to changes in certain ionic current densities [61] and of inadequately representing rate dependence of intracellular calcium levels [12].

Another relevant model of human ventricular cells was proposed by Iyer *et al.* (IMW04) [45]. This model provides a detailed description of calcium homeostasis and reproduces diverse aspects of the excitation-contraction coupling (ECC). However, important limitations have been reported for this model, including the fact that it is extremely sensitive to variations in the sodium potassium pump (I_{NaK}) and to the inward rectifier potassium (I_{K1}) current densities [61]. It also produces quite long APs and relatively flat restitution curves in tissue [62]. In addition, the most relevant ionic currents in the IMW04 model are described using Markovian chains, with the consequent increase in complexity (more than 60 state variables), which imposes serious restrictions on the size of the time step required for stability and increases the overall computational time when using this model in tissue simulations [62].

At the beginning of this thesis, a new model of human ventricular AP was proposed by Grandi *et al.* (GPB) [15]. The development of this model departs from

the rabbit ECC model proposed by Shannon *et al.* [63], which includes the subsarcolemmal and junctional compartments in the formulation of the currents and provides a detailed description of calcium handling. The GPB model includes new definitions of ionic current densities and kinetics according to recent experimental data on human myocytes. This model is defined for two types of cells, namely endocardial and epicardial. These two cell types differ only by the maximal conductivity of the fast and slow components of the transient outward potassium current (I_{to}). The GPB model improves the AP response to frequency changes and offers a better performance against blockades of potassium currents (I_{K1}, I_{Ks} and the rapid delayed rectifier potassium current I_{Kr}) with respect to the TP06 model. The major drawback of the GPB model is that it does not adequately reproduce S1S2 restitution properties nor APD rate adaptation dynamics. These drawbacks can be attributed to the fact that the GPB model was developed from a rabbit ventricular model, and the characteristics of S1S2 restitution and APD rate adaptation are notably different in the two species.

Parallel to the development of this thesis, O'Hara *et al.* proposed the *O'Hara-Rudy-dynamic* (ORd) model [64]. This new ventricular cell model is based on the most extended data set of healthy human cells. Data from more than 100 healthy human hearts were used to examine the steady state rate dependence, and restitution of the ventricular AP. The model was also studied under the effect of drugs that selectively block different channels (for example, mexiletine, ryanodine, nisoldipine, and E-4031). As it will be discussed later, the complexity of this model is greater than that of previous models. The major drawback of the ORd model is the rate dependence of the intracellular calcium ($[Ca^{2+}]_i$): While under physiological conditions $[Ca^{2+}]_i$ increases about a 30% with frequency, in the ORd model it increases about 300%.

In 2015, Himeno *et al.* proposed a new human ventricular cell model [65]. As opposed to the previously described models, the Himeno et al. model included a description of excitation-contraction. The model comparison performed in the present study was restricted to purely electrophysiological models.

Table 1.1 presents a summary with the main differences among the four models described above, i.e. TP06, IMW04, GPB and ORd.

1.3.5 The *Grandi-Pasqualini-Bers* model

When this thesis was started, the most detailed and recent human ventricular cell model published in the literature was the GPB model. Since the objective of the thesis was to computational modeling and simulation for the investigation of ventricular arrhythmias under ischemic conditions, the GPB model was taken as a starting point. After performing an in-depth evaluation on the ability of this model to represent experimental behavior in relation to a number of electrophysiological properties, the necessity to update the GPB model for the study of arrhythmias was identified. In this thesis different methodologies for the development and validation of an electrophysiological cardiac model are introduced and applied to update the GPB model. In this section a detailed description of the GPB model is presented.

	TP06	**IMW04**	**GPB**	**ORd**
♯ State variables	20	67	38	41
Computation time	Short	Very long	Long	Long
Cell types	Endo, mid, epi	Epi	Endo, epi	Endo, mid, epi
Steady-state AP properties	Physiological APD values, very low triangulation	Physiological APD values and triangulation	Physiological APD values and triangulation	Short APD values, but physiological triangulation
Steady-state calcium levels	Low diastolic and systolic values	Low diastolic and systolic values	Very low diastolic and systolic values	Low diastolic and systolic values
APD_{90} adaptation to abrupt heart rate changes	Very fast	Very slow	Rabbit characteristics	Physiological behavior
Sodium and calcium rate dependence	Very sensitive to increasing stimulation frequency	Physiological behavior	Physiological behavior	Very sensitive to increasing stimulation frequency
APD sensitivity to variations in ionic current densities	Lowly sensitive to I_{NaK}, $I_{Na,Ca}$, I_{Ks}, I_{K1}, I_{CaL}, I_{Kr} and I_{Na}	Highly sensitive to I_{NaK} and I_{K1}	Lowly sensitive to I_{Kr} and highly sensitive to I_{K1}	Lowly sensitive to I_{K1}, I_{CaL} and $I_{Na,Ca}$, and highly sensitive to I_{Kr}

Table 1.1: Differences between human ventricular cell models. Data are obtained from [12, 61, 62, 64] and from simulations performed in this thesis.

The GPB model describes the AP of endocardial and epicardial human myocytes. For both cell types the total transmembrane ionic current, I_{ion}, is given by:

$$I_{ion} = I_{Na_{tot}} + I_{Cl_{tot}} + I_{Ca_{tot}} + I_{K_{tot}},$$

where each of the individual currents denotes the current generated by the passage of sodium, chlorine, calcium, and potassium ions, respectively, through the cell membrane.

Sodium current. Following the approach of Shannon *et al.* [63], the sodium current was divided into two components: i) a subsarcolemmal component, and ii) a junctional component, which correspond to the cell compartments where the current is generated. Both components are formed by the same subcurrents:

$$I_{Na_{tot_{junc}}} = I_{Na_{junc}} + I_{Na,bk_{junc}} + 3 \cdot I_{ncx_{junc}} + 3 \cdot I_{NaK_{junc}} + I_{CaNa_{junc}}$$

$$I_{Na_{tot_{sl}}} = I_{Na_{sl}} + I_{Na,bk_{sl}} + 3 \cdot I_{ncx_{sl}} + 3 \cdot I_{NaK_{sl}} + I_{CaNa_{sl}}$$

$$I_{Na_{tot}} = I_{Na_{tot_{junc}}} + I_{Na_{tot_{sl}}}$$

where I_{Na} is the fast sodium current, $I_{Na,bk}$ is the background sodium current, I_{ncx} is the current of the sodium-calcium exchanger, I_{NaK} is the current of the sodium-potassium pump, and I_{CaNa} is the sodium current through the L-type calcium channels.

Chlorine current. The chlorine current, which is not present in other previous model as in TP06 or TP04. In the GPB models this current is described by:

$$I_{Cl_{tot}} = I_{ClCa} + I_{Cl,bk}$$

where I_{ClCa} is the calcium-activated chlorine current, and $I_{Cl,bk}$ is the background chlorine current.

Calcium current. The calcium current, as in the case of the sodium current, has two components, junctional and subsarcolemmal:

$$I_{Ca_{tot_{junc}}} = I_{Ca_{junc}} + I_{Ca,bk_{junc}} + I_{pCa_{junc}} - 2 \cdot I_{ncx_{junc}}$$

$$I_{Ca_{tot_{sl}}} = I_{Ca_{sl}} + I_{Ca,bk_{sl}} + I_{pCa_{sl}} - 2 \cdot I_{ncx_{sl}}$$

$$I_{Ca_{tot}} = I_{Ca_{tot_{junc}}} + I_{Ca_{tot_{sl}}}$$

where I_{Ca} is the calcium current through the L-type calcium channels, $I_{Ca,bk}$ is the background calcium current, I_{pCa} is the sarcolemmal calcium pump current, and I_{ncx} is the current of the sodium-calcium exchanger.

Potassium current. The potassium current is defined as follows:

$$I_{K_{tot}} = I_{to} + I_{Kr} + I_{Ks} + I_{K1} - 2 \cdot I_{NaK} + I_{CaK} + I_{Kp}$$

where I_{to} is the transient outward potassium current (decomposed into a fast and a slow component), I_{Kr} is the rapidly activating potassium current, I_{Ks} is the slowly activating potassium current (decomposed into junctional and subsarcolemmal components), I_{K1} is the inward rectifier potassium current, I_{NaK} is the

current of the sodium-potassium pump (decomposed into junctional and subsarcolemmal components), I_{CaK} is the potassium current through the L-type calcium channels (decomposed into junctional and subsarcolemmal components), and I_{Kp} is the plateau potassium current. In the GPB model, differentiation between endocardial and epicardial cells is set by assigning different contributions to the fast and slow I_{to} components.

1.3.6 Acute ischemia models

Over the past 20 years, cardiac ischemia has been studied using mathematical modeling and computer simulations. These techniques have become a useful tool in analyzing the electrophysiology of the myocardial arrhythmias [66]. In one of the first works by Ferrero *et al.* [67], the authors studied how the metabolic changes produced by the ischemia in the cell affect the electrophysiological behavior of the cardiac tissue. This study was limited by the utilization of two dimensional tissues and this limitation was also present in further studies [68]. Following these results, different works have extended this concept, accounting for heterogeneity caused by ischemia [69], realistic fiber orientation and transmural heterogeneity [70, 71], and how reduced repolarization increases arrhythmic risk in the heterogeneous substrate caused by acute myocardial ischemia [72].

At the cell level, AP under myocardial ischemia is modeled adding the three main effects to the electrophysiological cardiac models: hyperkalemia, hypoxia and acidosis. The hyperkalemia is simulated by increasing the extracellular potassium to levels around 10 mM as it has been experimentally reported [73]. The hypoxia is simulated by adding the ATP-sensitivity $[K^+]_i$ current ($I_{K_{ATP}}$), a current discovered by Noma [74]. When distribution of oxygen is reduced, the cell is not able to generate ATP from ADP. Due to this situation, ATP concentration is reduced in the cell and $I_{K_{ATP}}$ channels open. Finally, acidosis is usually modeled by a reduction of the ionic conductances of the I_{Na} and the I_{CaL} currents according to the experimental results of [67, 75]. While all three of these effects are present during a cardiac ischemia, the hyperkalemia plays the most important role.

For the simulation of the ischemia, different scales need to be considered when the myocardial it is studied because some of the electrophysiological consequences of ventricular ischemia must be analyzed in tissue or in the entire organ. For example, how the effective refractory period increase or how the conduction velocity decreases under ischemic conditions must be studied at least in a fiber of ventricular myocytes. Another example is the study of reentrant patterns and vulnerable windows in acutely-ischemic ventricle which must be analyzed on the organ level. In this case, an ischemic region is placed in a bi-ventricle model with fiber orientation, and, according to the experimental findings from Coronel *et al.* [73], the ischemic region is composed of a normal zone (NZ), transitional border zones (BZ), and the central zone (CZ) of ischemia. The BZ corresponds to a linear variation in electrophysiological properties between the NZ and the CZ as shown in experiments [73]. For this simulations, an important parameter in the simulation of ventricular ischemia is the washed zone (not affected by ischemia) in the endocardium as a re-

sult of the interaction between the blood inside of the ventricle and the endocardial tissue [23].

In this complex scenario, the AP model represents the corner stone. A good AP model that is able of reproducing the cardiac behavior under arrhythmias is a key element for the *in silico* cardiac modeling.

1.4 Objectives and Outline of the Thesis

1.4.1 Aim of the thesis

The main objective of this thesis is the proposal of novel methodologies to improve development and validation of cardiac computational models. In particular, this thesis focused on building a human ventricular cell model able to represent experimental evidences regarding a range of electrophysiological properties, which included well-established markers of arrhythmic risk. The developed model could then be used to investigate ventricular arrhythmias and, in particular, those arising under conditions of hyperkalemia, a component of myocardial ischemia.

As described at the beginning of this general introduction, mathematical modeling and simulation of cardiac electrical activity provides an ideal framework where to join clinical data and experimental observations to gain understanding of cardiac electrophysiology and underlying mechanisms. The use of cardiac modeling and simulation in combination with other techniques, such as signal processing of cardiac electrical signals, can be a powerful tool to aid in the prevention of cardiac arrhythmias as well as in the improvement of their diagnosis and therapy.

To this end, it is very important to have cardiac computational models able to reproduce available clinical and experimental evidences. Cardiac action potential models are a key element in the development of whole-heart *in silico* models. The more faithfully the action potential model represents experimental behavior, the more useful it will be for investigation of cardiac electrical activity and the generation of cardiac arrhythmias.

1.4.2 Specific objectives

The general objectives of this thesis are:

- *To develop new methodologies for the development and validation of electrophysiological models*: During the development of a cardiac model, many simplifications are required to be able to isolate parts of the model and to adjust the parameters of this part to the experimentally measured values. The increase in computational capacity permits consideration of more elements in the development process and could help reduce these simplifications. In particular, the following situations have been considered in this thesis:
  - *Considering the entire model of an ionic channel when the parameters of the channel are adjusted*: The usual process to model the behavior of an ionic channel involves in the measurement of different elements of the model considering them independent of each other because of the

experimental protocol used for the measurement. While in many cases this approximation could be valid, with the increasing complexity of the models, the interaction between the different elements of the model also increases. For this reason, it is necessary to consider the possible interactions of the different elements of the model in the experimental measurements.

  - *Considering simultaneously all of the ionic conductances when the model is adjusted*: One of the most important parts in the development of a cardiac model is the selection of the value for the ionic conductances. This action is notably difficult because ionic conductances cannot be measured directly. To select each value, they are usually considered independently to adjust some electrophysiological properties. One of the limitations of using this adjustment technique of *one-at-a-time* is that the interactions or the cross effects are neglected. For this reason, one of the objectives of this thesis is to develop techniques that allow selecting the cardiac ionic conductances by modifying them at the same time and considering all of the interactions or the cross effects.
  - *Considering the differences between the simulations in isolated cell and in tissue to fit as closely as possible to the experiments*: Due to the sensitivity of some ionic currents to the process of cell isolation, the experiments in cardiac cells are usually performed using small pieces of tissue. Nevertheless, due to computational reasons, most of the adjustments in cardiac models are performed using simulations at the cell level. One of the objectives of this thesis is to study how this simplification could affect the development of a cardiac model and how it could be overcome.

- *To apply all of these methodologies for the development of a human ventricular action potential model*: In recent years, several models of the human ventricular action potential have been proposed, because of the increase in available data. However, while the available data increases the models are limited in representing certain physiological situations. The objective of this thesis is to incorporate the new technique to the modification of a human ventricular AP model to try to approximate its behavior, as much as possible, to what has been observed experimentally.

1.4.3 Outline of the thesis

The thesis is organized as follows:

- Chapter 2 describes an initial analysis of the GPB model and a first update of it. The GPB model was analyzed for the purpose of investigating ventricular arrhythmias occurring in the context of hyperkalemia, a component of myocardial ischemia. After evaluating the model, the necessity to modify it to solve issues related to different electrophysiological properties, like APD rate adaptation to abrupt frequency changes among others, was identified. The

update of the GPB model, denoted as the CRLP model, was first presented at the CinC Conference, while a full analysis of the updated model, including evaluation of its performance under hyperkalaemic conditions, was published in a scientific journal:

  - **J. Carro**, J. F. Rodríguez Matas, P. Laguna, E. Pueyo. *Analysis and Improvement of a Human Ventricular Cell Model for Investigation of Cardiac Arrhythmias*. XXXVII International Conference on Computers in Cardiology, Belfast (UK), pp. 817 - 820 (Sep, 2010).
  - **J. Carro**, J. F. Rodríguez, P. Laguna, E. Pueyo. *A Human Ventricular Cell Model for Investigation of Cardiac Arrhythmias under Hyperkalaemic Conditions*. Phil Trans A, n. 639, pp. 4205 - 4232 (Nov, 2011).

- Chapter 3 presents an algorithm to adjust the ionic conductances of a cardiac computational model by considering electrophysiological markers as constraints. The need for such an algorithm came from the fact that, after evaluation of the CRLP model developed in chapter 2, additional characteristics were determined to be necessary for investigation of cardiac arrhythmias. Specifically, in this chapter intracellular potassium dynamics were introduced into the CRLP model developed in chapter 2 to investigate arrhythmias arising in the context of hyperkalemic conditions. To avoid the imbalance in the total potassium current, a new algorithm was proposed to adjust ionic current conductances of the updated computational model in such a way that representation of experimentally measured electrophysiological markers is either improved or at least maintained with respect to the model before the update. The initial results of this chapter were presented at a scientific conference. The final algorithm with illustration of its application to the study of conditions involving large changes in potassium concentration has been accepted to be published in an international journal:

  - **J. Carro**, J. F. Rodríguez Matas, and E. Pueyo, *A Response Surface Optimization approach to adjust ionic current conductances of cardiac electrophysiological models*, in Gordon Research Conference in Cardiac Arrhythmia Mechanisms, Lucca, Italy, 2015.
  - **J. Carro**, E. Pueyo, J. F. Rodríguez. *A response surface optimization approach to adjust ionic current conductances of cardiac electrophysiological models. Application to the study of potassium level changes*. PLOS One (Accepted).

- In Chapter 4, limitations in the development and validation of electrophysiological models caused by the differences between the experimental protocols and the simulations are analyzed. In the previous chapters of this thesis, for the development and validation of the new versions of the model available experimental measures were readily used to adjust model parameters or to compare with simulation results. To evaluate whether this is a suitable

approximation, two scenarios involving scales ranging from ion channels to tissue were studied. This study allowed us to determine when it is possible to use them directly and when more complicated simulations are required. The results of this chapter at the ionic level were presented at an international conference, and the complete study evaluating both scenarios was published in a scientific journal:

  - **J. Carro**, J. F. Rodríguez-Matas, V. Monasterio, and E. Pueyo. *Limitations in electrophysiological model development and validation caused by differences between simulations and experimental protocols.* Progress in Biophysics and Molecular Biology, vol 129, pp. 53 - 64, (Oct, 2017).
  - **J. Carro**, J. F. Rodríguez Matas, E. Pueyo. *In Silico Simulations of Experimental Protocols for Cardiac Modeling.* XXXVI Annual International Conference of the IEEE Engineering in Medicine and Biology Society, Chicago (USA), pp. 5695 - 5698 (Aug, 2014).

- In Chapter 5, a modification of the calcium current is proposed to improve the shape of the AP before the *plateau* phase. Based on the results obtained in Chapter 4, rather than directly comparing experimental and model characterizations, *in silico* simulation of the experimental protocol was used to adjust the new version of the model. To do that, the algorithm proposed in Chapter 3 was adapted to update model expressions at the ionic level. In addition, a new validation process considering the entire cell was described. The obtained results were presented at two international conferences:

  - **J. Carro**, J. F. Rodríguez Matas, and E. Pueyo, *A Methodology to Improve Human Ventricular Models for the Investigation of Cardiac Arrhythmias*, in 61^{st} Annual Meeting of the Biophysical Society, New Orleans, USA, 2017.
  - **J. Carro**, J. F. Rodríguez Matas, and E. Pueyo, *Multiscale Methods for Definition of Ionic Variables in Electrophysiological Models*, in European Medical and Biological Engineering Conference (EMBEC) Tampere, Finland, 2017.

- Chapter 6 presents the final update of the model. All the modifications to the CRLP model proposed in chapter 2, as described in Chapters 3 and 5, were considered and the optimization algorithm proposed in Chapter 3 was used to adjust ionic current conductances and calcium handling characteristics. In this chapter the optimization function was redefined and a large number of experimental datasets recorded from healthy human ventricular cells or tissues were used. Based on the results obtained in Chapter 4, only those electrophysiological markers whose values are comparable when evaluated in simulated single cells and tissues were considered, as some of the experimental data had been recorded in tissue and simulations were run in cells. Additional electrophysiological markers were used for validation purposes by comparing experimental data with tissue simulation results. The

results of this chapter are part of a paper that is in preparation and will be submitted to an international journal.

- Finally, Chapter 7 presents the most important conclusions of the thesis and discusses possible future research lines.

Chapter 2

A New Paradigm for Electrophysiological Model Development

2.1 Introduction

Despite the fact that the human ventricular AP models currently available in the literature are able to reproduce certain electrophysiological properties observed experimentally, they fail in representing other relevant aspects, as pointed out in Chapter1. To obtain a model suitable for the study of human ventricular electrophysiology, with a focus on the investigation of ventricular arrhythmias, in this chapter a human ventricular AP model was developed departing from the GPB model. The methodology proposed for model development was based on the computation of well-established electrophysiological markers and the results of a sensitivity analysis of the modulation of those markers by variations in the characteristics of major ionic currents. Using that methodology key limitations of the GPB model were unraveled and inadequacies in the definitions of specific ionic current characteristics were identified. Based on those findings, gating kinetics of the I_{CaL} current were reformulated by introducing both fast and slow voltage-dependent inactivation gates [51], maximal I_{NaK} was reduced to best match experimental APD_{90} rate adaptation data, and the I_{Kl} current was redefined by accounting for recent experimental data published in the literature [76]. The new developed model, herein denoted by CRLP, was tested and compared with the original GPB model and with the widely used TP06 model. Model comparison was based on twelve cellular electrophysiological markers computed using five different stimulation protocols, as in [12]. Our results show that the introduced modifications brought most markers into the physiological range, and considerably improved others with respect to the GPB and

TP06 models. In addition, the CRLP model was tested by simulating hyperkalemic conditions in tissue. Under those conditions, potassium starts to pour out of ischemic myocardial cells causing depolarization of the myocardium at rest, slowing conduction and decreasing excitability. Recovery of excitability is known to outlast repolarization, a phenomenon termed post-repolarization refractoriness. Our results show that under hyperkalemia APD_{90} progressively decreased with the level of extracellular potassium, $[K^+]_o$, whereas the effective refractory period (ERP) increased after a threshold in the level of $[K^+]_o$ was surpassed. Conduction velocity (CV) decreased with $[K^+]_o$ and conduction was blocked above $[K^+]_o = 10.4$ mM. Additionally, APD_{90} alternans appeared for $[K^+]_o > 9.8$ mM. These results suggest that the model is suitable to represent areas of inhomogeneities of resting potential and dispersion in recovery of excitability corresponding to different hyperkalemic levels within the tissue. Those areas of inhomogeneities could provide a setting for unidirectional block that could become the substrate for arrhythmias in ischemic hearts.

2.2 Methods

Electrophysiological markers were used in this study to guide the modifications applied onto the GPB model to generate the proposed CRLP model. Specifically, markers related to S1S2 restitution and APD_{90} rate adaptation dynamics were identified as not being adequately reproduced by the GPB model and appropriate modifications were performed. Those and other markers were also used to evaluate the performance of the CRLP model and to compare it with that of the TP06 and GPB models.

In the following subsections, the cellular electrophysiological markers used in this study are presented, and the protocols used to compute them are described.

2.2.1 Selected markers

- *APD_{90}*: APD was traditionally considered as the main preclinical marker of drug cardiotoxicity. APD prolongation was linked to long QT syndrome and increased risk of developing Torsades de Pointes [77, 78]. APD_{90} was used in this study to denote AP duration at 90% repolarization (Figure 2.1.a)).

- *Triangulation*: This marker quantifies the shape of the final part of the AP and was calculated as the difference between APD at 50% and 90% repolarization (Figure 2.1.a)). Low triangulation values indicate square APs, while high values indicate triangular APs. Triangulation was proposed as a marker of pro-arrhythmia [77], with long APD_{90} values without triangular APs considered as anti-arrhythmic, and triangular APs considered as pro-arrhythmic in general.

- *Systolic and diastolic intracellular calcium ($[Ca^{2+}]_i$) levels*: Calcium transient properties evaluated at different frequencies was reported as risk markers

[79, 80]. In this study, diastolic (level at rest) and systolic (level at peak) calcium transient levels were evaluated at 0.5 Hz and 1 Hz (Figure 2.1.b)).

- *Time constants of APD_{90} adaptation to abrupt changes in CL*: Adaptation of ventricular repolarization duration to abrupt changes in cycle length (CL) was proposed as an arrhythmic risk marker [81]. In this study, the dynamics of APD_{90} adaptation to abrupt changes in CL were fitted by two exponentials with associated time constants τ_{fast} and τ_{slow} (Figure 2.1.c)), following the methodology proposed in [13].

- *Maximum slope of APD_{90} restitution curves*: The maximum slope of the APD_{90} restitution (APDR) curve was suggested as an arrhythmic risk marker [82, 83]. The APDR curve describes the relationship between APD_{90} and the diastolic interval (DI) (Figures 2.1.d)-e)). In this study APDR was evaluated using the S1S2 and the dynamic protocols (see Section 2.2.2).

- *Rate dependence of Na^+ and Ca^{2+} concentrations*: The importance of intracellular sodium, $[Na^+]_i$, and intracellular calcium, $[Ca^{2+}]_i$, dynamics in arrhythmogenesis was extensively reported [84, 85]. In this study, systolic $[Na^+]_i$ and $[Ca^{2+}]_i$ levels were evaluated for increasing stimulation frequencies (Figure 2.1.f)).

2.2.2 Stimulation Protocols

Five stimulation protocols were applied to evaluate the electrophysiological markers presented in section 2.2.

- *Steady-state protocol*: A train of 3,000 stimulation pulses was delivered and steady-state was guaranteed to be reached. Simulations were carried out using two different CL values (1,000 and 2,000 ms). The evaluated markers were: APD_{90} at 1 Hz, Triangulation at 1 Hz, Systolic $[Ca^{2+}]_i$ at 0.5 and 1 Hz, and Diastolic $[Ca^{2+}]_i$ at 0.5 and 1 Hz (Figures 2.1.a) and 2.1.b)).

- *Abrupt changes in CL protocol*: The cell was stimulated with a CL of 1,000 ms for 8 minutes, then with a CL of 600 ms for additional 8 minutes and finally with a CL of 1,000 ms for 8 minutes (Figure 2.1.c)). The APD_{90} dynamics after the first abrupt CL change were fitted by two exponentials with time constants τ_{fast} and τ_{slow}. APD_{90} adaptation dynamics after the second abrupt CL change provided very similar results to those obtained for the first CL change, in accordance with [12, 13], and were not reported.

- *S1S2 protocol*: A train of 10 basic stimulations (S1) was applied to the cell or tissue at a CL of 1,000 ms followed by an extra stimulus (S2) delivered at coupling intervals (CI) ranging from 1,000 to 250 ms in variable steps (100 ms for DI>300 ms, 5 ms for 150<DI<300 ms, and 1 ms for 5<DI<150 ms). The S1S2 restitution curve was obtained by plotting the APD_{90} corresponding to the extra stimulus versus the previous DI for each of the tested CI values (Figure 2.1.d)).

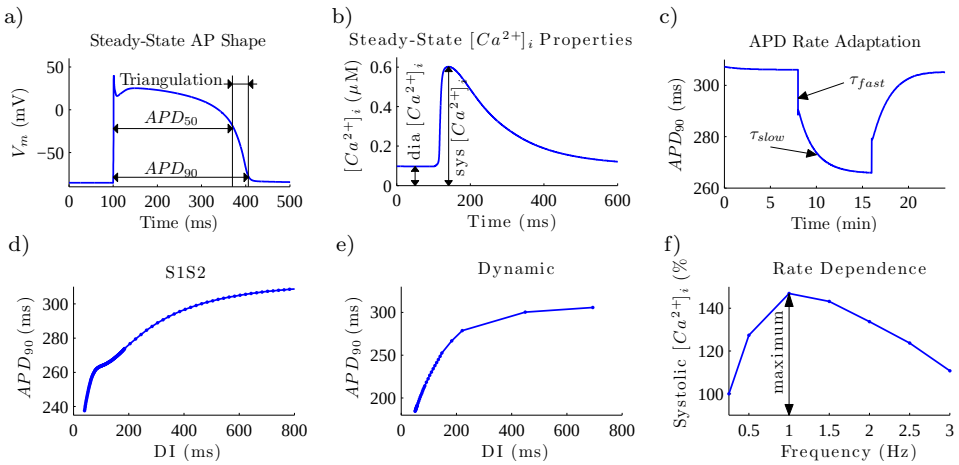

Figure 2.1: Graphical description (using simulation results) of the markers of arrhythmic risk used in this study: a) Steady-state AP properties (APD_{90}, AP triangulation); b) Steady-state $[Ca^{2+}]_i$ properties (systolic 'sys' and diastolic 'dia' values); c) APD_{90} daptation to abrupt changes in CL (from 1,000 ms to 600 ms and again to 1,000 ms), characterized by time constants τ_{fast} and τ_{slow}; d) APDR curve computed using the S1S2 protocol; e) APDR curve computed using the dynamic protocol; f) Normalized rate dependence of systolic concentrations, with normalization performed with respect to the lowest tested frequency, i.e. 0.25 Hz. For a better understanding of the protocols used to compute the markers shown in panels a)-f), see the description provided in section 2.2.2.

- *Dynamic protocol*: In this protocol 100 stimulations were applied at a given CL, with the CL ranging from 1,000 to 50 ms. The APDR curve was obtained by plotting the steady-state APD_{90} (corresponding to the 100^{th} stimulus of each CL) versus the corresponding steady-state DI (Figure 2.1.e)).
- *Rate dependence protocol*: The systolic values of both $[Na^+]_i$ and $[Ca^{2+}]_i$ concentrations were measured at different frequencies (0.25, 0.5, 1, 1.5, 2, 2.5 and 3 Hz) and normalized to the level of the minimum frequency. For each frequency, the cell was stimulated during 10 minutes to reach steady-state and $[Na^+]_i$ and $[Ca^{2+}]_i$ were measured at the end of the 10-minute period. The maximum normalized concentration value was computed and used as a marker (Figure 2.1.f)).

2.2.3 The CRLP Model

Taking the GPB model as a starting point, the CRLP model was built by reformulating two ionic currents (I_{CaL} and I_{K1}) and redefining a number of model parameters, including G_{Na} (maximum I_{Na} conductance) and G_{NaK} (maximal I_{NaK} value). Those changes were motivated by the possibility of improving the performance exhibited by the GPB model on two particular aspects: i) the shape and maximum slope of the S1S2 APD_{90} restitution curve, and ii) the response of the APD_{90} to abrupt changes in heart rate (see below). The failure of the GPB model in reproducing experimental data on those two aspects could be attributed to an inheritance from the Shannon rabbit ventricular model from which the GPB model was developed. In this regard, the development of the CRLP model from the GPB model was made by considering human data only [61]. The following paragraphs describe the introduced modifications, as well as the data and criteria used in the development process. A full description of the CRLP model can be found in Appendix B.

To keep as much consistency as possible with the original GPB model, the CRLP model was developed for the same type of myocardial cells as the GPB model, namely endocardial and epicardial. Differences between the two cell types were based on the definition of the I_{to} fast and slow components, in the same way as previously described for the GPB model.

L-Type Calcium Current (I_{CaL}). To obtain an APD_{90} adaptation response to abrupt changes in CL in better concordance with experimental data, the L-type calcium current was reformulated. The voltage-dependent inactivation gate f of the GPB model was replaced with the product of a fast, f, and a slow, f_2, inactivation gates, as in [51]. The new equations for the I_{CaL} current in the CRLP model were:

$$I_{Ca_{junc}} = F_{junc_{Ca_L}} \cdot \bar{I}_{Ca_j} \cdot d \cdot f \cdot f_2 \cdot \left(1 - f_{CaB_j}\right)$$

$$I_{Ca_{sl}} = F_{sl_{Ca_L}} \cdot \bar{I}_{Ca_{sl}} \cdot d \cdot f \cdot f_2 \cdot \left(1 - f_{CaB_{sl}}\right)$$

$$I_{CaNa_{junc}} = F_{junc_{Ca_L}} \cdot \bar{I}_{Na_j} \cdot d \cdot f \cdot f_2 \cdot \left(1 - f_{CaB_j}\right)$$

$$I_{CaNa_{sl}} = F_{sl_{Ca_L}} \cdot \bar{I}_{Na_{sl}} \cdot d \cdot f \cdot f_2 \cdot \left(1 - f_{CaB_{sl}}\right)$$

$$I_{CaK} = \bar{I}_K \cdot d \cdot f \cdot f_2 \cdot \left(F_{junc_{Ca_L}} \cdot \left(1 - f_{CaBj}\right) + F_{sl_{Ca_L}} \cdot \left(1 - f_{CaBsl}\right) \right)$$

$$I_{Ca} = I_{Ca_{junc}} + I_{Ca_{sl}}$$
$$I_{Ca_{Na}} = I_{Ca_{Na_{junc}}} + I_{Ca_{Na_{sl}}}$$
$$I_{CaL} = I_{Ca} + I_{CaK} + I_{Ca_{Na}}$$

As indicated in [61], the replacement of one current component by another one is not a simple task. Splitting the f gate in the GPB model into two new gates required the readjustment of the time constants τ_{f_2} associated with the slow voltage-dependent inactivation gate f_2 and the time constant τ_d associated with the activation gate d in order to obtain a meaningful I_{CaL} current-voltage curve (splitting the f gate without readjusting the time constants would have led to a current-voltage curve having two relative minima).

Readjustment of τ_{f_2} was based on available experimental data [2, 4–7]. Figure 2.2.a) depicts τ_f and τ_{f_2} along with experimental data [2, 4–7]. Since the experimental data does not cover the entire voltage range, the readjustment was performed by best fitting the tail of the τ_{f_2} curve while obtaining a current-voltage curve within the range of experimental data. The other voltage-dependent inactivation time constant, τ_f, was kept as in [51]. The equations describing f and f_2 were:

$$f_{ss} = \frac{1}{1 + e^{\frac{V_m + 20}{7}}}$$
$$\alpha_f = 1102.5 \cdot e^{-\left(\frac{V_m + 27}{15}\right)^2}$$
$$\beta_f = \frac{200}{1 + e^{\frac{13 - V_m}{10}}}$$
$$\gamma_f = \frac{180}{1 + e^{\frac{V_m + 30}{10}}} + 20$$
$$\tau_f = \alpha_f + \beta_f + \gamma_f$$
$$\frac{\mathrm{d}f}{\mathrm{d}t} = \frac{f_{ss} - f}{\tau_f}$$

$$f_{2_{ss}} = \frac{0.67}{1 + e^{\frac{V_m + 35}{7}}} + 0.33$$
$$\alpha_{f_2} = 300 \cdot e^{\frac{-(V_m + 25)^2}{170}}$$
$$\beta_{f_2} = \frac{31}{1 + e^{\frac{25 - V_m}{10}}}$$
$$\gamma_{f_2} = \frac{16}{1 + e^{\frac{V_m + 30}{10}}}$$

$$\tau_{f_2} = \alpha_{f_2} + \beta_{f_2} + \gamma_{f_2}$$
$$\frac{\mathrm{d}f_2}{\mathrm{d}t} = \frac{f_{2_{ss}} - f_2}{\tau_{f_2}}$$

where V_m denotes transmembrane voltage.

Readjustment of τ_d was based on the description provided in [51]:

$$d_{ss} = \frac{1}{1 + e^{\frac{-(V_m+5)}{6}}}$$
$$\alpha_d = \frac{1.4}{1 + e^{\frac{-35-V_m}{13}}} + 0.25$$
$$\beta_d = \frac{1.4}{1 + e^{\frac{V_m+5}{5}}}$$
$$\gamma_d = \frac{1}{1 + e^{\frac{50-V_m}{20}}}$$
$$\tau_d = \alpha_d \cdot \beta_d + \gamma_d$$
$$\frac{\mathrm{d}d}{\mathrm{d}t} = \frac{d_{ss} - d}{\tau_d}$$

The definitions of the calcium-dependent inactivation gates, f_{CaB_j} and $f_{CaB_{sl}}$, were taken as in the GPB model:

$$\frac{\mathrm{d}f_{CaB_j}}{\mathrm{d}t} = 1.7 \cdot Ca_j \cdot \left(1 - f_{CaB_j}\right) - 11.9 \cdot 10^{-3} \cdot f_{CaB_j}$$
$$\frac{\mathrm{d}f_{CaB_{sl}}}{\mathrm{d}t} = 1.7 \cdot Ca_{sl} \cdot (1 - f_{CaB_{sl}}) - 11.9 \cdot 10^{-3} \cdot f_{CaB_{sl}}$$

Additionally, based on the results of the sensitivity of APD_{90} to variations in the maximal I_{CaL} conductivity and the actual APD_{90} value in the GPB model (see below, Tables 2.1 and 2.2), the relative permeabilities of the L-type calcium channels were set to:

$$p_{Ca} = 1.9887 \cdot 10^{-4}\ cm/s$$
$$p_K = 5.4675 \cdot 10^{-8}\ cm/s$$
$$p_{Na} = 3.0375 \cdot 10^{-9}\ cm/s$$

$$\bar{I}_{Ca_j} = \frac{p_{Ca} \cdot V_m \cdot Frdy \cdot FoRT \cdot \left(Ca_j \cdot e^{2 \cdot V_m \cdot FoRT} - Ca_o\right)}{e^{2 \cdot V_m \cdot FoRT} - 1}$$
$$\bar{I}_{Ca_{sl}} = \frac{p_{Ca} \cdot V_m \cdot Frdy \cdot FoRT \cdot \left(Ca_{sl} \cdot e^{2 \cdot V_m \cdot FoRT} - Ca_o\right)}{e^{2 \cdot V_m \cdot FoRT} - 1}$$
$$\bar{I}_{Na_j} = \frac{p_{Na} \cdot V_m \cdot Frdy \cdot FoRT \cdot \left(Na_j \cdot e^{V_m \cdot FoRT} - Na_o\right)}{e^{V_m \cdot FoRT} - 1}$$

$$\bar{I}_{Na_{sl}} = \frac{p_{Na} \cdot V_m \cdot Frdy \cdot FoRT \cdot \left(Na_{sl} \cdot e^{V_m \cdot FoRT} - Na_o\right)}{e^{V_m \cdot FoRT} - 1}$$

$$\bar{I}_K = \frac{p_K \cdot V_m \cdot Frdy \cdot FoRT \cdot \left(K_i \cdot e^{V_m \cdot FoRT} - K_o\right)}{e^{V_m \cdot FoRT} - 1}$$

where $Frdy$ is Faraday's constant, $FoRT$ is the ratio between Faraday's constant and the product of the gas constant and the absolute temperature, $\bar{I}_{k_m}$ is the maximal current for ion k in the compartment m, and p_k is the relative permeability of ion k.

The current-voltage curve obtained with the new definition of the I_{CaL} current was compared with experimental data [1–3] and with the original definition of the GPB model. Figure 2.2.b) shows the different current-voltage curves, where it can be observed that the new definition of I_{CaL} was in good agreement with available experimental data [1–3], with the additional benefit of contributing to physiological model response in terms of S1S2 APD_{90} restitution and APD_{90} rate adaptation dynamics.

Inward Rectifier K Current (I_{K1}). The I_{K1} current was redefined using recent experimental data from human ventricular cells published in the literature [76]. The new definition for I_{K1} was as follows:

$$a_{K1} = \frac{4.094}{1.0 + e^{0.1217 \cdot (V_m - E_K - 49.934)}}$$

$$b_{K1} = \frac{15.720 \cdot e^{0.0674 \cdot (V_m - E_K - 3.257)} + e^{0.0618 \cdot (V_m - E_K - 594.31)}}{1.0 + e^{-0.1629 \cdot (V_m - E_K + 14.207)}}$$

$$K1_{ss} = \frac{a_{K1}}{a_{K1} + b_{K1}}$$

$$I_{K1} = 0.5715 \cdot \sqrt{\frac{[K^+]_o}{5.4}} \cdot K1_{ss} \cdot (V_m - E_K)$$

where E_K is the $[K^+]$ reversal potential. Figure 2.2.c) shows the modified I_{K1} current compared with the experimental data from [76] and with I_{K1} from the GPB model.

Na/K Pump Current (I_{NaK}). In order to improve the APD_{90} adaptation response to abrupt changes in CL, maximal I_{NaK} was reduced by 45% with respect to its value in the GPB model. That reduction was set based on the results of the sensitivity analysis for the τ_{slow} marker that is described above.

$[K^+]_i$ and G_{Na}. A more physiological value for $[K^+]_i$ of 138 mM was used in our model. Considering this value for $[K^+]_i$ made the model more excitable as compared to the original GPB model because of the increased availability of sodium channels. Therefore, in order to obtain physiological values for the maximal upstroke velocity, dV/dt, in tissue, the maximum conductance of the sodium current, G_{Na}, was reduced to 18.864 mS/μF. This modification led to a maximal upstroke velocity of 228 mV/ms in the simulated one-dimensional (1D) tissue (see below), which was in good agreement with the experimental results reported in [8].

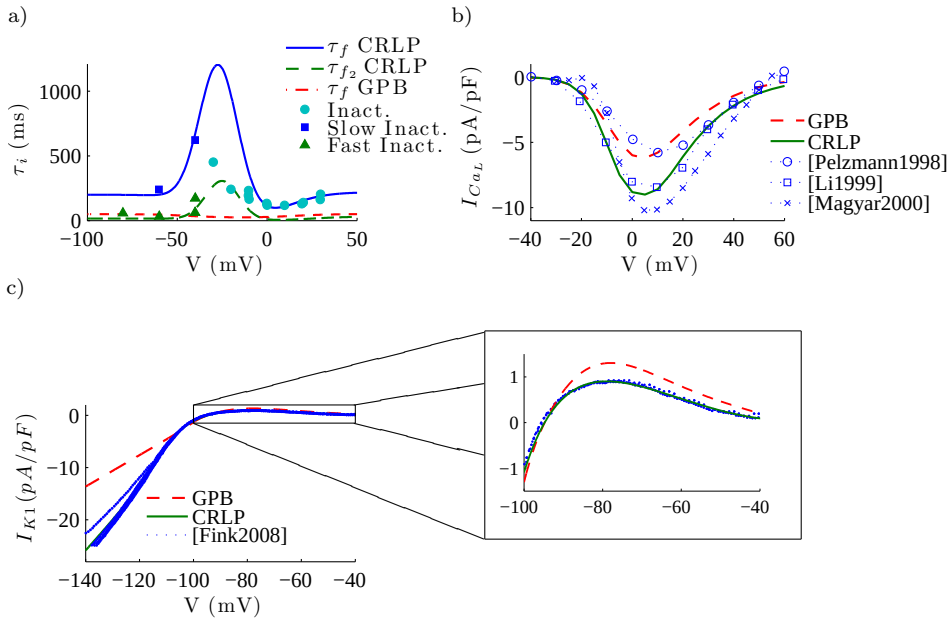

Figure 2.2: Characteristics of I_{CaL} and I_{K1} in simulations and experiments: a) Simulated I_{CaL} voltage-dependent inactivation time constants τ_i as a function of voltage, where $i \in \{f, f_2\}$. Experimental data, represented by markers, were taken from [2, 4–7]; b) I_{CaL} current density versus voltage, with experimental data taken from [1–3]; c) I_{K1} current density versus voltage with experimental data taken from [76]. To compare simulated and experimental data under the same conditions, $[K^+]_i = 138$ mM and $[K^+]_o = 4$ mM were used for the curves shown in panel c), with $[K^+]_i$ denoting the intracellular potassium concentration.

Numerical methods and implementation

The cell membrane was modeled as an electrical circuit [26]. Mathematically, the transmembrane voltage V_m was described by the following ordinary differential equation:

$$C_m \frac{\mathrm{d}V_m}{\mathrm{d}t} = -\left(I_{ion} - I_{stim}\right), \tag{2.1}$$

where t is time, I_{ion} is the sum of all transmembrane ionic currents, I_{stim} is the externally applied stimulation current and C_m is the cell capacitance per unit surface area.

Propagation of the electrical activity in a 1D fiber was described by the following parabolic reaction-diffusion equation [86]:

$$C_m \frac{\partial V_m}{\partial t} = -\left(I_{ion} - I_{stim}\right) + \frac{\partial}{\partial x}\left(\sigma \frac{\partial V}{\partial x}\right), \tag{2.2}$$

where σ is the diffusion coefficient of the tissue and x denotes the coordinate along the fiber.

Physical units in the model were as follows: time t was given in milliseconds, transmembrane potential V_m in millivolts, current densities in picoamperes per picofarad and ionic concentrations in millimoles per liter.

The GPB and CRLP models were implemented in Fortran based on the original codes provided by Eleonora Grandi. The TP06 model was also implemented in Fortran from the original C codes available at Kirsten ten Tusscher's web page: www-binf.bio.uu.nl/khwjtuss.

Cells and tissue were stimulated with square transmembrane current pulses twice the diastolic threshold in amplitude and 1-ms duration. For single cell simulations, forward Euler with a time step $\Delta t = 0.002$ ms was used to integrate the system of ordinary differential equations governing the cellular electrical behavior. For the 1D simulations, a homogeneous 4-cm long fiber composed of epicardial cells was considered. A semi-implicit operator-splitting scheme [87] was used to solve equation 2.2 with a space discretization of $\Delta x = 0.1$ mm and a time step of $\Delta t = 0.002$ ms. A value of $\sigma = 0.0013$ cm^2/ms was used, corresponding to a maximum CV of 74 cm/s, which is in agreement with experimentally reported CV values [88]. The cell capacitance was set to $C_m = 1$ μF/cm^2. Five positions within the fiber were selected for further analysis in each simulation. Those positions were located at 1.5, 1.75, 2, 2.25 and 2.5 cm from the stimulation end of the cable. Reported APD_{90} and CV values were computed as mean values over those positions. In all cases, the Rush and Larsen integration scheme [89] was used to integrate the Hodgkin-Huxley type equations for the gating variables of the various time-dependent currents (m, h, and j for I_{Na}; x_{to_f}, x_{to_s}, y_{to_f} and y_{to_s} for I_{to}; x_{kr} for I_{Kr}; x_{ks} for I_{Ks} and d, f and f_2 for I_{CaL}).

To test the sensitivity of the numerical solution to the time and space discretization indicated above, simulations were performed using a time increment of 0.5 μs and a spatial discretization of 0.05 mm. Differences of less than 0.2% for

the steady-state markers computed in isolated cells were obtained when compared with the default time and space steps used in this study. In tissue, CV and APD_{90} varied by less than 1.5% and 0.02%, respectively. Also, other stimulus durations (from 1 to 3 ms) and amplitudes (from 1.5 to 2 times the diastolic threshold) were tested and were confirmed to provide very similar results (differences in terms of APD_{90}, maximal upstroke velocity as well as CV in tissue were in all cases below 0.2%, 1.6% and 0.8%, respectively).

2.2.4 Conducted Simulations

Sensitivity Analysis

A sensitivity analysis was performed to the original GPB model following the methodology described in [12]. The aim was to elucidate how different ionic current properties modulate the investigated electrophysiological markers. In the sensitivity analysis, each parameter was varied at a time by ±30%. Also, variations of ±15% were considered to assess markers' response to different degrees of variation. These percentages are in agreement with variability levels reported in experiments performed in human ventricular tissue [2, 76, 90–94].

The parameters considered in the sensitivity analysis were:

- G_{CaL}: Maximal conductance of the L-Type Calcium Current (I_{CaL}).
- τ_f: Time constant of the fast voltage-dependent inactivation gate (f) of the I_{CaL} current.
- τ_{f2} : Time constant of the slow voltage-dependent inactivation gate (f_2) of the I_{CaL} current.
- G_{Kr} : Maximal conductance of the rapidly activating potassium current (I_{Kr}).
- G_{Ks} : Maximal conductance of the slowly activating potassium current (I_{Ks}).
- τ_{xs} : Time constant of the activation gate (x_{Ks}) of the I_{Ks} current.
- G_{K1} : Maximal conductance of the inward rectifier potassium current (I_{K1}).
- G_{NaK} : Maximal value of the sodium-potassium pump current (I_{NaK}).
- G_{ncx} : Maximal value of the sodium-calcium exchanger current (I_{ncx}).
- G_{to} : Maximal conductance of the transient outward potassium current (I_{to}).

For each marker c and parameter p, the percentage of change ($D_{c,p,a}$) and sensitivity ($S_{c,p,a}$) were calculated as follows [12]:

$$D_{c,p,a} = \frac{C_{p,a} - C_{control}}{C_{control}} \cdot 100$$

$$S_{c,p,a} = \frac{D_{c,p,a} - D_{c,p,-a}}{2a} \cdot 100$$

where $C_{p,a}$ is the value of marker c when the parameter p is varied by the percentage a, and $C_{control}$ is the value of marker c under control conditions. As shown above, sensitivity ($S_{c,p,a}$) was calculated as the ratio of the difference between the percentage of change ($D_{c,p,a} - D_{c,p,-a}$) and the interval of change ($2a$). In this study we used this definition particularized for $a = 30\%$:

$$S_{c,p,30} = \frac{D_{c,p,+30} - D_{c,p,-30}}{0.6}$$

Larger percentages of variation ($\pm 60\%$ and $\pm 90\%$) in model parameters were additionally investigated to confirm the validity of the sensitivity analysis results under more severe ionic alterations.

Potassium Current Blocks

The following cases of total and partial potassium current blocks were simulated:

- I_{Ks}: To simulate the effect of 1 μM of HMR-1556, I_{Ks} was completely blocked.
- I_{Kr}: To simulate the effect of 50 nM of dofetilide, I_{Kr} was completely blocked.
- I_{K1}: To simulate the effect of 10 μM of $BaCl_2$, I_{K1} was reduced by 50%.

Restitution in Tissue

CV and APD_{90} restitution were additionally investigated in tissue by applying the S1S2 protocol described in 2.2.2, with the only difference that the extra stimulus (S2) was in this case decreased in steps of 5 ms.

Hyperkalemic Conditions

Hyperkalemic conditions were simulated by increasing $[K^+]_o$ from 4 mM to 15 mM. For each $[K^+]_o$ value, the diastolic threshold used to compute the stimulus amplitude was determined as follows: the model was first stabilized until the product of the gates $h \cdot j$ reached 99% of the steady-state value $h_{ss} \cdot j_{ss}$. Stimulation current pulses of variable amplitude were applied at one end of the cable and the diastolic threshold was defined as the minimum amplitude required for an AP to propagate along the fiber. With the model initialized at 1 Hz steady-state, ERP was determined by stimulating the tissue with a train of 10 basic stimulations (S1) delivered at a CL of 1,000 ms, followed by an extra stimulus (S2) delivered at different times taken in 1 ms steps. Steady-state CV and APD_{90} were measured after the last S1 stimulus.

2.3 Results

2.3.1 Results for Control Conditions

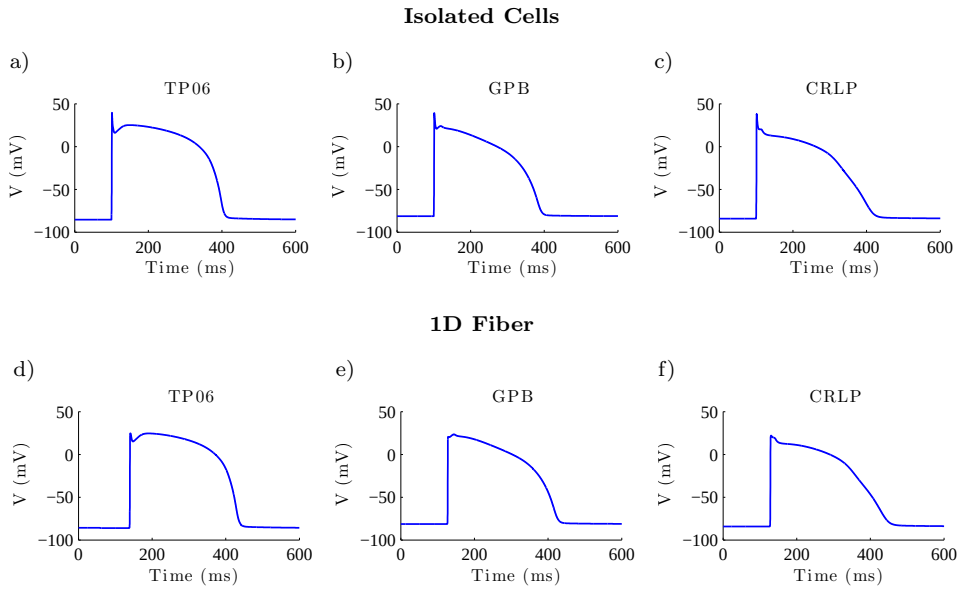

Figure 2.3: APs computed with the TP06, GPB and CRLP models for isolated cells and 1D tissue at CL = 1000 ms. a) TP06 cellular AP; b) GPB cellular AP; c) CRLP cellular AP; d) TP06 tissue AP; e) GPB tissue AP; f) CRLP tissue AP.

APs in Cell and Tissue

Figure 2.3 presents APs computed from the TP06, GPB and CRLP models for an isolated epicardial cell and for an epicardial cell coupled in tissue. In all cases APs correspond to steady-state pacing at CL = 1000 ms. As can be appreciated from the figure, the AP duration was of the same order in the three models. However, the AP shape was notably more triangular for the GPB and CRLP models as compared to the TP06 model, which presented a flatter plateau phase. Also, phase 1 of the AP substantially differed from one model to another, particulary when comparing TP06 with the other two models. Those differences were to some extent attenuated when comparing APs measured in tissue. It is also clear from the figure that maximal upstroke velocity was considerably reduced for tissue APs as compared to cell APs. While for the GPB and CRLP models maximum voltage occurred at the upstroke peak in both cell and tissue, for the TP06 model the maximum voltage at the plateau was even larger than at the upstroke peak in tissue AP, as previously noted in [62] for the TNNP04 model from which the TP06 model was developed.

Sensitivity Analysis

The results of the sensitivity analysis applied to the epicardial version of the GPB model are presented in Table 2.1. This table shows the dependence of a large number of electrophysiological markers on the I_{CaL} current. Not only markers related to systolic and diastolic $[Ca^{2+}]_i$ levels, but also APD_{90} and S1S2 restitution slope were mostly sensitive to variations in I_{CaL}. Also, Table 2.1 shows the importance of the I_{K1} current for AP triangulation. I_{NaK} was determinant for $[Na^{+}]_i$ rate dependence as well as for the time constant of the slow phase of APD_{90} rate adaptation. Note that APD_{90} rate adaptation dynamics computed from the GPB model did not present a characteristic biphasic behavior as reported in experimental studies [95], but adaptation was completed in only one slow phase. For that reason the marker τ_{fast} described in subsection 2.2 is not shown in Table 2.1. Finally, I_{ncx} was relevant for $[Ca^{2+}]_i$ rate dependence. Table 2.1 together with the analysis presented in the following subsection were the road map to carry out the various model improvements proposed in this work, which were described in subsection 2.2.

To confirm that the results of the sensitivity analysis presented in Table 2.1 were not dependent on the limit (30%) considered for parameter variations, simulations were performed considering larger percentages of variations of up to 90%. Despite the fact that in some cases a highly nonlinear modulation of specific electrophysiological markers by certain ionic mechanisms was observed (e.g. triangulation modulation by G_{K1}, systolic $[Ca^{2+}]_i$ modulation by G_{CaL} or τ_{slow} modulation by G_{NaK}), results corroborated the mechanisms identified as determinant for the investigated markers in the sensitivity analysis.

Electrophysiological markers

Table 2.2 shows the values of the computed markers for the epicardial versions of the three models analyzed in this study (TP06, GPB and CRLP). Simulation results were compared against a variety of experimental data taken from [2, 8–10, 79, 95–98].

Results indicated that the GPB model performed better than the TP06 model with respect to the following markers: AP triangulation, steady-state systolic and diastolic $[Ca^{2+}]_i$ levels at 0.5 Hz and rate dependence of $[Na^{+}]_i$ and $[Ca^{2+}]_i$. Those markers are illustrated for the three analyzed models in Figure 2.4.a), 2.4.b), 2.4.f) and 2.4.g). However, according to other analyzed markers, the GPB model rendered worse performance than the TP06 model, as was the case for the S1S2 restitution curve and the APD_{90} adaptation to abrupt changes in CL. Regarding the APD_{90} adaptation, two phases of APD_{90} rate adaptation were experimentally reported in [95]: a first phase with a short time constant and a second phase with a longer time constant. As described above, the APD_{90} rate response in the GPB model did not present the first fast phase (Figure 2.4.c)). For the S1S2 restitution curves (Figure 2.4.d)), the TP06 model was in better agreement with the experimental data of [95, 98] than the GPB model.

For the CRLP model, seven out of the twelve analyzed markers were within physiological range and other three markers were closer to the physiological range

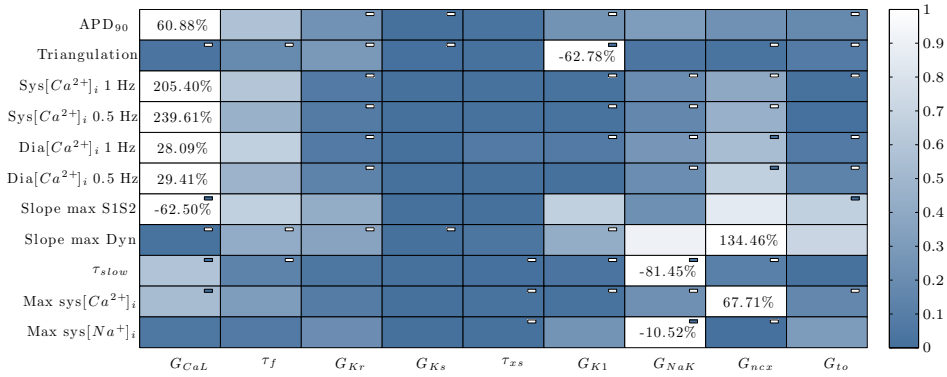

Table 2.1: Results of the sensitivity analysis applied to the GPB model. The blue scale indicates relative sensitivity for each marker. White color indicates maximum relative sensitivity and dark blue color indicates that property and parameter are independent. Percentages in the white boxes indicate the absolute sensitivity of the property. A minus sign in a box indicates that marker and model parameter vary inversely. 'Sys' stands for systolic and 'Dia' stands for diastolic.

as compared to the GPB and TP06 models. As for systolic and diastolic $[Ca^{2+}]_i$ levels at 1 Hz, TP06 outperforms CRLP. A significant change in the shape of the S1S2 restitution curve was observed for the CRLP model as compared to the GPB model (Figure 2.4.d)). The behavior shown by the CRLP model was in agreement with experimental data [95].

Potassium Current Blocks

Table 2.3 summarizes the effect of potassium current blocks on epicardial APs computed using the three tested models. Results are given as percentage of variation of the APD_{90} value with respect to control conditions. In those cases where more than one current was blocked, the variation refers to the APD_{90} value obtained when only the first current was blocked. Experimental values are taken from [54]. It is clear from Table 2.3 that the GPB model performs better than the TP06 model regarding current blocks. The CRLP model performs similar to the GPB model. Figure 2.5 illustrates the effect of current blocks on the AP shape for the GPB and CRLP models.

Restitution in Fiber

Figure 2.6 shows CV and APD_{90} restitution curves computed by applying the S1S2 protocol to the simulated 1D fiber. Regarding CV restitution, the three models present similar behaviors, with only notable differences (>5 cm/s) observed between the TP06 model and the other two models (GPB and CRLP) in the final

marker	TP06	GPB	CRLP	Physiol.
APD_{90} (ms)	301.2	285.0	305.6	271-366
Triangulation (ms)	28.4	51.5	78	44-112
Sys $[Ca^{2+}]_i$ 1 Hz (μM)	0.886	0.383	0.602	1.59-2.01
Sys $[Ca^{2+}]_i$ 0.5 Hz (μM)	0.199	0.345	0.523	0.71-1.68
Dia $[Ca^{2+}]_i$ 1 HZ (μM)	0.104	0.089	0.097	0.20-0.33
Dia $[Ca^{2+}]_i$ 0.5 Hz (μM)	0.068	0.085	0.091	0.14-0.32
$S_{max_{\mathrm{S1S2}}}$ (—)	1.3	0.2	1.0	0.79-4.25
$S_{max_{\mathrm{DYN}}}$ (—)	1.0	1.1	0.9	—
τ_{fast} (s)	13.3	—	10.2	—
τ_{slow} (s)	124.8	56.3	105.6	70-110
Max. sys. $[Ca^{2+}]_i$ (%)	1157	178	147	130-170
Max. sys. $[Na^{+}]_i$ (%)	217	132	134	145

Table 2.2: markers of arrhythmic risk for the TP06, GPB and CRLP human models. Black color indicates within physiological range. Dark gray color indicates out of physiological range but better than previous models. Light gray color indicates out of physiological range. Experimental data are from [2, 8–10, 79, 95–98].

Current		Ref.	TP06	GPB	CRLP	Exper.
I_{Ks}	0%	Control	74.9	0.7	0.6	< 2.8
I_{Kr}	0%	Control	15.9	18.6	14.1	44±4
I_{Kr} I_{Ks}	0% 0%	I_{Kr} block	—	1.4	0.8	9
I_{K1}	50%	Control	3.6	11.5	14.6	4.8±1.5
I_{Kr} I_{K1}	0% 50%	I_{Kr} block	8.9	15.6	21.1	33

Table 2.3: Percentages of variation in APD_{90} caused by blocking different potassium currents. Black color indicates within physiological range. Dark gray color indicates out of physiological range but better than previous models. Light gray color indicates out of physiological range.

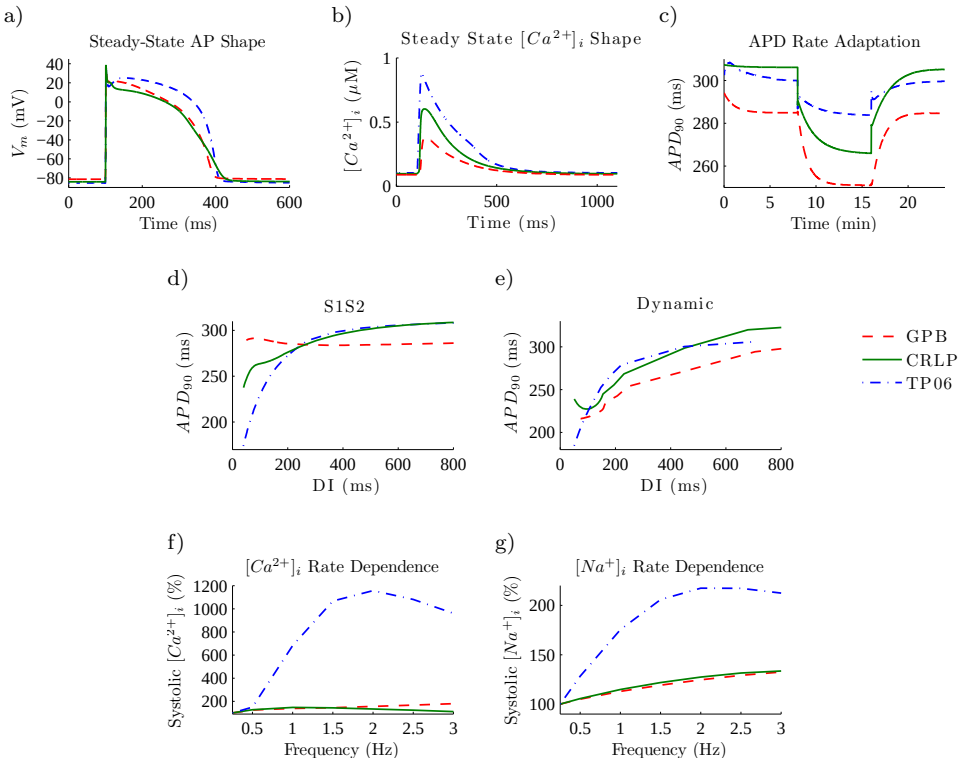

Figure 2.4: markers of arrhythmic risk from TP06, GPB and CRLP models: a) Steady-state AP for CL = 1000 ms; b) Steady-state Ca transient for CL = 1000 ms. c) APD_{90} rate adaptation to abrupt changes in CL (from 1000 ms to 600 ms); d) S1S2 restitution curve; e) Dynamic restitution curve; f) Normalized $[Ca^{2+}]_i$ rate dependence; g) Normalized $[Na^{+}]_i$ rate dependence. For panels f) and g) normalization is performed with respect to the lowest tested frequency, i.e. 0.25 Hz.

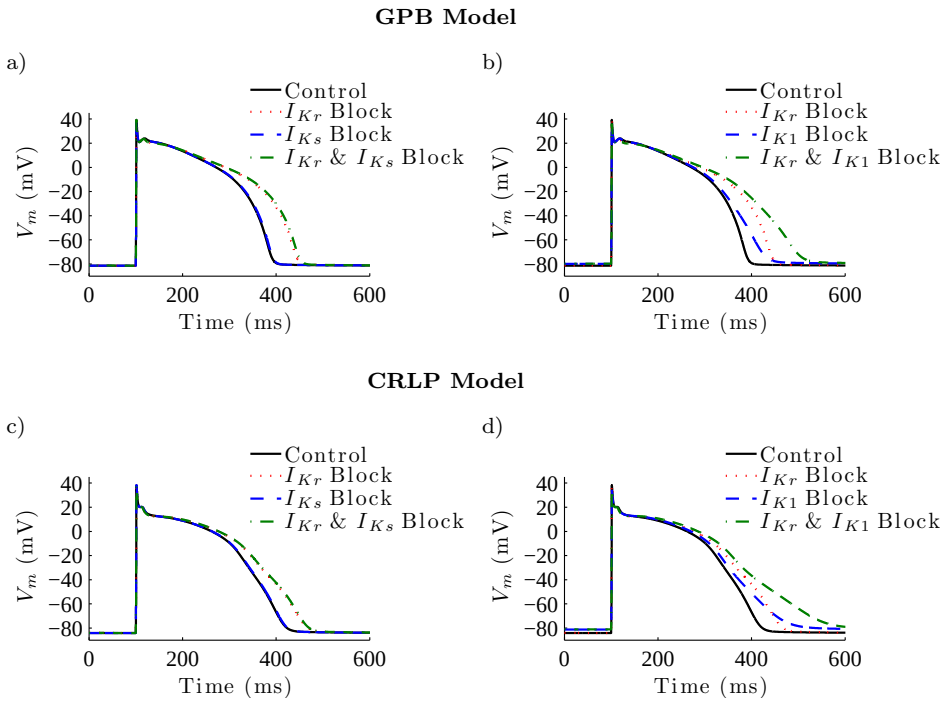

Figure 2.5: Effect of blocking potassium currents for the GPB and CRLP models: a) Effect of completely blocking I_{Kr} and I_{Ks} currents in the GPB model; b) Effect of completely blocking I_{Kr} and partially blocking I_{K1} in the GPB model; c) Effect of completely blocking I_{Kr} and I_{Ks} currents in the CRLP model; d) Effect of completely blocking I_{Kr} and partially blocking I_{K1} in the CRLP model.

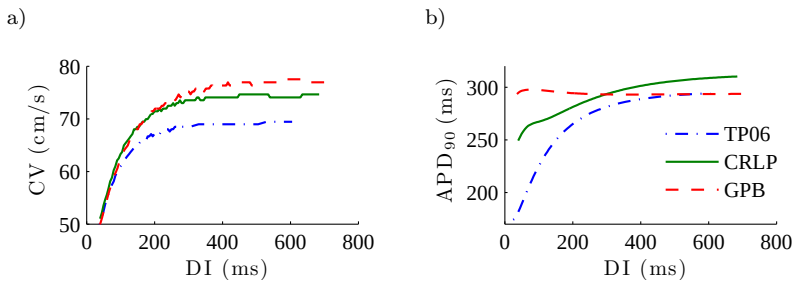

Figure 2.6: CV and APD_{90} restitution curves for the TP06, GPB and CRLP models in a simulated 1D fiber.

part of the curve, i.e. for DI values above 200 ms. Regarding APD_{90} restitution, both the TP06 and CRLP model present steep restitution curves, with high slope (close to 1) only for a narrow DI interval in the case of the CRLP model and for a much wider DI range in the case of the TP06 model (with slope values above 1). The GPB model shows a relatively flat APD_{90} restitution curve. Those results are in good correspondence with the observations from restitution curves measured in isolated cells (Figure 2.4.d)).

2.3.2 Results for Hyperkalemic Conditions

AP properties

Figures 2.7.a) and 2.7.c) show a comparison of the AP shape computed in single cell and tissue for different levels of $[K^+]_o$ using the CRLP model. Figures 2.7.b) and 2.7.d) show the effect of varying $[K^+]_o$ on the resting potential in single cell and tissue. As expected, hyperkalemia shortens the APD_{90} and leads to elevated resting potential, in both cells and tissue.

From Figure 2.7.c) it is also clear that for high $[K^+]_o$ levels, the AP shape varies between even and odd beats, thus leading to the occurrence of AP alternans. Further analysis on the alternating AP behavior and the $[K^+]_o$ threshold for its occurrence can be found below.

Conduction Velocity

Figure 2.8.a) shows CV as a function of $[K^+]_o$ computed from the simulated 1D fiber using the CRLP model. As expected, hyperkalemia leads to a decrease in CV. However, "supernormal conduction" is not observed for $[K^+]_o$ levels below physiological values (5.4 mM) as has been observed in other studies [99, 100]. Our results also show that conduction block occurs for $[K^+]_o > 10.4$.

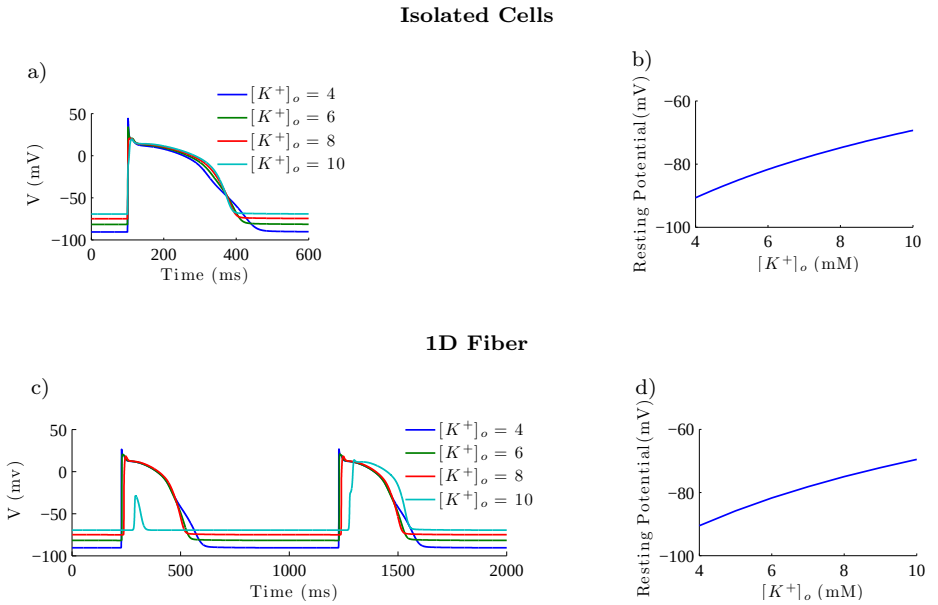

Figure 2.7: Simulated hyperkalemia in cell and tissue using the CRLP model. a) AP shape for varying $[K^+]_o$ in isolated cells; b) Resting potential for varying $[K^+]_o$ in isolated cells; c) AP shape for varying $[K^+]_o$ in 1D fiber; d) Resting potential for varying $[K^+]_o$ in 1D fiber.

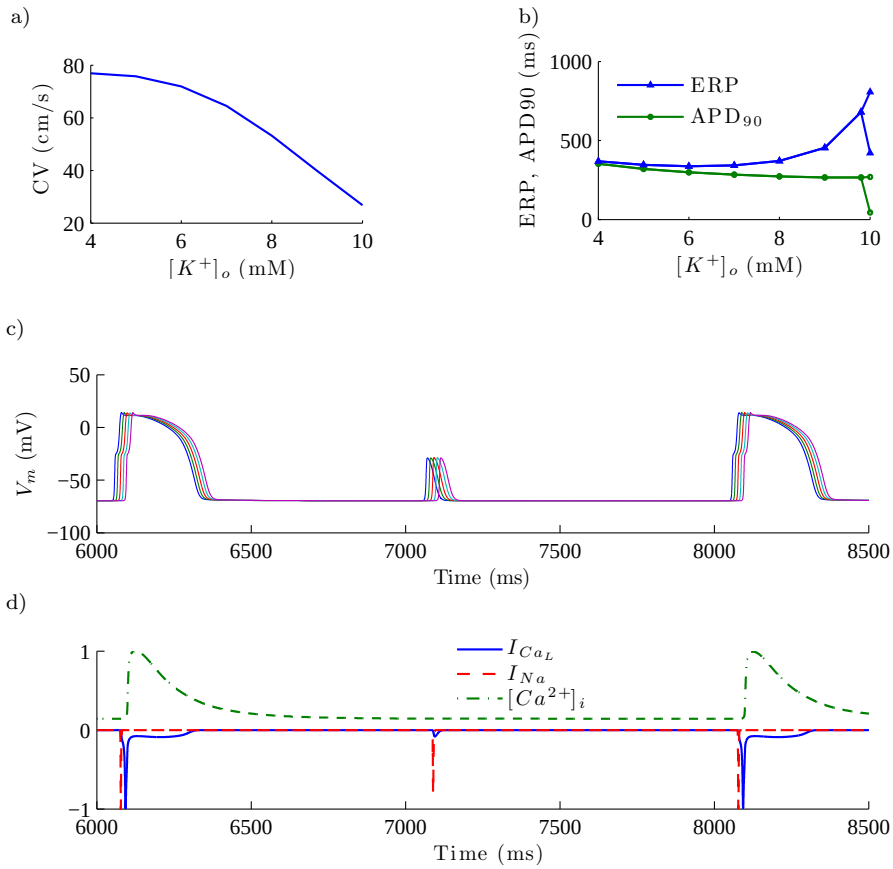

Figure 2.8: Behavior of the CRLP model under hyperkalemic conditions in a 1D fiber: a) CV versus $[K^+]_o$; b) dependence of ERP and APD_{90} with $[K^+]_o$; c) example of alternans for $[K^+]_o = 10.0$ mM, each color representing a different position in the fiber; d) value of different currents normalized to the maximal value of each one in the same example as the previous results.

Action Potential Duration and Effective Refractory Period

Figure 2.8.b) shows ERP and APD_{90} of the last basic (S1) beat for different $[K^+]_o$ values computed in the simulated 1D fiber using the CRLP model. Results show that hyperkalemia causes postrepolarization refractoriness. The difference between ERP and APD_{90} remains almost constant for $[K^+]_o \leq 6$ mM, with this difference increasing rapidly for $[K^+]_o > 6$ mM. For $[K^+]_o > 9.8$ mM, alternans appear in the tissue, causing the ERP and APD_{90} curves to branch out (Figure 2.8.b)). This characteristic of the ERP and APD_{90} curves has not been reported in other human ventricular simulation studies of the literature, but is in agreement with experimental results in other species and with clinical data [101–103]. We tested the same hyperkalemic conditions in simulated TP06 and GPB 1D fibers and we could not observe branching out of the ERP or APD_{90} curves after increasing $[K^+]_o$ up to 15 mM.

Figure 2.8.c) depicts AP propagation in the simulated CRLP 1D fiber for $[K^+]_o = 10$ mM. Alternans were observed for all computed positions within the fiber. Figure 2.8.d) shows I_{CaL}, I_{Na} and $[Ca^{2+}]_i$, each normalized to its maximum value, for the same time period shown in Figure 2.8.c). Results indicate that conduction relies on I_{Na} even for the highly depressed APs. For the long APs, the AP upstroke is divided into two components, the first one characterized by a steep upstroke and supported by I_{Na}, and the second one supported by I_{CaL}, in agreement with the results reported in [67].

2.4 Discussion and conclusions

In this chapter a new human ventricular cell model, the CRLP model, was developed based on the recently proposed GPB model. The CRLP model combines recent experimental measurements of potassium currents and reformulates the L-type calcium current by introducing fast and slow voltage-dependent inactivation gates, similar to the formulation proposed in the TP06 model. That new formulation led to I_{CaL} dynamics that were in good agreement with experimental data and, more notably, allowed the CRLP model to accurately reproduce S1S2 restitution and APD_{90} rate adaptation characteristics. All the modifications were made with the aim of retaining the advantages that the GPB model has over previous models, such as the TP06 model, while improving the performance on other electrophysiological aspects. The novelty of this study was that model development was not based only on the incorporation of new data from experiments on individual ionic currents or concentrations. More importantly, the development was driven by a new paradigm consisting in analyzing the ability of the model to replicate a set of well-established electrophysiological markers and on a sensitivity analysis of those markers to variations in model parameters. The proposed model development framework allows assessing model performance under a variety of conditions, either physiological or pathological. This provides useful information for the adjustment of different model parameters that do not directly depend on individual current measurements or concentrations, and which would be otherwise set in an *ad hoc*

manner.

2.4.1 New model characteristics

The introduction of fast and slow I_{CaL} inactivation gates in the CRLP model led to a more physiological APD_{90} rate adaptation response to abrupt changes in CL as compared to the GPB model. However, by doing so, a larger I_{CaL} current was obtained for the CRLP model, which led to the reformulation of I_{K1} and readjustments of other parameters to keep APD_{90} within physiological values. The resulting APD_{90} value for the CRLP model was closer to the APD_{90} value of the TP06 model, without significantly altering the AP triangulation of the GPB model, which was well within the reported physiological range. The other modifications introduced into the CRLP model rendered most of the investigated markers to be within the physiological range or otherwise closer to the physiological range as compared to the GPB and TP06 models. In this regard, only for systolic and diastolic $[Ca^{2+}]_i$ levels at 1 Hz the TP06 model outperformed CRLP. In addition, the CRLP model showed improved performance with respect to the GPB model regarding the S1S2 restitution, not only by bringing the maximum S1S2 restitution slope within the physiological range, but also by providing a shape for the restitution curve in good agreement with experimental measurements [95].

Even though the model modifications introduced in this work significantly improved the performance of the CRLP model over the GPB model in reproducing experimental data related to a number of electrophysiological markers, they have minimally affected the behavior of the model against potassium current blocks. In this regard, the CRLP model still provides results in very good agreement with available experimental data regarding AP response to I_{Kr}, I_{Ks} and I_{K1} blocks [54].

2.4.2 Simulation of hyperkalemic conditions

Simulations under hyperkalemic conditions showed that APD_{90} progressively decreased with the level of $[K^+]_o$, whereas ERP increased after a threshold in $[K^+]_o$ was reached ($[K^+]_o \approx 6$ mM). CV decreased with hyperkalemia and conduction was blocked above $[K^+]_o = 10.4$ mM. These results suggest that the longer ERP values and the occurrence of conduction block above $[K^+]_o = 10.4$ mM in the central zone of acutely ischemic tissue could cause areas of conduction block that could set a substrate for reentrant arrhythmias. Additionally, alternans were observed in ERP and APD_{90} for $[K^+]_o > 9.8$ mM. These results are in agreement with experimental studies where alternans were observed in the cells of the heart's ischemic zone [101, 102]. To the authors' knowledge, this is the first time that those observations are reported using a human ventricular AP model. That type of behavior was not observed in either the TP06 or the GPB models. For the TP06 model, conduction block occurred for $[K^+]_o \approx 15$ mM without the occurrence of alternans [104]. For the GPB model, conduction block occurred for $[K^+]_o \approx 9$ mM and alternans were not observed either.

2.4.3 Data sources

As described in [61], one of the problems on reutilization of model components in electrophysiology is the inclusion of components adjusted with data from different species. For that reason, in this work all model developments were made by using model components formulated based on human data only [51] or by fitting equations to additional human data available from the literature [76]. We did not try modifying other ionic currents or concentrations for which human data was not available. Regarding the types of human data used in the study, they all corresponded to adult humans, except for the data taken from the study by Pelzmann *et al.* [1], in which I_{CaL} was measured in children. Those data were used because the study clearly showed that there were not significant differences in the I_{CaL} current characteristics measured in children as compared to adults.

2.4.4 Model limitations

The developed CRLP model has a number of limitations, some of them inherited from the GPB model on which it was based, and others independent of it. Inherited from the GPB model is the absence of intracellular potassium dynamics ($[K^+]_i$ is kept constant in the GPB and CRLP models). $[K^+]_i$ dynamics play an important role in modeling hyperkalemic conditions, and is, therefore, a pivotal element for the accurate computational investigation of ventricular arrhythmias under such conditions. In addition, phase 1 of the AP shows an atypical behavior for the CRLP model. This may be caused by the I_{to} current. However, no attempt to modify this current has been made mainly because new human data was not available for that purpose. This current happens to be the only one whose definition differentiates endocardial and epicardial cells in the GPB model and in the CRLP model as well. In this regard, both models lack a description for the electrophysiology of midmyocardial cells. Another limitation of the CRLP model has to do with calcium handling. The results of the analysis conducted in this study point out the importance that the I_{CaL} current as well as $[Ca^{2+}]_i$ dynamics have over different electrophysiological markers. Many studies have attempted to provide accurate definitions of $[Ca^{2+}]_i$ dynamics in human ventricular cells, but this is still an area of intensive research. The present study suggests the need for continuing with the development of more reliable calcium dynamics models that allow improving the performance of whole cell AP models.

On top of the above described limitations, a comment is in order regarding the comparison of human ventricular AP models. It is clear that each model has been developed to reproduce certain electrophysiological behaviors observed from experimental recordings. Also, considering the huge variability in the experimental data, model comparison becomes a challenging task for which a model should never be qualified as being an improvement over another one just because it is able to reproduce specific experimental observations that the other model is not able to reproduce. In this study we used the term improvement exclusively to refer to the fact that, considering the set of investigated electrophysiological markers, the CRLP model provides a response that is more in line with the averaged experimen-

tal data used for evaluation purposes. The following chapters attempt to resolve some of the limitations enumerated above. For this purpose, novel methodologies have been developed and will be presented accordingly.

Chapter 3

Improvement of Existing Electrophysiological Models

3.1 Introduction

Departing from the CRLP model developed in Chapter 2, this chapter aims at improving its performance by including a relevant characteristic for investigation of ventricular arrhythmias arising under conditions of hyperkalemia, one of the components of myocardial ischemia. Such a characteristic refers to formulation of intracellular potassium dynamics, which were lacking both in the CRLP model as well as in the GPB model from which it was built. When potassium dynamics are incorporated into a model, an imbalance in the potassium currents may be originated, which may in turn lead to a drift in the intracellular potassium concentration. A way to overcome this is by readjusting model parameters to maintain potassium homeostasis.

As mentioned in Chapter 1, an AP model is described by a system of coupled differential equations that involve the transmembrane current flow as well as dynamic changes in intracellular ionic concentrations. For each ionic current a mathematical formulation is employed to represent characteristics like gating or permeability of the corresponding ion channels. Those formulations rely on a number of model parameters whose values are commonly estimated based on experimental data obtained from specific protocols for each ionic current. In this context parameter estimation presents various shortcomings intrinsic to the voltage-clamp experimental protocols [105]: i) insufficient separation of ionic current activation and inactivation processes; ii) use of non-selective pharmacological ion channel blockers; and iii) measurement of non-physiological solutions.

Despite these limitations, most parameter values of individual ionic currents have been identified in the past using independent sets of experiments. However, parameters describing ionic current conductances have not always been successfully characterized from experimental datasets, in large part due to the sensitivity of some ion channels to the cell isolation procedure performed before application of the voltage-clamp protocols [106]. Also, experimental studies may have purposely selected cells with large ionic currents, which interfere with model development based on such data [47]. For those reasons, a common procedure to identify individual ionic current conductances is based on model parameter fitting aimed at reproducing plausible values of electrophysiological AP properties like APD, triangulation or upstroke velocity [15, 46]. Other models include also constraints based on experimental data measured after blocking certain ionic currents [107], imposed to obtain a correct input resistance [47] or based on additional properties like APD rate adaptation and rate dependence of ionic concentrations as proposed in Chapter 2.

Cardiac electrophysiological computational models are commonly used to analyze the effect of drugs or to study the mechanisms underlying pathological conditions. Under those circumstances, the correct characterization of ionic current conductances is crucial. Overestimation or underestimation of current conductance values could lead to completely erroneous predictions. For this reason, while for many years the adjustment of current conductances in cardiac computational models has been frequently performed manually [108], a number of techniques have been developed in recent years to help in the process of parameter identification. Gradient descent methods [109, 110] and genetic algorithms [111–114] have been used for this purpose in several studies. Gradient descent methods rely on computing local gradients of the error function to determine a search direction towards a minimum. On the other hand, genetic algorithms use ideas from evolutionary biology and test different combinations (populations) of parameters to optimize the error function. In each iteration they create a new population based on the best results from previous iterations.

Gradient descent methods and genetic algorithms have a small degree of parallelization and, thus, other techniques with higher parallelization capability could better exploit the possibilities of current computing infrastructures. In this chapter, a novel methodology is proposed for identification of parameters describing ionic current conductances of cardiac electrophysiological models by using an optimization algorithm with trust region management [115]. The algorithm minimizes an objective function subject to non-linear constraints associated with a number of electrophysiological properties. The objective function and constraints are approximated by polynomial response surfaces that allow the optimization algorithm searching for a solution to the problem without performing a direct evaluation of the model. The use of a response surface helps to reduce the number of iterations of the algorithm and, thus, reduce the time cost of optimizing the model. To guarantee the ability of the model to represent physiological behavior, the region where the solution is searched for is limited based on experimentally reported values of electrophysiological properties like APD, AP triangulation, diastolic and systolic

intracellular calcium concentrations and time constants of APD rate adaptation to abrupt changes in cycle length (CL). The proposed methodology is applied to adjust the ionic conductances of the human ventricular CRLP model proposed in Chapter 2 after incorporation of intracellular potassium, $[K^+]_i$, dynamics. The modified CRLP model is compared against the most commonly used human ventricular AP models, namely the TP06 [51], GPB [15], ORd [64] models as well as with the CRLP model.

The relevance of accounting for $[K^+]_i$ dynamics is demonstrated by simulating a number of transitions in the extracellular potassium concentration, as in hemodialysis studies [116], and comparing the behavior of the original and modified CRLP models.

3.2 Materials and Methods

3.2.1 Optimization problem

General formulation

A minimization problem with constraints can be written as:

$$\min f(\mathbf{x}) \tag{3.1}$$

subject to

$$\mathbf{h}(\mathbf{x}) = \mathbf{0}, \tag{3.2}$$

$$\mathbf{g}(\mathbf{x}) \geq \mathbf{0}, \tag{3.3}$$

$$\mathbf{x}^L \leq \mathbf{x} \leq \mathbf{x}^U, \tag{3.4}$$

where $\mathbf{x}$ is the vector of decision variables, $\mathbf{x}^L$ and $\mathbf{x}^U$ their respective lower and upper bounds, $\mathbf{f}(\mathbf{x})$ is the objective function, and $\mathbf{h}(\mathbf{x})$ and $\mathbf{g}(\mathbf{x})$ are vector functions of equality and inequality constraints, respectively.

Particularization to ionic conductances estimation

The general minimization problem described in previous section was particularized in this study for estimation of ionic current conductances. Since different ionic current conductances G_i may differ by orders of magnitude, the following scaling was adopted for each of the elements of vector $\mathbf{x}$:

$$x_i = 20 \cdot log_{10} \frac{G_i}{G_i^0},$$

where G_i is the unscaled ionic current conductance and G_i^0 is its initial value in the model.

The objective function is defined for each particular problem. In this study, it was represented by the integral of the total potassium current during a cardiac cycle at 1 Hz steady-state pacing, as fully described in 3.2.2. No equality constraint function was defined in this case. The inequality constrain function was

defined by imposing a number of electrophysiological properties to remain within experimentally observed ranges:

$$\mathbf{m}_{LL} \leq \mathbf{m}(\mathbf{x}) \leq \mathbf{m}_{UU} \tag{3.5}$$

where $\mathbf{m}_{LL}$ and $\mathbf{m}_{UU}$ are the lower and upper bounds delimiting physiological ranges, respectively, and $\mathbf{m}(\mathbf{x})$ is the vector of electrophysiological properties calculated for $\mathbf{x}$.

Eq. 3.5 was reformulated to be consistent with the general formulation of the inequality constraints described in eq. 3.3:

$$g_j(\mathbf{x}) = \left| \frac{m_j(\mathbf{x}) - m_{j,CR}}{m_{j,RR}} \right| - 1 \leq 0,$$

where $m_{j,CR} = {}^{(m_{j,UL} + m_{j,LL})}/_{2}$ is the central point of the experimental range for the electrophysiological property j and $m_{j,RR} = {}^{(m_{j,UL} - m_{j,LL})}/_{2}$ is the distance between $m_{j,CR}$ and each of the limits of the experimental range.

Optimization using response surfaces

The optimization algorithm used in this study seeks for a solution of the minimization problem, Eqs. 3.1-3.4, by solving a sequence of approximate constrained optimization problems within a region of trust. For the iteration k of the algorithm, the approximate problem reads as:

$$\min \tilde{f}(\mathbf{x}) \tag{3.6}$$

subject to

$$\tilde{\mathbf{h}}(\mathbf{x}) = \mathbf{0}, \tag{3.7}$$

$$\tilde{\mathbf{g}}(\mathbf{x}) \geq \mathbf{0}, \tag{3.8}$$

$$\|\mathbf{x}\| \leq \Delta^k, \tag{3.9}$$

where $\tilde{f}(\mathbf{x})$, $\tilde{\mathbf{h}}(\mathbf{x})$ and $\tilde{\mathbf{g}}(\mathbf{x})$ are response surface approximations (RSA) of $f(\mathbf{x})$, $\mathbf{h}(\mathbf{x})$, and $\mathbf{g}(\mathbf{x})$ around $\mathbf{x}^k$, respectively, and Δ^k is the corresponding trust region radius. The trust region radius defines a region of trust in which the RSA is assumed to be reliable. The validity of the RSA can be evaluated through the trust region ratio test. For the objective function $f(\mathbf{x})$, the trust region ratio for iteration k was defined as:

$$\rho_0^k = \frac{f(\mathbf{x}^k) - f(\mathbf{x}^{k,*})}{\tilde{f}(\mathbf{x}^k) - \tilde{f}(\mathbf{x}^{k,*})}, \tag{3.10}$$

where $x^{k,*}$ is a solution of the minimization problem given by Eqs. 3.6-3.9. This definition of the trust region ratio is based on the consideration that $\rho_0^k \to 1$ as the trust region radius $\Delta^k \to 0$. If $\rho_0^k \leq 0$, the approximation is deemed as unacceptable and, consequently, the trust region radius is reduced. If $\rho_0^k \approx 1$ and $\|\mathbf{x}^{k,*} - \mathbf{x}^k\| = \Delta^k$, the RSA is evaluated as acceptable and Δ^k is increased. If

$0 < \rho_0^k < 1$, Δ^k is kept unchanged, but the RSA is rebuilt around $x^{k,*}$. Note that $\rho_0^k >> 1$ is also indicative of poor RSA and Δ^k is reduced, but the optimizer is considered to be moving in the right direction. The update of the trust region radius offers significant flexibility depending on the implementation. A particular updating rule will be presented in the following section.

The algorithm proposed in this work is based on the one described in [115] but it simplifies some aspects on how to manage and use the response surfaces and it reduces the number of times the database needs to be generated. Instead of considering the augmented Lagrangian of the problem, the proposal of this study is based on generating the response surface of the model and looking for the minimum in this surface. Subsequently, this solution is validated by using the trust region test in both the minimization function and the constraints of the model. This notably reduces the computational cost, as the database is generated once per iteration rather than every time there is a change in the parameters of the augmented Lagrangian.

Database generation and response surface approximation

One of the key elements of the minimization algorithm is building the RSA of the objective and constraint functions that will be used to solve the approximate minimization problem. To construct a response surface for a function of n variables, a large number of sample points are required. Also, to construct a reliable RSA, the sample points must be adequately distributed. Sampling techniques based on design of experiments are commonly used for this purpose [117]. In this study, full factorial designs, which require 3^n sampling points, were considered. A full factorial design consists of a three-level factorial: the corner points of a hypercube, plus the center of the hypercube and of each facet, plus the midpoints of the lines connecting the corners of the hypercube. In the next sections, the set of results of the sampling technique in an iteration of the algorithm for both the minimization and constraint functions will be referred to as *database*. Second order polynomial response surfaces were used in all cases.

Minimization algorithm

The minimization algorithm implemented in this work is shown in Fig. 3.1. The database was computed only once per iteration of the algorithm or whenever the solution was rejected and the trust region radius was reduced. The trust region ratio was used to validate the RSA for the objective function and constraints independently.

The basic steps of the algorithm shown in Fig. 3.1 are briefly described in the following. The index k indicates the iteration of the algorithm, i indicates the variable index and j represents the constraint index.

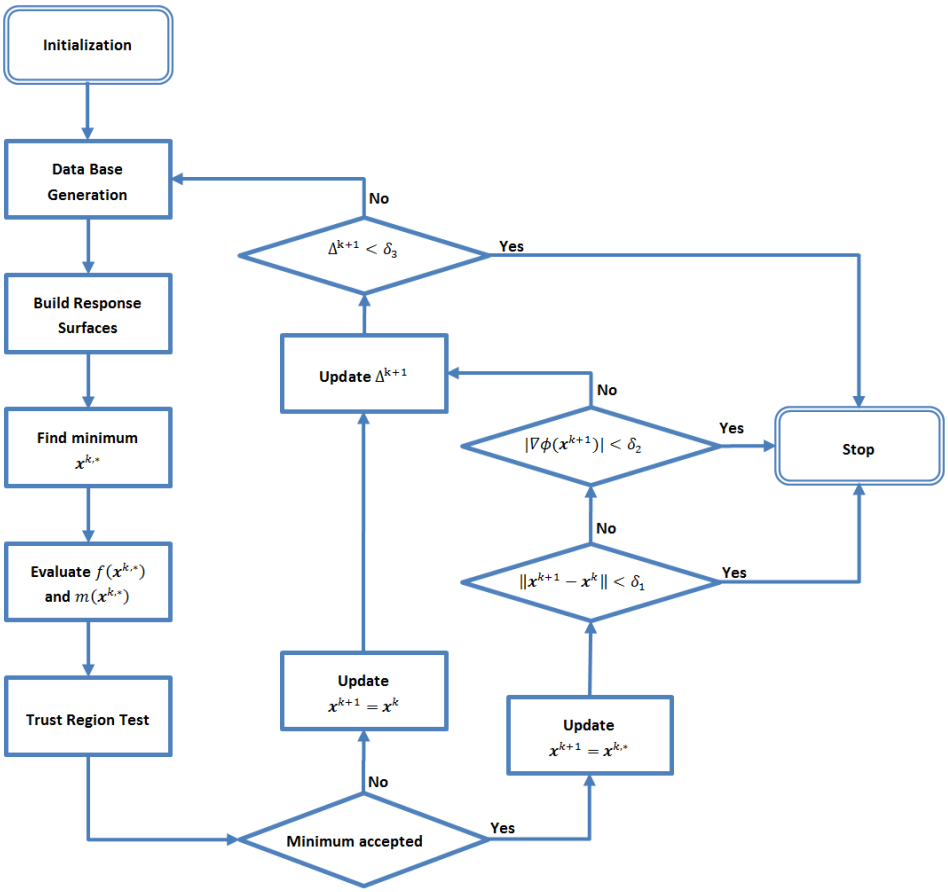

Figure 3.1: Flow chart of the proposed algorithm.

Step 0: Initialization

Define values for the tolerances δ_1 (solution tolerance), δ_2 (gradient tolerance) and δ_3 (improvement tolerance), the minimum acceptable value ρ_L for the trust region ratio to consider a trust region as acceptable and an upper limit $\Delta^{\max}$ for the trust region radius. Define an initial value Δ^0 for the size of the trust region and a starting point $\mathbf{x}^0$ for the variables of the problem. Set the iteration counter at $k = 0$.

Step 1: Database generation

Compute the database as described in section 3.2.1.

Step 2: Response surfaces

Build the RSA of the objective function and constraints of the problem around the current iterate $\mathbf{x}^k$.

Step 3: Find the minimum of the approximate problem

Find the minimum $\mathbf{x}^{k,*}$ of the constrained minimization problem defined by Eqs. 3.4-3.9 in the trust region limited by Δ^k.

Step 4: Trust region test

Evaluate f and each of the properties m_i in $\mathbf{x}^{k,*}$ and calculate the trust region ratio for the objective and constraint functions as in Eq. 3.10.

$$\begin{aligned} \rho_0^k &= \frac{f(\mathbf{x}^{k,*}) - f(\mathbf{x}^k)}{\widetilde{f}(\mathbf{x}^{k,*}) - \widetilde{f}(\mathbf{x}^k)} \\ \rho_j^k &= \frac{m_j(\mathbf{x}^{k,*}) - m_j(\mathbf{x}^k)}{\widetilde{m}_j(\mathbf{x}^{k,*}) - \widetilde{m}_j(\mathbf{x}^k)},\ 1 \leq j \leq M. \end{aligned}$$

The solution $\mathbf{x}^{k,*}$ was accepted when $\rho_0^k > 0$ and one of the following two criteria was met: i) the constraints in $\mathbf{g}(\mathbf{x})$ were feasible or; ii) $|\rho_j^k - 1| \leq \rho_L, \forall j$. For this work, $\rho_L = 0.25$ was used. If the solution was accepted, the flag $flg_{TR}^k = true$ was set and $\mathbf{x}^{k+1} := \mathbf{x}^{k,*}$, otherwise $flg_{TR}^k = false$ and $\mathbf{x}^{k+1} := \mathbf{x}^k$.

Step 5: Trust region radius update

The trust region radius was updated as follows:

$$\Delta^{k+1} = \begin{cases} 0.25\Delta^k & \text{if} \quad flg_{TR}^k = false, \\ \Delta^k & \text{if} \quad flg_{TR}^k = true \ \text{ and } \ \|\mathbf{x}^{k,*} - \mathbf{x}^k\| < \Delta^k, \\ 2\Delta^k & \text{if} \quad flg_{TR}^k = true \ \text{ and } \ \|\mathbf{x}^{k,*} - \mathbf{x}^k\| = \Delta^k. \end{cases}$$

Step 6: Algorithm termination

The algorithm ended if one of the following conditions was satisfied:

1. $\|\mathbf{x}^{k+1} - \mathbf{x}^k\| < \delta_1$ and $flg_{TR}^k = true$: The distance between the last two accepted iterates was too small to be significant.

2. $\|\boldsymbol{\nabla}\phi(\mathbf{x}^{k+1})| < \delta_2$ and $flg_{TR}^k = true$: The gradient of the Lagrangian function was too small. The Lagrangian function was defined as:

$$\phi(\mathbf{x}) = f(\mathbf{x}) + \sum_{j=1}^{M} \lambda_j^k \cdot m_j(\mathbf{x})$$

   where λ_j^k are the Lagrange multipliers obtained in the constrained minimization problem defined by Eqs. 3.4-3.9 in the trust region (limited by Δ^k) in Step 3.

3. $\Delta^{k+1} < \delta_3$: The trust region radius became too small.

If none of these criteria was satisfied, then set $k := k + 1$ and go to step 1.

3.2.2 Upgrade of the CRLP model

$[K^+]_i$ dynamics in the CRLP model

One of the differences between the CRLP model and the ORd and TP06 models lies in the representation of $[K^+]_i$ dynamics. As mentioned above, in the CRLP model, as well as in the GPB model, $[K^+]_i$ was assumed to be constant. Under steady-state conditions, $[K^+]_i$ variations during an AP can be neglected. Nevertheless, when there is a change in the investigated conditions or if the model is somewhat altered, $[K^+]_i$ may reach a new steady-state value. This is the case, for instance, when the stimulation frequency is varied, as $[K^+]_i$ becomes reduced in response to increased stimulation frequency [64, 118]. Another scenario where $[K^+]_i$ dynamics are relevant is in the simulation of acute ischemia. Dutta et al. showed the limitations of using the GPB model with constant $[K^+]_i$ [119]. In the present chapter, the methodology described in section 3.2.1 was used to incorporate $[K^+]_i$ dynamics into the CRLP model while retaining its capacity to reproduce experimentally observed values of arrhythmic risk-related markers.

$[K^+]_i$ dynamics were introduced through the following equation:

$$\frac{d}{dt}[K^+]_i = -I_{K_{tot}} \cdot \frac{C_{mem}}{V_{myo} \cdot F_{rdy}} \tag{3.11}$$

where $I_{K_{tot}}$ is the total potassium current, C_{mem} is the membrane specific capacitance, V_{myo} is the bulk cytosol volume and F_{rdy} is Faraday's constant.

$I_{K_{tot}}$ was calculated as the sum of all potassium currents and the stimulus current:

$$I_{K_{tot}} = I_{to} + I_{Kr} + I_{Ks} + I_{K1} - 2 \cdot I_{NaK} + I_{CaK} + I_{Kp} + I_{stim} \tag{3.12}$$

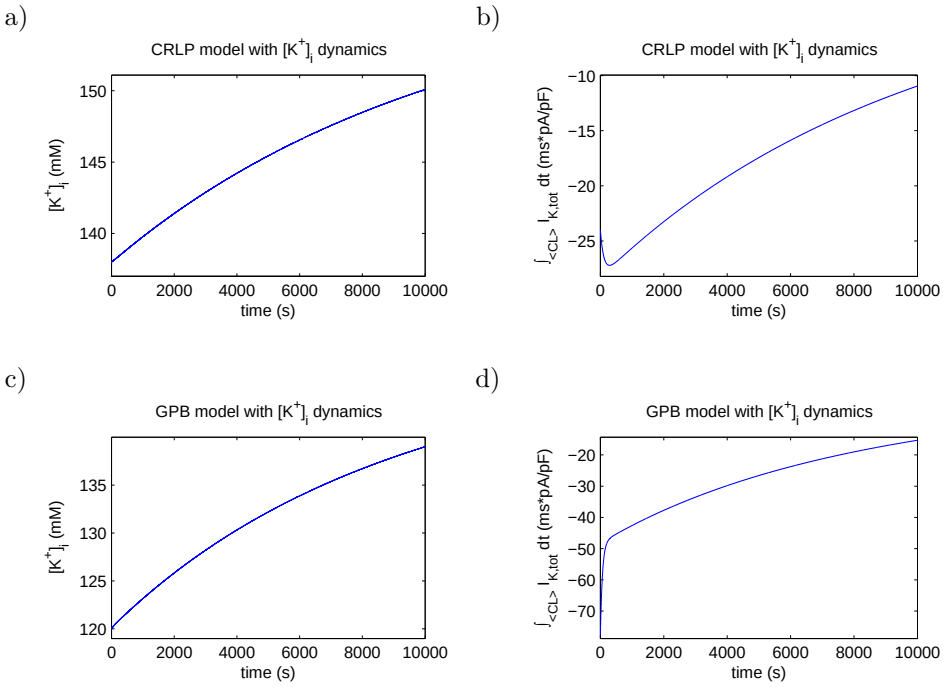

Figure 3.2: Temporal evolution of $[K^+]_i$ in CRLP and GPB epicardiacl cell models after introducing $[K^+]_i$ dynamics: a) and c) show $[K^+]_i$ evolution when the models (CRLP and GPB, respectively) are stimulated with a CL of 1000 ms. b) and d) show the evolution of the integral of $I_{K_{tot}}$ during one cycle for the same simulation as in a) and c).

where I_{to} is the *transient outward* potassium current, I_{Kr} is the *rapidly activating* potassium current, I_{Ks} is the *slowly activating* potassium current, I_{K1} is the *inward rectifier* potassium current, I_{NaK} is the *sodium-potassium pump* current, I_{CaK} is the current generate by potassium ions passing through the *L-type calcium channels*, I_{Kp} is the *plateau* potassium current, and I_{stim} is the stimulus current.

If Eq. 3.11 is directly added to the CRLP and GPB models, $[K^+]_i$ drifts (Fig. 3.2, panels a) and c), respectively). The continuous increase in $[K^+]_i$ is due to a larger potassium influx in each cardiac beat, which can in turn be explained by an imbalance in the potassium current. Although it is not straightforward to establish a physiological range for $[K^+]_i$ because there are no experimental measurements of this concentration, all human ventricular cell models published in the literature, despite having different $[K^+]_i$ values under steady-state conditions, they all lie within the range 120-145 mM. This range is in agreement with the corresponding experimentally reported values for the resting membrane potential, which is close to the Nernst potential for potassium [64].

In Fig. 3.2, panels b) and d), the integral of the total potassium current during one cardiac cycle is shown, which gives an idea of how far the models are from equilibrium. The above noted issue associated with the introduction of $[K^+]_i$ dynamics into the CRLP model can be sorted out by readjusting the current conductances to maintain $[K^+]_i$ homeostasis. Since, at the same time, the performance of the model in terms of representation of electrophysiological behavior wants to be retained, a constrained optimization problem was formulated in this study. This problem was tackled by applying the response surface-based optimization methods presented in 3.2.1.

For further model assessment, optimization was performed as described in the next paragraph while considering different initial $[K^+]_i$ values in the range 120-145 mM.

Optimization-driven model parameter update

A new set of current conductances for the modified CRLP model was sought such that potassium homeostasis was preserved while a number of electrophysiological properties were guaranteed to remain within experimental limits. This was stated as a constrained optimization problem of the form:

$$\min \left(\int_{<CL>} I_{K_{tot}}(\mathbf{x}) \right)^2 \tag{3.13}$$

subject to

$$\mathbf{m}_{LL} \leq \mathbf{m}(\mathbf{x}) \leq \mathbf{m}_{UU}, \tag{3.14}$$

$$\mathbf{x}^L \leq \mathbf{x} \leq \mathbf{x}^U, \tag{3.15}$$

where $\mathbf{x}$ is the vector of scaled current conductances (see 3.2.1), with lower an upper bounds $\mathbf{x}^L$ and $\mathbf{x}^U$, respectively, $\int_{<CL>}$ represents the integral during a cardiac cycle and $\mathbf{m}$ is a vector function of selected electrophysiological properties with lower and upper physiological bounds defined by vectors $\mathbf{m}_{LL}$ and $\mathbf{m}_{UU}$. Initialization was defined based on the epicardial CRLP model (where $[K^+]_i$ takes a constant value of 138 mM). Other initializations were additionally tested, as described in 3.2.2.

Constraint functions

Seven ventricular electrophysiological properties of epicardial cells were considered for definition of inequality constraints in 3.2.2:

- **APD_{90}**: APD is considered the main preclinical marker of drug cardiotoxicity. APD prolongation has been linked to long QT syndrome and increased risk of developing Torsades de Pointes [77, 78]. In this study, APD_{90} was used to denote AP duration at 90% repolarization.
- **Triangulation**: This marker quantifies the shape of the final part of the AP and is defined as the difference between APD at 90% and 50% of repolarization. Low triangulation values indicate square APs, while high values

indicate triangular APs. Triangulation has been proposed as a marker of pro-arrhythmia [77], with long APD_{90} values without triangular APs considered as anti-arrhythmic and with triangular APs considered as pro-arrhythmic in general.

- **Systolic and diastolic intracellular calcium ($[Ca^{2+}]_i$) levels**: Calcium transient properties evaluated at different pacing frequencies have been reported as arrhythmic risk markers [79, 80]. In this study, diastolic (resting level) and systolic (peak value) calcium transient levels were evaluated at 0.5 Hz and 1 Hz steady-state pacing.

- **Time constants of APD_{90} adaptation to abrupt changes in CL**: Adaptation of ventricular repolarization duration to abrupt changes in CL has been proposed as an arrhythmic risk marker [81]. In this study, the dynamics of APD_{90} adaptation to abrupt changes in CL were fitted by two exponentials with associated time constants τ_{fast} and τ_{slow}, following the methodology proposed in Pueyo *et al.* [13]. Only τ_{slow} has been considered since there is no available quantitative experimental data on τ_{fast} values.

Two stimulation protocols were used to calculate the above described markers:

- **Steady-state protocol**: A train of 3,000 stimulation pulses was delivered at a given CL. Simulations were carried out using two different CL values: 1,000 and 2,000 ms. The evaluated markers were: APD_{90} and triangulation at 1,000 ms; and diastolic and systolic $[Ca^{2+}]_i$ at 1,000 and 2,000 ms.

- **Abrupt changes in CL protocol**: The cell was stimulated with a CL of 1,000 ms for 8 minutes and then with a CL of 600 ms for additional 8 minutes. APD_{90} dynamics after the abrupt CL change were best fitted by two exponentials, the second of which was characterized by τ_{slow}.

Physiological bounds for constraint functions

Lower and upper bounds $\mathbf{m}_{LL}$ and $\mathbf{m}_{UU}$ were defined according to physiological experimental values reported in the literature for the analyzed properties. The selected range for APD_{90} was 280-310 ms. Even though some studies have reported wider ranges, up to 271-366 ms [2, 8, 96], a restricted interval was used to keep the model within the same range of existing human ventricular cell models [15, 46, 51, 64, 120]. The range for triangulation was 44-112 ms [2, 96]. For the diastolic and systolic $[Ca^{2+}]_i$ levels at 1 Hz and 0.5 Hz stimulation, the CRLP model, as occurs with other recent human ventricular AP models (GPB, ORd, TP06, TP04) [12, 15, 46, 51, 64, 120, 121], is out of the physiological range reported in the literature [10, 97]. For that reason, the physiological range was extended to ensure a feasible solution of the optimization problem. Nevertheless, the optimal solution was evaluated to confirm that either it let the model lie within physiological range or at least improved the results of the CRLP model. The physiological range for τ_{slow} was set to 70-110 s [95]. Table 3.1 summarizes the evaluated markers and

	Physiol. Range	Selected Range	CRLP Model	This work
APD_{90} (ms)	271-366	280-310	305.6	280.9
Triangulation (ms)	44-112	44-112	78	84.6
Sys. $[Ca^{2+}]_i$ 1Hz (μM)	1.59-2.01	0.602-2.01	0.602	0.701
Sys. $[Ca^{2+}]_i$ 0.5Hz (μM)	0.71-1.68	0.523-1.68	0.523	0.664
Dia. $[Ca^{2+}]_i$ 1Hz (μM)	0.20-0.33	0.097-0.33	0.097	0.100
Dia. $[Ca^{2+}]_i$ 0.5Hz (μM)	0.14-0.32	0.091-0.32	0.091	0.096
τ_{slow} (s)	70-110	70-110	105.6	106.0
$\int_{CL} I_{K_{tot}} \cdot dt$ (ms·pA/pF)			-28.52	$-3.9 \cdot 10^{-9}$

Table 3.1: Electrophysiological markers evaluated in the proposed response surface approximation-based optimization.

their physiological ranges in the second column, whereas the third column indicates the lower and upper bounds used for the optimization.

Sensitivity Analysis

Prior to solving the minimization problem, a sensitivity analysis was performed on the CRLP model following the methodology described by Romero *et al.*[12]. The aim was to identify the conductances that most notably influenced the objective function (the integral of the total potassium current) and the constraints (electrophysiological properties) in order to define the set of decision variables for the optimization.

For the sensitivity analysis, the conductances were varied by ±30% one at a time. Fourteen conductances were considered in the sensitivity analysis, namely: G_{to}, the maximal conductance of the transient outward potassium current; G_{Ks}, the maximal conductance of the slowly activating potassium current; G_{pCa}, the maximal conductance of the sarcolemmal calcium pump; G_{Kr}, the maximal conductance of the rapidly activating potassium current; G_{Kp}, the maximal conductance of the plateau potassium current; G_{NaK}, the maximal activity of the Na-K pump; G_{ncx}, the maximal activity of the Na-Ca exchanger; G_{CaL}, the maximal conductance of the L-Type calcium current; G_{K1}, the maximal conductance of the inward rectifier potassium current; G_{Na}, the maximal conductance of the fast sodium current; G_{ClCa}, the maximal conductance of the calcium-activated chloride current; $G_{Na,Bk}$, the maximal conductance of the background sodium current; $G_{Cl,bk}$, the maximal conductance of the background chloride current; and $G_{Ca,bk}$, the maximal conductance of the background calcium current.

For each property m and conductance p, the percentage of change ($D_{m;p;a}$) and sensitivity ($S_{m;p;a}$) were calculated as follows [12]:

$$D_{m;p;a} = \frac{M_{p;a} - M_{control}}{M_{control}} \cdot 100,$$

$$S_{m;p;a} = \frac{D_{m;p;a} - D_{m;p;-a}}{2 \cdot a} \cdot 100,$$

where $M_{p;a}$ is the value of property m when the conductance p is varied by the percentage a and $M_{control}$ is the value of property m under control conditions. As shown above, sensitivity ($S_{m;p;a}$) is calculated as the ratio of the difference between the percentage of change ($D_{m;p;a} - D_{m;p;-a}$) and the interval of change ($2 \cdot a$). In particular, for this study $a = 30\%$:

$$S_{m;p;0.3} = \frac{D_{m;p;0.3} - D_{m;p;-0.3}}{2 \cdot 0.3} \cdot 100 = \frac{M_{p;0.3} - M_{p;-0.3}}{M_{control}} \cdot \frac{10^5}{6}$$

Sensitivity was calculated for each of the electrophysiological markers described in section 3.2.2 and for the integral of the total potassium current ($I_{K_{tot}}$) during one cardiac cycle at 1 Hz steady-state pacing.

Model Comparison

Considering the difficulty of directly comparing the absolute value of each conductance for different computational models, due to the dependence on the whole current formulation, ionic current traces calculated during a cardiac cycle at 1 Hz steady-state pacing were compared for the CRLP, TP06, GPB and ORd models. The comparisons aimed at verifying that the modified CRLP model had current densities of similar magnitude and ionic currents of similar shapes as calculated with other published models.

3.2.3 Frequency-dependence behavior

Pacing at different frequencies was simulated to assess whether the modified CRLP model retained the frequency-dependence behavior of the original CRLP model. To this end, APD_{90} was calculated at steady-state for CLs ranging from 250 to 5000 ms (in each case computed after pacing for 3,000 cycles).

3.2.4 Simulation of changes in potassium concentration

Hypokalemic and hyperkalemic conditions were simulated with the original and the modified CRLP models. Two types of simulations were performed to compare the models with the experimental results.

First, the effect of changing $[K^+]_o$ was assessed when the cell was not stimulated to compare with the experimental results described in [122]. Subsquently, and following the experiments performed in [116], the extracellular potassium concentration, $[K^+]_o$, was increased from 2 mM to 7 mM in 0.5 mM steps using a homogeneous 4-cm long fiber composed of epicardial cells. The physiological $[K^+]_o$ value of 5.4 mM replaced the value of 5.5 mM in the simulations [116]. The conductivity σ, defining the velocity of the stimulus propagation, was set to render a Conduction Velocity (CV) close to 65 cm/s under control conditions [88]. The cell capacitance was set to $C_m = 1\ \mu\text{F/cm}^2$. For each $[K^+]_o$ value, the model was first stabilized (without stimulation) until the product of the gates $h \cdot j$ reached 99%

of the steady-state value $h_{ss} \cdot j_{ss}$, which was subsequently followed by 1 Hz pacing simulation. Stimulus current pulses twice the diastolic threshold were applied at one end of the cable. The diastolic threshold was defined as the minimum amplitude required for propagating five pulses along the fiber. The model was studied by stimulating the tissue with a train of 100 basic stimulations (S1) delivered at a CL of 1,000 ms. $[K^+]_i$ was measured at the end of each stimulus at five different positions along the cable situated at distances from the origin of 1.5, 1.75, 2, 2.25 and 2.5 cm. The average value over the five locations was calculated.

3.2.5 Implementation

The CRLP model was implemented in Matlab based on the original CellML file [120]. The code used to compute the simulations and to calculate the different markers is freely available at `https://github.com/ChusCarro/MatCardiacMLab/releases/tag/0.1.0`.

The minimization algorithm was implemented in Matlab. For 1D tissue simulations, a semi-implicit operator-splitting scheme implemented in Fortran was used to solve the propagation [87] with a space discretization of $\Delta x = 0.1$ mm and a time discretization of $\Delta t = 0.002$ ms, as in [120].

All computations were performed by using the high performance computing cluster (ICTS) "NANBIOSIS". Details about the cluster can be found at: `http://www.nanbiosis.es/u27-e1-hermes-cluster`

3.3 Results

3.3.1 Sensitivity Analysis

Results of the sensitivity analysis applied to the epicardial version of the CRLP model are shown in Figure 3.3. The value of the integral of the total potassium current, $I_{K_{tot}}$, in one cardiac cycle was highly dependent on the conductance of the background chloride current, $G_{Cl,bk}$, and the L-type calcium current, G_{CaL} (S_{30} values of -412.62% and 396.83%, respectively). Other currents were also found to play an important role in regulating potassium homeostasis: G_{NaK}, 199.46%; G_{K1}, -152.06%; G_{to}, -110.57%; G_{Kr}, -81.16%; and G_{ncx} 62.72%. The currents with the largest effect on the APD were found to be the same as for the objective function, although the sensitivities were notably reduced: $G_{Cl,bk}$, -48.56%; and G_{CaL}, 33.41%. Triangulation was mainly modulated by: G_{K1}, -57.7664%; and G_{Kr}, -20.1113%. Diastolic and systolic $[Ca^{2+}]_i$ values were mostly influenced by G_{CaL} (27.65% and 171.71%, respectively). These markers were also influenced by changes in the following conductances: G_{NaK} (-16.08%, -78.62%), G_{ncx} (-15.74%, -74.48%), $G_{Cl,bk}$ (-14.53%, -80.66%) and $G_{Ca,bk}$ (11.51%, 47.46%). Regarding τ_{slow}, G_{NaK} was the conductance with the largest effect on this marker (-128.37%), with the remaining conductances not playing a significant role.

Based on these results, five conductances were selected as decision variables for the minimization problem described in 3.2.2, namely: $G_{Cl,bk}$, G_{CaL}, G_{ncx}, G_{K1}, and G_{to}. Of note, G_{NaK} was discarded because any modification on this conductance

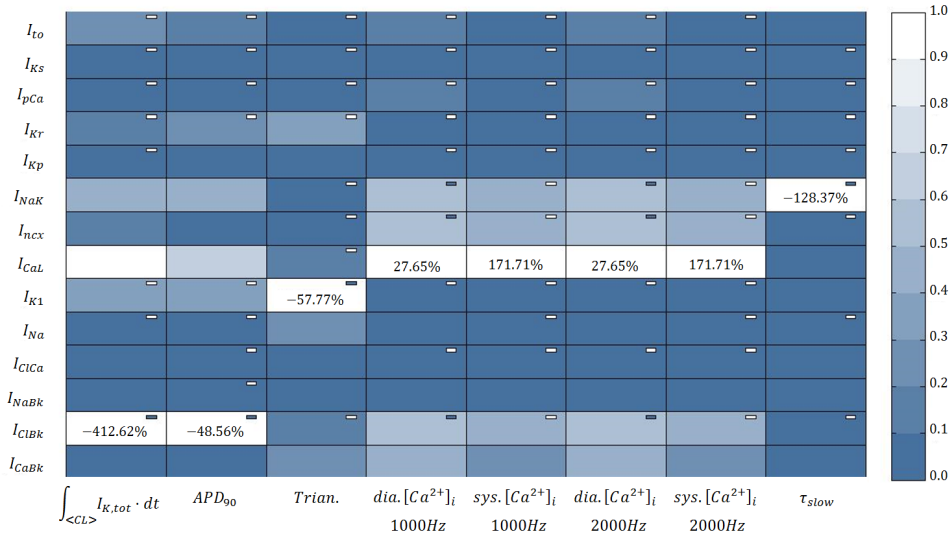

Figure 3.3: Results of the sensitivity analysis applied to the original CRLP model. The blue scale indicates relative sensitivity for each marker. White color indicates maximum relative sensitivity and dark blue color indicates that property and parameter are independent. Percentages in the white boxes indicate the absolute sensitivity of the property. A minus sign in a box indicates that marker and model parameter vary inversely. 'Trian' stands for Triangulation, 'Sys' stands for systolic and 'Dia' stands for diastolic.

significantly influenced τ_{slow}, with this effect not being counterbalanced by changes in any other conductance (see Figure 3.3).

3.3.2 Non-linear optimization

The optimization algorithm found a minimum after four iterations. Variations in the updated current conductances with respect to their initial values were: $G_{Cl,bk}$, +19.34%; G_{CaL}, +3.93%; G_{ncx}, -33.25%; G_{K1}, -14.08%; and G_{to}, +22.35%.

With this new set of conductance values, and after introducing $[K^+]_i$ dynamics in the model, $[K^+]_i$ stabilized at 138 mM. The value of the electrophysiological markers are described in table 3.1. All markers were within physiological ranges or closer than with the original CRLP model (last column in table 3.1).

When the model was optimized while considering different initial $[K^+]_i$ values in the range 120-145 mM, results were practically coincident with those reported above for $[K^+]_i$ initialized at 138 mM. At steady-state, $[K^+]_i$ reached a value of 138 mM as well, differences in the values of the markers where below 1% and the maximum difference between optimal conductances was lower than 2.5%. In this case, the algorithm required six iterations rather than four to reach the optimal solution.

3.3.3 Model Comparison

To evaluate the impact of the new values for the estimated ionic conductances in the modified CRLP model, the AP and the associated ionic currents (I_{CaL}, I_{K1}, I_{ncx}, $I_{Cl,bk}$ and I_{to}) were compared with the equivalent properties in the original CRLP model and in other human ventricular cell models. The results are shown in Fig. 3.4. Other currents that were not considered for the optimization but that could be altered as well, like I_{Kr}, I_{Ks} and I_{Kp}, are shown in Fig. 3.5.

The main differences in the AP between the original and modified CRLP models were a decrease in the membrane potential during the *plateau* phase as well as shortening of the APD. There were small differences in the peak value of some currents, but in all cases the modified CRLP model was within the range of the other models or within experimentally reported bounds. I_{CaL} peak was larger in the modified model with respect to the GPB model and the original CRLP model, but smaller than in the TP06 model. I_{K1} peak was slightly smaller in the modified model with respect to the original CRLP model, which had the smallest peak value among all ventricular models, but in any case within the range reported experimentally (0.4-1.8 pA/pF[76, 96]).

An important finding was that, while G_{ncx} and $G_{Cl,bk}$ in the modified CRLP model were significantly different from those in the original CRLP model (-33.25% and +19.34% respectively), the effects in terms of ionic current traces led to both I_{ncx} and $I_{Cl,bk}$ not being notably different from those in the original CRLP model. The I_{Kp} current remained as in the original model, while I_{Ks} was different but took really small values in both cases. I_{Kr} was diminished in amplitude by 32.6% and its integral during a cycle was reduced by 30% with respect to the CRLP model. The extent of APD prolongation following blockade of this current was 10% for the

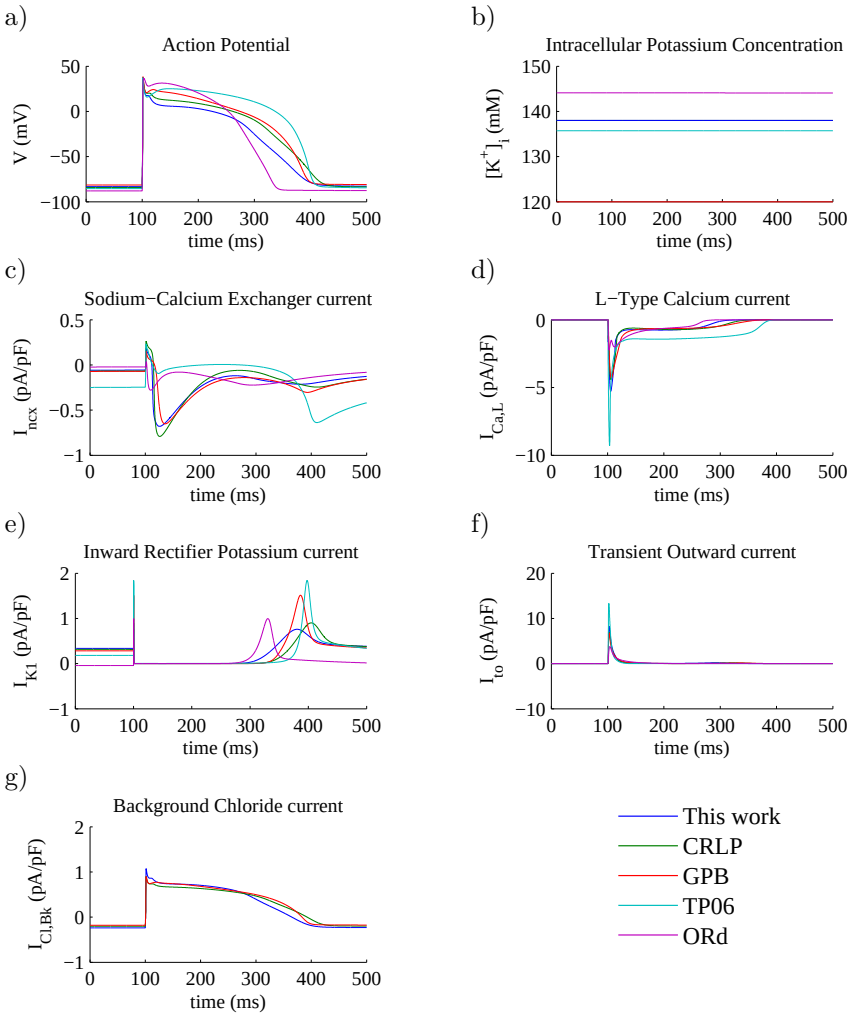

Figure 3.4: Model comparison. Blue lines represent the results of this work with inclusion of $[K^+]_i$ dynamics, green lines represent the CRLP model, red lines represent the GPB model, cyan lines represent the TP06 model and purple lines represent the ORd model. All the figures show results at steady-state (after pacing for 3,000 cycles at a CL of 1000 ms). a) Action potential; b) Intracellular potassium concentration; c) Sodium-calcium exchanger Current; d) L-type calcium current; e) Inward potassium current; f) Transient outward potassium current; and g) Background chloride Current.

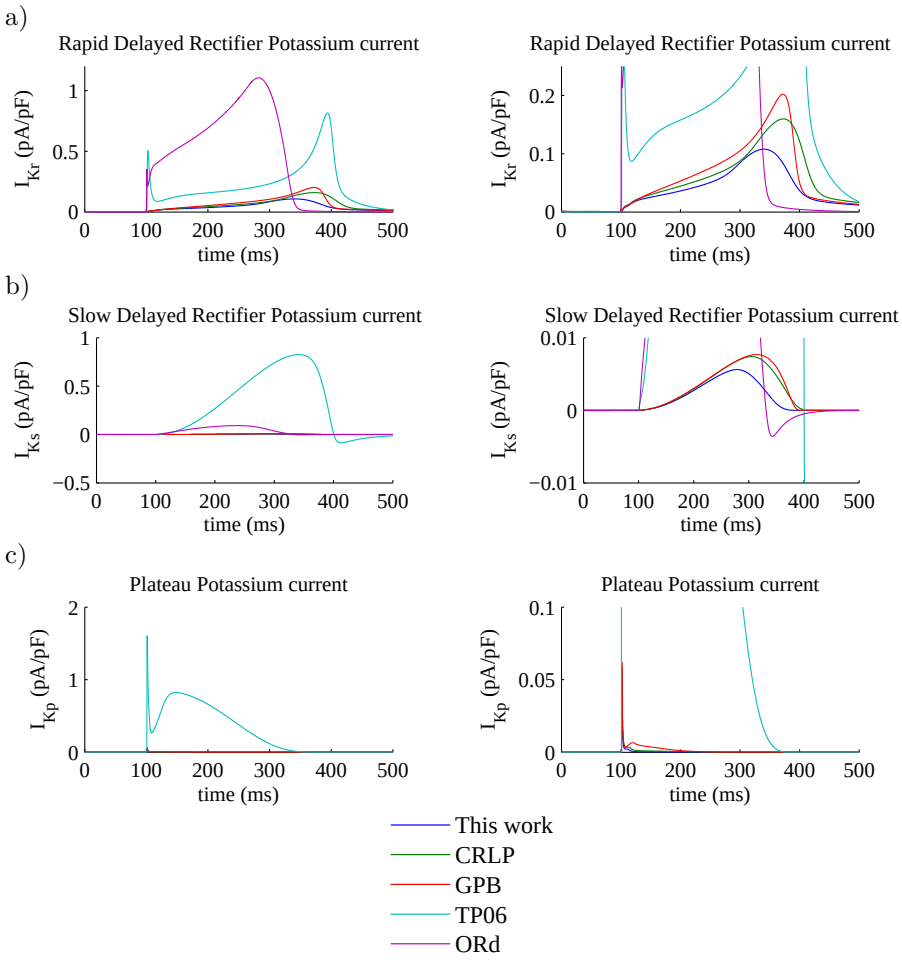

Figure 3.5: Model comparison. The colors in this figure are the same as those used in Fig.3.4. Results are shown at steady-state (after pacing for 3,000 cycles at a CL of 1000 ms). The graphics on the right are zoomed versions of the graphics on the left. a) Rapid delayed rectifier potassium current; b) Slow delayed rectifier potassium current; and c) Plateau potassium current.

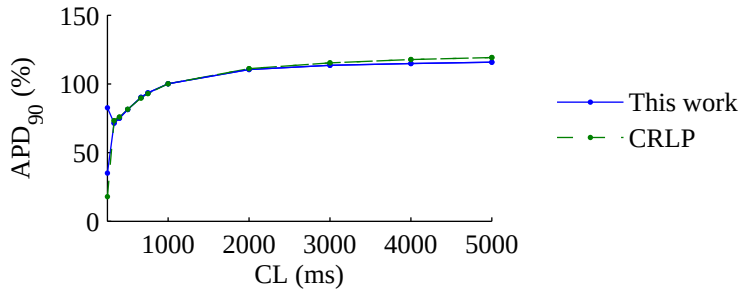

Figure 3.6: Steady-state APD_{90} values as a function of pacing CL.

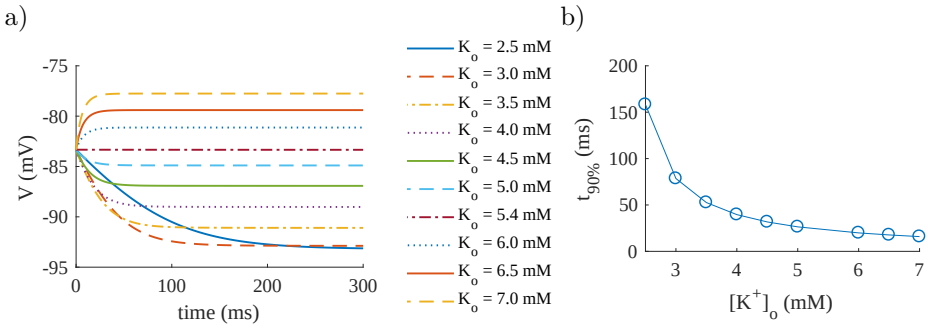

Figure 3.7: Results for an unstimulated cell simulated with the modified CRLP model following changes in $[K^+]_o$. a) Temporal evolution of membrane potential; b) Time to achieve 90% of the steady-state membrane potential ($t_{90\%}$).

modified CRLP model, as compared to 14% for the original CRLP model, being both values within experimentally defined limits [54].

3.3.4 Frequency response

Fig. 3.6 shows steady-state normalized APD_{90} values calculated with the original and modified CRLP models. Normalization was performed with respect to the APD_{90} value for CL=1000 ms. Both models presented very similar behaviors, with the only relevant difference being observed for CL=250 ms. For this CL, the modified CRLP model showed alternans, while the original CRLP model did not.

3.3.5 Response to changes in extracellular potassium

Fig. 3.7a shows the temporal evolution of membrane potential following changes in $[K^+]_o$ for an unstimulated cell simulated with the modified CRLP model. During the first 100 ms, membrane potential varied following the corresponding change in $[K^+]_o$, in line with the results reported in [122]. Figure 3.7b shows the time

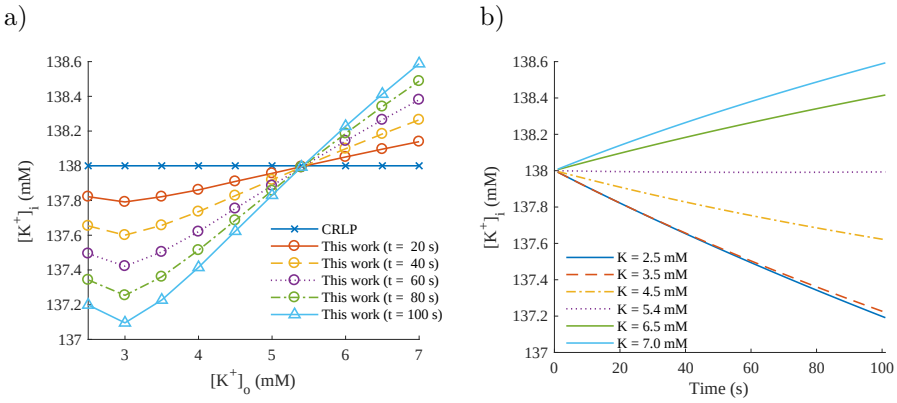

Figure 3.8: $[K^+]_i$ evolution following $[K^+]_o$ changes simulated with the modified CRLP model. a) $[K^+]_i$ dependence on $[K^+]_o$ at different time instants; b) time course of $[K^+]_i$ for different $[K^+]_o$ values.

needed to reach 90% of the steady-state membrane potential ($t_{90\%}$). The value for $t_{90\%}$ in the simulation for the same change in $[K^+]_o$ than in [122] (from 4.4 mM to 6.6 mM) was 16.2 ms, which is somewhat faster than the experimentally reported results in [122] for rabbit (80 ms) and rat (147 ms) ventricular myocytes.

Fig. 3.8a shows a snapshot of $[K^+]_i$ values calculated with the modified CRLP model at different times following changes in $[K^+]_o$ as described in 3.2.4. Fig. 3.8b shows the temporal evolution of $[K^+]_i$ in response to changes in $[K^+]_o$. Under control conditions, $[K^+]_i$ remained constant in time. As expected, following simulated hyperkalemia ($[K^+]_o > 5.4\ mM$), $[K^+]_i$ increased as $[K^+]_o$ increased, whereas for simulated hypokalemia ($[K^+]_o < 5.4\ mM$), $[K^+]_i$ decreased in response to $[K^+]_o$ decreases. For $[K^+]_o \leq 2.0\ mM$, tissue became inexcitable. In table 3.2, the steady-state value of $[K^+]_i$ in the optimized CRLP model is shown for each simulated $[K^+]_o$ value.

3.3.6 Computational Cost

Each iteration of the optimization algorithm involved computations associated with a number of stimulation protocols. In Table 3.3, a summary of the computational cost is shown for each of the protocols. In each iteration, the protocols were run twice: one for the generation of the database (243 simulations in parallel) and another one for the evaluation of the solution (6 simulations in parallel). The variance in the computation times is due to the fact that computations were run in different nodes of a high performance computing cluster, namely the one described in section 3.2.5. The four iterations of the optimization algorithm were computed in 23 hours and 16 minutes.

$[K^+]_o$ (mM)	$[K^+]_i$ (mM)
2.5	73.5
3.0	84.8
3.5	95.8
4.0	107.2
4.5	118.3
5.0	129.3
5.4	138.0
6.0	151.4
6.5	161.6
7.0	172.5

Table 3.2: Steady-state values of $[K^+]_i$ for different $[K^+]_o$ values as calculated with the optimized CRLP model.

Protocol	Mean	STD	Max
Steady-state CL = 1000 ms	01:31:45	00:41:31	02:29:31
Steady-state CL = 2000 ms	02:35:38	01:03:47	03:41:11
APD Rate Adaptation	00:28:36	00:14:17	00:53:57

Table 3.3: Computational cost of the different protocols used for the optimization.

3.4 Discussion

In this chapter a mathematical framework to adjust ionic current conductances of cardiac AP models by using response surface approximation-based optimization is proposed. The framework has been applied to update the CRLP human ventricular AP model, described in Chapter 1, by incorporating $[K^+]_i$ dynamics. Such incorporation involves readjustment of ionic current conductances to avoid drifting in intracellular potassium. While adjusting for current conductances, a number of electrophysiological properties are required to remain within available experimental ranges by properly defining constraints to the optimization problem that is being solved. The proposed framework can be easily extended to solve other problems frequently arising when developing cardiac computational models, for instance related to the update of existing models to reproduce the response to pharmacological ion channel inhibitions on top of baseline conditions. In the following subsections, the main aspects of the proposed methodology and the results obtained in this work are discussed.

3.4.1 Response surface optimization

The use of response surfaces to minimize an objective function subject to a number of constraints, as proposed in this chapter, allows reaching a solution to the proposed problem in a small number of iterations, thus reducing the computational

cost with respect to other previously published approaches. In [115], Rodriguez *et al.* proposed an algorithm that uses augmented Lagrangian techniques and relies on successively building RSA of the augmented Lagrangian to solve a minimization problem like that defined by Eqs. 3.1-3.4. In this chapter, the trust region ratio was used to independently validate the RSA for the objective function and the constraints instead of considering the augmented Lagrangian of the problem. Our proposal led to a reduction in the number of times the database was generated and, thus, simplified the implementation. The model that is optimized in the present work is much more complex than those used in [115], but the number of times the database was generated was smaller than in all the cases described in [115].

Also, differently to other optimization algorithms based on e.g. Genetic Algorithms [112, 114], the response surface approach proposed in this chapter guarantees the convergence to a local minimum of the problem when the response surfaces are built such that they match the objective function up to the first order around the point where the approximation is built. In addition, our response surface approach allows identifying a potential minimum anywhere within the trust region, not necessarily contained in the database.

Finally, in this chapter the proposed optimization algorithm was used to solve a problem where a new characteristic was added to a human ventricular cell model, the CRLP model, while a number of electrophysiological markers were guaranteed to remain within physiological range or closer to it than with the original CRLP model. In other studies, like [123], the aim of the analysis is similar, but, as opposed to the present study, the objective function is defined to include multiple electrophysiological properties, for some of which a physiological range may be available while for others it may not, rather than considering the electrophsyiological properties as elements to define the constraints imposed in the optimization. In any case, the same response surface approximation-based optimization algorithm employed in the present study could be applied to the problem defined in [123].

3.4.2 Database generation

The size of the database depends on the selected sampling technique. In this chapter a three-level full factorial design was used for sampling, which involved 3^N sample points, with N the number of variables to be adjusted (five in this study). However, the proposed optimization framework is independent of the sampling strategy or the size of the database as long as the database provides enough information to fit the response surface. For instance, increasing the factorial number from 3 to 5 (the database size increased from $3^5 = 243$ to $5^5 = 3125$ sample points) only reduced the total number of iterations from 4 to 3, without changing the identified optimum. However, the computational cost increased tenfold.

The advantage of using factorial designs is that they provide unbiased information for parameter identification with polynomial RSAs since they provide optimal space filling [117]. However, other sampling strategies are also possible. Monte Carlo simulations represent a very flexible sampling strategy where the optimal number of sampling points can be defined in terms of the type of RSA to be used.

In this regard, Monte Carlo simulations were used in [124] to perform sensitivity analysis in electrophysiological models by means of linear multivariate regression. In addition to generating the required data for model fitting, Monte Carlo simulations were also used to perform population-based simulation studies, as in Wamsley *et al.* [125].

In this chapter, the full factorial technique was implemented in order to guarantee that the algorithm was not limited by the sampling technique since the generated database is sufficient to build a second order response surface. However, as mentioned above, other techniques could be tested to reduce the computational cost when a larger number of current conductances are involved or when large parallel computing capacity is not available.

3.4.3 Computational cost

The major benefit of the methodology proposed in this chapter in terms of computational cost is the high degree of parallelization. It should be noted that the global computation time depends mainly on two factors: the employed cell model and the stimulation protocols that are performed. As compared to the CRLP or GPB models, which take long computation times, the computational time for a model like TP06 could be reduced to just a few hours. For the computations of this study a high performance computing cluster was used. The number of simulations involved per iteration makes it possible to use other types of infrastructures such as GPUs.

Nevertheless, the computation times associated with the presented methodology based on response surface approximations are short if compared with those for the same optimization solved by using a genetic algorithm, which could require around 100 generations and would cost more than 350 hours, even if all individuals in the population were simulated in parallel. In [112], 500 generations were needed to fit the model, which would still involve longer computation times.

3.4.4 Definition of the optimization problem

In this chapter, the integral of the total potassium current ($I_{K_{tot}}$) during one cardiac cycle was selected as the objective function for minimization. This selection was made to maintain $[K^+]_i$ homeostasis after incorporation of $[K^+]_i$ dynamics into the CRLP human ventricular model. Optimal current conductances were identified, with additional constraints imposed to guarantee that fundamental electrophysiological properties took values within experimental limits. For some of those properties the physiological range reported in experimental studies of the literature is extremely large. To avoid a solution for the modified CRLP model that, although in physiological range, was very far from the average experimental behavior, the range of allowed APD values was somewhat restricted, as described in 3.2.2.

3.4.5 Model comparison

The adjusted CRLP model developed in this study was compared with previous human ventricular AP models published in the literature, namely the CRLP, GPB, TP06 and ORd models. This comparison was made in terms of AP traces, $[K^+]_i$ concentrations and I_{CaL}, I_{K1}, I_{ncx}, $I_{Cl,bk}$ and I_{to} currents. In practically all cases, the results obtained for the adjusted CRLP model were along the lines of those obtained with the other models. The only current that was found to be smaller for the modified CRLP model as compared to the other models, including the original CRLP model, was I_{Kr}. This reduced current led to shorter APD prolongation following I_{Kr} blockade, but still within experimentally reported limits. Specifically, in [54] an average APD prolongation of 56.3% with a standard deviation of 34.6% was reported. The difference between the mean experimental prolongation and that obtained for the modified CRLP model was within twice the experimental standard deviation.

One of the differences between the GPB / CRLP models and the other human ventricular models is the inclusion of the $I_{Cl,bk}$ current. This current was expected to have a minor role in modulating electrophysiological properties, but, as reported in [121], APD showed the highest sensitivity (-86%) to changes in the maximal ionic conductance of the $I_{Cl,bk}$ current. In the CRLP model, this sensitivity was reduced (-46%) but it was still large. As there is similarity between the sensitivities of the APD and the integral of the total potassium current to variations in ionic conductances (see Figure 3.3), the $I_{Cl,bk}$ current ended up having a very important indirect role in modulating potassium balance.

As shown in the presented results, major differences between the modified and the original CRLP models include APD shortening and decrease in the membrane potential during the *plateau* phase. Regarding the latter, experimental results [126] show that the plateau voltage takes values around 18 mV, while in the modified CRLP model the plateau voltage is 8 mV. Differences in I_{ncx} and $I_{Cl,bk}$, even if not large, could still underlie those major deviations of the modified CRLP model with respect to the original one. Future studies could include the membrane potential during the *plateau* phase as an electrophysiological marker to be included in the optimization algorithm for model refinement. This could definitely have an impact on balancing the currents involved in this phase of the AP.

Our results demonstrate that with the proposed methodology it was possible to successfully update the CRLP model by incorporating $[K^+]_i$ dynamics while keeping the model's ability to reproduce risk-related markers for investigation of cardiac arrhythmias. As described in Table 3.1, the evaluated risk markers remain within experimental limits or are closer to their physiological values than with the original CRLP model.

3.4.6 Response to potassium concentration changes

While for some investigations the assumption of constant $[K^+]_i$ may be valid, there are many situations where $[K^+]_i$ varies, for instance following changes in the frequency of stimulation or in $[K^+]_o$ values. As shown in 3.2.2, the assumption of

constant $[K^+]_i$ may also hide an imbalance between potassium currents and $[K^+]_i$, as the latter is not allowed to change.

Simulation results obtained when varying the level of $[K^+]_o$ allowed confirming that both the incorporation of $[K^+]_i$ dynamics and the use of the optimization algorithm to readjust the ionic conductances improved the CRLP model for simulation of abnormal conditions (see section 3.3.5). Although there are no experimental measurements of $[K^+]_i$, the model can be assessed by using measurements that indirectly validate its behavior. On the one hand, the model is able to reproduce behaviors similar to those of the experimental results presented in [122]. On the other hand, the inclusion of $[K^+]_i$ dynamics make it possible to evaluate variations in $[K^+]_i$ in response to $[K^+]_o$ changes like those reported in hemodialysis scenarios [116]. In this latter case, simulated $[K^+]_i$ variations were in the expected direction as to compensate for the effects of changing $[K^+]_o$.

When $[K^+]_o$ increases, there is an increase in the Nernst potential for potassium and, thus, a reduction in the driving force of potassium, which diminishes the amount of potassium leaving the cell. Additionally, an increase in $[K^+]_o$ alters the current through the sodium-potassium pump. Both effects contribute to increase $[K^+]_i$, which leads to a reduction in the Nernst potential for potassium, thus returning the cell to an equilibrium state.

3.5 Conclusions

The optimization framework proposed in this chapter allows estimating ionic current conductances of AP models at an affordable computational cost while guaranteeing physiologically plausible values of selected electrophysiological properties. This framework has been applied to introduce $[K^+]_i$ dynamics into the CRLP human ventricular AP model developed in Chapter 1. Solving the formulated optimization problem avoids the imbalance generated in the CRLP model after introducing $[K^+]_i$ dynamics, without deteriorating the performance of the model in terms of representation of electrophysiological behavior and arrhythmic risk-related properties. The updated CRLP model built in this chapter is thus suitable for investigation of cardiac arrhythmias, particularly under conditions involving large changes in $[K^+]_i$.

Chapter 4

Limitations in Electrophysiological Model Development and Validation

4.1 Introduction

Chapter 2 and chapter 3 deal with methodologies for the development and update of electrophysiological models. Importantly, methodologies are also required for validation of new or updated model formulations based on available experimental data. Any methodology proposed for such purpose should consider all variables and spatio-temporal scales involved in the corresponding modeling and simulation. This becomes a challenging task, particularly for complex biophysically detailed models. From the earliest mathematical model of an electrical cell's action potential (AP) developed by Hodgkin and Huxley in the fifties, the complexity of current AP models has grown considerably. The advent of new experimental techniques has made large sets of experimental data readily available, which has motivated the development of more complex models to accurately describe cellular electrical activity. Whereas growing in model complexity is a natural consequence of the increased knowledge [127], the more complex the model, the more difficult the identification of model parameters tends to be. An AP model involves the sum of different transmembrane ionic currents and the balance between intra- and extracellular ionic concentrations. Each ionic current follows a mathematical formulation in which several effects are modeled, e.g., ion channel activation and inactivation gating or current conductance. For each effect, a number of model parameters are

identified based on data from experimental protocols specific for each particular ionic current.

The experimental protocols used to obtain most of the parameters of each ionic current are performed in isolated cells. But, due to the sensitivity of some ionic channels to the cell isolation procedure applied prior to voltage-clamp experiments [106], the conductances of the ionic currents in cardiac models are often not estimated from direct measurements of the current density. Instead, individual channel conductances are adjusted so that measures from model-generated APs closely match experimental AP measurements in tissue such as AP duration (APD) or others. In the Courtemanche-Ramirez-Nattel (CRN) model [47], the ionic conductances G_{Na}, G_{K1}, G_{to}, G_{Kr} and G_{Ks} were fitted to obtain a correct input resistance, AP morphology, AP amplitude (APA) and upstroke velocity (dV/dt_{max}). In a late version of the Luo-Rudy (LR) model [107], G_{Ks} was fitted to get the right APD prolongation when the I_{Ks} current was blocked. Taking those models as an example, in the tenTusscher-Noble-Noble-Panfilov (TNNP04) model [46], G_{Ks} was set to obtain physiologically plausible APD values for each cell type (epicardial, midmyocardial and endocardial). In the Grandi-Pasqualini-Bers (GPB) model [15], G_{Na} was set so as to reproduce experimental measurements of APA and maximum value of the transmembrane potential (V_{max}). In the O'Hara-Rudy dynamic (ORd) model [64], the potassium current conductances were fitted to reproduce the experimental effect on the APD when they were blocked. In the Carro-Rodríguez-Laguna-Pueyo (CRLP) model [120], using the sensitivity analysis proposed in [12], G_{K1}, G_{NaK}, G_{CaL}, and G_{Na} were fitted to obtain not only APD values within physiological ranges, but also other markers of arrhythmic risk, including time constants of APD rate adaptation or rate dependence of ionic concentrations.

On the contrary, the parameters that model current kinetics (gating parameters) are usually identified from single-cell experiments. The calibration process is usually performed using a nonlinear least square fitting of voltage clamp data by assuming that each parameter's effect is independent from the rest (e.g., the steady-state of an inactivation gate is calibrated against experimental results while considering that the time constant of the gate does not affect such results, which might not be correct). However, when the complexity of the model increases, the interaction between effects becomes increasingly important. Therefore, assuming independence of the effects when identifying model parameters may be misleading. While other techniques have been proposed in recent years to improve the fitting of the gating parameters [109, 128–130], none of the models analyzed in the present thesis have used such techniques.

Once model parameters have been identified, the resulting AP models are validated against experimental measurements commonly obtained also from tissue preparations. Characteristics such as resting membrane potential (V_{min}) and upstroke velocity (dV/dt_{max}) are usually compared between model-generated and experimental APs. In the CRN model, the role of different ionic conductances, the morphology of the AP and the behavior of the model for different pacing cycle lengths (CLs) were compared with experimental observations. In the updated version of the LR model [107], the theoretical APD restitution curve was compared

with experimental restitution curves obtained from optical recordings of cardiac APs. In the TNNP04 model, simulated APD restitution curves (at 90% repolarization, APD_{90}) were evaluated in single cells to validate the model against experimental results measured in tissue preparations. Also in this model, propagation in a homogeneous one-dimensional (1D) tissue was simulated to validate the model in terms of Conduction Velocity (CV). In a subsequent version of the model, the ten Tusscher-Panfilov (TP06) model [51], simulated APD restitution curves (at 90% and 50% repolarization) in single cells were compared with experimental results. The GPB model was validated by comparing the predicted APD_{90} prolongation caused by blockade of different potassium currents with experimental results. The CRLP model, as the GPB model, was validated by comparing APD_{90} prolongation caused by potassium current blockades with experimental results, but also by comparing a number of computed markers not used in the fitting process.

For the aforementioned reasons, issues may appear in the calibration and/or validation of electrophysiological models caused by two related aspects: submodel variable relationships and cell-to-cell interactions during AP propagation. Regarding the first of such aspects, model parameters related to ion channel gating kinetics are commonly obtained by considering each gate of the channel independently. Regarding the second one, ionic conductances are adjusted or validated against experimental data obtained from tissue preparations while considering single cell computer simulations. In both circumstances, differences caused by not considering the corresponding interactions introduce non-negligible cross-effects between model parameters that are not considered in the fitting process.

Other studies have analyzed issues related to the two aspects mentioned above. In [131] differences between models of the same species to represent electrophysiological properties and how these differences propagate to tissue simulations were analyzed. In [132] how the uncertainty in the definition of gating variables propagates in multi-scale models was studied and the need to use observations across multiple scales was highlighted. In [133] problems caused by the use of observations across multiple scales and how to characterize the relationships between model parameters and the effect they have in the multi-scale model outputs was explored.

In this chapter, experimental protocols are simulated *in silico* to analyze the consequences of the corresponding interactions in two scenarios involving scales ranging from ion channels to tissue: 1) characterization of L-type calcium voltage-dependent inactivation; 2) identification of ionic current conductances with the largest contribution to steady-state AP markers. In the first case, differences between the mathematical model, simulation results and experimental measurements are analyzed to evaluate how interactions between model components affect the development and validation of mathematical ion channel models. In the second case, differences between AP-based markers simulated in isolated cells and in homogeneous 1D tissue are analyzed to evaluate how propagation affects their values as well as to assess the contribution of each ionic current to each marker.

4.2 Materials and Methods

4.2.1 L-type calcium channel gating

In AP models, ionic currents are controlled by activation and inactivation gates. Gates are modeled by functions varying between 0 and 1. Below a threshold potential, the activation gates are closed (the function value is 0) and the inactivation gates are open (value 1). When transmembrane potential increases, the activation gates open (their values increase towards 1) and the inactivation gates close (their values decrease towards 0). In particular for the I_{CaL} current, all human ventricular cell models analyzed in this thesis have one voltage-dependent activation gate d. This activation gate d multiplies the expression for the inactivation gating, whose formulation largely differs between models. In this chapter four of the most recently developed human ventricular cell models were considered: the GPB model, the TP06 model, the ORd model and the CRLP model. Voltage-dependent inactivation of the L-type calcium current was studied in all of them.

The TP06 model is one of the most extensively used human ventricular AP models. It represents an improved version of the model published in 2004 [46] in which the calcium dynamics, the slow delayed rectifier potassium current (I_{Ks}) and I_{CaL} were reformulated. The TP06 model is based on experimental data from human cardiomyocytes for most ionic currents and is defined for three types of cells: epicardial, midmyocardial and endocardial. In the TP06 model, voltage-dependent I_{CaL} inactivation is modeled as the product of a fast, f_2, and a slow, f, voltage-dependent inactivation gates as well as a calcium-dependent inactivation gate, f_{Ca}:

$$Inact_{Ca,L}^{TP06} = f \cdot f_2 \cdot f_{Ca}$$

These gates have different time constants (τ_{f_2}, τ_f and $\tau_{f_{Ca}}$) and steady-state values ($f_{2,\infty}$, f_∞ and $f_{Ca,\infty}$). This formulation is based on experiments that indicate the presence of both fast and slow voltage-dependent I_{CaL} recovery processes [1, 134, 135].

The GPB model is based on the rabbit AP model proposed in [63], which includes subsarcolemmal and junctional compartments in the formulation of the currents and provides a detailed description of calcium handling. The GPB model includes new definitions of ionic current densities and kinetics and is defined for endocardial and epicardial cells. In the GPB model, voltage-dependent I_{CaL} inactivation is modeled by a single voltage-dependent gate f and two calcium-dependent gates, one for the subsarcolemmal compartment, $f_{Ca,sl}$, and another one for the junctional compartment, $f_{Ca,j}$. The formulation of I_{CaL} inactivation in the GPB model is as follows:

$$Inact_{Ca,L}^{GPB} = f \cdot (A_j \cdot f_{Ca,j} + A_{sl} \cdot f_{Ca,sl})$$

where A_j and A_{sl} are the ratios of calcium-dependent inactivation channels in the junctional and the subsarcolemmal compartment, respectively ($A_j + A_{sl} = 1$).

The CRLP model is a modification of the GPB model. As in the original model, the modified CRLP model describes the AP of endocardial and epicardial human

ventricular myocytes. As described in previous chapters, the CRLP model includes reformulation of I_{CaL}, readjustment of the parameters describing I_{K1} and redefinition of a number of other model parameters, including G_{Na} (maximum I_{Na} conductance) and G_{NaK} (maximal I_{NaK} value). In the CRLP model, the formulation of voltage-dependent I_{CaL} inactivation is similar to that of the TP06 model. However, the associated voltage-dependent inactivation time constants were adjusted to better match experimental evidences on APD adaptation to CL changes. The calcium-dependent inactivation gates were maintained as in the original GPB model. The formulation of I_{CaL} inactivation in the CRLP model is as follows:

$$Inact_{Ca,L}^{CRLP} = f \cdot f_2 \cdot (A_j \cdot f_{Ca,j} + A_{sl} \cdot f_{Ca,sl})$$

The ORd model is the most recent human ventricular AP model out of the four analyzed models and it has the most complex I_{CaL} definition. I_{CaL} inactivation is modeled as a weighted average involving voltage-dependent gates. The gates f_f and f_s represent the behavior of the voltage-dependent gates when there is no calcium. The gates $f_{Ca,f}$, $f_{Ca,s}$ and j_{Ca} represent the behavior of the voltage-dependent gates when calcium is present. The calcium-dependent gate n modulates the relative weight of both families of gates. The n gate is modeled via a Markov chain. The gates f_f, f_s, $f_{Ca,f}$, $f_{Ca,s}$ and j_{Ca} have different time constants, $\tau_{f,f}$, $\tau_{f,s}$, $\tau_{f,Ca,f}$, $\tau_{f,Ca,s}$ and τ_j, but the same steady-state value f_{ss}. As discussed by Thomas O'Hara in the online version of the article presenting the model [64], there are some issues related to the I_{Na} current formulation in the model. The authors propose to replace the I_{Na} current formulation of the original ORd model with the formulation proposed in the TP06 model. In this work we analyze the original ORd model and the ORd model with the I_{Na} current of the TP06 model (ORd_{Na}). The formulation of I_{CaL} inactivation in the ORd and ORd_{Na} models is as follows:

$$\begin{aligned} Inact_{Ca,L}^{ORd} = {} & (A_{f,f} \cdot f_f + A_{f,s} \cdot f_s) \cdot (1 - n) + \\ & j_{Ca} \cdot (A_{f,Ca,f} \cdot f_{Ca,f} + A_{f,Ca,s} \cdot f_{Ca,s}) \cdot n \end{aligned}$$

where $A_{f,f}$ and $A_{f,Ca,f}$ are the ratios of the fast voltage-dependent inactivation gates f_f and $f_{Ca,f}$, respectively, and $A_{f,s}$ and $A_{f,Ca,s}$ are the ratios of the slow voltage-dependent inactivation gates f_s and $f_{Ca,s}$, respectively.

4.2.2 Characterization of L-type calcium voltage-dependent inactivation

Voltage-dependent I_{CaL} inactivation is experimentally characterized using the paired-pulse protocol, which is illustrated in Figure 4.1. This protocol consists of clamping the membrane potential from a holding potential V_{hold} to different pre-pulse potentials V_{pre} during a specified time interval t_{pre}. After this time, the potential is clamped to a pulse potential V_{pulse} during an interval t_{pulse}. Following this, the membrane potential is clamped back to V_{hold}. Variations of this protocol introduce a separation between the pre-pulse and the pulse potential, during which the potential is set to V_{hold} for a short period of time, t_{sep}, before clamping the membrane

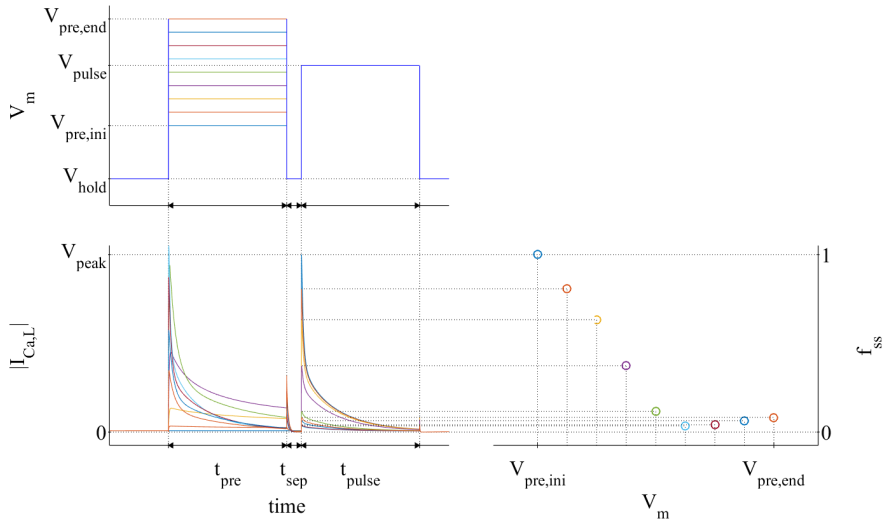

Figure 4.1: Paired-pulse voltage clamp protocol and measurement of the steady-state value f_{ss} of voltage-dependent inactivation.

potential to V_{pulse}. Steady-state voltage-dependent I_{CaL} inactivation is obtained during the t_{pulse} interval. In this part of the test, peak I_{CaL} current is measured for each potential used as pre-pulse and results are normalized by the peak value of the current measured for the minimum pre-pulse potential. The resulting curve is used in the models as the steady-state value of voltage-dependent inactivation (f_{ss}).

Human ventricular cell models use different experimental datasets to define their voltage-dependent I_{CaL} inactivation functions. With the aim of comparing the simulation results of steady-state I_{CaL} inactivation with experimental results, the same experimental dataset that was used to adjust each model in the original articles was considered. For the TP06 model no indication was provided on the experimental dataset used to fit steady-state voltage-dependent I_{CaL} inactivation, whereas in the previous version of the model [46] data from [1] was used. For the TP06 model the authors redefined the I_{CaL} expression by adding a second voltage-dependent inactivation gate. Only the I/V curve for I_{CaL} was compared with experimental results from [3]. The GPB model used experimental results from [2] and the ORd model from [3].

Each set of experimental results was based on a different configuration of the paired-pulse protocol to characterize steady-state voltage-dependent I_{CaL} inactivation (Table 4.1). Also, different calcium concentrations in the extracellular solution and in the patch pipette solution, varying from 1.8 to 5.4 mM and from 0 to 2.0 mM, respectively, were used for each experimental dataset.

	[1]	[2]	[3]
V_{hold} (mV)	-45	-80	-80
V_{pulse} (mV)	10	10	5
$V_{pre,ini}$ (mV)	-40	-100	-55
$V_{pre,fin}$ (mV)	40	60	15
ΔV_{pre} (mV)	5	10	5
t_{pre} (ms)	400	400	500
t_{sep} (ms)	10	5	0
t_{pulse} (ms)	400	300	390

Table 4.1: Paired-pulse test parameters in experimental protocols.

In this chapter, *in silico* simulations were performed in which the experimental paired-pulse tests were implemented for I_{CaL} characterization. Intracellular and extracellular concentrations were set at the values used in the experimental protocols against which simulated data were compared. In particular, free intracellular calcium ($[Ca^{2+}]_i$) was set as the value of the pipette solutions of the experiments, with the time derivative being set to zero (i.e. $d[Ca^{2+}]_i/dt = 0$). All the calcium buffers and the diffusion and transportation of calcium inside the cell were maintained as in the original models. This allowed calcium concentrations in all remaining intracellular compartments to follow the dynamics described in the corresponding model equations. The same values for V_{hold}, V_{pre}, and V_{pulse} as in the corresponding experiments (see Table 4.1) were used. All currents except for I_{CaL} were blocked.

4.2.3 Steady-state AP markers

To study the effect of considering data measured at tissue level for characterization of single cell models, AP markers calculated at single cell and tissue levels with the four ventricular models were compared. The following markers were analyzed: i) Action potential duration at different percentages of repolarization (90%, 75%, 50%, 25%); ii) Triangulation; and iii) Minimum and Maximum Transmembrane Potential and Transmembrane Potential Velocity. The maximum value of the AP is used in many models to adjust the cardiac conductances [15, 47] whereas the minimum potential is used for model validation [64]. These values are, however, very sensitive to cellular electrophysiological changes like, for instance, those associated with hyperkalemia, where the resting membrane potential can be increased from -85 mV to up to -60 mV and the maximum potential falls, in combination with a potential splitting of the AP upstroke into more than one component [20].

4.2.4 Ionic contributors to AP markers

To evaluate the role played by each ionic current in contributing to each electrophysiological marker, the results of the simulations carried out by varying individual

ionic conductances were adjusted by a first order response surface model:

$$M_j \approx C_j + \sum_{i=1}^{N} \Delta_i \cdot m_{j,i}$$

where M_j is the value of the electrophysiological marker j under the analyzed condition, C_j is the value of the marker j under control conditions, $m_{i,j}$ is the weight of the current i in contributing to the marker j and Δ_i is the variation of the ionic conductance:

$$\Delta_i = \frac{G_i - G_{i,0}}{G_{i,0}}$$

where $G_{i,0}$ and G_i are the values of the ionic conductance under control and under the analyzed condition, respectively.

For each individual marker, if the results for the different evaluated conditions $k = 1, \ldots, K$ are concatenated, the above system can be expressed in matrix form as:

$$\begin{bmatrix} M_{j,1} \\ M_{j,2} \\ \vdots \\ M_{j,K} \end{bmatrix} \approx \begin{bmatrix} \Delta_{1,1} & \cdots & \Delta_{N,1} \\ \Delta_{1,2} & \cdots & \Delta_{N,2} \\ \vdots & \ddots & \vdots \\ \Delta_{1,K} & \cdots & \Delta_{N,K} \end{bmatrix} \cdot \begin{bmatrix} m_{j,1} \\ m_{j,2} \\ \vdots \\ m_{j,K} \end{bmatrix} + C_j \cdot \begin{bmatrix} 1 \\ 1 \\ \vdots \\ 1 \end{bmatrix}$$

$$\downarrow$$

$$\overline{M}_j \approx \overline{\overline{\Delta}} \cdot \overline{m}_j + C_j \cdot \overline{J}_{K,1}$$

where $M_{j,k}$ is the value of the marker j and $\Delta_{i,k}$ is the variation of the ionic conductance i at condition k. Using this notation, the weights of the ionic conductances can be calculated as follows:

$$\overline{m}_j = \left(\overline{\overline{\Delta}}^T \cdot \overline{\overline{\Delta}} \right)^{-1} \cdot \overline{\overline{\Delta}}^T \cdot \left(\overline{M}_j - C_j \cdot \overline{J}_{K,1} \right)$$

4.2.5 Computational simulations

The models were stimulated with square current pulses with an amplitude twice the diastolic threshold and a duration of 1 ms. Depending on the simulation scale, the diastolic threshold was defined as the minimum amplitude required to (a) generate five APs (single cell simulations) or (b) propagate five APs (1D tissue simulations).

To simulate steady-state conditions, models were stabilized with a train of 100 stimulations at a CL of 1000 ms. Electrophysiological markers were calculated from the last simulated beat. Every model was first simulated under control conditions and subsequentyly after varying each ionic conductance by ±15 and ±30%.

For 1D tissue simulations, a homogeneous 3-cm fiber composed of epicardial cells was used. The value of the conductivity, σ, was set to obtain a Conduction Velocity (CV) close to 65 cm/s [88]. The cell capacitance was set to $C_m = 1\ \mu\text{F/cm}^2$. The

AP markers were computed as the mean value of the markers measured at five different positions within the fiber located at: 1, 1.25, 1.5, 1.75 and 2 cm.

For single cell simulations, a forward Euler scheme was used to solve the models with a time step of $\Delta t = 0.002$ ms for GPB, ORd and CRLP, and $\Delta t = 0.02$ ms for TP06. For 1D tissue simulations, a semi-implicit operator-splitting scheme was used to solve the propagation [87] with a space discretization of $\Delta x = 0.1$ mm and the same Δt used in single cell simulations.

The results from single cell and in 1D tissue simulations were compared using the absolute (E_a) and relative (E_r) differences:

$$E_a = M_j^{cell} - M_j^{tissue}$$

$$E_r(\%) = \frac{M_j^{cell} - M_j^{tissue}}{M_j^{tissue}} \cdot 100$$

where M_j^{cell} and M_j^{tissue} are the values of the electrophysiological marker j in cell and tissue for the condition under analysis.

4.3 Results

4.3.1 Characterization of L-type calcium voltage-dependent inactivation

Results of the paired-pulse protocol for steady-state voltage-dependent I_{CaL} inactivation are shown in Figure 4.2. Each model was compared with the set of experimental data that was used to characterize voltage-dependent I_{CaL} inactivation in the original article were the model was presented.

The TP06 model was able to adequately reproduce the experiments from [1] (see Figure 4.2.a)). In this case, the modeled steady-state voltage-dependent I_{CaL} inactivation is the product of the steady-states values ($f_{2,ss}$, f_{ss}) of the two inactivation gates (f_2, f). The results from the *in silico* simulations, which account for additional interactive effects, were closer to the experimental data than those obtained by evaluation of the corresponding I_{CaL} mathematical equations. Figure 4.3.a) shows that, for the TP06 model, the slow inactivation gate f did not reach steady-state for high V_{pre} potential values (V_{pre} = -5 mV and V_{pre} = 40 mV). Figure 4.3.a) also shows that the calcium-dependent inactivation gate has a less significant effect than the other gates, being this effect slightly more pronounced at lower V_{pre} potentials. Finally, one of the most significant differences between the model outcome (multiplication of the steady-state values of the gates, black dashed line in Figure 4.2.a) and the result of the *in silico* simulations (yellow crosses) was that the curves were shifted.

Simulation results obtained with the GPB model fit quite well the model definition (see Figure 4.2.b)). Differences between model outcome and *in silico* simulation increased as f_{ss} decreased. As shown in Figure 4.3.b), the separation pulse produced different effects depending on the pre-pulse potential. For V_{pre} = -100 mV, the effect was minimal, but in the other two cases shown in the figure (V_{pre} = -20 mV and V_{pre} = 60 mV), the value of f increased during the separation pulse.

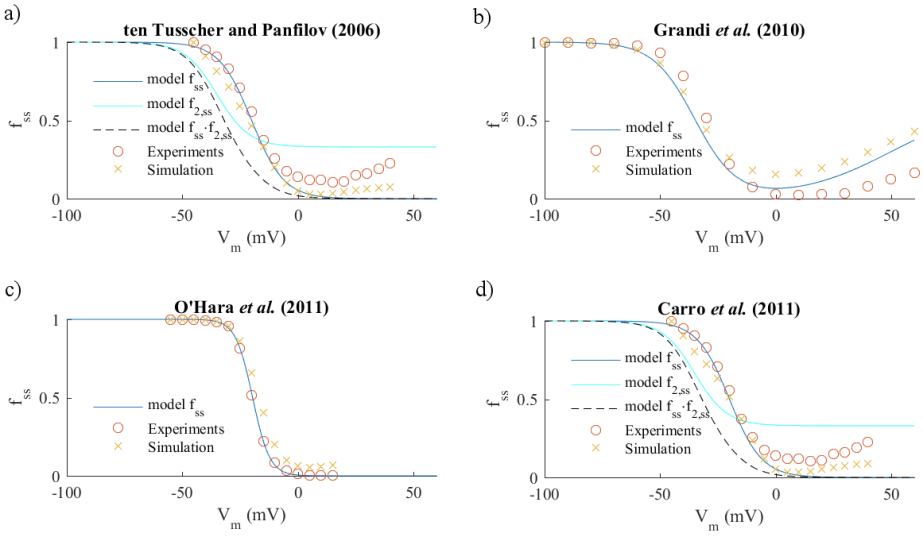

Figure 4.2: Comparison between model definition (continuous and discontinuous lines), *in silico* simulations (yellow crosses) and experimental results (red circles) for f_{ss}. a) TP06 model and data from [1]. b) GPB model and data from [2]. c) ORd model and data from [3]. d) CRLP model and data from [1].

Calcium-dependent inactivation gates had minimal effects, as these gates remained open during most of the protocol duration. Finally, differences between experiments [2] and *in silico* simulations increased for positive potentials (Figure 4.2.b).

Simulation results with the ORd model showed a significant discrepancy with experimental data for potentials between -20 mV and -10 mV (see Figure 4.2.c)). The largest difference was observed for a pre-pulse potential of -15 mV. The simulated probability at this potential was 18% larger than the one obtained in the experiments. The evolution of the voltage-dependent I_{CaL} gate variables during the pre-pulse potential is shown in Figure 4.3.c). For potentials below -15 mV, the n gate was nearly closed and the effects of f_s and f_f gates dominated. On the contrary, for positive potentials, the effects of the gates $f_{Ca,f}$, $f_{Ca,s}$ and j_{Ca} prevailed. This figure also shows that for potentials above -15 mV, the fast inactivation gates, but not the slow ones, reached a steady-state value during the pre-pulse. For high pre-pulse potentials, the gate f_{Ca} was not able to reach steady-state (close to 0), but the gate j was. However, the multiplication of both gates almost achieved a steady-state value.

The results obtained with the CRLP model were very similar to those found for the TP06 model. This was expected, since both models have a very similar formulation for I_{CaL} inactivation. However, the difference between the results of the CRLP model and the experiments from [1] was smaller than for the TP06 model (see Figure 4.2.d)).

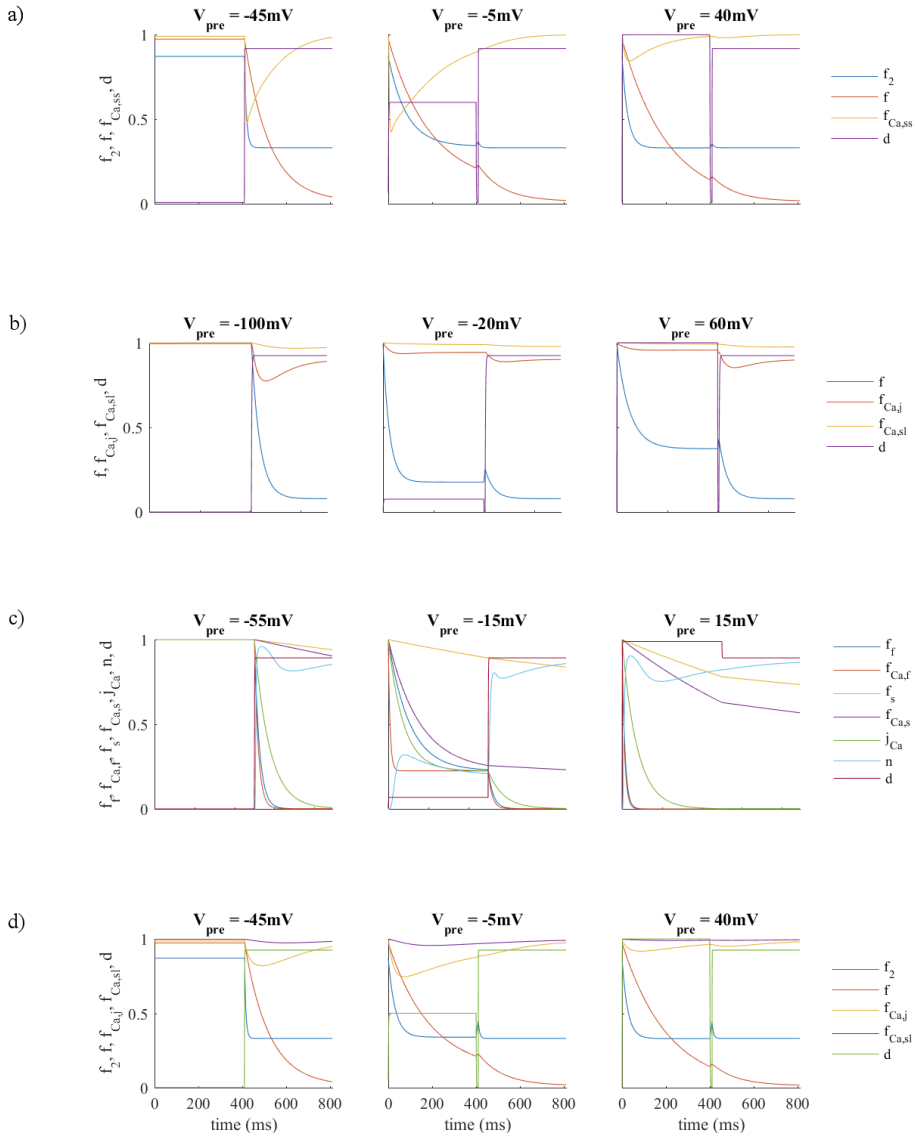

Figure 4.3: Temporal evolution of the I_{CaL} gates during simulation of the paired-pulse protocol (see text for specific values of t_{pre}, t_{sep} and t_{pulse} used in the simulations): a) TP06 model. b) GPB model. c) ORd model. d) CRLP model

	TP06		GPB		CRLP		ORd		ORd_{Na}	
	Cell	Fiber	Cell	Fiber	Cell	Fiber	Cell	Fiber	Cell	Fiber
APD_{90} (ms)	300.5	300.2	286.1	283.5	306.2	306.7	224.3	224.2	223.2	224.0
APD_{75} (ms)	292.1	292.4	272.6	271.8	281.1	284.5	208.1	208.6	206.2	208.5
APD_{50} (ms)	272.4	277.0	235.0	243.8	228.1	239.6	177.8	179.1	174.4	179.2
APD_{25} (ms)	212.3	242.1	127.3	180.4	111.8	179.1	137.0	144.1	126.5	144.3
$Trian.$ (ms)	28.1	23.2	51.1	39.7	78.1	67.1	46.5	45.1	48.8	44.8
V_{max} (mV)	38.5	24.6	38.7	23.4	38.1	21.9	36.2	31.1	41.9	30.9
V_{min} (mV)	-85.4	-85.4	-81.4	-81.4	-84.1	-84.2	-87.8	-87.8	-87.8	-87.9
$\frac{dV}{dt}_{max}$ (V/s)	292.6	193.7	322.8	234.5	335.4	227.5	234.9	78.1	364.2	237.9
$\frac{dV}{dt}_{min}$ (V/s)	-9.5	-3.3	-6.2	-1.4	-5.9	-0.8	-1.8	-1.1	-2.9	-1.2

Table 4.2: Comparison of electrophysiological markers simulated in single cell and 1D tissue under control conditions.

4.3.2 Ionic contributors to AP markers

The results of the analyzed AP markers under control conditions are shown in Table 4.2 for the four analyzed models. Table 4.3 shows absolute and relative differences between cell and tissue values for each electrophysiological marker. APD was very similar in cell and tissue simulations at 90% and 75% repolarization. The differences between cell and tissue increased at lower percentages of repolarization: the relative differences for APD at 50% repolarization were between -0.7% and -3.6% and considerably higher at 25% repolarization, between 4.9% and 37.4%. The differences in Triangulation were mainly due to differences in APD_{50}. Due to the smaller values of Triangulation, the relative differences for this AP marker were higher (between 3.0% and 28.8%). The GPB model and the CRLP model were the ones that showed larger differences between cell and tissue results. On the contrary, the ORd model was the one showing less differences between cell and tissue in the AP-based electrophysiological markers.

The value of the resting potential (V_{min}) was the same in cell and tissue. On the contrary, peak AP value (V_{max}) showed large differences between cell and tissue simulations (from 16.3% to 73.5%). Similarly, large differences were quantified for dV/dt_{max} and dV/dt_{min}. The ORd model showed the smallest differences in those voltage-related electrophysiological markers except for dV/dt_{max}. The other three models showed similar values, in particular for the absolute differences.

For the TP06 model, the I_{CaL} current played different roles in cell and tissue simulations (see Figure 4.4). While in tissue it was the most important current to determine V_{max}, in cell its effect on V_{max} was negligible. A similar effect was observed for the $Triangulation$, where I_{CaL} was a highly relevant current in tissue simulations, whereas in cell simulations it had almost no effect on $Triangulation$. On the contrary, the impact of I_{Na} current in cell was notably diminished in tissue simulations. For V_{max}, the weight of the I_{Na} current in cell was 51.6%, while in tissue it was nearly 5%. This also happened with the I_{to} current, although to a lesser extent. G_{to} conductance affected dV/dt_{min} in cell simulations, whereas in

	E_a					$E_r(\%)$				
	TP06	GPB	CRLP	ORd	ORd_{Na}	TP06	GPB	CRLP	ORd	ORd_{Na}
APD_{90} (ms)	0.3	2.6	-0.5	0.1	-0.8	0.1	0.9	-0.2	0.0	-0.3
APD_{75} (ms)	-0.3	0.8	-3.4	-0.5	-2.3	-0.1	0.3	-1.2	-0.2	-1.1
APD_{50} (ms)	-4.6	-8.8	-11.5	-1.3	-4.8	-1.7	-3.6	-4.8	-0.7	-2.7
APD_{25} (ms)	-29.8	-53.9	-67.3	-7.1	-17.8	-12.3	-29.4	-37.6	-4.9	-12.3
$Trian.$ (ms)	4.9	11.4	11.0	1.4	4.0	20.7	28.8	16.4	3.0	9.0
V_{max} (mV)	13.9	15.3	16.2	5.1	11.0	56.4	65.7	73.5	16.6	35.5
V_{min} (mV)	0.0	0.0	0.1	0.0	0.1	0.0	0.0	0.0	0.0	0.0
$\frac{dV}{dt}_{max}$ (V/s)	98.9	88.3	107.9	156.8	126.3	51.1	37.7	47.5	200.7	53.1
$\frac{dV}{dt}_{min}$ (V/s)	-6.2	-4.8	-5.1	-0.7	-1.7	187.8	343.2	616.3	52.5	143.1

Table 4.3: Absolute (Ea) and relative (Er) differences between electrophysiological markers in single cell and 1D tissue simulations.

tissue simulations this marker was mainly controlled by I_{CaL}.

The more influential currents in the GPB model differed from the TP06 model (Figure 4.5). In this model, the $I_{Cl,bk}$ current, which is not present in the TP06 model, was the most relevant contributor to APD in both cell and tissue simulations. Other effects were similar in both models. As an example, the I_{Na} current contribution was reduced in the GPB model when the electrophysiological markers were calculated in tissue as compared to cell. This reduction was found for all markers except for dV/dt_{max}. Similarly to the TP06 model, one current had a larger contribution to V_{max} in tissue than in cell, but in the GPB model that current was I_{to}. The same behavior was found for $Triangulation$ and I_{K1}.

The APD of the ORd model was mainly controlled by I_{Kr} in cell, whereas in tissue the I_{Na} current also played an important role. The original ORd model showed large differences in the role played by the I_{Na} current in tissue compared with the one in cell (Figure 4.6). In cell simulations, when I_{Na} conductance was increased, the APD at different percentages of repolarization was slightly decreased. On the contrary, in tissue, when I_{Na} conductance was increased, the APD was considerably prolonged. These differences in the ORd model disappeared when the I_{Na} current formulation was replaced with the one described in the TP06 model. For V_{max}, when I_{Na} was replaced with the one defined in the TP06 model (Figure 4.7), the different behavior between cell and tissue simulations was interchanged.

The APD of the CRLP model highly depended on the conductance of the $I_{Cl,bk}$ current (see Figure 4.8). This behavior is inherited from the GPB model but its weight in the CRLP model was found to be slightly smaller than in the GPB model. Likewise, the role of the I_{CaL} current was very similar to the one in the GPB model. The only difference was the role in dV/dt_{min}: in the CRLP model it was larger than in the GPB model due to the particular AP shape at the beginning of the plateau phase for the CRLP model, which is related to the definition of I_{CaL} formulation. Also, the contribution of I_{K1} to Triangulation was 16% larger in tissue than in cell simulations.

TP06 Model

	APD_{90}		APD_{75}		APD_{50}		APD_{25}		*Triangulation*		V_{max}		V_{min}		$\frac{dV}{dt}_{max}$		$\frac{dV}{dt}_{min}$	
	Cell	Fiber	Cell	Fiber	Cell	Fiber	Cell	Fiber	Cell	Fiber	Cell	Fiber	Cell	Fiber	Cell	Fiber	Cell	Fiber
G_{Ks}	-24.7	-24.3	-25.4	-24.9	-26.1	-25.6	-26.9	-25.4	-10.4	-8.5								-12.8
G_{to}												-5.6					98.5	37.5
G_{NaCa}	-2.9	-3.1	-3.1	-3.3	-3.4	-3.6						-5.7	-0.6	-0.6				-43.0
G_{NaK}	-2.8						-10.8			-15.8	23.8		2.0	2.0	10.1	25.9	57.3	-17.7
G_{pK}							-4.4					-23.3						
G_{pCa}													0.2	0.2				
G_{bCa}										8.6	-5.7		-1.0	-1.0			-13.5	13.6
G_{bNa}													-0.3	-0.3				
G_{CaL}	26.1	26.4	26.3	26.4	28.5	26.6	41.6	25.1		25.0	-8.9	40.4	-0.9	-0.9			-67.9	94.8
G_{Na}					-3.6		-27.6		27.0		51.6	6.5			87.2	77.1	126.9	34.2
G_{K1}	-5.6	-6.0	-3.6	-4.1					-45.1	-55.8			1.0	1.0	-17.1			
G_{Kr}	-13.1	-13.3	-12.6	-12.8	-10.9	-11.4	-8.6	-8.6	-34.4	-36.3								

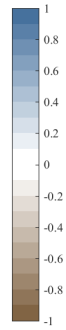

Figure 4.4: Contribution of ionic conductances to electrophysiological markers simulated in tissue and cell with the TP06 model. Dark colors (blue or brown) indicate maximum correlation between changes in a conductance and changes in a marker; white color indicates no correlation. Percentages in boxes indicate the contribution of changes in a conductance to changes in a marker. Minus signs indicate that conductances and markers vary inversely; plus signs indicate that conductances and markers vary in the same direction.

GPB Model

	APD_{90}		APD_{75}		APD_{50}		APD_{25}		*Triangulation*		V_{max}		V_{min}		$\frac{dV}{dt}_{max}$		$\frac{dV}{dt}_{min}$	
	Cell	Fiber	Cell	Fiber	Cell	Fiber	Cell	Fiber	Cell	Fiber	Cell	Fiber	Cell	Fiber	Cell	Fiber	Cell	Fiber
$G_{Ca,bk}$												-5.6	-0.8	-0.7	-8.5			
$G_{Cl,bk}$	-88.6	-85.5	-93.3	-89.6	-104.9	-99.2	-80.9	-103.1	-13.7				-0.9	-0.9	-9.3			
$G_{Na,bk}$													-0.5	-0.5				
G_{ClCa}																		
G_{Na}					-10.6		-68.2		32.5		54.0	16.8			50.1	74.5	114.3	42.2
G_{Kp}																		
G_{pCa}																		
G_{to}	-9.9	-9.3	-10.5	-9.6	-11.1		-10.3			-12.7		-32.0					85.0	
G_{ncx}	15.2	14.4	15.9	14.8	18.8	16.2	37.7	20.0				8.3						
G_{NaK}											7.4	6.5	0.3	0.3			15.6	
G_{K1}	-14.2	-14.8	-9.8	-10.7			-11.4		-62.2	-82.5	9.3		2.0	2.0	28.3	13.4	19.6	102.8
G_{Ks}																		
G_{Kr}	-14.2	-13.2	-14.4	-13.4	-13.4	-13.0			-17.7	-14.5								
G_{CaL}	64.7	62.6	68.1	65.3	78.9	72.4	59.1	71.6				16.0					-24.5	

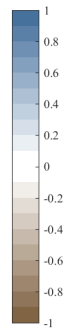

Figure 4.5: Contribution of ionic conductances to AP markers simulated in cell and tissue with the GPB model. The legend of the figure is the same as in see Figure 4.4.

ORd Model

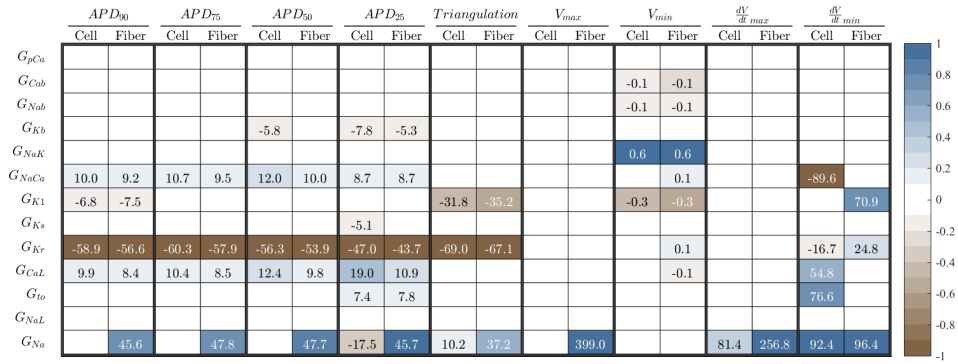

Figure 4.6: Contribution of ionic conductances to AP markers simulated in cell and tissue with the ORd model. The legend of the figure is the same as in see Figure 4.4.

ORd Model with I_{Na} from TP06

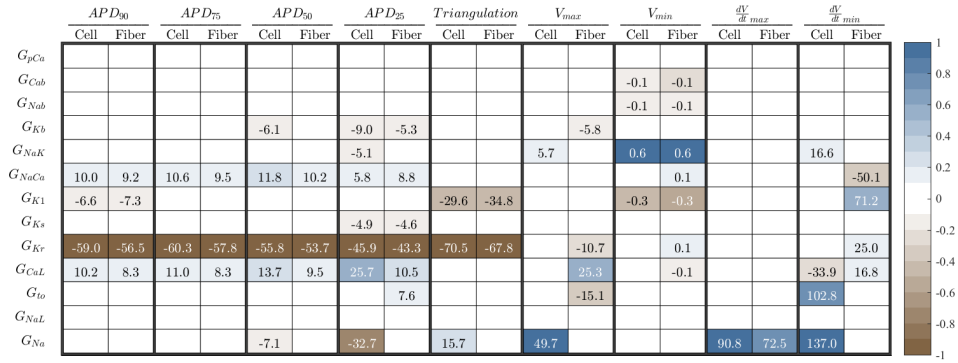

Figure 4.7: Contribution of ionic conductances to AP markers simulated in cell and tissue with the ORd_{Na} model. The legend of the figure is the same as in see Figure 4.4.

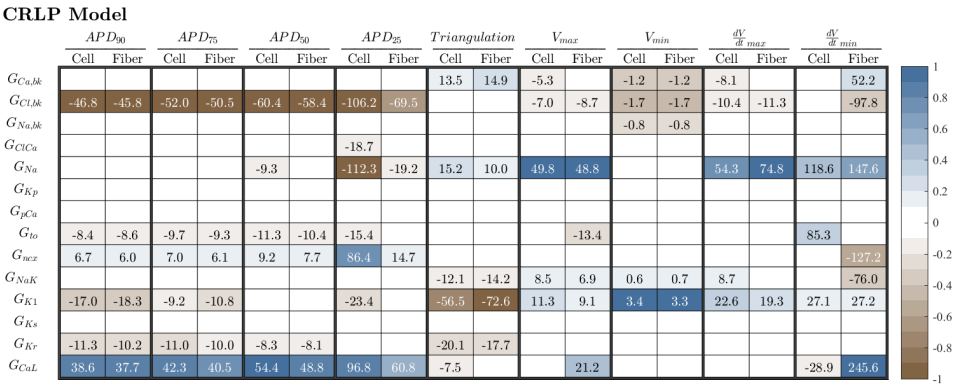

Figure 4.8: Contribution of ionic conductances to AP markers simulated in cell and tissue with the CRLP model. The legend of the figure is the same as in see Figure 4.4.

4.4 Discussion

This chapter has been focused on analyzing issues arising during model development and validation, namely: i) the effect of submodel variable interactions in the characterization of ion channel gating, and ii) the effect of cell-to-cell interactions in the evaluation of ionic contributors to AP markers. A methodology for validating computational model formulations has been introduced. The proposed methodology consists in performing *in silico* simulations using the same protocol as in the experiments used to characterize a given current or AP marker. The methodology accounts for all variables and scales involved in modeling and simulation as well as their interactions. It has been applied to evaluate voltage-dependent I_{CaL} inactivation and contributors to electrophysiological AP markers in four human ventricular models presenting different ionic formulations.

4.4.1 Effect of submodel variable interactions in the evaluation of voltage-dependent L-Type Calcium Current inactivation

In the case of voltage-dependent I_{CaL} inactivation, our results show large differences between I_{CaL} inactivation as calculated from the model equation and I_{CaL} inactivation from the *in silico* simulations. Such differences were due to the interaction between voltage-dependent I_{CaL} inactivation gating and other effects such as I_{CaL} activation gating, protocol definition or duration of the voltage pulses used to calculate inactivation properties. This suggests that, when proposing any new model formulation, consistency between such formulation and the corresponding experimental data that is aimed at being reproduced needs to be first verified considering all involved factors.

In the TP06 model, the product of the steady-state values of the two voltage-dependent I_{CaL} inactivation gates was very different from the experimental behav-

ior. However, the results of the *in silico* simulations obtained with this model were in good agreement with the experiments. There are two effects that explain these results: i) normalization by I_{CaL} current peak at the minimum pre-pulse potential, as performed in the experimental protocol [1], is done for a transmembrane potential value where the product of the two voltage-dependent inactivation gates is less than 1; ii) voltage-dependent inactivation gates do not reach a steady-state value at the end of the pre-pulse interval for some potentials. One of the most significant differences between the model outcome (multiplication of the steady-state values of the gates) and the result of the *in silico* simulations is that the curves representing steady-state voltage-dependent inactivation (Figure 4.2.a)) were shifted. This shift made the *in silico* simulations approximate the experimental behavior due to the performed current peak normalization at a potential where inactivation probability is less than one.

The GPB model and the associated *in silico* simulations provided similar results to the experiments used to fit the steady-state value of voltage-dependent inactivation gating. Differences were mainly caused by the protocol used to measured f_{ss}, as explained in the following: the separation pulse had a different effect depending on the pre-pulse potential. For pre-pulse potentials similar to V_{hold} the value of f_{ss} obtained at V_{pulse} is minimally affected since the steady-state values of f for V_{hold} and V_{pre} are very similar. However, for larger values of V_{pre}, and therefore larger differences between V_{hold} and V_{pre}, the steady-state value of f corresponding to V_{pre} is very different to the steady-state value corresponding to V_{hold}, which corresponds to one. This causes that during the separation pulse the value of f increases (see Figure 4.2.b)) and the difference in f_{ss} between the model definition and the simulation increases with V_{pre}. In addition, the interaction with voltage-dependent activation, represented by gate d, always reduced the measured value, but the normalization, using the result of the minimum pre-pulse potential, nearly corrected this behavior. Finally, differences between experiments [2] and *in silico* simulations get larger where differences between the model definition for f_{ss} and experimental data are larger (see Figure 4.2.b) for positive potentials). These results suggest that a simple I_{CaL} inactivation formulation like that in the GPB model, with only one voltage-dependent inactivation gate, suffices to reproduce the experimental behavior of steady-state voltage-dependent I_{CaL} inactivation [2].

In the ORd model, the definition of voltage-dependent I_{CaL} inactivation as a weighted sum of fast and slow inactivation gates is consistent with how experimentalists calculate inactivation time constants [1, 64]. Time constants are calculated by fitting a biexponential function to the inactivation phase of the experimental current traces. However, important discrepancies between *in silico* ORd simulations and the experiments used to develop the model [3] were found for pre-pulse potentials between -20 mV and -10 mV. There are two possible causes behind such discrepancies: i) the time constant of the slow voltage-dependent inactivation gate; ii) the definition of voltage-dependent I_{CaL} inactivation as the sum of two gates. The first cause has to do with the fact that ORd model time constants are identified based on a simple-pulse test protocol of 75 ms duration, whereas the slow time constant of voltage-dependent I_{CaL} inactivation in the ORd model is of the

order of 10 seconds. The slowness of the inactivation gate prevents reaching the steady-state value by the end of the pre-pulse, which overestimates the value of f_{ss} at V_{pulse}. This is reinforced by the fact that voltage-dependent I_{CaL} inactivation is formulated as a sum of two gates. If inactivation is expressed as a product, as in the case of the TP06 model, when one of the gates reaches zero, the product reaches zero. However, for the ORd model the situation is more complex. Due to the interaction between the inactivation gates and the n and j_{Ca} gates in this model, as shown in section 4.3.1, the result for potentials above -10 mV is equivalent to the product of two gates since the j_{Ca} gate is almost zero, and therefore the result from the simulation is similar to the model formulation of f_{ss} and experiments. On the contrary, for potentials between -20 mV and -10 mV, where by the end of the pre-pulse the j_{Ca} gate is far from zero and the slow inactivation gates, in particular $f_{Ca,s}$, are far from reaching their steady-state value, the f_{ss} value obtained from the simulation is considerably larger than the f_{ss} value defined in the model formulation and the experiments.

For the CRLP model, similarly to the TP06 model, the largest differences between model equations, *in silico* simulations and experiments are due to the time constants of the activation and inactivation gates. Nevertheless, the results of the *in silico* simulations with this model reproduced the experimental observations slightly better than the TP06 model. In the CRLP model, the voltage-dependent I_{CaL} inactivation gate f_2 is faster than in the TP06 model (as defined by the time constant τ_{f2}). Due to this gate being faster, the effect of the separation pulse was larger than in the TP06 model, as during this interval the f_2 gate opened more than in the TP06 model (see Figure 4.3.d)). As a consequence, the CRLP model yielded a larger f_{ss} value in the *in silico* measurements, which was closer to the experimental values. This effect was not very pronounced but it could be better observed for voltages where f_2 is larger (around -20 mV).

This chapter has focused on the difficulties of fitting model parameters associated with the steady-state value of I_{CaL} inactivation using data obtained from voltage-clamp experiments. Such difficulties arise from submodel variable interactions in the I_{CaL} formulation. This situation is a common problem to many gating variables in cardiac electrophysiological models. In this regard, most experimental protocols cannot measure the behavior of one gate at a time, but instead measure the behavior of all gates of the same nature (activation, inactivation, etc.) together (e.g. for I_{CaL} inactivation the experimental protocol measures fast and slow inactivation together). Therefore model development needs to consider the coexistence of all gates during parameter identification to accurately reproduce experimental results. This issue is also present in the estimation of the time constants associated with the different gates. In this regard, the gating interactions associated with an experiment implies that the identified time constants associated with the experimental data cannot, in general, be associated with an individual gate of the model.

Some studies have explored the effect of gating interactions on voltage-clamp data [129, 130]. The voltage-clamp protocol is not designed to measure this directly, but the corresponding effects are included in the experimental results. Nev-

ertheless, most of these techniques have been developed for currents with only one inactivation and one activation gate. Approaches to extend those methods to better calibrate complex gate combinations remain to be investigated.

4.4.2 Effect of cell-to-cell interactions in the evaluation of ionic contributors to AP markers

While the ionic currents identified as having the largest contribution to each analyzed AP-based marker varied from one model to another, the differences between single cell and tissue simulations were comparable for all the analyzed markers in the four considered human ventricular models.

As expected, measurement of depolarization-related AP markers in single cell simulations was significantly affected by the externally applied stimulation current. In particular, dV/dt_{max} in single cell simulations was quite different from that obtained in tissue for all considered models. Although some models use dV/dt_{max} or V_{max} measured in single cell simulations to adjust I_{Na} [15, 47, 64], our results suggest that I_{Na} should be adjusted with the results obtained from, at least, a 1D tissue simulation as in [120], particularly considering that many experiments are performed in tissue.

For repolarization-related AP markers, the largest differences between cell and tissue were observed for Triangulation and APD_{25}. The results for APD_{90} and APD_{75} were very consistent between cell and tissue, while small discrepancies were found for APD_{50}. Although differences for APD_{90} and APD_{50} were small, their added contribution together with the small value of Triangulation caused a relatively large accumulated difference for this marker. For this reason, Triangulation should be used with caution as a marker in single cell simulations when used to calibrate an AP model.

Importantly, the differences between markers computed from single cell and 1D tissue simulations were not only the reflect of a constant bias, as shown in Table 4.2 and in Table 4.3. For repolarization markers, those differences reflected the different contribution of ionic currents to the markers. Computational studies using single cell simulations to analyze the sensitivity of different ionic current conductances on the repolarization behavior of the model should only consider markers with a validated correspondence between cell and tissue simulations or, otherwise, use markers computed from tissue rather than from single cell simulations.

4.5 Conclusions

When proposing a new model, or when evaluating an existing model, consistency between simulated and experimental data should be verified considering all involved effects and scales. The closer the experimental conditions are reproduced in the computer simulations, the more robust the process of model development and validation will be.

As discussed in this paper, proper characterization and validation of a given model should be performed with the *in silico* simulation of the experimental proto-

col. In this way, the effects of the interaction between model variables are accounted for and modeling inconsistencies are avoided.

While the information provided by electrophysiological markers is very valuable for model development and validation, markers should be computed using simulations that resemble as closely as possible the conditions associated with the experimental measurements, or, at least, the consistency of the marker at different scales should be previously validated.

As a final remark, complex models represent a real challenge for parameter identification and validation. This does not mean that models should be necessarily simple, but that complex models require additional testing to fully verify adequate performance.

Chapter 5

Reformulation of Ionic Current Expression

5.1 Introduction

The human ventricular AP model proposed in Chapter 2 and subsequently updated in chapter 3, despite reproducing experimental observations in relation to a range of electrophysiological characteristics (see also Chapter 4), renders an AP lacking the peak-and-dome morphology characteristic of ventricular epicardial cells. Specifically, the end of phase 1 is followed by an atypical low-magnitude bump that precedes the AP plateau phase. In this chapter a readjustment of I_{CaL} voltage-dependent inactivation gates is proposed to provide a more physiological AP shape while guaranteeing an improved fitting of the model to experimental data in relation to all the electrophysiological properties the model had been validated against in previous chapters.

The proposed readjustment lies on the methodologies described in chapters 3 and 4. As a first step, the time constants of I_{CaL} voltage-dependent inactivation gates were modified to render a more realistic AP shape. Due to the implications that a partial modification of an ionic model may have on the performance of the model, as highlighted in chapter 4, the steady-state value of I_{CaL} voltage-dependent inactivation gates was adjusted to better reproduce experimental current data available from three different studies [1–3] by using the algorithm proposed in the chapter 3 and the *in silico* simulation of these experimental protocols described in chapter 4. Finally, the model was evaluated at cell and tissue levels to confirm that its performance was maintained or improved with respect to the model of chapter 2 for all evaluated electrophysiological properties.

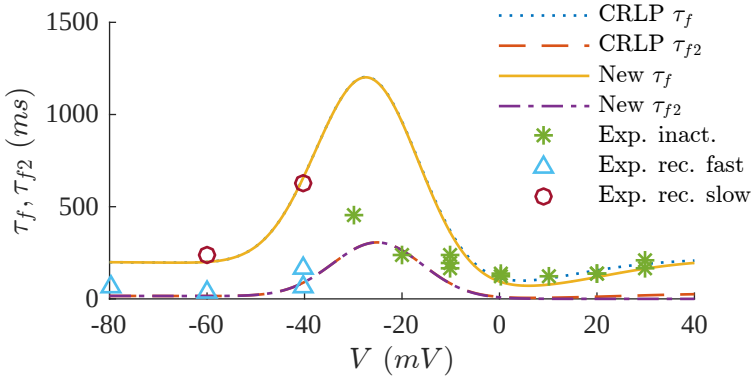

Figure 5.1: Time constants of I_{CaL} voltage-dependent inactivation in the CRLP model and following the readjustment proposed in this chapter. Comparison with experimental data [2, 4–7] is provided as well.

5.2 Methods

5.2.1 Modification of I_{CaL} voltage-dependent inactivation time constants

To improve the AP shape of the CRLP model, the time constants of the slow (τ_f) and fast (τ_{f2}) I_{CaL} voltage-dependent inactivation gates were modified. After evaluating all model parameters defining the currents with a major contribution to the AP part immediately following phase one, namely I_{CaL} and I_{to}, those two time constants were identified as the ones with the largest influence on the AP shape in that specific part. In particular, exploration of the parameter space led to redefinition of the β components of both time constants τ_f and τ_{f2}, as follows:

$$\beta_f = \frac{200}{1 + e^{\frac{20.6 - V}{10}}} \tag{5.1}$$

$$\beta_{f2} = 0 \tag{5.2}$$

where V is membrane potential.

The effect of varying β_f and β_{f2} is shown in Figure 5.2 and Figure 5.3. In Figure 5.1, the new I_{CaL} inactivation time constants are compared with the original ones and with the experimental data from [2, 4–7].

5.2.2 Adjustment of I_{CaL} voltage-dependent inactivation steady-state

To best fit I_{CaL} voltage-dependent inactivation steady-state after readjustment of the time constants described in previous section, the expression of the steady-state value for inactivation gates f and f_2 was parameterized as follows:

$$g_{ss} = \frac{1 - g_{ss,\infty}}{1 + e^{\frac{V - V_{g,1/2}}{q_g}}} + g_{ss,\infty} \tag{5.3}$$

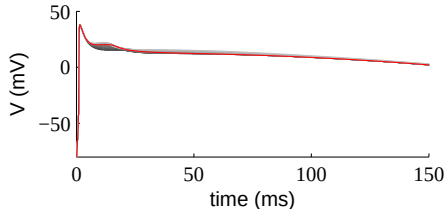

Figure 5.2: Effect of varying β_{f2} in the AP shape. Red line represents control conditions. Dark grey lines correspond to reductions in β_{f2}, while light grey lines correspond to increases in β_{f2}.

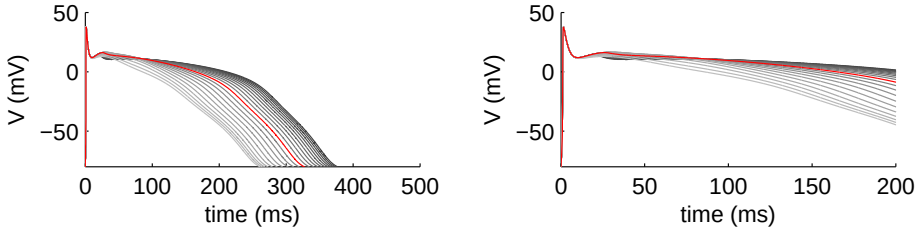

Figure 5.3: Effect of varying β_f in the AP shape after having modified β_{f2} in the CRLP model. Red line represents control conditions. Dark grey lines correspond to reductions in β_f, while light grey lines correspond to increases in β_f.

where g represents f or f_2 (depending on the gate under consideration), V is membrane potential, $g_{ss,\infty}$ is the steady-state value of gate g when V tends to infinity, q_g is a parameter controlling the maximum slope of g_{ss} and $V_{g,1/2}$ is half-inactivation voltage for gate g.

Optimization problem

A minimization problem was defined in which the value of the parameters $f_{ss,\infty}$, $f_{2,ss,\infty}$, q_f, q_{f2}, $V_{f,1/2}$, $V_{f2,1/2}$ are searched for to best fit experimental steady-state I_{CaL} voltage dependent inactivation data. The response surface optimization approach described in chapter 3 was used to solve the minimization problem. The objective function of the minimization problem was defined in terms of the mean square error between a set of experimental data [1–3] and the corresponding results of the *in silico* simulations (see chapter 4) as follows:

$$mse_i = \frac{1}{n_i} \sum_{j=1}^{n_i} \left(f_{ss,exp_i}(V_j) - f_{ss,sim_i}(V_j) \right)^2 \tag{5.4}$$

where n_i is the number of prepulse voltages used in experiment i, $f_{ss,exp}(V_j)$ is the experimental result for voltage V_j in experiment i and $f_{ss,sim}(V_j)$ is the *in silico* result for voltage V_j in the simulation of the experiment i.

Since several experimental measurements of I_{CaL} inactivation were available, the objective function was defined as the addition of the mean square errors for the different experiments weighted by the number of cells used in each experiment to reduce the mean square error of the simulations in comparison with the experimental results:

$$\min_{f_{ss,\infty}, f_{2,ss,\infty}, q_f, q_{f2}, V_{f,1/2}, V_{f2,1/2}} \sum_{i=1}^{N_{exp}} N_i \cdot mse_i \tag{5.5}$$

where N_{exp} is the number of experimental studies used in the minimization problem and N_i is the number of cells used in experiment i.

Constraints

For the above minimization problem, the following constraints were imposed on the aforementioned gating parameters:

- **C1**: Both gates must have the same slope ($q_f = q_{f2}$).
- **C2**: $V_{f,1/2}$ must be smaller or equal to $V_{f2,1/2}$.
- **C3**: When V tends to infinity, the values of f_{ss} and $f_{2,ss}$ must be the same as in the original model (0 and 0.33, respectively).
- **C4**: $f_{2,ss}$ must tend to 0 when V tends to infinity.

Each constraint was approximated using a second order response surface built with a full factorial experimental design (see chapter 3). The second order response surface was enough to find a solution within a reasonable time.

An additional step was included to validate that the solution to the minimization problem led to physiological results at current, cell and tissue levels. At the ionic level, the *in silico* simulation of I_{CaL} voltage-dependent inactivation steady-state was required to decrease monotonically and have only one inflection point at negative voltages. At cell and tissue levels, a set of electrophysiological markers were computed, including: systolic and diastolic intracellular calcium concentration ($[Ca^{2+}]_i$), AP duration (APD) at 90% of repolarization (APD_{90}), AP triangulation at 1Hz and 0.5 Hz and APD adaptation to abrupt cycle length changes (from a cycle length of 1000 ms to a cycle length of 600 ms). A complete description of these markers and the protocols used to compute them can be found in section 2.2. Each marker was computed for varying I_{CaL} conductance ranging from -30% to +30% of the original value in the CRLP model. A solution of the minimization problem was accepted at the cell level when, for some value of G_{CaL}, all markers were within physiological range or, in the case of markers that were originally out of physiological range, when they were at an equal or closer distance to the physiological range than for the CRLP model. For the definition of physiological range, the same values described in chapter 2 (see Table 2.2) were used, as proposed in [12].

Solution for I_{CaL} voltage-dependent inactivation

After selecting the minimum set of requirements as constraints, the minimization problem was solved once more using a fourth order response surface for the objective function and constraints to increase the sampling of the searching space. Based on the conclusions of chapter 4, the solution was additionally evaluated in tissue. A homogeneous 3-cm long fiber composed of epicardial cells was considered. Cell capacitance was set to $C_m = 1\ \mu\text{F/cm}^2$. Values for evaluated electrophsyiological markers were computed as the mean of the values measured at five different positions within the cable located at: 1, 1.25, 1.5, 1.75 and 2 cm. Numerical simulations were solved using ELVIRA software [87].

5.2.3 Numerical methods and implementation

Cells and tissues were stimulated with square transmembrane current pulses twice the diastolic threshold in amplitude and 1-ms duration. The diastolic threshold in fiber simulations was calculated as the minimum value that generated ten pulses that propagated through the fiber with a CL of 1000ms as described in [136]. For cell simulations, the diastolic threshold was calculated as the minimum value that generated ten pulses.

When comparing with experimental data, extracellular concentrations in the model were defined to have the same values as those described for the bath solution of each experimental study.

Computations at cell and ionic levels were performed using MatCardiacMLab Simulator (`http://github.com/ChusCarro/MatCardiacMLab`). This MatLab-based software uses the `ode15s` solver with a maximum step of 0.1 ms to solve the ODEs of the model. The original CellML file of the CRLP model was considered. Fiber simulations were implemented in FORTRAN and simulated using the software ELVIRA. The value of the conductivity, σ, was calculated to obtain a CV value close to 65 cm/s [88]. The fiber was stimulated at one end. A semi-implicit operator-splitting scheme [87] was used to solve the model with a space discretization of $\Delta x = 0.1$ mm and a time step of $\Delta t = 0.002$ ms. Cell capacitance was set to $C_m = 1\ \mu F/cm^2$.

5.3 Results

5.3.1 Solution to the minimization problem

Table 5.1 summarizes the results of the optimization algorithm for each combination of constraints. In each of the tested cases, which are identified by letters A to L, one, two, three or four constraints in the set {C1, C2, C3, C4 } were imposed. As can be observed from Table 5.1, all the solutions that allowed q_f and q_{f2} to be different (C1 not satisfied) rendered non-valid results at the ionic level. Only one solution where $V_{f,1/2}$ was larger than $V_{f2,1/2}$ (C2 not satisfied) rendered a valid solution at the ionic level. In that case, the distance between $V_{f,1/2}$ and $V_{f2,1/2}$ was smaller than in simulations G, H, and I, which were associated with non-valid solutions (either at ionic or cell levels). When constraint C2 was active, $V_{f,1/2}$ was always equal to $V_{f2,1/2}$.

Simulation results accepted as valid after evaluation at the ionic level (G, J, K, L) were subsequently evaluated at cell and tissue levels by computation of a set of electrophysiological markers. The three solutions that increased the value of $f_{2,ss,\infty}$ (H, J, K) greatly reduced the value of APD_{90} and, of note, varying G_{CaL} within the percentages indicated in section 5.2.2 did not lead to APD_{90} values within physiological range. Only the solution obtained after having imposed the four constraints rendered a valid solution at both cell and tissue scales.

5.3.2 New definition of I_{CaL} current

The solution obtained from the minimization problem with all constraints led to the following definition of I_{CaL} voltage-dependent inactivation steady-state:

$$f_{ss} = \frac{1}{1 + e^{\frac{V+24.63}{5.87}}} \tag{5.6}$$

$$f_{2,ss} = \frac{0.67}{1 + e^{\frac{V+24.63}{5.87}}} + 0.33 \tag{5.7}$$

The mean square error between data simulated with the modified CRLP model and experimental data, calculated according to the expression in equation 5.5, was

C1	C2	C3	C4	Id	Improvement	Validation	
						Ionic	Cell
No	No	No	No	A	62.74%	No	—
			Yes	B	54.93%	No	—
		Yes	Yes	C	41.59%	No	—
	Yes	No	No	D	53.44%	No	—
			Yes	E	54.27%	No	—
		Yes	Yes	F	35.28%	No	—
Yes	No	No	No	G	43.06%	No	—
			Yes	H	20.60%	Yes	No
		Yes	Yes	I	19.79%	No	—
	Yes	No	No	J	38.57%	Yes	No
			Yes	K	18.66%	Yes	No
		Yes	Yes	L	17.14%	Yes	Yes

Table 5.1: Results of the minimization problem and subsequent validation. Improvement represents the error for each combination of constraints normalized by the error before the optimization.

20% lower than the corresponding error for the initial CRLP model. Fig. 5.4 shows how the proposed solution satisfactorily reproduced available experimental data.

In tissue, the obtained solution rendered values of APD, triangulation and APD adaptation to abrupt cycle length changes within physiological range, although systolic and diastolic $[Ca^{2+}]_i$ values were somewhat further away from physiological range than for the initial CRLP model (see Table 5.2).

Marker	Physiological Range	CRLP	This Work
APD_{90} (ms)	271-366	305.7	279.2
Triangulation (ms)	44-112	67.1	67.8
Sys. $[Ca^{2+}]_i$ @ 1Hz (mM)	1.59-2.01	0.605	0.335
Sys. $[Ca^{2+}]_i$ @ 0.5Hz (mM)	0.71-1.68	0.538	0.305
Dia. $[Ca^{2+}]_i$ @ 1Hz (mM)	0.20-0.33	0.097	0.090
Dia. $[Ca^{2+}]_i$ @ 0.5Hz (mM)	0.14-0.32	0.092	0.087
τ_{slow} (s)	70-110	101.9	99.5

Table 5.2: Evaluation of electrophysiological markers in tissue for the initial and adjusted CRLP models (third and fourth columns). Available physiological ranges are provided in the second column [12].

In Figure 5.5, simulated electrophysiological markers in tissue are shown. Following the readjustment proposed in this chapter, the AP presents a physiological shape at the end of phase 1.

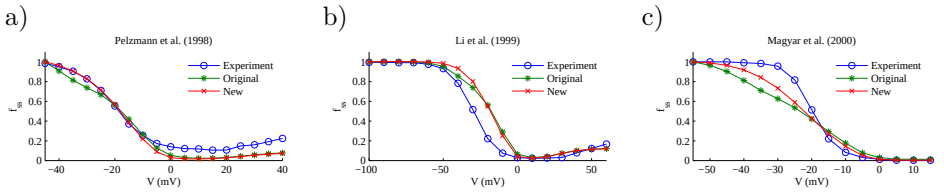

Figure 5.4: Comparison between the results of the *in silico* simulations for the CRLP model and the adjusted model of this chapter and the experimental results of [1–3].

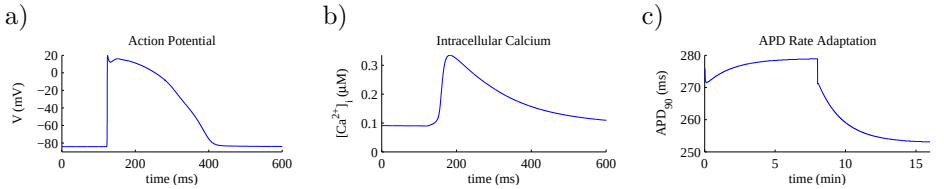

Figure 5.5: Results of tissue simulations computed with the readjusted CRLP model proposed in this chapter. a) AP at a cycle length of 1000 ms. b) $[Ca^{2+}]_i$ at a cycle length of 1000 ms. c) APD adaptation to abrupt cycle length changes.

5.4 Discussion

In cardiac electrophysiological modeling and simulation, there are ionic currents whose definition is particularly challenging. Many ionic parameters can not be directly measured due to the interaction with other model components or due to technical limitations. As an example, some gating dynamics are so fast that its activity overlaps with the capacitive current, thus preventing its direct measurement. In other cases, experimental protocols have been designed to specifically isolate the effects of one parameter of interest in a given model, but, when the complexity of the model increases, it is not possible to isolate it completely. For those reasons: i) when an ionic current is aimed at being formulated, its definition, or at least its validation, should be performed considering the whole model of the ionic current; ii) when an element of an ionic current is modified, the other elements should be readjusted to guarantee that model ionic behavior is in agreement with experimental evidences.

This chapter focused on adjusting the formulation of the time constants of I_{CaL} voltage-dependent inactivation to improve the AP shape of the CRLP model at the end of phase 1. As shown in chapter 4, due to the interactions between different elements of the I_{CaL} current, simulation of *in silico* protocols should be run to adjust parameters defining I_{CaL} voltage-dependent inactivation steady-state, thus accounting for the effects on the whole ionic current.

5.4.1 Development and validation of a new ionic current formulation

A minimization problem was mathematically defined to adjust the formulation of the I_{CaL} current in the CRLP model. Different sets of experimental data providing steady-state measurements of I_{CaL} voltage-dependent inactivation were considered to fit the ionic gating parameters. If no constraints were imposed on the minimization problem, the obtained result was associated with a very small error, but rendered unphysiological results due to the fact the two inactivation gates (fast and slow) did not act in a coordinated way as in the experiments. For that reason, constraints were imposed when fitting the parameters describing voltage-dependent inactivation steady-state. These constraints were selected based on the formulation of I_{CaL} gating proposed in [51]. Our results showed that to all constraints were necessary to reproduce experimental results on I_{CaL} inactivation and at the same time guarantee that electrophysiological markers (APD_{90}, AP triangulation, APD adaptation to abrupt cycle length changes and systolic and diastolic $[Ca^{2+}]_i$ levels) were within physiological ranges.

This chapter considered evaluations at ionic, cell and tissue scales that were performed as a model validation step once the solution to the above described constrained minimization problem had been obtained. Future studies could develop the methods to integrate at least part of the validation rules as constraints in the formulation of the minimization problem.

5.4.2 Reproducing experimental data from different laboratories

One of the difficulties in using different experimental datasets to adjust the parameters of an ionic current is that each dataset is commonly measured under specific experimental conditions. For this reason, the results of different experimental studies can not be directly compared and, consequently, they cannot be used concomitantly when for parameter estimation without considering such differences. On the other hand, the benefit of having experimental datasets recorded under different conditions provides a wider range of data that can be taken into account for model adjustment. Thus, if used correctly, the fact of having highly heterogeneous experimental sets of data can be seen as an advantage rather than a limitation.

Specifically, in this chapter the use of the described experimental datasets made it possible to improve the overall behavior of I_{CaL} voltage-dependent inactivation steady-state without modifying the theoretical expression of the involved gates but rather by modifying the values of the associated parameters. Replication of the experimental data in [1] and [3] with the optimized I_{CaL} model led to differences between *in silico* and experimental results were remarkably smaller than for the initial CRLP model. Only when comparing with the experimental data in [2], the observed differences were small. In overall terms, the optimization problem proposed and solved in this chapter led to relevant improvements in almost all performed evaluations.

5.5 Conclusions

In this chapter the expression of the I_{CaL} current in the CRLP model has been adjusted to correct for the unphysiological shape of the AP following phase 1. Although the CRLP model, developed in chapter 2 and updated in chapter 3, had been tested against various sets of experimental data, considering different scales and interactions between model components as reported in chapter 4, it presented a rather uncommon bump following AP transient repolarization in phase 1. *In silico* simulations of experimental protocols described in chapter 4 were ran and the corresponding results were included as part of an optimization problem with a number of carefully defined constraints, which was solved to adjust model variables in such a way that experimental outcomes were more closely represented. The methodology described in chapter 3 was used for optimization solving. To guarantee that model overfitting was avoided, validation was performed at ionic, cell and tissue scales.

Chapter 6

A Human Ventricular Electrophysiological Model with Improved Description of Experimental Behavior

6.1 Introduction

In chapter 3 and chapter 5, updates to the model described in chapter 2 were addressed. The update in chapter 3 allowed the inclusion of intracellular potassium dynamics, while the update in chapter 5 involved refining the expression of the L-type calcium current, I_{CaL}, to render an AP shape closer to experimental shapes, particularly regarding AP phase 1. When developing the CRLP model in chapter 2, departing from the GPB model, a paradigm based on reproducing a set of experimentally measured electrophysiological markers was used to guide the development process. Within that paradigm, model variables or parameters were updated one at a time along the iterations of the proposed methodology. When $[K^+]_i$ dynamics were included in the CRLP model (chapter 3), an optimization algorithm was used to update several ionic conductances concomitantly, while guaranteeing that the set of electrophysiological markers remained within physiological ranges or, otherwise, their values were closer to the physiological range than with the original CRLP model. When updating the expression of the I_{CaL} current (chapter 5), the methodologies described in chapter 4 were used and parameters related to the steady-state

value of voltage-dependent inactivation gates were modified while considering the effect on global gating behavior and the improvement in *in silico* simulations of experimental results.

As discussed in chapter 4, when comparing simulations of electrophysiological models against experimental results, *in silico* simulations should replicate the corresponding experimental protocols as closely as possible. For that purpose, the conditions in which the experiments were performed should be carefully taken into account. In addition, the spatial scales involved in the experiments should be considered when comparing, for instance, simulated and experimental electrophysiological properties. Regarding the latter, experiments performed to characterize the AP usually employ small pieces of tissue to avoid the problem of sensitivity of some ion channels to the cell isolation procedure [106]. However, for computational reasons, simulations are commonly carried out using single cell models. As shown in chapter 4, this may represent a limitation, particularly for a number of markers whose values highly differ when evaluated in single cells or tissues. Importantly, not only do results differ from cell to tissue but the underlying ionic contributions can be different as well. This makes identification of ionic current conductances even more challenging.

Another important point to consider when comparing *in silico* results with experimental measurements is the definition of experimentally-based physiological ranges. In chapter 2, physiological ranges were defined following the criteria used in [12]. Specifically, the upper and lower limits of the physiological range of a given electrophysiological property were determined by the maximum and the minimum value of that property found in the literature. This definition has two main limitations. The first limitation refers to the fact that in many experimental studies only an average value of a set of experiments is provided. Consequently, if the maximum or the minimum value is selected based on such average values, the physiological range will surely be smaller than the experimental range. The second limitation is in regards of the fact that, in each experimental study, electrophysiological properties are measured by using different bath solutions. This means that part of the differences found between experimental studies could be due to differences in the extracellular ionic concentrations.

The main objective of this chapter is to integrate all the initial formulations and subsequent updates of the CRLP model proposed in previous chapters and to readjust the ionic conductances of the integrated model to improve replication of experimental electrophysiological measures. All the methodologies introduced throughout the thesis are used to build this human ventricular AP model. In particular, to compare the simulation and experimental results, each experiment was initially considered individually, making sure that the conditions underlying the experiment were replicated as faithfully as possible. In line with the conclusions reported in chapter 4, a physiological range was established for each individual experiment by using the mean value and the standard deviation reported in the corresponding study (see section 6.2 for details). Additionally, based on the mentioned differences found between cell and tissue in many electrophysiological properties, only those that remain essentially the same in one and another scale were consid-

ered for model development, while other properties were included in the validation process, in which tissue simulation results were contrasted with experimental tissue data.

The final version of the CRLP model built in this chapter is compared with that of the most recent human ventricular cell models: *ten Tusscher-Panfilov* (TP06) [51], *Grandi-Pasqualini-Bers* (GPB) model [15], *O'Hara-Rudy-dynamic* (ORd) model [64], and the original *Carro-Rodríguez-Laguna-Pueyo* (CRLP) model [120]. Results are in all cases compared against experimental results and conditions where one or another model best represents experimental outcomes are highlighted.

6.2 Methods

6.2.1 Adjustment of ionic conductances

The CRLP model with the updates of chapter 3 and chapter 5 was considered as a starting point. The ionic conductances of that model were redefined following the procedure introduced in chapter 3 with the following modifications:

- All the ionic conductances and the calcium diffusion coefficients between the intracellular spaces were considered as variables to be adjusted.
- A large number of markers obtained from different experimental datasets were considered. In the simulation of each dataset, the stimulation protocol was reproduced and the specific experimental conditions were considered by setting the values of the extracellular ionic concentrations as those in the experiments.
- A new optimization function was proposed to make as many markers as possible lie within established physiological ranges.

Details on each of the above aspects are provided in the following paragraphs.

Minimization function

With the aim of developing a model that closely reproduces the average behavior of human ventricular epicardial cells, a minimization function was introduced that accounts for the sum of errors associated with the different evaluated electrophysiological markers. For each marker, m_i, the error was defined in terms of the experimental mean and standard error of the mean (SEM) as follows:

$$err_{m_i}(\mathbf{x}) = \frac{\mu_i - m_i(\mathbf{x})}{SEM_i} \tag{6.1}$$

where μ_i is the experimental mean value of marker m_i; $m_i(\mathbf{x})$ is the simulated value of marker m_i obtained for model parameter values in vector $\mathbf{x}$; and SEM_i is the experimental standard error of the mean of marker m_i.

The objective function was defined as the sum of the square of the errors associated with all evaluated electrophysiological markers as follows:

$$f(\mathbf{x}) = \sum_{i=1}^{M} (err_{m_i}(\mathbf{x}))^2 = \sum_{i=1}^{M} \left(\frac{\mu_i - m_i(\mathbf{x})}{SEM_i} \right)^2 \tag{6.2}$$

where M is the total number of electrophysiological markers evaluated in the optimization problem.

Of note, SEM represents the confidence in the experimental average value of a marker and depends on the number of experiments and on the sample standard deviation. If the sample standard deviation is high but there are a larger number of experiments, the mean experimental value could be trusted more than another one for which the sample standard deviation was lower but was obtained from a fewer number of experiments. When the difference between the simulated and mean experimental values of the marker is within the SEM, the error for that marker is between -1 and 1. Consequently, The defined objective function reduces the error for markers within that range and increases it for markers out of that range.

Experimental data sets

The following experimental datasets were included in the optimization problem defined to fit ionic current conductances:

- **TESZT**: AP traces from healthy human ventricular endocardial tissues at steady-state were acquired at the University of Szeged. After reaching steady-state following pacing at a CL of 1000 ms, 10 pulses were recorded. Following this, different drugs were added to inhibit potassium currents: 1 μM of HMR-1556 and 100 nM of L735,821 corresponding to approximately 95% I_{Ks} block [137, 138]; 50 nM of dofetilide corresponding to 15% I_{Kr} block [139]; 1 μM of dofetilide and 1 μM of E-4031 corresponding to 70% I_{Kr} block [34, 139]; 100 μM of $BaCl_2$ corresponding to 75% I_{K1} block [140]. After reaching steady-state following each of the above drug actions, 10 pulses were recorded at a pacing CL of 1000 ms.

  For each AP recording, two markers were measured: APD_{90} and resting membrane potential (V_{rest}). According to the results presented in chapter 4, these two markers show similar values and underlying mechanisms when evaluated at cell or tissue levels. In Table 6.1, evaluation of these two markers in the TESZT dataset, both at baseline and following each of the described pharmacological potassium inhibitions, are summarized. For potassium inhibition experiments, results are expressed as percentage of variation with respect to control conditions.

  The bath solution in the experiments of the TESZT dataset is described in [64]. Values of ion concentrations in the bath solution were as follows: $[Ca^{2+}]_o = 1.8\ mM$, $[K^+]_o = 4.0\ mM$, $[Na^+]_o = 135.0\ mM$, $[Cl^-]_o = 124.6\ mM$.

Experiment	Marker	Mean	SEM	n
Control	APD_{90} (ms)	293.85	10.41	23
	V_{rest}	-86.75	0.92	
I_{K1} block 75%	Variation in APD_{90} (%)	+19.25	3.09	6
	Variation of V_{rest} (%)	-4.56	1.95	
I_{Kr} block 15%	Variation in APD_{90} (%)	+51.17	8.57	11
	Variation of V_{rest} (%)	+0.67	1.11	
I_{Kr} block 70%	Variation in APD_{90} (%)	+51.17	8.57	11
	Variation of V_{rest} (%)	+0.67	1.11	
I_{Ks} block 95%	Variation in APD_{90} (%)	+1.53	1.42	6
	Variation of V_{rest} (%)	-0.19	1.59	

Table 6.1: Evaluation of APD_{90} and V_{rest} in the TESZT dataset.

- **CLVPET**: AP traces from healthy human ventricular endocardial tissues under variable CL stimulation were acquired at the University of Szeged. After reaching steady-state following pacing at a CL of 1000 ms, stimulati at CLs varying from 300 ms to 5000 ms were applied. For each CL, 25 pulses were delivered and the AP corresponding to the last pulse was recorded. As in the TESZT dataset, drugs were subsequently added to inhibit potassium currents. The same drugs, and at the same concentrations, were supplied to the tissues in this case.

  For AP recordings under control conditions, the variation in the APD with respect to steady-state APD at CL = 1000 ms was quantified. For AP recordings under potassium inhibitions, the variation in the APD with respect to the APD at the same CL under control conditions was quantified. In Table 6.2, evaluation of variations in APD_{90} are summarized.

  The bath solution in the experiments of the CLVPET dataset is described in [64]. Values of ion concentrations in the bath solution were as follows: $[Ca^{2+}]_o = 1.8\ mM$, $[K^+]_o = 4.0\ mM$, $[Na^+]_o = 135.0\ mM$, $[Cl^-]_o = 124.6\ mM$.

- **Drouin *et al.* (1995)** [8]: APD_{90} values from epicardial and endocardial cells of human ventricular tissues were measured. APD_{90} was quantified at different CLs spanning from 1000 ms to 10000 ms. In Table 6.3, evaluation of APD_{90} is summarized.

  The bath solution used in this experiments is described in [8]. Values of ion concentrations in the bath solution were as follows: $[Ca^{2+}]_o = 2.7\ mM$, $[K^+]_o = 4.0\ mM$, $[Na^+]_o = 150.8\ mM$, $[Cl^-]_o = 141.4\ mM$.

- **Pieske *et al.* (2002)** [9]: Intracellular sodium ($[Na^+]_i$) concentrations were measured at the following CLs: 333, 500, 1000 and 4000 ms. In this study, the absolute value of $[Na^+]_i$ at CL = 1000 ms and the variations in $[Na^+]_i$

Experiment	Marker	CL	Mean	SEM	n
Control	ΔAPD_{90} (%)	300 ms	-24.98	1.38	21
		400 ms	-20.35	1.48	
		500 ms	-14.57	1.05	
		700 ms	-8.61	1.00	
		1000 ms	-3.12	0.60	
		1500 ms	+4.28	1.02	
		2000 ms	+8.75	1.16	
		3000 ms	+13.86	2.22	
		5000 ms	+16.32	1.55	
I_{K1} Blocked	ΔAPD_{90} (%)	400 ms	-9.68	5.35	6
		500 ms	-0.37	4.74	
		700 ms	+10.93	3.75	
		1000 ms	+20.55	3.66	
		1500 ms	+29.32	4.33	
		2000 ms	+32.56	4.96	
		3000 ms	+37.49	6.09	
		5000 ms	+41.93	7.17	
I_{Kr} Blocked	ΔAPD_{90} (%)	500 ms	+19.51	5.45	9
		700 ms	+41.52	8.43	
		1000 ms	+53.68	9.05	
		1500 ms	+68.72	10.41	
		2000 ms	+82.65	11.10	
		3000 ms	+100.00	12.80	
		5000 ms	+127.33	15.73	
I_{Ks} Blocked	ΔAPD_{90} (%)	300 ms	-23.80	2.68	5
		400 ms	-17.94	2.52	
		500 ms	-14.22	2.37	
		700 ms	-8.22	1.81	
		1000 ms	-2.62	1.59	
		1500 ms	+2.82	1.52	
		2000 ms	+6.59	2.02	
		3000 ms	+9.13	2.71	
		5000 ms	+11.96	3.79	

Table 6.2: Evaluation of variations in APD_{90} in the CLVPET dataset.

Experiment	Marker	CL	Mean	SEM	n
ENDO	APD_{90} (ms)	1000 ms	329.5	15.6	14
		2000 ms	345.3	17.2	
		3000 ms	362.2	20.5	
		4000 ms	369.5	21.2	
		5000 ms	378.1	20.8	
		6000 ms	393.0	22.8	
		10000 ms	406.5	25.5	
EPI	APD_{90} (ms)	1000 ms	350.6	14.6	14
		2000 ms	382.1	19.5	
		3000 ms	392.0	19.9	
		4000 ms	406.5	18.9	
		5000 ms	418.8	17.2	
		6000 ms	424.4	17.2	
		10000 ms	463.1	14.6	

Table 6.3: Evaluation of APD_{90} in the study by Drouin *et al.* [8].

Experiment	Marker	Mean	SEM	n
$CL = 1000\ ms$	$[Na^+]_i$ (mM)	18.58	3.91	7
$CL = 4000\ ms$	Variation in $[Na^+]_i$ (%)	-15.34	17.5	7
$CL = 500\ ms$	Variation in $[Na^+]_i$ (%)	+10.66	22.8	7
$CL = 333\ ms$	Variation in $[Na^+]_i$ (%)	+21.74	25.3	7

Table 6.4: Evaluation of $[Na^+]_i$ and its variations in the study by Pieske *et al.* [9].

for other CLs expressed as a percentage with respect to CL = 1000 ms were quantified. In Table 6.4, evaluation of these markers is summarized.

Values of ion concentrations in the bath solution were as follows: $[Ca^{2+}]_o = 1.0\ mM$, $[K^+]_o = 5.4\ mM$, $[Na^+]_o = 152.0\ mM$, $[Cl^-]_o = 157.8\ mM$.

- **Schmidt *et al.* (1998)** [10]: Intracellular calcium ($[Ca^{2+}]_i$) concentrations were measured at the following CLs: 333, 400, 500, 575, 666, 750, 1000, 1400, 2000, 3000 and 8000 ms. In this study, the absolute systolic and diastolic values of $[Ca^{2+}]_i$ for CL = 1000 ms and the variations in those values for other CLs expressed as a percentage with respect to CL = 1000 ms were quantified. In Table 6.5, evaluation of these markers is summarized.

  The concentration of the main ions in the bath solution was: $[Ca^{2+}]_o = 2.5\ mM$, $[K^+]_o = 5.9\ mM$, $[Na^+]_o = 126.2\ mM$, $[Cl^-]_o = 133.3\ mM$.

- **Coppini *et al.* (2013)** [11]: Intracellular calcium ($[Ca^{2+}]_i$) concentrations were measured at the following CLs: 1000, 2000, and 5000 ms. The following markers were evaluated:

Experiment	Marker	Mean	SEM	n
$CL = 1000\ ms$	Diastolic $[Ca^{2+}]_i$ (μM)	1.798	0.0887	6
	Systolic $[Ca^{2+}]_i$ (μM)	0.256	0.0295	
$CL = 333\ ms$	Var. in Diastolic $[Ca^{2+}]_i$ (%)	+48.26	17.83	6
	Var. of Systolic $[Ca^{2+}]_i$ (%)	-2.22	5.22	
$CL = 400\ ms$	Var. in Diastolic $[Ca^{2+}]_i$ (%)	+34.45	13.23	6
	Var. of Systolic $[Ca^{2+}]_i$ (%)	+8.89	5.51	
$CL = 500\ ms$	Var. in Diastolic $[Ca^{2+}]_i$ (%)	+25.83	13.23	6
	Var. of Systolic $[Ca^{2+}]_i$ (%)	+14.11	5.61	
$CL = 575\ ms$	Var. in Diastolic $[Ca^{2+}]_i$ (%)	+18.96	12.06	6
	Var. of Systolic $[Ca^{2+}]_i$ (%)	+10.92	5.71	
$CL = 666\ ms$	Var. in Diastolic $[Ca^{2+}]_i$ (%)	+6.87	9.75	6
	Var. of Systolic $[Ca^{2+}]_i$ (%)	+8.41	5.22	
$CL = 750\ ms$	Var. in Diastolic $[Ca^{2+}]_i$ (%)	+6.32	9.21	6
	Var. of Systolic $[Ca^{2+}]_i$ (%)	+5.61	5.028	
$CL = 1400\ ms$	Var. in Diastolic $[Ca^{2+}]_i$ (%)	-4.60	10.93	6
	Var. of Systolic $[Ca^{2+}]_i$ (%)	-5.71	4.74	
$CL = 2000\ ms$	Var. of Diastolic $[Ca^{2+}]_i$ (%)	+2.85	11.51	6
	Var. of Systolic $[Ca^{2+}]_i$ (%)	-16.63	3.97	
$CL = 3000\ ms$	Var. in Diastolic $[Ca^{2+}]_i$ (%)	+1.09	9.21	6
	Var. of Systolic $[Ca^{2+}]_i$ (%)	-21.95	3.48	
$CL = 8000\ ms$	Var. in Diastolic $[Ca^{2+}]_i$ (%)	+3.43	12.06	6
	Var. of Systolic $[Ca^{2+}]_i$ (%)	-27.56	3.29	

Table 6.5: Evaluation of $[Ca^{2+}]_i$ and its variations in the study by Schmidt *et al.* [10].

Experiment	Marker	Mean	SEM	n
$CL = 1000\ ms$	Diastolic $[Ca^{2+}]_i$ (μM)	0.139	0.00994	6
	$\Delta[Ca^{2+}]_i$ (μM)	0.3528	0.0176	
	$t_{Ca_i,50\%}$ (ms)	170.27	26.37	
	$t_{Ca_i,90\%}$ (ms)	356.21	46.15	
$CL = 2000\ ms$	Var. of Diastolic $[Ca^{2+}]_i$ (%)	-3.66	6.70	6
$CL = 5000\ ms$	Var. of Diastolic $[Ca^{2+}]_i$ (%)	-7.82	5.83	6
	$\Delta[Ca^{2+}]_i$ (μM)	0.343	0.0163	
	$t_{Ca_i,50\%}$ (ms)	239.33	35.16	
	$t_{Ca_i,90\%}$ (ms)	517.57	52.73	

Table 6.6: Evaluation of $[Ca^{2+}]_i$ characteristics in the study by Coppini *et al.* [11].

Marker	Mean	SEM	n
$t_{90\%,1000\rightarrow600}$ (ms)	119.5	21.57	2
$t_{90\%,600\rightarrow1000}$ (ms)	243.0	59.40	

Table 6.7: Evaluation of time for APD rate adaptation in the study by Pueyo *et al.* [13].

  - *Diastolic* $[Ca^{2+}]_i$: Absolute value for CL = 1000 ms and percentage of variation at CL = 2000 and 5000 ms with respect to CL = 1000 ms.
  - *Difference between systolic and diastolic* $[Ca^{2+}]_i$ *levels, denoted by* $\Delta[Ca^{2+}]_i$: Absolute values for CL 1000 and 5000 ms.
  - *Time constants*: Time from the peak to 50% and 90% recovery of the $[Ca^{2+}]_i$ transient, denoted by $t_{Ca_i,50\%}$ and $t_{Ca_i,90\%}$, respectively: Absolute values for CL = 1000 and 5000 ms.

  In Table 6.6, evaluation of these markers is summarized.

  Values of ion concentrations in the bath solution were as follows: $[Ca^{2+}]_o = 1.8\ mM$, $[K^+]_o = 4.0\ mM$, $[Na^+]_o = 132.0\ mM$, $[Cl^-]_o = 142.0\ mM$.

- **Pueyo *et al.* (2010)** [13]: APD rate adaptation to abrupt CL changes when varying CL from 1000 to 600 ms and from 600 to 1000 ms were measured. In this study, following a period of steady-state pacing at a CL of 1000 ms, stimuli were delivered at a CL of 600 ms for 10 minutes and, subsequently, at a CL of 1000 ms for additional 10 minutes. In each transition, the time to reach 90% of the final APD value was measured, denoted by $t_{90\%,1000\rightarrow600}$ and $t_{90\%,600\rightarrow1000}$, respectively. In Table 6.7, evaluation of this marker is summarized.

  Values of ion concentrations in the bath solution were as follows: $[Ca^{2+}]_o = 1.0\ mM$, $[K^+]_o = 4.0\ mM$, $[Na^+]_o = 144.0\ mM$, $[Cl^-]_o = 128.0\ mM$.

Simulation of experimental protocols

The experimental protocols were simulated in isolated cells using a biphasic stimulation current as described in [118]. While biphasic stimulation does not remove differences between cell and tissue simulation results as discussed in chapter 4, it provides a better approximation for the variations in $[Na^+]_i$ and $[K^+]_i$ with the frequency of stimulation, owing the fact that the ionic load during each cycle is 0. The amplitude of the biphasic stimulation current was set to twice the diastolic threshold of the model. The duration of the positive square pulse of the biphasic stimulation was set to 1 ms.

The model was first stabilized until steady-state conditions were reached. In particular, the following stimulation protocols were applied when comparing with the different experimental datasets:

- For the TESZT and CLVPET datasets, the model was first stimulated during 50 minutes at a CL of 1000 ms. The TESZT protocol involved evaluation during the last cycle. The CLVPET protocol involved replication at different CLs after this pre-stimulation.
- For the experiments of Drouin *et al.*, Pieske *et al.*, Schmidt *et al.* and Coppini *et al.*, the model was stimulated during 50 minutes at different CLs. Electrophyisiological markers were evaluated during the last cycle.
- For the experiments published by Pueyo *et al.*, the model was first stimulated during 50 minutes at a CL of 1000 ms, CL was subsequently reduced to 600 ms and stimulation applied for 10 minutes and, finally, CL was increased to 1000 ms and stimulation applied for other 10 minutes.

Optimization algorithm

The optimization algorithm was as described in chapter 3. Design variables included all the ionic conductances of the model as well as parameters related to diffusion of intracellular calcium, namely:

- G_{Na}: conductance of the fast sodium current (I_{Na}).
- $G_{Na,bk}$: conductance of the background sodium current ($I_{Na,bk}$).
- G_{Kr}: conductance of the rapidly activating potassium current (I_{Kr}).
- G_{Ks}: conductance of the slowly activating potassium current (I_{Ks}).
- G_{Kp}: conductance of the plateau potassium current (I_{Kp}).
- G_{to}: conductance of the transient outward potassium current (I_{to}).
- G_{K1}: conductance of the inward rectifier potassium current (I_{K1}).
- G_{ClCa}: conductance of the calcium-activated chloride current (I_{ClCa}).

- $G_{Cl,bk}$: conductance of the background chloride current ($I_{Cl,bk}$).
- G_{CaL}: conductance of the L-type calcium current (I_{CaL}).
- $G_{Ca,bk}$: conductance of the background calcium current ($I_{Ca,bk}$).
- $\bar{I}_{NaK}$: maximum current carried through the sodium-potassium pump.
- $\bar{I}_{ncx}$: maximum current carried through the sodium-calcium exchanger.
- $\bar{I}_{PMCA}$: maximum current carried through the sarcolemmal calcium pump.
- $J_{Ca_{junc,sl}}$: diffusion of calcium from the junctional to the subsarcolemmal compartment.
- $J_{Ca_{sl,myo}}$: diffusion of calcium from the subsarcolemmal compartment to the myoplasm.
- $J_{SR_{leak}}$: diffusion of calcium from the sarcoplasmatic reticulum to the myoplasm.
- $J_{SR_{Ca_{rel}}}$: calcium release from the sarcoplasmatic reticulum to the junctional compartment.
- $J_{ser_{Ca}}$: calcium release from the sarcoplasmatic reticulum to the myoplasm.

As in chapter 3, all these variables were scaled to deal with their different orders of magnitude:

$$x_i = 20 \cdot log_{10}\left(\frac{y_i}{y_i^0}\right), \tag{6.3}$$

where y_i^0 and y_i are the initial and current values of the i^{th} variable and x_i is its scaled value.

The initial radius for the trust region was selected as 2.5 for all the variables. The minimum tolerance for the scaled variables, δ_1, was set to 0.01. The minimum tolerance for the optimization function, δ_2, was set to 0.01. The minimum gradient, δ_3, was taken as 0.01. To create the database of markers in each iteration, 500 randomly-selected combinations of the design variables in the trust region were simulated in each iteration of the optimization algorithm. For each marker, a first-order response surface was calculated. To guarantee positivity of the response surface of the objective function, a response surface of first order was created for the error and later, it was squared.

Valid ranges for electrophysiological markers were defined based on experimental observations and simulated values of the electrophysiological markers under control conditions. Specifically, the upper and lower limits were defined as follows:

$$m_{j,UL} = \max\left\{\mu_{m_j,exp} + 2 \cdot \sigma_{m_j,exp};\ m_{j,control}\right\}$$

$$m_{j,LL} = \min\left\{\mu_{m_j,exp} - 2 \cdot \sigma_{m_j,exp};\ m_{j,control}\right\}$$

where $m_{j,UL}$ is the upper limit for marker m_j, $m_{j,LL}$ is the lower limit for marker m_j, $\mu_{m_j,exp}$ is the mean of the experimental observations for marker m_j, $\sigma_{m_j,exp}$ is the standard deviation of the experimental observations for marker m_j and $m_{j,control}$ is the simulated value of the marker under control conditions.

All markers were considered as constraints for the optimization algorithm. As in chapter 3, these constraints were defined to be consistent with the general formulation of the inequality constraints:

$$g_j(\mathbf{x}) = \left| \frac{m_j(\mathbf{x}) - m_{j,CR}}{m_{j,RR}} \right| - 1 \leq 0,$$

where $m_{j,CR} = {}^{(m_{j,UL} + m_{j,LL})}/_2$ is the central point of the valid range for the electrophysiological marker j and $m_{j,RR} = {}^{(m_{j,UL} - m_{j,LL})}/_2$ is the distance between $m_{j,CR}$ and each of the limits of the valid range.

Implementation

The model was implemented in CellML using the original CellML model published in [120]. For the simulations, the model was exported to C++ and included in the application of the DENIS project (`http://denis.usj.es`). The tool to export the model can be found here: `https://bitbucket.org/usj_bsicos/denis-cellml2c/src/v0.1/`. The original code of the DENIS application can be found here: `https://bitbucket.org/usj_bsicos/denis-myocyte/src/beta_v1.0/`. The equations of the model were solved using Fordward-Euler integrator with a time step of 0.002 ms. Post-processing of simulation results and implementation of the optimization algorithm were developed in MatLab® 2017a (The Mathworks Inc.).

6.2.2 Model comparison

The behavior of the optimized model was compared against the original CRLP model and other commonly employed human ventricular cell models (TP06, GPB, ORd). Electrophysiological markers were computed in single cells for each of those models.

6.2.3 Model validation

The optimized model was validated against experimental results by using a set of electrophysiological markers different from the ones used for model development.

In chapter 4, markers like triangulation and upstroke or maximal potential were shown to be highly different when evaluated in cells or tissues. These markers, not having been used for model optimization, were used for validation. Evaluation was performed by using a 3 cm-long homogeneous fiber model of endocardial ventricular cells. The conditions of the experiments against which simulation results were compared were reproduced by adjusting the external ionic concentrations. The value of σ was calculated to obtain a CV close to 65 cm/s [88] under control

conditions. The cell capacitance was set to $C_m = 1\ \mu F/cm^2$. Each marker was evaluated at five positions within the fiber. Those positions were located at 1.00, 1.25, 1.50, 1.75 and 2.00 cm from the stimulation end of the cable. The mean value of each marker over the five positions was calculated.

The same evaluation described for the optimized CRLP model was performed for the initial CRLP model to assess the effect of the model optimization introduced in this chapter.

Experimental dataset

The TESZT dataset described above provided experimental results on the following AP markers:

- **Triangulation**: Difference between the APD_{90} and the APD_{50}.
- **Upstroke**: Maximum of the temporal derivative of the membrane potential.
- **Maximum potential**: Maximum of the membrane potential.

On top of evaluating these markers under control conditions, the percentages of variation in each marker following ionic current inhibitions (I_{K1}, I_{Kr} or I_{Ks} blockades) with respect to control conditions were measured. The bath solution in these experiments is described in [64]: $[Ca^{2+}]_o = 1.8\ mM$, $[K^+]_o = 4.0\ mM$, $[Na^+]_o = 135.0\ mM$, $[Cl^-]_o = 124.6\ mM$.

For the steady-state simulations in fiber, we simulate 5 minutes of activity. We reduced the simulation time for the fiber simulations in order to be able to obtain the results in a reasonable time.

Implementation

Simulations were performed in a homogeneous 3-cm long fiber composed of endocardial cells. A semi-implicit operator-splitting scheme [87] was used to solve the model with a space discretization of $\Delta x = 0.1$ mm and a time step of $\Delta t = 0.002$ ms. The value of σ was selected to get a maximum CV of 65 cm/s, which is in agreement with experimentally reported CV values [88]. The cell capacitance was set to C_m=1μF/cm^2. Fiber simulations were implemented in FORTRAN.

6.3 Results

6.3.1 Model optimization

Following model optimization, the variation in the ionic conductances of the optimized model with respect to the initial CRLP model varied between -23% and 30%. The original model had an error of 1783.4 (according to the formula defined in section 6.2). After 13 iterations of the optimization algorithm, the error was 1360.5, thus representing a reduction in the error of 23.7%.

While in the initial CRLP model 77.2% of the markers were in physiological range, this value increased to 81.2% after the optimization. Figure 6.1 shows the

Blockage	Marker	Physiol. min	Physiol. mean	Physiol. max	This work	CRLP	ORd	GPB	TP06
Control	APD_{90} (ms)	194.0	293.8	393.6	328.6	334.2	279.6	283.0	285.4
	V_{min} (mV)	-95.6	-86.8	-77.9	-87.4	-90.7	-96.2	-81.6	-93.8
75% I_{K1}	ΔAPD_{90} (%)	4.1	19.3	34.4	13.3	34.1	10.1	26.1	6.3
	ΔV_{min} (%)	-14.1	-4.6	5.0	-32.4	-25.0	1.0	-4.6	-3.9
15% I_{Kr}	ΔAPD_{90} (%)	9.3	39.1	68.8	2.7	2.9	9.6	2.4	2.4
	ΔV_{min} (%)	-5.1	-1.2	2.8	0.2	0.0	0.0	0.0	0.0
70% I_{Kr}	ΔAPD_{90} (%)	-5.5	58.1	121.7	15.2	15.9	71.6	13.1	13.0
	ΔV_{min} (%)	-6.4	1.7	9.8	0.8	-0.1	0.0	0.0	0.0
95% I_{Ks}	ΔAPD_{90} (%)	-5.4	1.5	8.5	0.5	0.6	6.3	0.7	55.9
	ΔV_{min} (%)	-8.0	-0.2	7.6	0.0	0.0	0.0	0.0	0.2

Table 6.8: Results of steady-state AP markers for a CL of 1000 ms computed with the optimized CRLP model and other published human ventricular cell models.

AP of a single epicardial cell simulated under control conditions with the optimized CRLP model and with other published human ventricular cell models. As can be noted, the peak and dome features improved in chapter 5 for the CRLP model were not modified following the model optimization introduced in this chapter.

The values of the optimized ionic conductances and the final description of the model can be found in Appendix C.

Steady-state AP markers

Table 6.8 summarizes the results of steady-state AP markers for a CL of 1000 ms under control conditions and following ionic current inhibitions. These results were compared with experimental measurements from the University of Szeged and the results of other recent human ventricular cell models, as described in 6.2. The first version of the CRLP model, proposed in chapter 2, had only two steady-state AP markers out of physiological range following inhibition of I_{K1} or I_{Kr} currents. These two markers were still out of physiological range for the new CRLP model. For I_{K1} inhibition, the variation in the resting membrane potential was slightly larger for the optimized CRLP model than for the initial model version. The lack of improvement for the new CRLP model can be explained by the modifications introduced into the model prior to the optimization, namely the introduction of $[K^+]_i$ dynamics and the modification of the I_{CaL} current, whereas subsequent optimization tried to compensate the effect of such variations on the resting membrane potential. Similar conclusions to those described above for I_{K1} block apply to the case of I_{Kr} block.

APD dependence on CL

Figure 6.2 shows the variation in APD_{90} for different CLs under control conditions as computed with the optimized CRLP model, the original CRLP model and other

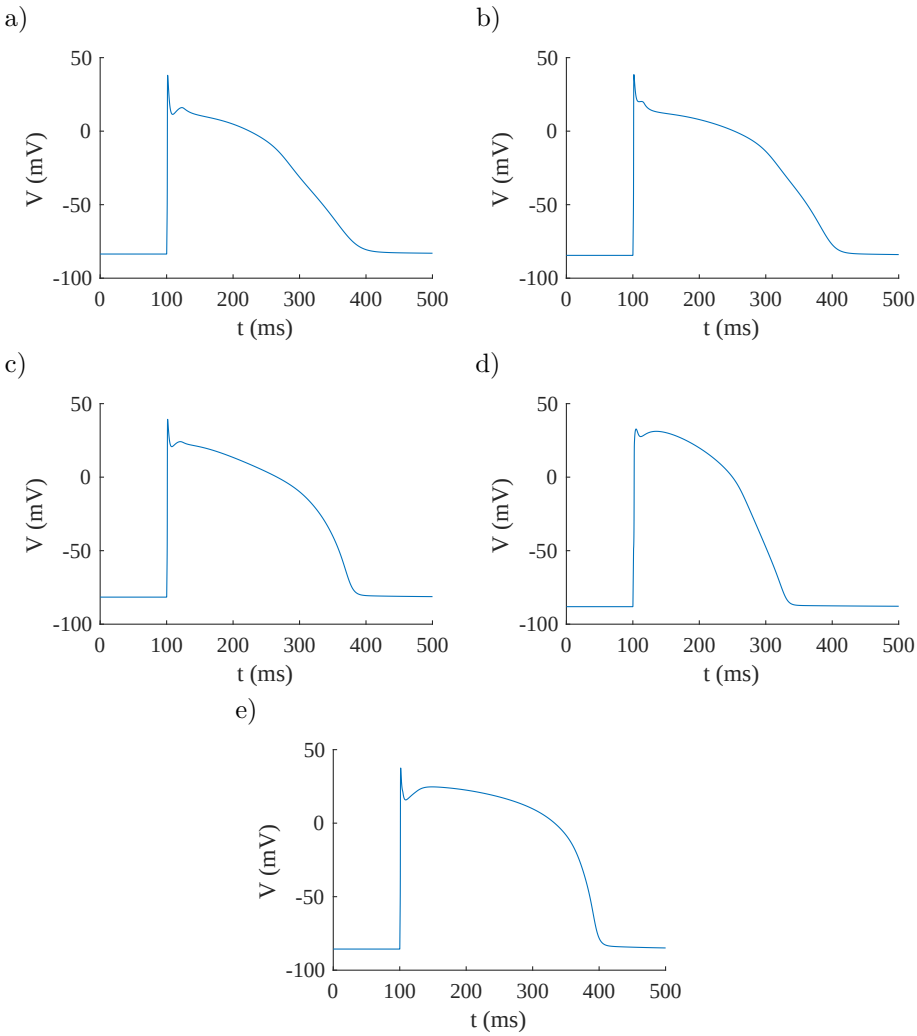

Figure 6.1: Action Potential of the different models under control conditions in single epicardial cells: a) optimized CRLP model; b) initial CRLP model; c) GPB model; d) ORd model; e) TP06 model.

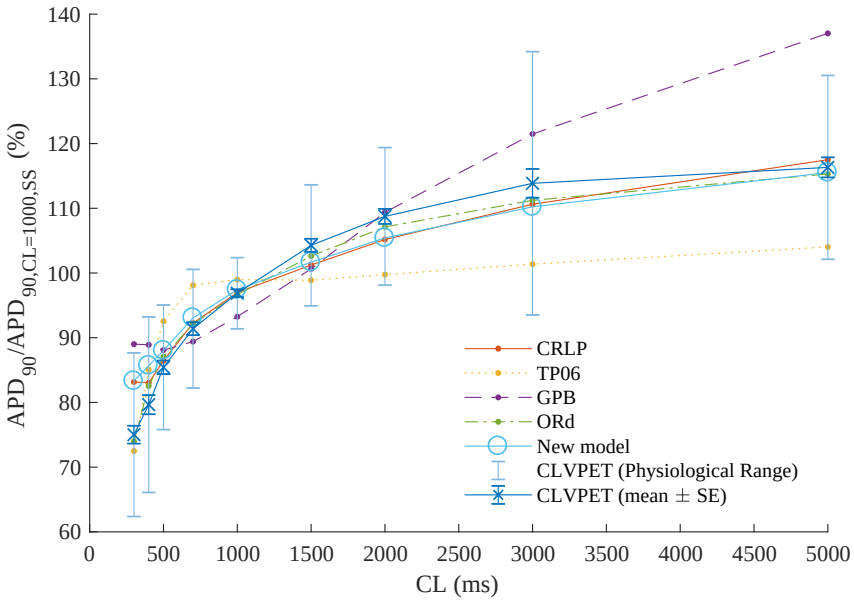

Figure 6.2: APD_{90} variation with CL under the same conditions of the CLVPET dataset.

published human ventricular cell models. Experimental results evaluated for the CLVPET dataset are presented for comparison. The APD_{90} value in cycle 25 of the CLVPET protocol expressed as a percentage of the APD_{90} value under steady-state conditions for a CL of 1000 ms is presented. While the initial CRLP model and the GPB model showed APD increases for decreasing CLs below 500 ms, the optimized CRLP model already corrected this type of behavior, showing APD decrases for decreasing CLs no matter the value of the CL. In fact, for long CLs, the optimized CRLP model shows results very close to the experimental outcomes.

Figure 6.3 shows results of APD variations with CL changes, in this case following ionic current inhibitions. APD values are normalized with respect to those corresponding to the same CL under control conditions. As can be observed, there is very good agreement between the new version of the CRLP model and most experimental results. Out of all the evaluated current inhibitions, the optimized CRLP model renders results that are within experimental limits in all cases except for the one corresponding to I_{Kr} inhibition.

Simulation results for APD_{90} variations with CL changes were also compared with the experimental results published in [8]. Figure 6.4 illustrates the results for endocardial and epicardial cells. The optimized CRLP model was within physiological ranges for all CLs. Endocardial cells showed longer APs than epicardial cells for the new CRLP model as well as for all other published human ventricular

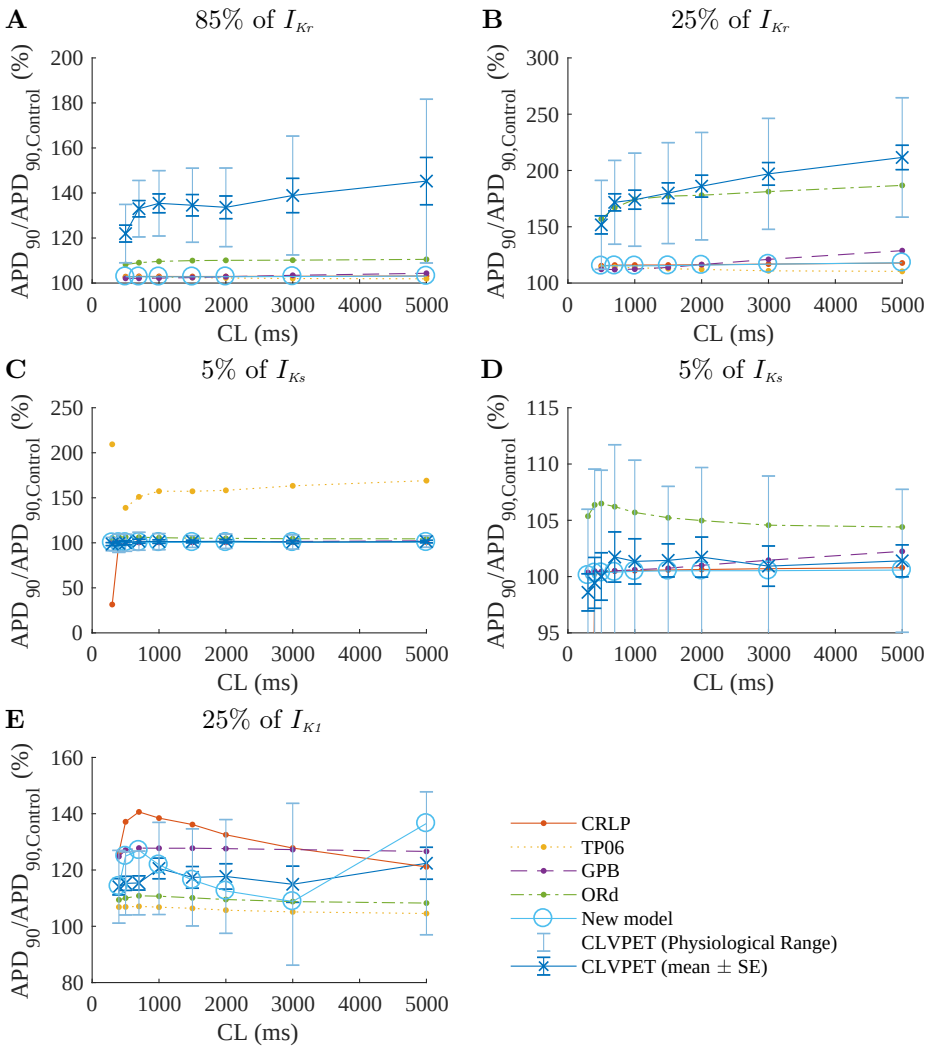

Figure 6.3: APD_{90} variation with CL under the same conditions of the CLVPET dataset following ionic current inhibitions: A) 15% I_{Kr} block; B) 70% I_{Kr} block; C) 95% I_{Ks} block; D) Zoomed graphic for 15% I_{Ks} block; E) 75% I_{K1} block.

Marker	Physiol.			This work	CRLP	ORd	GPB	TP06
	min	mean	max					
$[Na^+]_i$ (mM) [9]	0.00	18.58	39.27	9.04	10.06	6.92	8.10	8.06
Sys. $[Ca^{2+}]_i$ (μM) [10]	1.36	1.80	2.23	0.98	1.45	0.63	0.77	1.77
Dia. $[Ca^{2+}]_i$ (μM) [10]	0.11	0.26	0.40	0.11	0.12	0.09	0.10	0.13
Dia. $[Ca^{2+}]_i$ (μM) [11]	0.07	0.14	0.21	0.10	0.10	0.09	0.09	0.10

Table 6.9: Results of steady-state $[Na^+]_i$ and $[Ca^{2+}]_i$ for a CL of 1000 ms computed with the optimized CRLP model and other published human ventricular cell models.

cell models, including the initial CRLP model.

Intracellular sodium concentrations

In Table 6.9, steady-state $[Na^+]_i$ for a CL of 1000 ms is presented as calculated for different human ventricular cell models, including the optimized CRLP model introduced in this chapter. Figure 6.9 shows the variation in $[Na^+]_i$ for different CLs, compared with the physiological ranges measured in the experiments of [9]. All the tested AP models are within experimental ranges.

Intracellular calcium concentrations

In Table 6.9, steady-state diastolic and systolic $[Ca^{2+}]_i$ values for a CL of 1000 ms are presented as calculated for different human ventricular cell models, including the optimized CRLP model introduced in this chapter, while reproducing the conditions of the experiments described in [10, 11]. Whereas the diastolic $[Ca^{2+}]_i$ level in the optimized model was within the physiological ranges of both experimental studies, the systolic $[Ca^{2+}]_i$ level was somewhat below experimentally reported limits. Even if the optimization algorithm moved systolic $[Ca^{2+}]_i$ towards the physiological range, previous modifications introduced into the model had separated the simulated systolic level to such an extent that it was not possible for the optimization algorithm to completely move it into the expected range. Nevertheless, other commonly used human ventricular AP models present systolic $[Ca^{2+}]_i$ levels similar to those of the optimized CRLP model.

Figure 6.6 shows the variation in diastolic and systolic $[Ca^{2+}]_i$ levels for different CLs under the conditions of the experiments of [10]. Results are expressed as percentages with respect to the case when the pacing frequency was 1 Hz. For the comparison with the experimental data of [10], the optimized CRLP model is the only one with all simulated values lying within the experimentally reported limits.

Figure 6.7 shows variations in $[Ca^{2+}]_i$ characteristics for different CLs under the conditions of the experiments of Coppini *et al.* [11]. The difference between systolic and diastolic $[Ca^{2+}]_i$ levels was within experimental limits when computed for the optimized CRLP model (Figure 6.7.A), while all the other human ventricular cell models rendered results out of those limits. Variations in systolic $[Ca^{2+}]_i$, as well

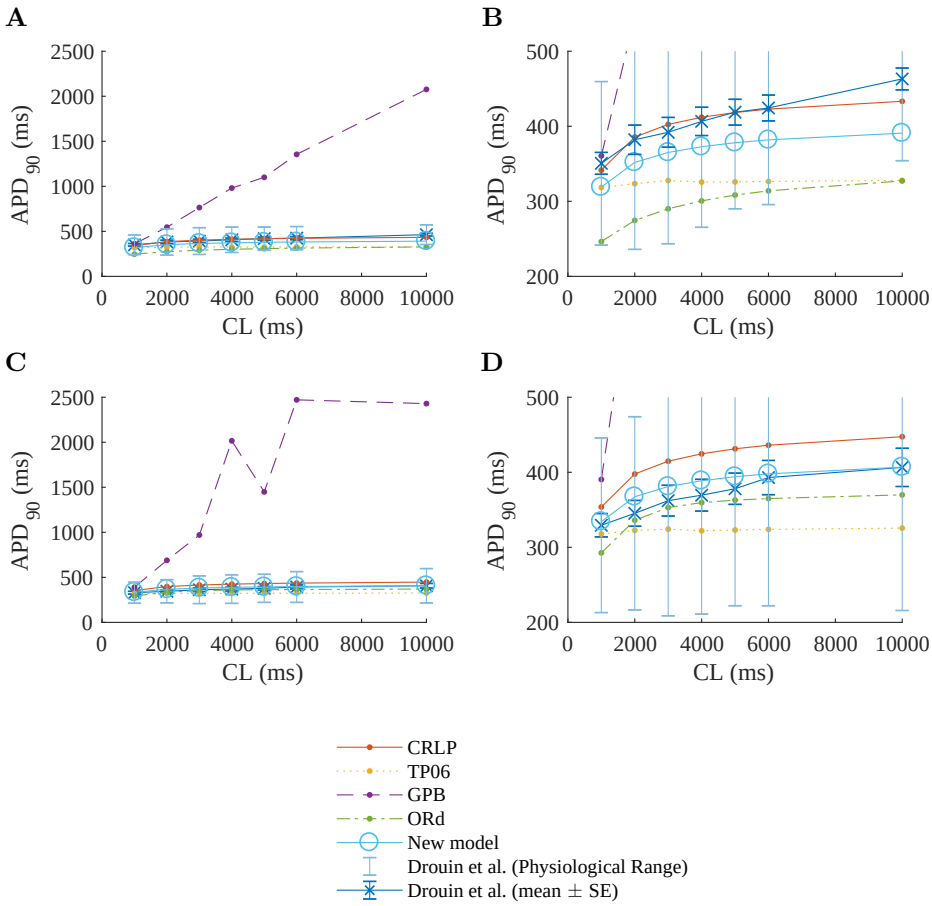

Figure 6.4: Simulations of the experiments by Drouin *et al.* [8]: A) APD_{90} variation with CL for epicardial cells. B) Zoomed version of the figure shown in A. C) APD_{90} variation with CL for endocardial cells. D) Zoomed version of the figure shown in C.

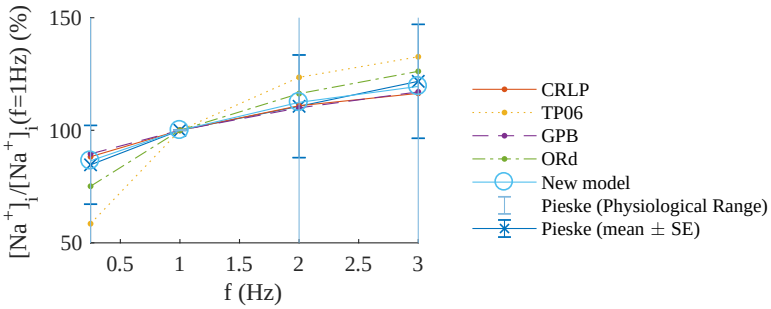

Figure 6.5: Variation in $[Na^+]_i$ under the same conditions of the experiments by Piekse *et al.* [9] for endocardial cells.

A

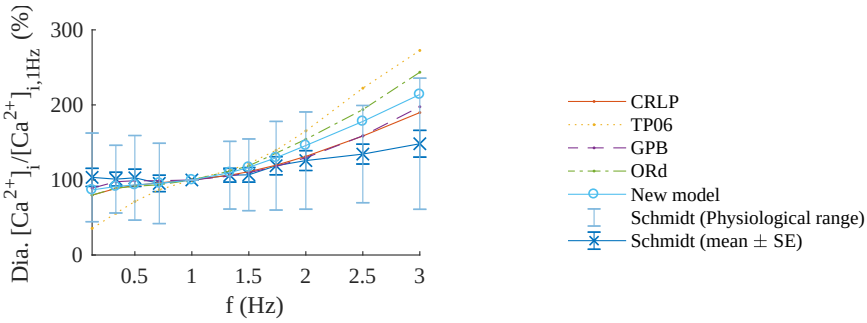

B

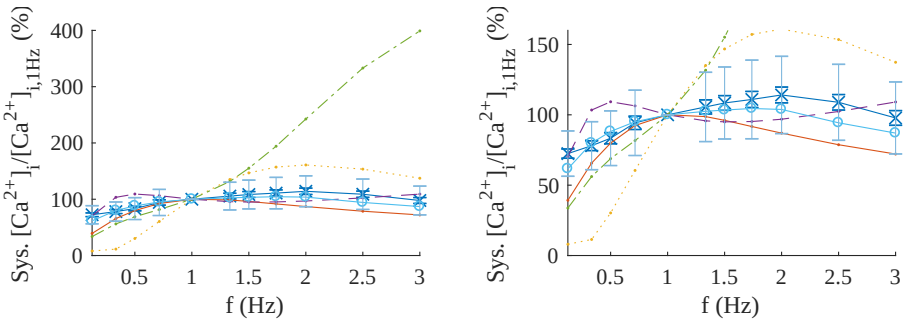

Figure 6.6: Variation in $[Ca^{2+}]_i$ under the same conditions of the experiments by Schmidt *et al.* [10]: A) Diastolic $[Ca^{2+}]_i$ normalized by the value when the frequency is 1Hz; B) Systolic $[Ca^{2+}]_i$ normalized by the value when the the frequency is 1Hz.

Marker	Physiol.			This work	CRLP	ORd	GPB	TP06
	min	mean	max					
$t_{90\%,1000\rightarrow600}$ (s)	58.5	119.5	180.5	260.5	314.5	254.2	157.9	299.9
$t_{90\%,600\rightarrow1000}$ (s)	75.0	243.0	411.0	265.3	346.4	352.2	184.4	350.1

Table 6.10: Results of APD adaptation to abrupt CL changes computed with all tested human ventricular models under the same conditions as in [13].

as time from $[Ca^{2+}]_i$ peak to 50% and 90% recovery, for different CLs was in very good agreement with experimental behavior (Figure 6.7.B, C and D).

APD adaptation to abrupt changes in the CL

Table 6.10 presents the results corresponding to APD adaptation to abrupt CL changes as calculated for all tested human ventricular cell models and the experiments of [13]. Only the GPB model rendered values of time for 90% adaptation lying within physiological ranges. The optimized CRLP model, despite being closer to the experimental limits than the initial CRLP model, only provided physiological results for CL increases, but not decreases, as happened with all other model except for the GPB model.

6.3.2 Model validation

Table 6.11 summarizes validation results for the optimized and the initial CRLP models. Under control conditions, both models rendered triangulation values out of physiological range, but upstroke velocity and V_{max} values within range. The effects of ionic current inhibitions over triangulation were practically within physiological range for both the new and the initial CRLP models. Only I_{K1} inhibition rendered results out of physiological range, particularly for the upstroke velocity and V_{max}. Of note, when I_{K1} was blocked in the optimized model, the ERP increased over 1000 ms and only out of two consecutive stimulations was able to propagate an AP.

6.4 Discussion

6.4.1 Model performance

The optimized CRLP model has been shown to produce a remarkably improved behavior with respect to the initial CRLP model when comparing simulated data with experimental evidences for a set of evaluated electrophysiological properties. A detailed discussion on this is presented in the following paragraphs, together with a comparison with other human ventricular cell models already published in the literature.

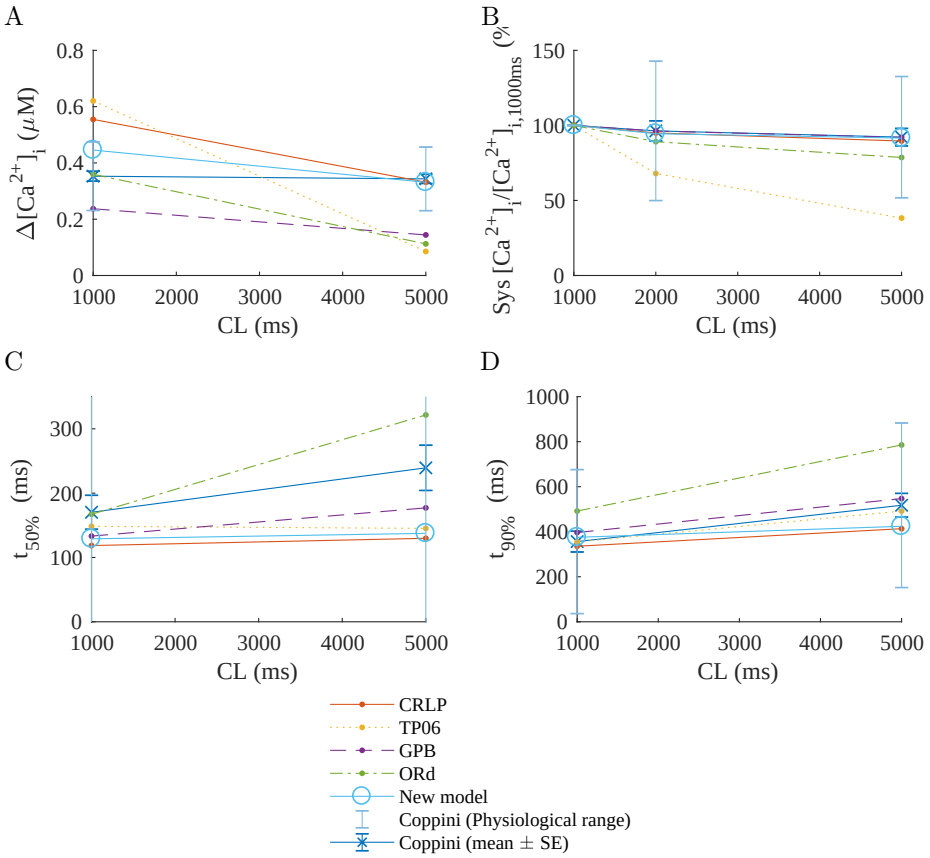

Figure 6.7: Variation in $[Ca^{2+}]_i$ characteristics under the same conditions of the experiments by Coppini *et al.* [11]: A) Difference between systolic and diastolic $[Ca^{2+}]_i$ levels as a function of CL; B) Systolic $[Ca^{2+}]_i$ for different CLs normalized by the value when CL is 1000 ms; C) Time from $[Ca^{2+}]_i$ peak to 50% as a function of CL; D) Time from $[Ca^{2+}]_i$ peak to 90% as a function of CL.

Blockage	Marker	Physiol. min	Physiol. mean	Physiol. max	This work	CRLP
Control	$Triangulation$ (ms)	44.6	65.2	85.8	137.9	111.1
	$Upstroke$ (mV/ms)	132.6	283.5	434.4	275.9	278.6
	V_{max} (mV)	15.7	28.0	40.3	25.1	27.4
75% I_{K1}	$\Delta Triangulation$ (%)	21.3	58.2	95.2	20.2	27.7
	$\Delta Upstroke$ (%)	-21.6	-5.6	10.4	-98.6	0.8
	ΔV_{max} (%)	-7.3	6.4	20.0	-69.3	-0.1
15% I_{Kr}	$\Delta Triangulation$ (%)	-3.5	66.6	136.8	4.5	0.8
	$\Delta Upstroke$ (%)	-37.0	-1.7	33.6	0.1	-0.7
	ΔV_{max} (%)	-44.8	-3.1	38.7	0.0	0.4
70% I_{Kr}	$\Delta Triangulation$ (%)	3.1	138.7	274.4	24.7	8.3
	$\Delta Upstroke$ (%)	-23.8	2.6	28.9	-1.5	1.9
	ΔV_{max} (%)	-25.7	-5.1	15.5	0.2	1.0
95% I_{Ks}	$\Delta Triangulation$ (%)	-9.6	2.4	14.4	0.2	2.3
	$\Delta Upstroke$ (%)	-13.3	-5.2	2.8	-0.1	-0.6
	ΔV_{max} (%)	-31.1	12.1	55.2	0.0	-7.1

Table 6.11: Validation results. Steady-state AP markers for a CL of 1000 ms calculated in tissue fibers simulated with the optimized and initial CRLP models.

Response to potassium current inhibitions

One of the limitations of the initial CRLP model was related to APD prolongation following potassium current inhibitions. Specifically, when the initial CRLP model was paced at low frequencies, I_{K1} inhibition prolonged the APD to a larger extent than experimentally observed. The optimization algorithm reduced the amount of APD prolongation induced by such inhibition and rendered percentages of APD change well within physiological ranges. On the other hand, the optimized CRLP model did not completely reproduce experimental evidences related to the effects of I_{K1} inhibition on resting membrane potential. This is due to the fact that the modifications introduced into the model before the optimization procedure (i.e. incorporation of $[K^+]_i$ dynamics and I_{CaL} current refinement) led to resting potentials further away from experimental data. While the optimization somewhat improved that behavior, this was not enough to provide resting membrane potential values lying within experimental limits. As a consequence, the ERP was extremely large and not all stimulations were able to propagate an AP in a simulated tissue fiber.

Following I_{Kr} inhibition, the optimized CRLP model led to APD prolongation values of lower magnitude than experimentally reported. To reach an APD prolongation of the same extent as in the experiments, the optimization algorithm employed to develop the new CRLP model was required to change some model parameters to a remarkably large extent as compared with the trust region of the algorithm. In the end, this effect was neglected by the algorithm. This can be

considered as a limitation of how the algorithm was applied by using initially the same trust region for all model conductances. More details on this limitation are discussed below (section 6.4.2).

APD dependence on CL

One limitation of the initial CRLP model, inherited from the GPB model, was the APD response to increasingly shorter CLs. Specifically, for increasingly shorter CLs below 500 ms, the APD increased rather than decreasing. For the optimized CRLP model, the APD decreased monotonically for increasingly shorter CLs, even if the slope of such a relationship was slightly lower than experimentally observed. APD dependence on CL was additionally investigated following ionic current inhbitions. The behavior of the optimized model was generally consistent with experimental data (see Figure 6.3). Nevertheless, there is still some room for improvement, particularly in regards of the relationship between APD and CL following I_{K1} inhibition.

Also, differences in the APD between endocardial and epicardial cells for different CLs were analyzed. The initial CRLP model proposed in this thesis was able to adequately replicate the experimental APD results reported by Drouin *et al.* [8] for epicardial cells, but it presented a significant error for endocardial cells. For the optimized model, epicardial cells presented APD values shorter than the original CRLP model while endocardial cells had APD values closer to the mean value of the experiments. While for all tested human ventricular cell models, APD values for endocardial cells were longer than for epicardial cells, Drouin *et al.* showed no statistically differences in the APD values for both celly types, even being slightly larger for epicardial cells. The optimized CRLP model rendered APD differences between both cell types lower than the initial CRLP model and therefore closer to experimental observations.

Intracellular sodium and calcium concentrations

$[Na^+]_i$ values present a large variation when measured in different experiments [9]. This results in a very wide physiological range for $[Na^+]_i$, with any concentration below 39.3 mM being considered as physiologically plausible. In the optimization algorithm applied to develop the new CRLP model, when a given electrophysiological marker presents large experimental variance, its weight in the objective function is reduced. It is thus not surprising that $[Na^+]_i$ values in the optimized CRLP model are further away from mean experimentally reported value than the initial CRLP model, but in any case of very similar magnitude than the values reported for other human ventricular cell models of the literature.

Regarding $[Ca^{2+}]_i$ values, calculated under the same conditions as in [10], the optimized CRLP model presented systolic values lower than the first version of the model and slightly out of physiological range. This can be attributed to the I_{CaL} current refinement proposed in chapter 5, which the optimization algorithm was not completely able to compensate for. Nevertheless, similar results were obtained with other common models, like the ORd and GPB models. On the other hand, the

optimized CRLP model was the only model able to replicate experimental behavior regarding changes in $[Ca^{2+}]_i$ characteristics with the frequency of stimulation. Specifically, when compared with the experimental data by Coppini *et al.* [11], the new CRLP model showed physiological values for systolic and diastolic $[Ca^{2+}]_i$ markers as well as for time from $[Ca^{2+}]_i$ peak to 90% recovery, with only time from $[Ca^{2+}]_i$ peak to 90% recovery presenting a less marked changed with pacing frequency than the mean experimental value.

APD adaptation to abrupt CL changes

The adaptation of ventricular repolarization duration to abrupt changes in CL has been proposed as an arrhythmic risk marker [81]. The adaptation time was considered in the development of the new CRLP model. The main limitation of including this marker in the optimization algorithm is that there are not systematic studies analyzing it. In [95], ten different combinations of CLs were studied but none of these combinations was used more than once in the experiments. Only in [13], two experiments conducted under the same experimental conditions were reported that served to define a physiological range for the adaptation time in the process of model development. Large differences were found between results simulated with the initial CRLP model and the experimental range. Although the optimized CRLP model rendered results still out of the experimental limits, the optimization algorithm allowed reducing the difference between the model and the mean experimental value by more than 27%. The difference between simulated and maximal experimental value of the adapation time was reduced by as much as 40.3% with respect to the initial CRLP model.

6.4.2 Optimization algorithm

The following paragraphs contain a discussion on a number of aspects of the optimization algorithm used in the development of the CRLP model.

Initialization

In this work, we used an initial trust region with the same radius for each ionic conductance aimed to be updated by the optimization algorithm. After optimization, some currents were shown to contribute to AP changes to a lower extent than expected based on experimental evidences. In particular, the effect of I_{Kr} block on the APD was remarkably lower than in available experimental data, and, while such an effect was within physiological range, the dependence with pacing frequency shown in the experiments was not reproduced by the model. Also, the increase in I_{Ks} conductance required for this conductance to have notable effects on the AP was far away from the range the algorithm considered. This could be explained by: i) all the radius are reduced when one electrophysiological marker is out of range; ii) the effect of variations in I_{Ks} conductance over the tested electrophysiological markers was very small, so the algorithm did not consider updating this variable.

A different strategy could be used to initialize the trust region. One possibility could be to initialize the trust region with a different radius for each variable to be updated by the optimization algorithm. The radius for each variable could, for instance, be made inversely proportional to the greatest sensitivity of the evaluated electrophysiological markers and directly proportional to the experimental variance of the marker with the largest sensitivity. Based on this or other ideas, future studies should address how to specifically define radius for each variable.

Objective function

In the optimization algorithm used in chapter 3 for incorporation of $[K^+]_i$ dynamics into the original CRLP model, the objective function was just defined by the integral of the total potassium current during a cardiac cycle. In this chapter, the objective function is defined as a sum of mulitple error functions reflecting differences between simulated and experimental data in relation to a number of electrophysiological properties. The weight assigned to each of the errors corresponding to different properties is challenging and has a large impact in the results obtained from the optimization procedure. In this chapter all errors were weighted by the same amount. As a consequence, if a specific AP phase is represented by several evaluated electrophysiological properties, the algorithm could be biased to fit that phase. Future studies could address how to weight the different error functions composing the objective function in such a way that the model renders improved results according to the criteria of interest.

The use of electrophysiological markers as part of an objective function to be optimized for cardiac AP model development has been explored in [123]. In that study the authors defined the objective function to be zero when the distance between the marker and the mean value is lower than the experimental standard error of the mean and to increase linearly out of this region. Limitations of this approach include the fact that several combinations of parameters could result in the same value of the objective function or that improvements in one marker that is close to physiological range could lead to a major deterioration in the value of other markers completely out of physiological range, as the error increases linearly. For this reason, in this chapter a minimization function was defined that assigns an error value different from zero when the marker is within physiological range and penalizes much more the fact of being out of range by using a quadratic function.

6.4.3 Validation

The main goal of the validation performed in this chapter was to evaluate that the model did not show abnormal behavior for electrophysiological properties not considered during the optimization phase. Future studies could extend validation to incorporate other properties or to standardize a benchmark for the evaluation of human ventricular models. This could help to improve our current understanding on the benefits and limitations of any proposed model and to improve model selection according to the specific problem to be investigated.

6.5 Conclusions

In this chapter, an optimization algorithm was proposed to update the CRLP model developed in previous chapters. The optimized CRLP model improved replication of electrophysiological properties measured experimentally. Simulated results of those properties were either within physiologically plausible ranges or at least closer to them than before the optimization. A comparison with other published human ventricular cell models was established.

Chapter 7

Conclusions and Future Work

7.1 Conclusions

In this thesis different techniques to improve the development and validation of cardiac electrophysiological models have been proposed and analyzed. Based on the increase in computational power, new strategies to reduce the number of hypothesis and/or assumptions when building an electrophysiological model were considered. The major conclusions of the thesis are summarized in the following.

7.1.1 Identification of major issues in electrophysiological model development and validation

The development and validation of a computational electrophysiological model is a complex process associated with a number of difficulties. Two main issues are: i) the limited amount of experimental data the model can be based; ii) the way in which information is extracted from experiments and used to build the models. Regarding the former, a reduced number of experimental samples and the possibly limited information available from those experimental samples may hamper the evaluation of cell and tissue electrical activities for some range of parameters or under specific conditions. In the case of human samples, this limitation is even more accentuated, as there are really few available sets of data, and even more so from healthy human hearts. Importantly, the experimental protocols applied over those data may not always provide the information necessary for model development or validation. Regarding the second limitation, the difficulty in obtaining valuable insights from experimental studies may be due to the interaction between different elements underlying cell or tissue electrical responses. For instance, it may be challenging to investigate specific characteristics of a particular ionic current, as in some cases it

may not be possible to completely isolate the effects of other currents. Or it may happen that interactions between activation and/or inactivation gating processes for a given ionic current hinders the evaluation of specific gating characteristics necessary to theoretically formulate ionic current expressions in the models.

The above described issues make it complex to develop and validate a computational electrophysiological model that can be used to reproduce experimental evidences at different scales. In this thesis, a number of techniques were proposed to minimize the impact of the above described issues and, when possible, to integrate them in the process of development and validation of the model. Of note, throughout the thesis the importance of considering the interactions between model components and spatio-temporal scales has been pointed out when evaluating simulated data. This involves the possibility of considering processes covering from ion channel characteristics and diffusion of ions in the cell up to the propagation of the electric wave in excitable cardiac tissue. Since sometimes it may not be possible to consider all model components at the same time due to computational restrictions, in this thesis the focus has been on showing when specific elements should necessarily be considered, when it is possible to simplify the model and when it may be convenient to consider only part of the available information. In particular, this thesis has highlighted the benefits of using *in silico* simulations of experimental protocols to evaluate all those possibilities, as long as *in silico* simulations replicate as closely as possible the conditions of the experiments against which the simulated data is compared. This is further discussed in the next section.

7.1.2 New techniques for improved model development and validation

Throughout this thesis, the uncertainty associated with experimental data used to build computational models has been analyzed and, when possible, integrated into the process of model development. Such an uncertainty is in relation to the large variance commonly observed over different experiments, the relatively low number of conducted experiments or the limited amount of cells/tissues used for characterization of the electrical properties of interest.

In some cases there is an additional intrinsic difficulty in obtaining experimental measures of specific model parameters or in extracting such measures from the recorded data. This would, for instance, apply to the evaluation of some gating characteristics of ionic currents. In this thesis, *in silico* simulation of experimental protocols is proposed to get indirect estimates of such characteristics. By using *in silico* simulation of experimental protocols, together with the application of other techniques, a model providing an improved representation of experimental observations was built. Even if this technique turns out to be very useful for identification of model ionic gating parameters, it becomes necessary to validate the model with the new ionic expression as a whole so as to assess possible effects at higher scales.

Another important challenge in computational model development and validation regards the identification of ionic current conductances. When investigating cardiac diseases or assessing the effects of drugs, accurate evaluation of the contri-

bution of each ionic current to the AP is very relevant. If a model with a highly unbalanced representation of ionic currents is used, the simulation of the effects of a drug or a disease that block one or several currents may provide totally meaningless results. As discussed throughout this thesis, it is possible to accurately estimate ionic current conductances by using techniques such as those proposed in this study. In particular, formulation of an optimization problem that integrates a number of relevant electrophysiological properties together with available experimental data can to a great extent serve to the purpose of identifying physiologically plausible conductance values that render the model suitable for investigation of cardiac diseases or drug effects. Since optimization solving is highly computationally demanding, approaches based on response surface approximations were proposed in this thesis, which allowed model optimization in a reasonable computational time. Also, such developed approaches are amenable to parallel computing, which means the time required to solve the optimization problem can be reduced by using computational architectures specifically designed to parallel programs, such as GPUs or high-throughput computer clusters.

Based on the above, one of the main conclusions of this thesis is the need for considering as many model elements as possible in both the development and validation processes. In some cases, the experimental data measured to study the behavior of a given ionic current are affected by other ionic currents, intracellular calcium handling or others factors, which may preclude investigation of certain cell characteristics without accounting for those other influences. A good practice can thus consist in developing/adjusting the model, or a part of it, by considering as many involved elements as possible, while trying to replicate as faithfully as possible the conditions underlying the experiments that are aimed to be reproduced.

In some cases the conditions or protocols of those experiments highly differ from one to another study, yet more in the case of data recorded at different laboratories. Although this might be seen as a limitation for model development and validation, the techniques proposed in this thesis have shown the capacity to integrate all those data no matter how different the experimental protocols underlying them are. An important aspect in the description of an experimental protocol is the value of the ion concentrations in the bath solution. Sometimes this aspect has been overlooked, but it can be relevant when accounting for data recorded under various conditions and a single in silico AP model is expected to reproduce different available evidences.

7.2 Future work

Some future research lines identified during the development of this thesis are:

- *Extend the proposed methodologies to populations of models representing electrophysiological variability*: In this thesis, an average computational AP model was considered. This average model is representative of the mean experimentally observed behavior in human ventricular cells, but, by definition, it does not aim to represent the well known cell-to-cell variability present in biological data, in general, and electrophysiological data, in particiular. All

the approaches proposed in this thesis for the development and validation of a computational electrophysiological model could be extended to consider a population of models aimed at covering the variability reported for different cells in experiemntal studies.

- *Application of the proposed methodologies to other human ventricular electrophysiological models*: Published human ventricular AP models present widely varied formulations of ionic currents, calcium handling and others. Whereas those models faithfully reproduce experimental observations regarding some electrophysiological properties, they fail to represent other properties, as highlighted in this thesis. The optimization methodologies presented in this thesis, and in particular those described in chapter 6, could be applied onto those other human ventricular AP models to improve their overall performance. Also, if the definition of a specific model component wants to be adjusted for one of those models, the optimization methodology could be as well applied to guarantee accurate representation of the corresponding experimental data following model adjustment.

- *Definition of a benchmark for validation of electrophysiological models*: Based on the developments presented in this thesis, a benchmark could be established to evaluate human ventricular AP models and identify those satisfying the criteria of interest. This benchmark could incorporate tests from the ionic to the tissue level, involving different stimulation protocols and considering different measurement conditions. This could be applied not only to average AP models, like the TP06, GPB, ORd or CRLP models, but also to models being part of populations generated based on those other AP models. For each research question to be investigated, the use of a set of selected models defined based on such a developed benchmark could be of major help.

- *Improved optimization solving by adapting the trust region radius to each estimated variable*: As indicated in chapter 6, the radius of the trust region would benefit from a definition adapted to the individual characteristics of each variable. Without such an adapted definition, some model variables end up being barely modified during the optimization solving due to the way the impact on the considered electrophysiological markers is accounted for. Future strategies could be investigated that allowed including variable normalization in the optimization to improve overall efficiency of the optimization algorithm.

- *Further update of model components*: In this thesis a response-surface-based algorithm was used for optimization of ionic current conductances. Also, improved definition of I_{CaL} voltage-dependent inactivation gates was addressed. The methodologies presented in this thesis could be extended to update other model components.

- *Development of new stimulation pulse*: In chapter 4, a comparison of a number of electrophysiological properties measured in simulated cells and tissues was provided. As described in that chapter, some properties presented highly

different values depending on the evaluated spatial scales. Since in some studies the computational cost of conducting tissue simulations may be a limiting factor, definition of stimulation protocols that rendered simulated results similar to those measured in tissue while in fact simulating single cells would be of major advantage. Those stimulation protocols could, for instance, be based on the stimulation that one cell receives from its neighbors in the tissue (electrotonic coupling). In addition, the influence of different ionic currents on the propagation of the electric wave should could be accounted for in the definition of those stimulation protocols.

Appendix

Appendix A

Publications derived from this Thesis

A.1 Publications in Journal Articles

- **J. Carro**, J. F. Rodríguez, P. Laguna, E. Pueyo. *A Human Ventricular Cell Model for Investigation of Cardiac Arrhythmias under Hyperkalaemic Conditions*. Phil Trans A, n. 639, pp. 4205 - 4232 (Nov, 2011). doi:10.1098/rsta.2011.0127

- **J. Carro**, J. F. Rodríguez-Matas, V. Monasterio, and E. Pueyo. *Limitations in electrophysiological model development and validation caused by differences between simulations and experimental protocols*. Progress in Biophysics and Molecular Biology, v. 129, pp. 53-64, 2017. doi: 10.1016/j.pbiomolbio.2016.11.006

- **J. Carro**, J. F. Rodríguez, E. Pueyo. *A response surface optimization approach to adjust ionic current conductances of cardiac electrophysiological models. Application to the study of potassium level changes*. PLOS One (Acepted). doi: 10.1371/journal.pone.0204411

- **J. Carro**, J. F. Rodríguez, E. Pueyo. *A Human Ventricular Electrophysiological Model with Improved Description of Experimental Behavior*. (In preparation).

A.2 Publications in Conference Proceedings

- **J. Carro**, J. F. Rodríguez Matas, P. Laguna, E. Pueyo. *Analysis and Improvement of a Human Ventricular Cell Model for Investigation of Cardiac*

Arrhythmias. XXXVII International Conference on Computers in Cardiology, Belfast (UK), pp. 817 - 820 (Sep, 2010).

- J. F. Rodríguez Matas, **J. Carro**, E. Pueyo, K. Burrage, B. Rodríguez. *Impact of Multiple Ionic Changes in Arrhythmic Risk Biomarkers in Human Ventricular Electrophysiology*. Biophysical Society 56^{th} Annual Meeting, San Diego (USA), v. 102, p. 543a (Ene, 2012). doi:10.1016/j.bpj.2011.11.2965

- **J. Carro**, J. F. Rodríguez Matas, E. Pueyo. *In Silico Simulations of Experimental Protocols for Cardiac Modeling*. XXXVI Annual International Conference of the IEEE Engineering in Medicine and Biology Society, Chicago (USA), pp. 5695 - 5698 (Aug, 2014).

- **J. Carro**, J. F. Rodríguez Matas, and E. Pueyo, *A Methodology to Improve Human Ventricular Models for the Investigation of Cardiac Arrhythmias*, in 61^{st} Annual Meeting of the Biophysical Society, New Orleans, USA, 2017.

A.3 Other Conferences

- **J. Carro**, J. F. Rodríguez Matas, and E. Pueyo, *A Response Surface Optimization approach to adjust ionic current conductances of cardiac electrophysiological models*, in Gordon Research Conference in Cardiac Arrhythmia Mechanisms, Lucca, Italy, 2015.

- **J. Carro**, J. F. Rodríguez Matas, and E. Pueyo, *Multiscale Methods for Definition of Ionic Variables in Electrophysiological Models*, in European Medical and Biological Engineering Conference (EMBEC) Tampere, Finland, 2017.

Appendix B

Description of the First Model

B.1 Model Parameters

B.1.1 Physical Constants

Name	Value	Units
R	8314	$J/(mol \cdot K)$
$Frdy$	96485	C/mol
T	310	K
$FoRT$	$Frdy/(R \cdot T)$	mV^{-1}
C_{mem}	$1.381 \cdot 10^{-10}$	F

B.1.2 Enviromental Parameters

Name	Value	Units
$Length_{cell}$	$100 \cdot 10^{-5}$	dm
$Radius_{cell}$	$10.25 \cdot 10^{-5}$	dm
V_{cell}	$\pi \cdot Radius_{cell}^2 \cdot Length_{cell}$	L
V_{myo}	$0.65 \cdot V_{cell}$	L
V_{sr}	$0.035 \cdot V_{cell}$	L
V_{sl}	$0.02 \cdot V_{cell}$	L
V_{junc}	$5.39 \cdot 10^{-4} \cdot V_{cell}$	L
$J_{Ca_{junc,sl}}$	$8.2413 \cdot 10^{-13}$	L/ms
$J_{Ca_{sl,myo}}$	$3.7243 \cdot 10^{-12}$	L/ms
$J_{Na_{junc,sl}}$	$1.8313 \cdot 10^{-14}$	L/ms
$J_{Na_{sl,myo}}$	$1.6386 \cdot 10^{-12}$	L/ms

B.1.3 Fractional Currents

Name	Value	Units
F_{junc}	0.11	$[-]$
F_{sl}	$1 - F_{junc}$	$[-]$
$F_{junc_{Ca_L}}$	0.9	$[-]$
$F_{sl_{Ca_L}}$	$1 - F_{junc_{Ca_L}}$	$[-]$

B.1.4 Ion Concentrations

Name	Value	Units
K_i	138	mM
K_o	5.4	mM
Cl_i	15	mM
Cl_o	150	mM
Ca_o	1.8	mM
Mg_i	1	mM
Na_o	140	mM

B.1.5 Sodium Transport

Name	Value	Units
G_{Na}	18.86	$mS/\mu F$
$G_{Na,bk}$	$0.597 \cdot 10^{-3}$	$mS/\mu F$
$\bar{I}_{NaK}$	0.99	pA/pF
Km_{Ko}	1.5	mM
Km_{Naip}	11	mM

B.1.6 Potassium Currents

Name	Value	Units
p_{NaK}	$1.833 \cdot 10^{-2}$	$[-]$
G_{K1}	$5.7153 \cdot 10^{-1}$	$mS/\mu F$
G_{Kp}	$2 \cdot 10^{-3}$	$mS/\mu F$
G_{Kr}	$3.5 \cdot 10^{-2}$	$mS/\mu F$
$G_{Ks_{junc}}$	$3.5 \cdot 10^{-3}$	$mS/\mu F$
$G_{Ks_{sl}}$	$3.5 \cdot 10^{-3}$	$mS/\mu F$
$G_{to_f,EPI}$	$1.144 \cdot 10^{-1}$	$mS/\mu F$
$G_{to_s,EPI}$	$1.56 \cdot 10^{-2}$	$mS/\mu F$
$G_{to_f,ENDO}$	$1.404 \cdot 10^{-3}$	$mS/\mu F$
$G_{to_s,ENDO}$	$3.7596 \cdot 10^{-2}$	$mS/\mu F$

B.1.7 Chlorine currents

Name	Value	Units
G_{ClCa}	0.054813	$mS/\mu F$
$G_{Cl,bk}$	$9 \cdot 10^{-3}$	$mS/\mu F$
Kd_{ClCa}	$100 \cdot 10^{-3}$	mM

B.1.8 Calcium Transport

Name	Value	Units
p_{Ca}	$1.9887 \cdot 10^{-4}$	$L/(F \cdot ms)$
p_K	$5.4675 \cdot 10^{-8}$	$L/(F \cdot ms)$
p_{Na}	$3.0375 \cdot 10^{-9}$	$L/(F \cdot ms)$
$\bar{I}_{ncx}$	4.5	pA/pF
Km_{Ca_i}	$3.59 \cdot 10^{-3}$	mM
Km_{Ca_o}	1.3	mM
Km_{Na_i}	12.29	mM
Km_{Na_o}	87.5	mM
k_{sat}	0.32	$[-]$
nu	0.27	$[-]$
Kd_{act}	$0.15 \cdot 10^{-3}$	mM
$\bar{I}_{PMCA}$	0.0673	pA/pF
Km_{pCa}	$0.5 \cdot 10^{-3}$	mM
$G_{Ca,bk}$	$5.513 \cdot 10^{-4}$	$mS/\mu F$

B.1.9 SR Calcium Fluxes

Name	Value	Units
$V_{max_{SR_{CaP}}}$	$5.3114 \cdot 10^{-3}$	mM/ms
$ec50_{SR}$	0.45	mM
$hill_{SR_{CaP}}$	1.787	$[-]$
ki_{Ca}	0.5	$mM^{-1} \cdot mS^{-1}$
ki_m	0.005	mS^{-1}
ko_{Ca}	10	$mM^{-2} \cdot ms^{-1}$
ko_m	0.06	mS^{-1}
ks	25	mS^{-1}
Km_f	$0.246 \cdot 10^{-3}$	mM
Km_r	1.7	mM
Max_{SR}	15	$[-]$
Min_{SR}	1	$[-]$

B.1.10 Buffering

Name	Value	Units
$B_{max_{CaM}}$	$24 \cdot 10^{-3}$	mM
$B_{max_{SR}}$	$17.1 \cdot 10^{-3}$	mM
$B_{max_{TnC_{high}}}$	$140 \cdot 10^{-3}$	mM
$B_{max_{TnC_{low}}}$	$70 \cdot 10^{-3}$	mM
$B_{max_{myosin}}$	$140 \cdot 10^{-3}$	mM
$B_{max_{Na_j}}$	7.561	mM
$B_{max_{Na_{sl}}}$	1.65	mM
$B_{max_{SL_{low_{sl}}}}$	$37.4 \cdot 10^{-3} \cdot V_{myo}/V_{sl}$	mM
$B_{max_{SL_{low_j}}}$	$4.6 \cdot 10^{-4} \cdot V_{myo}/V_{junc}$	mM
$B_{max_{SL_{high_{sl}}}}$	$13.4 \cdot 10^{-3} \cdot V_{myo}/V_{sl}$	mM
$B_{max_{SL_{high_j}}}$	$1.65 \cdot 10^{-4} \cdot V_{myo}/V_{junc}$	mM
$B_{max_{csqn}}$	$140 \cdot 10^{-3} \cdot V_{myo}/V_{sr}$	mM
$k_{off_{csqn}}$	65	mS^{-1}
$k_{off_{CaM}}$	$238 \cdot 10^{-3}$	mS^{-1}
$k_{off_{SR}}$	$60 \cdot 10^{-3}$	mS^{-1}
$k_{off_{TnC_{h_{Ca}}}}$	$0.032 \cdot 10^{-3}$	mS^{-1}
$k_{off_{TnC_{h_{Mg}}}}$	$3.33 \cdot 10^{-3}$	mS^{-1}
$k_{off_{TnC_l}}$	$19.6 \cdot 10^{-3}$	mS^{-1}
$k_{off_{myo_{Ca}}}$	$0.46 \cdot 10^{-3}$	mS^{-1}
$k_{off_{myo_{Mg}}}$	$0.057 \cdot 10^{-3}$	mS^{-1}
$k_{off_{sl_h}}$	$30 \cdot 10^{-3}$	mS^{-1}
$k_{off_{sl_l}}$	1.3	mS^{-1}
$k_{off_{Na}}$	$1 \cdot 10^{-3}$	mS^{-1}
$k_{on_{csqn}}$	100	$mM^{-1} \cdot mS^{-1}$
$k_{on_{CaM}}$	34	$mM^{-1} \cdot mS^{-1}$
$k_{on_{SR}}$	100	$mM^{-1} \cdot mS^{-1}$
$k_{on_{TnC_{h_{Ca}}}}$	2.37	$mM^{-1} \cdot mS^{-1}$
$k_{on_{TnC_{h_{Mg}}}}$	$3 \cdot 10^{-3}$	$mM^{-1} \cdot mS^{-1}$
$k_{on_{TnC_l}}$	32.7	$mM^{-1} \cdot mS^{-1}$
$k_{on_{myo_{Ca}}}$	13.8	$mM^{-1} \cdot mS^{-1}$
$k_{on_{myo_{Mg}}}$	0.0157	$mM^{-1} \cdot mS^{-1}$
$k_{on_{sl_h}}$	100	$mM^{-1} \cdot mS^{-1}$
$k_{on_{sl_l}}$	100	$mM^{-1} \cdot mS^{-1}$
$k_{on_{Na}}$	$0.1 \cdot 10^{-3}$	$mM^{-1} \cdot mS^{-1}$

B.2 Model Equations

B.2.1 Nerst Potentials

$$
\begin{aligned}
E_{Na_{junc}} &= \frac{1}{FoRT} \cdot \ln \frac{Na_o}{Na_j} \\
E_{Na_{sl}} &= \frac{1}{FoRT} \cdot \ln \frac{Na_o}{Na_{sl}} \\
E_{Ks} &= \frac{1}{FoRT} \cdot \ln \frac{K_o + p_{NaK} \cdot Na_o}{K_i + p_{NaK} \cdot Na_i} \\
E_K &= \frac{1}{FoRT} \cdot \ln \frac{K_o}{K_i} \\
E_{Ca_{junc}} &= \frac{1}{2 \cdot FoRT} \cdot \ln \frac{Ca_o}{Ca_j} \\
E_{Ca_{sl}} &= \frac{1}{2 \cdot FoRT} \cdot \ln \frac{Ca_o}{Ca_{sl}} \\
E_{Cl} &= \frac{1}{FoRT} \cdot \ln \frac{Cl_i}{Cl_o}
\end{aligned}
$$

B.2.2 I_{Na}:Fast Sodium Current

$$
\begin{aligned}
m_{ss} &= \frac{1}{\left(1 + e^{\frac{-(56.86+V)}{9.03}}\right)^2} \\
\tau_m &= 0.1292 \cdot e^{-\left(\frac{V+45.79}{15.54}\right)^2} + 0.06487 \cdot e^{-\left(\frac{V-4.823}{51.12}\right)^2} \\
\frac{\mathrm{d}m}{\mathrm{d}t} &= \frac{m_{ss} - m}{\tau_m}
\end{aligned}
$$

$$
\begin{aligned}
a_h =& \begin{cases} 0 & \text{if } V \geq -40 \\ 0.057 \cdot e^{\frac{-(V+80)}{6.8}} & \text{otherwise} \end{cases} \\
b_h =& \begin{cases} \frac{5.9231}{1+e^{\frac{-(V+10.66)}{11.1}}} & \text{if } V \geq -40 \\ 2.7 \cdot e^{0.079 \cdot V} + 3.1 \cdot 10^5 \cdot e^{0.3485 \cdot V} & \text{otherwise} \end{cases} \\
\tau_h =& \frac{1}{a_h + b_h} \\
h_{ss} =& \frac{1}{\left(1 + e^{\frac{V+71.55}{7.43}}\right)^2} \\
\frac{\mathrm{d}h}{\mathrm{d}t} =& \frac{h_{ss} - h}{\tau_h}
\end{aligned}
$$

$$
\begin{aligned}
a_j =& \begin{cases} 0 & \text{if } V \geq -40 \\ \frac{\left(-2.5428 \cdot 10^4 \cdot e^{0.2444 \cdot V} - 6.948 \cdot 10^{-6} \cdot e^{-0.04391 \cdot V}\right) \cdot (V+37.78)}{1+e^{0.311 \cdot (V+79.23)}} & \text{otherwise} \end{cases} \\
b_j =& \begin{cases} \frac{0.6 \cdot e^{0.057 \cdot V}}{1+e^{-0.1 \cdot (V+32)}} & \text{if } V \geq -40 \\ \frac{0.02424 \cdot e^{-0.01052 \cdot V}}{1+e^{-0.1378 \cdot (V+40.14)}} & \text{otherwise} \end{cases} \\
\tau_j =& \frac{1}{a_j + b_j} \\
j_{ss} =& \frac{1}{\left(1 + e^{\frac{V+71.55}{7.43}}\right)^2} \\
\frac{\mathrm{d}j}{\mathrm{d}t} =& \frac{j_{ss} - j}{\tau_j}
\end{aligned}
$$

$$
\begin{aligned}
I_{Najunc} =& F_{junc} \cdot G_{Na} \cdot m^3 \cdot h \cdot j \cdot \left(V - E_{Najunc}\right) \\
I_{Nasl} =& F_{sl} \cdot G_{Na} \cdot m^3 \cdot h \cdot j \cdot (V - E_{Nasl}) \\
I_{Na} =& I_{Najunc} + I_{Nasl}
\end{aligned}
$$

B.2.3 $I_{Na,bk}$: Background Sodium Current

$$
\begin{aligned}
I_{Na,bk_{junc}} =& F_{junc} \cdot G_{Na,bk} \cdot \left(V - E_{Najunc}\right) \\
I_{Na,bk_{sl}} =& F_{sl} \cdot G_{Na,bk} \cdot (V - E_{Nasl}) \\
I_{Na,bk} =& I_{Na,bk_{junc}} + I_{Na,bk_{sl}}
\end{aligned}
$$

B.2.4 I_{NaK}: Na-K Pump Current

$$
\begin{aligned}
\sigma =& \frac{e^{\frac{Na_o}{67.3}} - 1}{7} \\
f_{NaK} =& \frac{1}{1 + 0.1245 \cdot e^{-0.1 \cdot V \cdot FoRT} + 0.0365 \cdot \sigma \cdot e^{-V \cdot FoRT}} \\
I_{NaK_{junc}} =& \frac{F_{junc} \cdot \bar{I}_{NaK} \cdot f_{NaK} \cdot K_o}{\left(1 + \left(\frac{Km_{Naip}}{Na_j}\right)^4\right) \cdot (K_o + Km_{Ko})} \\
I_{NaK_{sl}} =& \frac{F_{sl} \cdot \bar{I}_{NaK} \cdot f_{NaK} \cdot K_o}{\left(1 + \left(\frac{Km_{Naip}}{Na_{sl}}\right)^4\right) \cdot (K_o + Km_{Ko})} \\
I_{NaK} =& I_{NaK_{junc}} + I_{NaK_{sl}}
\end{aligned}
$$

B.2.5 I_{Kr}: Rapidly Activating Potassium Current

$$
\begin{aligned}
x_{r_{ss}} =& \frac{1}{1 + e^{\frac{-(V+10)}{5}}} \\
\tau_{xr} =& \frac{3300}{\left(1 + e^{\frac{-22-V}{9}}\right) \cdot \left(1 + e^{\frac{V+11}{9}}\right)} + \frac{230}{1 + e^{\frac{V+40}{20}}} \\
\frac{\mathrm{d}x_{Kr}}{\mathrm{d}t} =& \frac{x_{r_{ss}} - x_{Kr}}{\tau_{xr}} \\
r_{Kr} =& \frac{1}{1 + e^{\frac{V+74}{24}}} \\
I_{Kr} =& G_{Kr} \cdot \sqrt{\frac{K_o}{5.4}} \cdot x_{Kr} \cdot r_{Kr} \cdot (V - E_K)
\end{aligned}
$$

B.2.6 I_{Ks}: Slowly Activating Potassium Current

$$
\begin{aligned}
x_{s_{ss}} =& \frac{1}{1 + e^{\frac{-(V+3.8)}{14.25}}} \\
\tau_{xs} =& \frac{990.1}{1 + e^{\frac{-(V+2.436)}{14.12}}} \\
\frac{\mathrm{d}x_{Ks}}{\mathrm{d}t} =& \frac{x_{s_{ss}} - x_{Ks}}{\tau_{xs}} \\
I_{Ksjunc} =& F_{junc} \cdot G_{Ksjunc} \cdot x_{Ks}^2 \cdot (V - E_{Ks}) \\
I_{Ks_{sl}} =& F_{sl} \cdot G_{Ks_{sl}} \cdot x_{Ks}^2 \cdot (V - E_{Ks}) \\
I_{Ks} =& I_{Ksjunc} + I_{Ks_{sl}}
\end{aligned}
$$

B.2.7 I_{Kp}: Plateau Potassium Current

$$
\begin{aligned}
kp_{Kp} =& \frac{1}{1+e^{7.488-\frac{V}{5.98}}} \\
I_{Kp} =& G_{Kp} \cdot kp_{Kp} \cdot (V - E_K)
\end{aligned}
$$

B.2.8 I_{to}: Transient Outward Potassium Current

$$
\begin{aligned}
x_{to_{ss}} =& \frac{1}{1+e^{\frac{-(V-19)}{13}}} \\
\tau_{x_{tos}} =& \frac{9}{1+e^{\frac{V+3}{15}}} + 0.5 \\
\frac{\mathrm{d}x_{to_s}}{\mathrm{d}t} =& \frac{x_{to_{ss}} - x_{to_s}}{\tau_{x_{tos}}} \\
y_{to_{ss}} =& \frac{1}{1+e^{\frac{V+19.5}{5}}} \\
\tau_{y_{tos}} =& \frac{800}{1+e^{\frac{V+60}{10}}} + 30 \\
\frac{\mathrm{d}y_{to_s}}{\mathrm{d}t} =& \frac{y_{to_{ss}} - y_{to_s}}{\tau_{y_{tos}}}
\end{aligned}
$$

$$
\begin{aligned}
\tau_{x_{tof}} =& 8.5 \cdot e^{-\left(\frac{V+45}{50}\right)^2} + 0.5 \\
\frac{\mathrm{d}x_{to_f}}{\mathrm{d}t} =& \frac{x_{to_{ss}} - x_{to_f}}{\tau_{x_{tof}}} \\
\tau_{y_{tof}} =& 85 \cdot e^{\frac{-(V+40)^2}{220}} + 7 \\
\frac{\mathrm{d}y_{to_f}}{\mathrm{d}t} =& \frac{y_{to_{ss}} - y_{to_f}}{\tau_{y_{tof}}}
\end{aligned}
$$

$$
\begin{aligned}
I_{to_s} =& G_{to_s} \cdot x_{to_s} \cdot y_{to_s} \cdot (V - E_K) \\
I_{to_f} =& G_{to_f} \cdot x_{to_f} \cdot y_{to_f} \cdot (V - E_K) \\
I_{to} =& I_{to_s} + I_{to_f}
\end{aligned}
$$

B.2.9 I_{K1}:Inward Rectifier Potassium Current

$$
\begin{aligned}
a_{K1} =& \frac{4.0938}{1+e^{0.12165\cdot(V-E_K-49.9344)}} \\
b_{K1} =& \frac{15.7197\cdot e^{0.06739\cdot(V-E_K-3.2571)}+e^{0.06175\cdot(V-E_K-594.31)}}{1+e^{-0.16285\cdot(V-E_K+14.2067)}} \\
K1_{ss} =& \frac{a_{K1}}{a_{K1}+b_{K1}} \\
I_{K1} =& G_{K1}\cdot\sqrt{\frac{K_o}{5.4}}\cdot K1_{ss}\cdot(V-E_K)
\end{aligned}
$$

B.2.10 I_{ClCa}: Calcium-Activated Chlorine Current

$$
\begin{aligned}
I_{ClCa_{junc}} =& \frac{F_{junc}\cdot G_{ClCa}}{1+\frac{Kd_{ClCa}}{Ca_j}}\cdot(V-E_{Cl}) \\
I_{ClCa_{sl}} =& \frac{F_{sl}\cdot G_{ClCa}}{1+\frac{Kd_{ClCa}}{Ca_{sl}}}\cdot(V-E_{Cl}) \\
I_{ClCa} =& I_{ClCa_{junc}}+I_{ClCa_{sl}}
\end{aligned}
$$

B.2.11 $I_{Cl,bk}$: Background Chlorine Current

$$
I_{Cl,bk} = G_{Cl,bk}\cdot(V-E_{Cl})
$$

B.2.12 I_{CaL}: L-type Calcium Current

Voltage-Dependent Activation Gate

$$
\begin{aligned}
d_{ss} =& \frac{1}{1+e^{\frac{-(V+5)}{6}}} \\
\alpha_d =& \frac{1.4}{1+e^{\frac{-35-V}{13}}}+0.25 \\
\beta_d =& \frac{1.4}{1+e^{\frac{V+5}{5}}} \\
\gamma_d =& \frac{1}{1+e^{\frac{50-V}{20}}} \\
\tau_d =& \alpha_d\cdot\beta_d+\gamma_d \\
\frac{\mathrm{d}d}{\mathrm{d}t} =& \frac{d_{ss}-d}{\tau_d}
\end{aligned}
$$

Voltage-Dependent Inactivation Gates

$$
\begin{aligned}
f_{ss} =& \frac{1}{1+e^{\frac{V+20}{7}}} \\
\alpha_f =& 1102.5 \cdot e^{-\left(\frac{V+27}{15}\right)^2} \\
\beta_f =& \frac{200}{1+e^{\frac{13-V}{10}}} \\
\gamma_f =& \frac{180}{1+e^{\frac{V+30}{10}}} + 20 \\
\tau_f =& \alpha_f + \beta_f + \gamma_f \\
\frac{\mathrm{d}f}{\mathrm{d}t} =& \frac{f_{ss} - f}{\tau_f}
\end{aligned}
$$

$$
\begin{aligned}
f_{2_{ss}} =& \frac{0.67}{1+e^{\frac{V+35}{7}}} + 0.33 \\
\alpha_{f_2} =& 300 \cdot e^{\frac{-(V+25)^2}{170}} \\
\beta_{f_2} =& \frac{31}{1+e^{\frac{25-V}{10}}} \\
\gamma_{f_2} =& \frac{16}{1+e^{\frac{V+30}{10}}} \\
\tau_{f_2} =& \alpha_{f_2} + \beta_{f_2} + \gamma_{f_2} \\
\frac{\mathrm{d}f_2}{\mathrm{d}t} =& \frac{f_{2_{ss}} - f_2}{\tau_{f_2}}
\end{aligned}
$$

Calcium-Dependent Inactivation Gates

$$
\begin{aligned}
\frac{\mathrm{d}f_{CaB_j}}{\mathrm{d}t} =& 1.7 \cdot Ca_j \cdot \left(1 - f_{CaB_j}\right) - 11.9 \cdot 10^{-3} \cdot f_{CaB_j} \\
\frac{\mathrm{d}f_{CaB_{sl}}}{\mathrm{d}t} =& 1.7 \cdot Ca_{sl} \cdot \left(1 - f_{CaB_{sl}}\right) - 11.9 \cdot 10^{-3} \cdot f_{CaB_{sl}}
\end{aligned}
$$

Currents

$$
\begin{aligned}
\bar{I}_{Ca_j} &= \frac{p_{Ca} \cdot V \cdot Frdy \cdot FoRT \cdot \left(Ca_j \cdot e^{2 \cdot V \cdot FoRT} - Ca_o\right)}{e^{2 \cdot V \cdot FoRT} - 1} \\
\bar{I}_{Ca_{sl}} &= \frac{p_{Ca} \cdot V \cdot Frdy \cdot FoRT \cdot \left(Ca_{sl} \cdot e^{2 \cdot V \cdot FoRT} - Ca_o\right)}{e^{2 \cdot V \cdot FoRT} - 1} \\
\bar{I}_{Na_j} &= \frac{p_{Na} \cdot V \cdot Frdy \cdot FoRT \cdot \left(Na_j \cdot e^{V \cdot FoRT} - Na_o\right)}{e^{V \cdot FoRT} - 1} \\
\bar{I}_{Na_{sl}} &= \frac{p_{Na} \cdot V \cdot Frdy \cdot FoRT \cdot \left(Na_{sl} \cdot e^{V \cdot FoRT} - Na_o\right)}{e^{V \cdot FoRT} - 1} \\
\bar{I}_K &= \frac{p_K \cdot V \cdot Frdy \cdot FoRT \cdot \left(K_i \cdot e^{V \cdot FoRT} - K_o\right)}{e^{V \cdot FoRT} - 1}
\end{aligned}
$$

$$
\begin{aligned}
I_{Ca_{junc}} &= Fjunc_{Ca_L} \cdot \bar{I}_{Ca_j} \cdot d \cdot f \cdot f_2 \cdot \left(1 - f_{CaB_j}\right) \\
I_{Ca_{sl}} &= Fsl_{Ca_L} \cdot \bar{I}_{Ca_{sl}} \cdot d \cdot f \cdot f_2 \cdot \left(1 - f_{CaB_{sl}}\right) \\
I_{CaNa_{junc}} &= Fjunc_{Ca_L} \cdot \bar{I}_{Na_j} \cdot d \cdot f \cdot f_2 \cdot \left(1 - f_{CaB_j}\right) \\
I_{CaNa_{sl}} &= Fsl_{Ca_L} \cdot \bar{I}_{Na_{sl}} \cdot d \cdot f \cdot f_2 \cdot \left(1 - f_{CaB_{sl}}\right) \\
I_{Ca_K} &= \bar{I}_K \cdot d \cdot f \cdot f_2 \cdot \left(Fjunc_{Ca_L} \cdot \left(1 - f_{CaB_j}\right) + Fsl_{Ca_L} \cdot \left(1 - f_{CaB_{sl}}\right)\right)
\end{aligned}
$$

$$
\begin{aligned}
I_{Ca} &= I_{Ca_{junc}} + I_{Ca_{sl}} \\
I_{Ca_{Na}} &= I_{CaNa_{junc}} + I_{CaNa_{sl}} \\
I_{CaL} &= I_{Ca} + I_{Ca_K} + I_{Ca_{Na}}
\end{aligned}
$$

B.2.13 I_{ncx}: Na-Ca Exchanger Current

$$
\begin{aligned}
Ka_{junc} =& \frac{1}{1+\left(\frac{Kd_{act}}{Ca_j}\right)^2} \\
Ka_{sl} =& \frac{1}{1+\left(\frac{Kd_{act}}{Ca_{sl}}\right)^2} \\
s1_{junc} =& e^{nu\cdot V\cdot FoRT}\cdot Na_j^3\cdot Ca_o \\
s1_{sl} =& e^{nu\cdot V\cdot FoRT}\cdot Na_{sl}^3\cdot Ca_o \\
s2_{junc} =& e^{(nu-1)\cdot V\cdot FoRT}\cdot Na_o^3\cdot Ca_j \\
s2_{sl} =& e^{(nu-1)\cdot V\cdot FoRT}\cdot Na_o^3\cdot Ca_{sl} \\
s3_{junc} =& Km_{Ca_i}\cdot Na_o^3\cdot\left(1+\left(\frac{Na_j}{Km_{Na_i}}\right)^3\right)+Km_{Na_o}^3\cdot Ca_j\cdot\left(1+\frac{Ca_j}{Km_{Ca_i}}\right) \\
& + Km_{Ca_o}\cdot Na_j^3+Na_j^3\cdot Ca_o+Na_o^3\cdot Ca_j \\
s3_{sl} =& Km_{Ca_i}\cdot Na_o^3\cdot\left(1+\left(\frac{Na_{sl}}{Km_{Na_i}}\right)^3\right)+Km_{Na_o}^3\cdot Ca_{sl}\cdot\left(1+\frac{Ca_{sl}}{Km_{Ca_i}}\right) \\
& + Km_{Ca_o}\cdot Na_{sl}^3+Na_{sl}^3\cdot Ca_o+Na_o^3\cdot Ca_{sl}
\end{aligned}
$$

$$
\begin{aligned}
I_{ncx_{junc}} =& \frac{F_{junc}\cdot\bar{I}_{ncx}\cdot Ka_{junc}\cdot(s1_{junc}-s2_{junc})}{s3_{junc}\cdot\left(1+k_{sat}\cdot e^{(nu-1)\cdot V\cdot FoRT}\right)} \\
I_{ncx_{sl}} =& \frac{F_{sl}\cdot\bar{I}_{ncx}\cdot Ka_{sl}\cdot(s1_{sl}-s2_{sl})}{s3_{sl}\cdot\left(1+k_{sat}\cdot e^{(nu-1)\cdot V\cdot FoRT}\right)} \\
I_{ncx} =& I_{ncx_{junc}}+I_{ncx_{sl}}
\end{aligned}
$$

B.2.14 I_{pCa}: Sarcolemmal Calcium Pump Current

$$
\begin{aligned}
I_{pCa_{junc}} =& \frac{F_{junc}\cdot\bar{I}_{PMCA}\cdot Ca_j^{1.6}}{Km_{pCa}^{1.6}+Ca_j^{1.6}} \\
I_{pCa_{sl}} =& \frac{F_{sl}\cdot\bar{I}_{PMCA}\cdot Ca_{sl}^{1.6}}{Km_{pCa}^{1.6}+Ca_{sl}^{1.6}} \\
I_{pCa} =& I_{pCa_{junc}}+I_{pCa_{sl}}
\end{aligned}
$$

B.2.15 $I_{Ca,bk}$: Background Calcium Current

$$
\begin{aligned}
I_{Ca,bk_{junc}} &= F_{junc} \cdot G_{Ca,bk} \cdot \left(V - E_{Ca_{junc}}\right) \\
I_{Ca,bk_{sl}} &= F_{sl} \cdot G_{Ca,bk} \cdot \left(V - E_{Ca_{sl}}\right) \\
I_{Ca,bk} &= I_{Ca,bk_{junc}} + I_{Ca,bk_{sl}}
\end{aligned}
$$

B.2.16 SR Fluxes: Calcium Release, SR Calcium Pump, SR Calcium Leak

$$
\begin{aligned}
k_{Ca_{SR}} &= Max_{SR} - \frac{Max_{SR} - Min_{SR}}{1 + \left(\frac{ec50_{SR}}{Ca_{SR}}\right)^{2.5}} \\
ko_{SR_{Ca}} &= \frac{ko_{Ca}}{k_{Ca_{SR}}} \\
ki_{SR_{Ca}} &= ki_{Ca} \cdot k_{Ca_{SR}} \\
RI &= 1 - Ry_{Rr} - Ry_{Ro} - Ry_{Ri} \\
\frac{\mathrm{d}Ry_{Rr}}{\mathrm{d}t} &= ki_m \cdot RI - ki_{SR_{Ca}} \cdot Ca_j \cdot Ry_{Rr} - \left(ko_{SR_{Ca}} \cdot Ca_j^2 \cdot Ry_{Rr} - ko_m \cdot Ry_{Ro}\right) \\
\frac{\mathrm{d}Ry_{Ro}}{\mathrm{d}t} &= ko_{SR_{Ca}} \cdot Ca_j^2 \cdot Ry_{Rr} - ko_m \cdot Ry_{Ro} - \left(ki_{SR_{Ca}} \cdot Ca_j \cdot Ry_{Ro} - ki_m \cdot Ry_{Ri}\right) \\
\frac{\mathrm{d}Ry_{Ri}}{\mathrm{d}t} &= ki_{SR_{Ca}} \cdot Ca_j \cdot Ry_{Ro} - ki_m \cdot Ry_{Ri} - \left(ko_m \cdot Ry_{Ri} - ko_{SR_{Ca}} \cdot Ca_j^2 \cdot RI\right) \\
J_{SR_{Ca_{rel}}} &= ks \cdot Ry_{Ro} \cdot \left(Ca_{SR} - Ca_j\right) \\
J_{ser_{Ca}} &= \frac{V_{max_{SR_{CaP}}} \cdot \left(\left(\frac{Ca_i}{Km_f}\right)^{hill_{SR_{CaP}}} - \left(\frac{Ca_{SR}}{Km_r}\right)^{hill_{SR_{CaP}}}\right)}{1 + \left(\frac{Ca_i}{Km_f}\right)^{hill_{SR_{CaP}}} + \left(\frac{Ca_{SR}}{Km_r}\right)^{hill_{SR_{CaP}}}} \\
J_{SR_{leak}} &= 5.348 \cdot 10^{-6} \cdot \left(Ca_{SR} - Ca_j\right)
\end{aligned}
$$

B.2.17 Ion Homeostasis

Sodium Buffers

$$
\begin{aligned}
\frac{\mathrm{d}NaB_j}{\mathrm{d}t} &= k_{on_{Na}} \cdot Na_j \cdot \left(B_{max_{Na_j}} - NaB_j\right) - k_{off_{Na}} \cdot NaB_j \\
\frac{\mathrm{d}NaB_{sl}}{\mathrm{d}t} &= k_{on_{Na}} \cdot Na_{sl} \cdot \left(B_{max_{Na_{sl}}} - NaB_{sl}\right) - k_{off_{Na}} \cdot NaB_{sl}
\end{aligned}
$$

Cytosolic Calcium Buffers

$$
\begin{aligned}
\frac{\mathrm{d}TnC_l}{\mathrm{d}t} =& k_{on_{TnC_l}} \cdot Ca_i \cdot \left(B_{max_{TnC_{low}}} - TnC_l\right) - k_{off_{TnC_l}} \cdot TnC_l \\
\frac{\mathrm{d}TnC_{h_c}}{\mathrm{d}t} =& k_{on_{TnC_{h_{Ca}}}} \cdot Ca_i \cdot \left(B_{max_{TnC_{high}}} - TnC_{h_c} - TnC_{h_m}\right) \\
& - k_{off_{TnC_{h_{Ca}}}} \cdot TnC_{h_c} \\
\frac{\mathrm{d}TnC_{h_m}}{\mathrm{d}t} =& k_{on_{TnC_{h_{Mg}}}} \cdot Mg_i \cdot \left(B_{max_{TnC_{high}}} - TnC_{h_c} - TnC_{h_m}\right) \\
& - k_{off_{TnC_{h_{Mg}}}} \cdot TnC_{h_m} \\
\frac{\mathrm{d}CaM}{\mathrm{d}t} =& k_{on_{CaM}} \cdot Ca_i \cdot (B_{max_{CaM}} - CaM) - k_{off_{CaM}} \cdot CaM \\
\frac{\mathrm{d}Myo_c}{\mathrm{d}t} =& k_{on_{myo_{Ca}}} \cdot Ca_i \cdot (B_{max_{myosin}} - Myo_c - Myo_m) \\
& - k_{off_{myo_{Ca}}} \cdot Myo_c \\
\frac{\mathrm{d}Myo_m}{\mathrm{d}t} =& k_{on_{myo_{Mg}}} \cdot Mg_i \cdot (B_{max_{myosin}} - Myo_c - Myo_m) \\
& - k_{off_{myo_{Mg}}} \cdot Myo_m \\
\frac{\mathrm{d}SRB}{\mathrm{d}t} =& k_{on_{SR}} \cdot Ca_i \cdot (B_{max_{SR}} - SRB) - k_{off_{SR}} \cdot SRB \\
J_{Ca_{B_{cytosol}}} =& \frac{\mathrm{d}TnC_l}{\mathrm{d}t} + \frac{\mathrm{d}TnC_{h_c}}{\mathrm{d}t} + \frac{\mathrm{d}TnC_{h_m}}{\mathrm{d}t} + \frac{\mathrm{d}CaM}{\mathrm{d}t} \\
& + \frac{\mathrm{d}Myo_c}{\mathrm{d}t} + \frac{\mathrm{d}Myo_m}{\mathrm{d}t} + \frac{\mathrm{d}SRB}{\mathrm{d}t}
\end{aligned}
$$

Junctional and SL Calcium Buffers

$$
\begin{aligned}
\frac{\mathrm{d}SLL_j}{\mathrm{d}t} =& k_{on_{sl_l}} \cdot Ca_j \cdot \left(B_{max_{SL_{low_j}}} - SLL_j\right) - k_{off_{sl_l}} \cdot SLL_j \\
\frac{\mathrm{d}SLL_{sl}}{\mathrm{d}t} =& k_{on_{sl_l}} \cdot Ca_{sl} \cdot \left(B_{max_{SL_{low_{sl}}}} - SLL_{sl}\right) - k_{off_{sl_l}} \cdot SLL_{sl} \\
\frac{\mathrm{d}SLH_j}{\mathrm{d}t} =& k_{on_{sl_h}} \cdot Ca_j \cdot \left(B_{max_{SL_{high_j}}} - SLH_j\right) - k_{off_{sl_h}} \cdot SLH_j \\
\frac{\mathrm{d}SLH_{sl}}{\mathrm{d}t} =& k_{on_{sl_h}} \cdot Ca_{sl} \cdot \left(B_{max_{SL_{high_{sl}}}} - SLH_{sl}\right) - k_{off_{sl_h}} \cdot SLH_{sl} \\
J_{Ca_{B_{junction}}} =& \frac{\mathrm{d}SLL_j}{\mathrm{d}t} + \frac{\mathrm{d}SLH_j}{\mathrm{d}t} \\
J_{Ca_{B_{sk}}} =& \frac{\mathrm{d}SLL_{sl}}{\mathrm{d}t} + \frac{\mathrm{d}SLH_{sl}}{\mathrm{d}t}
\end{aligned}
$$

Sodium Concentrations

$$\begin{aligned}
\frac{\mathrm{d}Na_j}{\mathrm{d}t} =& \frac{-I_{Na_{tot_{junc}}} \cdot C_{mem}}{V_{junc} \cdot Frdy} + \frac{J_{Na_{junc,sl}}}{V_{junc}} \cdot (Na_{sl} - Na_j) - \frac{\mathrm{d}NaB_j}{\mathrm{d}t} \\
\frac{\mathrm{d}Na_{sl}}{\mathrm{d}t} =& \frac{-I_{Na_{tot_{sl}}} \cdot C_{mem}}{V_{sl} \cdot Frdy} + \frac{J_{Na_{junc,sl}}}{V_{sl}} \cdot (Na_j - Na_{sl}) \\
&+ \frac{J_{Na_{sl,myo}}}{V_{sl}} \cdot (Na_i - Na_{sl}) - \frac{\mathrm{d}NaB_{sl}}{\mathrm{d}t} \\
\frac{\mathrm{d}Na_i}{\mathrm{d}t} =& \frac{J_{Na_{sl,myo}}}{V_{myo}} \cdot (Na_{sl} - Na_i)
\end{aligned}$$

Calcium Concentrations

$$\begin{aligned}
\frac{\mathrm{d}Csqn_b}{\mathrm{d}t} =& k_{on_{csqn}} \cdot Ca_{SR} \cdot \left(B_{max_{csqn}} - Csqn_b\right) - k_{off_{csqn}} \cdot Csqn_b \\
\frac{\mathrm{d}Ca_j}{\mathrm{d}t} =& \frac{-I_{Ca_{tot_{junc}}} \cdot C_{mem}}{V_{junc} \cdot 2 \cdot Frdy} + \frac{J_{Ca_{junc,sl}}}{V_{junc}} \cdot (Ca_{sl} - Ca_j) - J_{CaB_{junction}} \\
&+ \frac{J_{SR_{Ca_{rel}}} \cdot V_{sr}}{V_{junc}} + \frac{J_{SR_{leak}} \cdot V_{myo}}{V_{junc}} \\
\frac{\mathrm{d}Ca_{sl}}{\mathrm{d}t} =& \frac{-I_{Ca_{tot_{sl}}} \cdot C_{mem}}{V_{sl} \cdot 2 \cdot Frdy} + \frac{J_{Ca_{junc,sl}}}{V_{sl}} \cdot (Ca_j - Ca_{sl}) \\
&+ \frac{J_{Ca_{sl,myo}}}{V_{sl}} \cdot (Ca_i - Ca_{sl}) - J_{CaB_{sk}} \\
\frac{\mathrm{d}Ca_i}{\mathrm{d}t} =& \frac{-J_{ser_{Ca}} \cdot V_{sr}}{V_{myo}} - J_{CaB_{cytosol}} + \frac{J_{Ca_{sl,myo}}}{V_{myo}} \cdot (Ca_{sl} - Ca_i) \\
\frac{\mathrm{d}Ca_{SR}}{\mathrm{d}t} =& J_{ser_{Ca}} - \left(\frac{J_{SR_{leak}} \cdot V_{myo}}{V_{sr}} + J_{SR_{Ca_{rel}}}\right) - \frac{\mathrm{d}Csqn_b}{\mathrm{d}t}
\end{aligned}$$

B.2.18 Membrane Potential

$$\begin{aligned}
I_{Ca_{tot_{junc}}} =& I_{Ca_{junc}} + I_{Ca,bk_{junc}} + I_{pCa_{junc}} - 2 \cdot I_{ncx_{junc}} \\
I_{Ca_{tot_{sl}}} =& I_{Ca_{sl}} + I_{Ca,bk_{sl}} + I_{pCa_{sl}} - 2 \cdot I_{ncx_{sl}} \\
I_{Ca_{tot}} =& I_{Ca_{tot_{junc}}} + I_{Ca_{tot_{sl}}}
\end{aligned}$$

$$I_{K_{tot}} = I_{to} + I_{Kr} + I_{Ks} + I_{K1} - 2 \cdot I_{NaK} + I_{Ca_K} + I_{Kp}$$

$$
\begin{aligned}
I_{Na_{tot_{junc}}} &= I_{Na_{junc}} + I_{Na,bk_{junc}} + 3 \cdot I_{ncx_{junc}} + 3 \cdot I_{NaK_{junc}} + I_{CaNa_{junc}} \\
I_{Na_{tot_{sl}}} &= I_{Na_{sl}} + I_{Na,bk_{sl}} + 3 \cdot I_{ncx_{sl}} + 3 \cdot I_{NaK_{sl}} + I_{CaNa_{sl}} \\
I_{Na_{tot}} &= I_{Na_{tot_{junc}}} + I_{Na_{tot_{sl}}}
\end{aligned}
$$

$$
I_{Cl_{tot}} = I_{ClCa} + I_{Cl,bk}
$$

$$
\begin{aligned}
I_{tot} &= I_{Na_{tot}} + I_{Cl_{tot}} + I_{Ca_{tot}} + I_{K_{tot}} \\
\frac{\mathrm{d}V}{\mathrm{d}t} &= -\left(I_{tot} - I_{stim}\right)
\end{aligned}
$$

Appendix C

Description of the Final Model

This appendix includes only the parameters or equations that were modified with respect to the version described in Appendix B.

C.1 Model Parameters

C.1.1 Enviromental Parameters

Name	Value	Units
$J_{Ca_{junc,sl}}$	$7.861586 \cdot 10^{-13}$	L/ms
$J_{Ca_{sl,myo}}$	$3.734497 \cdot 10^{-12}$	L/ms

C.1.2 Fractional Currents

Name	Value	Units
F_{junc}	0.11	$[-]$
F_{sl}	$1 - F_{junc}$	$[-]$
$F_{junc_{Ca_L}}$	0.9	$[-]$
$F_{sl_{Ca_L}}$	$1 - F_{junc_{Ca_L}}$	$[-]$
$F_{to,s}$	0.12	$[-]$
$F_{to,f}$	$1 - F_{to,f}$	$[-]$

C.1.3 Sodium Transport

Name	Value	Units
G_{Na}	18.9024	$mS/\mu F$
$G_{Na,bk}$	$0.5181448 \cdot 10^{-3}$	$mS/\mu F$
$\bar{I}_{NaK}$	1.140666	pA/pF

C.1.4 Potassium Currents

Name	Value	Units
G_{K1}	$4.253697 \cdot 10^{-1}$	$mS/\mu F$
G_{Kp}	$2.173516 \cdot 10^{-3}$	$mS/\mu F$
G_{Kr}	$3.507879 \cdot 10^{-2}$	$mS/\mu F$
G_{Ks}	0.0034	$mS/\mu F$
$G_{to_{EPI}}$	$1.558487 \cdot 10^{-1}$	$mS/\mu F$
$G_{to_{ENDO}}$	$4.674482 \cdot 10^{-2}$	$mS/\mu F$

C.1.5 Chlorine currents

Name	Value	Units
G_{ClCa}	$4.757296 \cdot 10^{-2}$	$mS/\mu F$
$G_{Cl,bk}$	$9.417983 \cdot 10^{-3}$	$mS/\mu F$

C.1.6 Calcium Transport

Name	Value	Units
G_{CaL}	$4.7628 \cdot 10^{-4}$	$mS/\mu F$
p_{Ca}	1	$L \cdot \Omega/s$
p_K	$1.3746417 \cdot 10^{-4}$	$L \cdot \Omega/s$
p_{Na}	$7.63689 \cdot 10^{-6}$	$L \cdot \Omega/s$
$\bar{I}_{ncx}$	2.747111	pA/pF
$\bar{I}_{PMCA}$	$5.84106 \cdot 10^{-2}$	pA/pF
$G_{Ca,bk}$	$4.820643 \cdot 10^{-4}$	$mS/\mu F$

C.1.7 SR Calcium Fluxes

Name	Value	Units
$V_{max_{SR_{CaP}}}$	$4.609837 \cdot 10^{-3}$	mM/ms
ks	24.7507	mS^{-1}
$k_{SR,leak}$	$5.483405 \cdot 10^{-6}$	mS^{-1}

C.2 Model Equations

C.2.1 I_{to}: Transient Outward Potassium Current

$$
\begin{aligned}
I_{to_s} &= G_{to} \cdot F_{to,s} \cdot x_{to_s} \cdot y_{to_s} \cdot (V - E_K) \\
I_{to_f} &= G_{to} \cdot F_{to,f} \cdot x_{to_f} \cdot y_{to_f} \cdot (V - E_K) \\
I_{to} &= I_{to_s} + I_{to_f}
\end{aligned}
$$

C.2.2 I_{CaL}: L-type Calcium Current

Voltage-Dependent Activation Gate

Voltage-Dependent Inactivation Gates

$$
\begin{aligned}
f_{ss} =& \frac{1}{1+e^{\frac{V+24.63}{5.87}}} \\
\alpha_f =& 1102.5 \cdot e^{-\left(\frac{V+27}{15}\right)^2} \\
\beta_f =& \frac{200}{1+e^{\frac{20.6-V}{10}}} \\
\gamma_f =& \frac{180}{1+e^{\frac{V+30}{10}}} + 20 \\
\tau_f =& \alpha_f + \beta_f + \gamma_f \\
\frac{\mathrm{d}f}{\mathrm{d}t} =& \frac{f_{ss} - f}{\tau_f}
\end{aligned}
$$

$$
\begin{aligned}
f_{2_{ss}} =& \frac{0.67}{1+e^{\frac{V+24.63}{5.87}}} + 0.33 \\
\alpha_{f_2} =& 300 \cdot e^{\frac{-(V+25)^2}{170}} \\
\gamma_{f_2} =& \frac{16}{1+e^{\frac{V+30}{10}}} \\
\tau_{f_2} =& \alpha_{f_2} + \gamma_{f_2} \\
\frac{\mathrm{d}f_2}{\mathrm{d}t} =& \frac{f_{2_{ss}} - f_2}{\tau_{f_2}}
\end{aligned}
$$

Currents

$$
\begin{aligned}
\bar{I}_{Ca_j} =& G_{CaL} \cdot p_{Ca} \cdot \frac{V \cdot Frdy \cdot FoRT}{2} \cdot \frac{\left(Ca_j \cdot e^{2 \cdot V \cdot FoRT} - Ca_o\right)}{e^{2 \cdot V \cdot FoRT} - 1} \\
\bar{I}_{Ca_{sl}} =& G_{CaL} \cdot p_{Ca} \cdot \frac{V \cdot Frdy \cdot FoRT}{2} \cdot \frac{\left(Ca_{sl} \cdot e^{2 \cdot V \cdot FoRT} - Ca_o\right)}{e^{2 \cdot V \cdot FoRT} - 1} \\
\bar{I}_{Na_j} =& G_{CaL} \cdot p_{Na} \cdot V \cdot Frdy \cdot FoRT \cdot \frac{\left(Na_j \cdot e^{V \cdot FoRT} - Na_o\right)}{e^{V \cdot FoRT} - 1} \\
\bar{I}_{Na_{sl}} =& G_{CaL} \cdot p_{Na} \cdot V \cdot Frdy \cdot FoRT \cdot \frac{\left(Na_{sl} \cdot e^{V \cdot FoRT} - Na_o\right)}{e^{V \cdot FoRT} - 1} \\
\bar{I}_{K} =& G_{CaL} \cdot p_{K} \cdot V \cdot Frdy \cdot FoRT \cdot \frac{\left(K_i \cdot e^{V \cdot FoRT} - K_o\right)}{e^{V \cdot FoRT} - 1}
\end{aligned}
$$

$$
\begin{aligned}
I_{Ca_{junc}} &= F_{junc_{Ca_L}} \cdot \bar{I}_{Ca_j} \cdot d \cdot f \cdot f_2 \cdot \left(1 - f_{CaB_j}\right) \\
I_{Ca_{sl}} &= F_{sl_{Ca_L}} \cdot \bar{I}_{Ca_{sl}} \cdot d \cdot f \cdot f_2 \cdot \left(1 - f_{CaB_{sl}}\right) \\
I_{CaNa_{junc}} &= F_{junc_{Ca_L}} \cdot \bar{I}_{Na_j} \cdot d \cdot f \cdot f_2 \cdot \left(1 - f_{CaB_j}\right) \\
I_{CaNa_{sl}} &= F_{sl_{Ca_L}} \cdot \bar{I}_{Na_{sl}} \cdot d \cdot f \cdot f_2 \cdot \left(1 - f_{CaB_{sl}}\right) \\
I_{CaK} &= \bar{I}_K \cdot d \cdot f \cdot f_2 \cdot \left(F_{junc_{Ca_L}} \cdot \left(1 - f_{CaB_j}\right) + F_{sl_{Ca_L}} \cdot \left(1 - f_{CaB_{sl}}\right)\right)
\end{aligned}
$$

$$
\begin{aligned}
I_{Ca} &= I_{Ca_{junc}} + I_{Ca_{sl}} \\
I_{CaNa} &= I_{CaNa_{junc}} + I_{CaNa_{sl}} \\
I_{CaL} &= I_{Ca} + I_{CaK} + I_{CaNa}
\end{aligned}
$$

C.2.3 SR Fluxes: Calcium Release, SR Calcium Pump, SR Calcium Leak

$$
J_{SR_{leak}} = k_{SR_{leak}} \cdot 10^{-6} \cdot \left(Ca_{SR} - Ca_j\right)
$$

C.2.4 Ion Homeostasis

Potassium Concentrations

$$
\frac{\mathrm{d}K_i}{\mathrm{d}t} = - I_{K_{tot}} \cdot \frac{C_{mem}}{V_{myo} \cdot Frdy}
$$

C.2.5 Membrane Potential

$$
\begin{aligned}
I_{K_{tot}} &= I_{to} + I_{Kr} + I_{Ks} + I_{K1} - 2 \cdot I_{NaK} + I_{CaK} + I_{Kp} - I_{stim} \\
I_{tot} &= I_{Na_{tot}} + I_{Cl_{tot}} + I_{Ca_{tot}} + I_{K_{tot}}
\end{aligned}
$$

$$
\frac{\mathrm{d}V}{\mathrm{d}t} = - I_{tot}
$$

Appendix D

Acronyms

- *1D*: one-dimensional.
- *AP*: action potential.
- *APA*: action potential amplitude.
- *APD*: action potential duration.
- *APDR*: action potential duration restitution.
- *AV*: atrioventricular.
- *BZ*: border zone.
- *CI*: coupling interval.
- *CL*: cycle length.
- *CRLP*: *Carro-Rodríguez-Laguna-Pueyo* human ventricular cell model [120].
- *CRN*: *Courtemanche-Ramirez-Nattel* model [47].
- *CV*: conduction velocity.
- *CVDs*: cardiovascular diseases.
- *CZ*: central zone.
- *DI*: diastolic interval.
- *ECC*: excitation-contraction coupling.
- *ECG*: electrocardiogram.

- *ERP*: effective refractive period.
- *GPB*: *Grandi-Pascualini-Bers* human ventricular model [15].
- *HH*: *Hodgkin-Huxley* model [26].
- *IMW04*: Iyer *et al.* human ventricular cell model [45].
- *LR*: *Luo-Rudy* model [107].
- *NCD*: noncommunicable disease.
- *NZ*: normal zone.
- *ORd*:*O'Hara-Rudy-dynamic* human ventricular cell model [64].
- *RSA*: response surface approximations.
- *S1*: basic stimulus.
- *S2*: extra stimulus.
- *SA*: sinoatrial.
- *SEM*: standard error of the mean.
- *SR*: sarcoplasmic reticulum.
- *TNNP04*: *tenTusscher-Noble-Noble-Panfilov* human ventricular cell model [46].
- *TP06*: *tenTusscher-Panfilov* human ventricular cell model [51].

References

[1] Pelzmann B, Schaffer P, Bernhart E, Lang P, Machler H, Rigler B, and Koidl B. L-type calcium current in human ventricular myocytes at a physiological temperature from children with tetralogy of Fallot. *Cardiovasc Res*, 38:424–432, 1998. doi: 10.1016/S0008-6363(98)00002-9. http://doi.org/10.1016/S0008-6363(98)00002-9.

[2] Li G.-R, Yang B, Feng J, Bosch R. F, Carrier M, and Nattel S. Transmembrane I_{Ca} contributes to rate-dependent changes of action potentials in human ventricular myocytes. *Am J Physiol Heart Circ Physiol*, 276:H98–106, 1999. http://ajpheart.physiology.org/content/276/1/H98.

[3] Magyar J, Iost N, Körtvély Á, Bányász T, Virág L, Szigligeti P, Varró A, Opincariu M, Szécsi J, Papp J. G, and Nánási P. P. Effects of endothelin-1 on calcium and potassium currents in undiseased human ventricular myocytes. *Pflügers Arch*, 441:144–149, 2000. doi: 10.1007/s004240000400. http://doi.org/10.1007/s004240000400.

[4] Beuckelmann D. J, Näbauer M, and Erdmann E. Characteristics of calcium-current in isolated human ventricular myocytes from patients with terminal heart failure. *J Clin Invest*, 23:929–937, 1991. doi: 10.1016/0022-2828(91)90135-9. http://doi.org/10.1016/0022-2828(91)90135-9.

[5] Benitah J, Bailly P, D'Agrosa M, Da Ponte J, Delgado C, and Lorente P. Slow inward current in single cells isolated from adult human ventricles. *Pflügers Arch*, 421:176–187, 1992. doi: 10.1016/0022-2828(92)93321-A. http://doi.org/10.1016/0022-2828(92)93321-A.

[6] Mewes T and Ravens U. L-type calcium currents of human myocytes from ventricle of non-failing hearts and atrium. *J Mol Cell Cardiol*, 26:1307–1320, 1994. doi: 10.1006/jmcc.1994.1149. http://doi.org/10.1006/jmcc.1994.1149.

[7] Sun H, Leblanc N, and Nattel S. Mechanisms of inactivation of L-type calcium channels in human atrial myocytes. *Am J Physiol Heart Circ Physiol*, 33:

H1625–H1635, 1997. http://ajpheart.physiology.org/content/272/4/H1625.long.

[8] Drouin E, Charpentier F, Gauthier C, Laurent K, and Marec H. L. Electrophysiologic characteristics of cells spanning the left ventricular wall of human heart: Evidence for presence of M cells. *J Am Coll Cardiol*, 26: 185–192, 1995. doi: 10.1016/0735-1097(95)00167-X. https://doi.org/10.1016/0735-1097(95)00167-X.

[9] Pieske B, Maier L, Piacentino V. r, Weisser J, Hasenfuss G, and Houser S. Rate dependence of $[Na^+]_i$ and contractility in nonfailing and failing human myocardium. *Circulation*, 106:447–453, 2002. doi: 10.1161/01.CIR.0000023042.50192.F4. http://doi.org/10.1161/01.CIR.0000023042.50192.F4.

[10] Schmidt U, Hajjar R. J, Helm P. A, Kim C. S, Doye A. A, and Gwathmey J. K. Contribution of abnormal sarcoplasmic reticulum ATPase activity to systolic and diastolic dysfunction in human heart failure. *J Mol Cell Cardiol*, 30:1929–1937, 1998. doi: 10.1006/jmcc.1998.0748. http://doi.org/10.1006/jmcc.1998.0748.

[11] Coppini R, Ferrantini C, Yao L, Fan P, Del Lungo M, Stillitano F, Sartiani L, Tosi B, Suffredini S, Tesi C, Yacoub M, Olivotto I, Belardinelli L, Poggesi C, Cerbai E, and Mugelli A. Late sodium current inhibition reverses electromechanical dysfunction in human hypertrophic cardiomyopathyclinical perspective. *Circ*, 127(5):575–584, 2013. doi: 10.1161/CIRCULATIONAHA.112.134932. http://circ.ahajournals.org/content/127/5/575.

[12] Romero L, Pueyo E, Fink M, and Rodríguez B. Impact of ionic current variability on human ventricular cellular electrophysiology. *Am J Physiol Heart Circ Physiol*, 297:H1436–1445, 2009. doi: 10.1152/ajpheart.00263.2009. http://ajpheart.physiology.org/content/297/4/H1436.

[13] Pueyo E, Husti Z, Hornyik T, Baczkó I, Laguna P, Varró A, and Rodríguez B. Mechanisms of ventricular rate adaptation as a predictor of arrhythmic risk. *Am J Physiol Heart Circ Physiol*, 298:H1577–H1587, 2010. doi: 10.1152/ajpheart.00936.2009. http://doi.org/10.1152/ajpheart.00936.2009.

[14] Mendis S, Puska P, and Norrving B, editors. *Global Atlas on cardiovascular disease prevention and control*. World Health Organization in collaboration with the World Heart Federation and the World Stroke Organization, 2011. ISBN 9789241564373. http://apps.who.int/iris/bitstream/10665/44701/1/9789241564373_eng.pdf.

[15] Grandi E, Pasqualini F. S, and Bers D. M. A novel computational model of the human ventricular action potential and Ca transient. *J Mol Cell Cardiol*, 48:112–121, 2010. doi: 10.1016/j.yjmcc.2009.09.019. http://doi.org/10.1016/j.yjmcc.2009.09.019.

[16] Malmivuo J and Plonsey R. *Bioelectromagnetism - Principles and applications of bioelectric and biomagnetic fields*. Oxford University Press, 1995. ISBN 978-0195058239. doi: 10.1093/acprof:oso/9780195058239.001.0001.

[17] Durrer D, van Dam R. T, Freud G. E, Janse M. J, Meijler F. L, and Arzbaecher R. C. Total excitation of the isolated human heart. *Circ*, 41(6): 899–912, 1970. doi: 10.1161/01.CIR.41.6.899. `http://circ.ahajournals.org/content/41/6/899`.

[18] Zipes D. P and Wellens H. J. J. Sudden cardiac death. *Circ Res*, 98:2334–2351, 1998. doi: 10.1161/01.CIR.98.21.2334. `http://doi.org/10.1161/01.CIR.98.21.2334`.

[19] Rubart M and Zipes D. P. Mechanisms of sudden cardiac death. *J Clin Invest*, 115(9):2305–2315, 9 2005. doi: 10.1172/JCI26381. `https://www.jci.org/articles/view/26381`.

[20] Carmeliet E. Cardiac ionic currents and acute ischemia: from channels to arrhythmias. *Physiol Rev*, 79(3):917–1017, 1999. `http://physrev.physiology.org/content/79/3/917`.

[21] Janse M. J and Kleber A. G. Electrophysiological changes and ventricular arrhythmias in the early phase of regional myocardial ischemia. *Circ Res*, 49 (5):1069–1081, 1981.

[22] Janse M. J, van Capelle F. J, Morsink H, Kleber A. G, Wilms-Schopman F, Cardinal R, D'Alnoncourt C. N, and Durrer D. Flow of "injury" current and patterns of excitation during early ventricular arrhythmias in acute regional myocardial ischemia in isolated porcine and canine hearts. Evidence for two different arrhythmogenic mechanisms. *Circ Res*, 47(2):151–165, 1980.

[23] Wilensky R. L, Tranum-Jensen J, Coronel R, Wilde A. A, Fiolet J. W, and Janse M. J. The subendocardial border zone during acute ischemia of the rabbit heart: an electrophysiologic, metabolic, and morphologic correlative study. *Circ*, 74(5):1137–1146, 1986. doi: 10.1161/01.CIR.74.5.1137. `http://circ.ahajournals.org/content/74/5/1137`.

[24] Wolferth C. C, Bellet S, Livezey M. M, and Murphy F. D. Negative displacement of the rs-t segment in the electrocardiogram and its relationships to positive displacement; an experimental study. *Am Heart J*, 29(2):220–245, 1945. ISSN 0002-8703. doi: https://doi.org/10.1016/0002-8703(45)90519-9. `http://www.sciencedirect.com/science/article/pii/0002870345905199`.

[25] Holland R. P and Brooks H. Precordial and epicardial surface potentials during Myocardial ischemia in the pig. A theoretical and experimental analysis of the TQ and ST segments. *Circ Res*, 37(4):471–480, 1975. doi: 10.1161/01.RES.37.4.471. `http://circres.ahajournals.org/content/37/4/471`.

[26] Hodgkin A. L and Huxley A. F. A quantitative description of membrane current and its applications to conduction and excitation in nerve. *J Physiol*, 117(1-2):500–544, 1952. doi: 10.1016/S0092-8240(05)80004-7. https://www.ncbi.nlm.nih.gov/pmc/articles/PMC1392413/.

[27] Junge D. *Nerve and muscle excitation*. Sinauer Associates Inc., third edition, 1992.

[28] Nernst W. Zur kinetik der lösung befindlichen körper: Theorie der diffusion. *Z Phys Chem*, 3:613–637, 1888.

[29] Noble D. A modification of the Hodgkin-Huxley equations applicable to Purkinje fibre action and pace-maker potentials. *J Physiol*, 160(21):317–352, 1962. doi: 10.1113/jphysiol.1962.sp006849. http://doi.org/10.1113/jphysiol.1962.sp006849.

[30] Noble D. Successes and failures in modeling heart cell electrophysiology. *Heart Rhythm*, 8(11):1798–1803, 2011. doi: 10.1016/j.hrthm.2011.06.014. http://doi.org/10.1016/j.hrthm.2011.06.014.

[31] Carmeliet E. E. Chloride ions and the membrane potential of Purkinje fibres. *J Physiol*, 156(2):375–388, 1961. http://www.ncbi.nlm.nih.gov/pmc/articles/PMC1359892/.

[32] Hall A. E, Hutter O. F, and Noble D. Current—voltage relations of Purkinje fibres in sodium-deficient solutions. *J Physiol*, 166(1):225–240, 1963. http://www.ncbi.nlm.nih.gov/pmc/articles/PMC1359373/.

[33] Hutter O. F and Noble D. Rectifying properties of heart muscle. *Nature*, 188(4749):495, nov 1960. doi: 10.1038/188495a0. http://dx.doi.org/10.1038/188495a0.

[34] Sanguinetti M. C and Jurkiewicz N. K. Two components of cardiac delayed rectifier K^+ current. Differential sensitivity to block by class III antiarrhythmic agents. *J Gen Physiol*, 96(1):195–215, 1990. doi: 10.1085/jgp.96.1.195. http://jgp.rupress.org/content/96/1/195.

[35] Reuter H. The dependence of slow inward current in Purkinje fibres on the extracellular calcium-concentration. *J Physiol*, 192(2):479–92, 1967. doi: 10.1113/jphysiol.1967.sp008310. http://doi.org/10.1113/jphysiol.1967.sp008310.

[36] DiFrancesco D and Noble D. A model of cardiac electrical activity incorporating ionic pumps and concentration changes. *Phil Trans B*, 307(1133):353–398, 1985. doi: 10.1098/rstb.1985.0001. http://doi.org/10.1098/rstb.1985.0001.

[37] Beeler G. W and Reuter H. Reconstruction of the action potential of ventricular myocardial fibers. *J Physiol*, 268:177–210, 1977. doi: 10.1113/jphysiol.1977.sp011853. http://doi.org/10.1113/jphysiol.1977.sp011853.

[38] Hilgemann D and Noble D. Excitation-contraction coupling and extracellular calcium transients in rabbit atrium: reconstruction of basic cellular mechanisms. *Proc R Soc Lond B Biol Sci*, 230:163–205, 1987. doi: 10.1098/rspb.1987.0015. http://rspb.royalsocietypublishing.org/content/230/1259/163.long.

[39] Lindblad D. S, Murphey C. R, Clark J. W, and Giles W. R. A model of the action potential and underlying membrane currents in a rabbit atrial cell. *Am Physiol Soc*, 271(4):H1666–H1696, 1996. http://ajpheart.physiology.org/content/271/4/H1666.

[40] Luo C and Rudy Y. A model of the ventricular cardiac action potential: Depolarization, repolarization and their interaction. *Circ Res*, 68:1501–1526, 1991. doi: 10.1161/01.RES.68.6.1501. http://doi.org/10.1161/01.RES.68.6.1501.

[41] Noble D, Noble S. J, Bett G. C. L, Earm Y. E, Ho W. K, and So I. K. The role of sodium - calcium exchange during the cardiac action potential. *Ann New York Acad Sci*, 639(1):334–353, 1991. doi: 10.1111/j.1749-6632.1991.tb17323.x. http://dx.doi.org/10.1111/j.1749-6632.1991.tb17323.x.

[42] Winslow R. L, Kimball A. L, Varghese A, and Noble D. Simulating cardiac sinus and atrial network dynamics on the connection machine. *Physica D*, 64 (1–3):281–298, 1993. doi: 10.1016/0167-2789(93)90260-8. http://doi.org/10.1016/0167-2789(93)90260-8.

[43] Ramirez R. J, Nattel S, and Courtemanche M. Mathematical analysis of canine atrial action potentials: rate, regional factors, and electrical remodeling. *Am J Physiol-Heart C*, 279(4):H1767–H1785, 2000. http://ajpheart.physiology.org/content/279/4/H1767.long.

[44] Priebe L and Beuckelmann D. J. Simulation study of cellular electric properties in heart failure. *Circ Res*, 82(11):1206–1223, 1998. doi: 10.1161/01.RES.82.11.1206. http://doi.org/10.1161/01.RES.82.11.1206.

[45] Iyer V, Mazhari R, and Winslow R. L. A. Computational model of the human left ventricular epicardial myocyte. *Biophys J*, 87(3):1507–1525, 2004. doi: 10.1529/biophysj.104.043299. http://doi.org/10.1529/biophysj.104.043299.

[46] ten Tusscher K, Noble D, Noble P. J, and Panfilov A. A model for human ventricular tissue. *Am J Physiol Heart Circ Physiol*, 286(4):H1573–1589, 2004. doi: 10.1152/ajpheart.00794.2003. http://ajpheart.physiology.org/content/286/4/H1573.

[47] Courtemanche M, Ramirez R. J, and Nattel S. Ionic mechanisms underlying human atrial action potential properties: Insights from a mathematical model. *Am J of Physiol*, 275(1):H301–H321, 1998. http://ajpheart.physiology.org/content/275/1/H301.

[48] van Capelle F. J and Durrer D. Computer simulation of arrhythmias in a network of coupled excitable elements. *Circ Res*, 47(3):454–466, 1980. doi: 10.1161/01.RES.47.3.454. http://circres.ahajournals.org/cgi/doi/10.1161/01.RES.47.3.454.

[49] Leon L. J and Horácek B. M. Computer model of excitation and recovery in the anisotropic myocardium. I. Rectangular and cubic arrays of excitable elements. *J Electrocardiol*, 24(1):1–15, 1991. doi: 10.1016/0022-0736(91)90077-Y.

[50] Trayanova N. Discrete versus syncytial tissue behavior in a model of cardiac stimulation: I. Mathematical formulation. *IEEE T Bio-Med Eng*, 43 (12):1129–1140, 1996. http://ieeexplore.ieee.org/xpls/abs_all.jsp?arnumber=544337.

[51] ten Tusscher K and Panfilov A. Alternans and spiral breakup in a human ventricular tissue model. *Am J Physiol Heart Circ Physiol*, 291:H1088–H1100, 2006. doi: 10.1152/ajpheart.00109.2006. http://ajpheart.physiology.org/content/291/3/H1088.

[52] Bartos D. C, Grandi E, and Ripplinger C. M. Ion channels in the heart. *Compr Physiol*, 5(3):1423–1464, 2015. doi: 10.1002/cphy.c140069. http://doi.org/10.1002/cphy.c140069.

[53] Sanguinetti M. C, Jiang C, Curran M. E, and Keating M. T. A mechanistic link between an inherited and an acquird cardiac arrthytmia: HERG encodes the I_{Kr} potassium channel. *Cell*, 81(2):299–307, 1995. doi: 10.1016/0092-8674(95)90340-2. http://www.sciencedirect.com/science/article/pii/0092867495903402.

[54] Jost N, Virág L, Comtois P, Ördög B, Szuts V, Seprényi G, Bitay M, Kohajda Z, Koncz I, Nagy N, Szél T, Magyar J, Kovács M, Puskás L. G, Lengyel C, Wettwer E, Ravens U, Nánási P. P, Papp J. G, Varró A, and Nattel S. Molecular basis of repolarization reserve differences between dogs and man. *J Physiol*, 591:4189–4206, 2013. doi: 10.1113/jphysiol.2013.261198. http://doi.org/10.1113/jphysiol.2013.261198.

[55] Jost N, Virág L, Bitay M, Takács J, Lengyel C, Biliczki P, Nagy Z, Bogáts G, Lathrop D. A, Papp J. G, and Varró A. Restricting excessive cardiac action potential and qt prolongation. *Circ*, 112(10):1392–1399, 2005. doi: 10.1161/CIRCULATIONAHA.105.550111. http://circ.ahajournals.org/content/112/10/1392.

[56] Lopatin A and Nichols C. Inward rectifiers in the heart: An update on I_{K1}. *J Mol Cell Cardiol*, 33:625–638, 2001. doi: 10.1006/jmcc.2001.1344. http://dx.doi.org/10.1006/jmcc.2001.1344.

[57] Bueno-Orovio A, Sánchez C, Pueyo E, and Rodriguez B. Na/K pump regulation of cardiac repolarization: insights from a systems biology approach. *Pflüg Archiv*, 466(2):183–193, 2014. doi: 10.1007/s00424-013-1293-1. http://dx.doi.org/10.1007/s00424-013-1293-1.

[58] Luo C and Rudy Y. A dynamic model of the cardiac ventricular action potential: I. Simulations of ionic currents and concentration changes. *Circ Res*, 74:1071–1096, 1994. doi: 10.1161/res.74.6.7514509. https://www.ahajournals.org/doi/abs/10.1161/res.74.6.7514509.

[59] Philipson K. D and Nicoll D. A. Sodium-calcium exchange. *Curr Opin Cell Biol*, 4(4):678–683, 1992. doi: 10.1016/0955-0674(92)90089-U. http://www.sciencedirect.com/science/article/pii/095506749290089U.

[60] J M. L. A mechanism for Na/Ca transport. *J Gen Physiol*, 70:681–695, 1977. doi: 10.1085/jgp.70.6.681. http://doi.org/10.1085/jgp.70.6.681.

[61] Niederer S. A, Fink M, Noble D, and Smith N. P. A meta-analysis of cardiac electrophysiology computational models. *Exp Physiol*, 94:486–495, 2009. doi: 10.1113/expphysiol.2008.044610. http://doi.org/10.1113/expphysiol.2008.044610.

[62] Bueno-Orovio A, Cherry E. M, and Fenton F. H. Minimal model for human ventricular action potentials in tissue. *J Theor Biol*, 253:544–560, 2008. doi: 10.1016/j.jtbi.2008.03.029. http://doi.org/10.1016/j.jtbi.2008.03.029.

[63] Shannon T. R, Wang F, Puglisi J, Weber C, and Bers D. M. A mathematical treatment of integrated Ca dynamics within the ventricular myocyte. *Biophys J*, 87(5):3351–3371, 2004. doi: 10.1529/biophysj.104.047449. http://doi.org/10.1529/biophysj.104.047449.

[64] O'Hara T, Virág L, Varró A, and Rudy Y. Simulation of the undiseased human cardiac ventricular action potential: Model formulation and experimental validation. *PLOS Comput Bio*, 7(5), 2011. doi: 10.1371/journal.pcbi.1002061. http://doi.org/10.1371/journal.pcbi.1002061.

[65] Himeno Y, Asakura K, Cha C, Memida H, Powell T, Amano A, and Noma A. A human ventricular myocyte model with a refined representation of excitation-contraction coupling. *Biophys J*, 109:415 – 427, 7 2015. doi: doi:10.1016/j.bpj.2015.06.017. http://dx.doi.org/10.1016/j.bpj.2015.06.017.

[66] Rodríguez B, Trayanova N, and Noble D. Modeling cardiac ischemia. *Ann NY Acad Sci*, 1080(1):395–414, 2006. doi: 10.1196/annals.1380.029. http://dx.doi.org/10.1196/annals.1380.029.

[67] Ferrero J. M, Trenor B, Rodríguez B, and Saiz J. Electrical acticvity and reentry during acute regional myocardial ischemia: Insights from simulations. *Int J Bifurcat Chaos*, 13(12):3703–3715, 2003. doi: 10.1142/S0218127403008806. http://doi.org/10.1142/S0218127403008806.

[68] Tice B. M, Rodriguez B, and Trayanova N. A. Arrthythmogenicity of transmural heterogeneities in a realistic model of regional ischemia. *Heart Rhythm*, 2:1547–5271, 2005. doi: 10.1016/j.hrthm.2005.02.820. http://dx.doi.org/10.1016/j.hrthm.2005.02.820.

[69] Weiss D. L, Ifland M, Sachse F. B, Seemann G, and Dössel O. Modeling of cardiac ischemia in human myocytes and tissue including spatiotemporal electrophysiological variations. *Biomed Eng*, 54, 2009. doi: 10.1515/BMT.2009.016. http://doi.org/10.1515/BMT.2009.016.

[70] Heidenreich E. A, Ferrero J. M, and Rodríguez J. F. *Modeling the Human Heart Under Acute Ischemia*, pages 81–103. Springer Netherlands, Dordrecht, 2012. ISBN 978-94-007-4552-0. doi: 10.1007/978-94-007-4552-0_4. https://doi.org/10.1007/978-94-007-4552-0_4.

[71] Mena A, Migliavacca F, M F. J, and Rodriguez Matas J. F. Vulnerability in regionally ischemic human heart. Effect of the extracellular potassium concentration. *J Comput Sci*, 24:160–168, 2018. doi: 10.1016/j.jocs.2017.11.009. https://doi.org/10.1016/j.jocs.2017.11.009.

[72] Dutta S, Mincholé A, Zacur E, Quinn T. A, Taggart P, and Rodriguez B. Early afterdepolarizations promote transmural reentry in ischemic human ventricles with reduced repolarization reserve. *Prog Biophys Mol Bio*, 120(1):236–248, 2016. doi: https://doi.org/10.1016/j.pbiomolbio.2016.01.008. http://www.sciencedirect.com/science/article/pii/S0079610716000109.

[73] Coronel R, Fiolet J. W, Wilms-Schopman F. J, Schaapherder A. F, Johnson T. A, Gettes L. S, and Janse M. J. Distribution of extracellular potassium and its relation to electrophysiologic changes during acute myocardial ischemia in the isolated perfused porcine heart. *Circ*, 77(5):1125–1138, 1988. doi: 10.1161/01.CIR.77.5.1125. http://circ.ahajournals.org/content/77/5/1125.

[74] A. N. ATP-regulated K^+ channels in cardiac muscle. *Nature*, 305(5930):147–148, 1983. doi: 10.1038/305147a0. http://doi.org/10.1038/305147a0.

[75] Yatani A, Brown A. M, and Akaike N. Effect of extracellular ph on sodium current in isolated, single rat ventricular cells. *J Membrane Biol*, 78(2):163–168, Jun 1984. doi: 10.1007/BF01869203. https://doi.org/10.1007/BF01869203.

[76] Fink M, Noble D, Virag L, Varro A, and Giles W. R. Contributions of HERG K+ current to repolarization of the human ventricular action potential. *Prog Biophys Mol Bio*, 96:357–376, 2008. doi: 10.1016/j.pbiomolbio.2007.07.011. http://doi.org/10.1016/j.pbiomolbio.2007.07.011.

[77] Hondeghem L. M, Carlsson L, and Duker G. Instability and triangulation of the action potential predict serious proarrhythmia, but action potential duration prolongation is antiarrhythmic. *Circ*, 103:2004–2013, 2001. doi: 10.1161/01.CIR.103.15.2004. http://doi.org/10.1161/01.CIR.103.15.2004.

[78] Volders P. G, Vos M. A, Szabo B, Sipido K. R, de Groot S. H, Gorgels A. P, Wellens H. J, and Lazzara R. Progress in the understanding of cardiac early afterdepolarizations and torsades de pointes: time to revise current concepts. *Cardiovasc Res*, 46:376–392, 2000. doi: 10.1016/S0008-6363(00)00022-5. http://doi.org/10.1016/S0008-6363(00)00022-5.

[79] Pieske B, Maier L. S, Bers D. M, and Hasenfuss G. Ca^{2+} handling and sarcoplasmic reticulum Ca^{2+} content in isolated failing and nonfailing human myocardium. *Circ Res*, 85:38–46, 1999. doi: 10.1161/01.RES.85.1.38. https://doi.org/10.1161/01.RES.85.1.38.

[80] Bers D. M and Despa S. Cardiac myocytes Ca^{2+} and Na^{+} regulation in normal and failing hearts. *J Pharm Sci*, 100:315–322, 2006. doi: 10.1254/jphs.CPJ06001X. http://doi.org/10.1254/jphs.CPJ06001X.

[81] Pueyo E, Smetana P, Caminal P, de Luna A. B, Malik M, and Laguna P. Characterization of QT interval adaptation to RR interval changes and its use as a risk-stratifier of arrhythmic mortality in amiodarone-treated survivors of acute myocardial infarction. *IEEE Trans Biomed Eng*, 51:1511–1520, 2004. doi: 10.1109/TBME.2004.828050. http://doi.org/10.1109/TBME.2004.828050.

[82] Nolasco J. B and Dahlen R. W. A graphic method for the study of alternation in cardiac action potentials. *J Appl Physiol*, 25:191–196, 1968. http://jap.physiology.org/content/25/2/191.long.

[83] Weiss J. N, Karma A, Shiferaw U. Y, Chen P. S, Garfinkel A, and Qu Z. From pulses to pulseless: the saga of cardiac alternans. *Circ Res*, 98:1244–1253, 2006. doi: 10.1161/01.RES.0000224540.97431.f0. http://doi.org/10.1161/01.RES.0000224540.97431.f0.

[84] Levi A. J, Dalton G. R, Hancox J. C, Mitcheson J. S, Issberner J, Bates J. A, Evans S. J, Howarth F. C, Hobai I. A, and Jones J. V. Role of intracellular sodium overload in the genesis of cardiac arrhythmias. *J Cardiovasc Electrophysiol*, 8:700–721, 1997. doi: 10.1111/j.1540-8167.1997.tb01834.x. http://doi.org/10.1111/j.1540-8167.1997.tb01834.x.

[85] Murphy E and Eisner D. A. Regulation of intracellular and mitochondiral sodium in health and disease. *Circ Res*, 104:292–303, 2009. doi: 10.1161/CIRCRESAHA.108.189050. http://circres.ahajournals.org/content/104/3/292.

[86] Keener J and Sneyd J. *Mahematical physiology*. Springer-Verlag, 1998. ISBN 978-0-387-98381-3. doi: 10.1007/b98841. http://doi.org/10.1007/b98841.

[87] Heidenreich E, Ferrero J. M, Doblaré M, and Rodríguez J. F. Adaptive macro finite elements for the numerical solution of monodomain equations in cardiac electrophysiology. *Ann Biomed Eng*, 38(7):2331–2345, 2010. doi: 10.1007/s10439-010-9997-2. http://doi.org/10.1007/s10439-010-9997-2.

[88] Taggart P, Sutton P, T O, Coronel R, Trimlett R, and Pugsley W. Inhomogeneous transmural conduction during early ischemia in patients with coronary artery disease. *J Mol Cell Cardiol*, 32:621–639, 2000. doi: 10.1006/jmcc.2000.1105. http://doi.org/10.1006/jmcc.2000.1105.

[89] Rush S and Larsen H. A practical algorithm for solving dynamic membrane equations. *IEEE Trans Biomed Eng*, 25(4):389–392, 1978. doi: 10.1109/TBME.1978.326270. http://doi.org/10.1109/TBME.1978.326270.

[90] Fülöp L, Bányász T, Magyar J, Szentandrássy N, Varró A, and Nánási P. P. Reopening of L-type calcium channels in human ventricular myocytes during applied epicardial action potentials. *Acta Physiol Scand*, 180:37–94, 2004. doi: 10.1046/j.0001-6772.2003.01223.x. http://doi.org/10.1046/j.0001-6772.2003.01223.x.

[91] Iost N, Virág L, Opincariu M, Szécsi J, Varró A, and Papp J. G. Delayed rectifier potassium current in undiseased human ventricular myocytes. *Cardiovasc Res*, 40(3):508–515, 1998. doi: 10.1016/S0008-6363(98)00204-1. https://doi.org/10.1016/S0008-6363(98)00204-1.

[92] Szentadrassy N, Banyasz T, Biro T, Szabo G, Toth B. I, Magyar J, Lazar J, Varro A, Kovacs L, and Nanasi P. P. Apico-basal inhomogeneity in distribution of ion channels in canine and human ventricular myocardium. *Cardiovasc Res*, 65(4):851–860, 2005. doi: 10.1016/j.cardiores.2004.11.022. https://doi.org/10.1016/j.cardiores.2004.11.022.

[93] Verkerk A. O, Wilders R, Veldkamp M. W, de Geringel W, Kirkels J. H, and Tan1 H. L. Gender Disparities in Cardiac Cellular Electrophysiology and Arrhythmia Susceptibility in Human Failing Ventricular Myocytes. *Int Heart J*, 46(6):1105–1118, 2005. doi: 10.1536/ihj.46.1105. http://doi.org/10.1536/ihj.46.1105.

[94] Virág L, Iost N, Opincariu M, Szolnoky J, Szécsi J, Bogáts G, Szenohradszky P, Varró A, and Papp J. G. The slow component of the delayed rectifier potassium current in undiseased human ventricular myocytes. *Cardiovasc Res*, 49:790–797, 2001. doi: 10.1016/S0008-6363(00)00306-0. http://doi.org/10.1016/S0008-6363(00)00306-0.

[95] Franz M. R, Swerdlow C. D, Liem L. B, and Schaefer J. Cycle length dependence of human actionpPotential duration in vivo. *Am Clin Inves*, 82:972–979, 1988. doi: 10.1016/S0735-1097(10)80281-5. https://doi.org/10.1016/S0735-1097(10)80281-5.

[96] Li G.-R, Feng J, Yue L, and Carrier M. Transmural heterogeneity of action potentials and I_{to1} in myocytes isolated from the human right ventricle. *Am J Physiol Heart Circ Physiol*, 275:H369–377, 1998. http://ajpheart.physiology.org/content/275/2/H369.

[97] Beuckelmann D. J, Nabauer M, and Erdmann E. Intracellular calcium handling in isolated ventricular myocytes from patients with terminal heart failure. *Am Heart J*, 85:1046–1055, 1992. doi: 10.1161/01.CIR.85.3.1046. https://doi.org/10.1161/01.CIR.85.3.1046.

[98] Nash M. P, Gradley C. P, Sutto P. M, Clayton R. H, Kallis P, Hayward M. P, Paterson D. J, and Taggart P. Whole heart action potential duration restitution properties in cardiac patients: a combined clinical and modeling study. *Exp Physiol*, 91:339–354, 2006. doi: 10.1113/expphysiol.2005.031070. http://doi.org/10.1113/expphysiol.2005.031070.

[99] Shaw R. M and Rudy Y. Electrophysiologic effects of acute myocardial ischemia: A mechanistic investigation of action potential conduction and conduction failure. *Circ Res*, 80:124–138, 1997. doi: 10.1016/S0008-6363(97)00093-X. http://doi.org/10.1016/S0008-6363(97)00093-X.

[100] Kagiyama Y, Hill J. L, and Gettes L. S. Interaction of acidosis and increased extracellular potassium on action potential characteristics and conduction in guinea-pig ventricular muscle. *Circ Res*, 51:614–623, 1982. doi: 10.1161/01.RES.51.5.614. http://doi.org/10.1161/01.RES.51.5.614.

[101] Dilly S. G and Lab M. J. Electrophysiological alternans and restitution during acute regional ischaemia in myocardium of anaesthetized pig. *J Physiol*, 402(1):315–333, 1988. doi: 10.1113/jphysiol.1988.sp017206. http://doi.org/10.1113/jphysiol.1988.sp017206.

[102] Kurz R. W, Mohabir R, Ren X.-L, and Franz M. R. Ischaemia induced alternans of action potential duration in the intact-heart: dependence on coronary flow, preload and cycle length. *Eur Heart J*, 14(10):1410–1420, 1993. doi: 10.1093/eurheartj/14.10.1410. http://doi.org/10.1093/eurheartj/14.10.1410.

[103] Martínez J. P, Olmos S, Wagner G, and Laguna P. Characterization of repolarization alternans during ischemia: time-course and spatial analysis. *IEEE Trans Biomed Eng*, 53(4):701–711, 2006. doi: 10.1109/TBME.2006.870233. http://doi.org/10.1109/TBME.2006.870233.

[104] Rodríguez J. F, Heidenreich E. A, Romero L, Ferrero J. M, and Doblare M. Post-repolarization refractoriness in human ventricular cardiac cells. In *Computers in Cardiology*, volume 35, pages 581–584, 2008. doi: 10.1109/CIC.2008.4749108. http://doi.org/10.1109/CIC.2008.4749108.

[105] Krogh-Madsen T, Sobie E. A, and Christini D. J. Improving cardiomyocyte model fidelity and utility via dynamic electrophysiology protocols and optimization algorithms. *J Physiol*, 594(9):2525–2536, 2016. ISSN 1469-7793. doi: 10.1113/JP270618. http://dx.doi.org/10.1113/JP270618.

[106] Yue L, Feng J, Li G. R, and Nattel S. Transient outward and delayed rectifier currents in canine atrium: properties and role of isolation methods. *Am J Physiol*, 270(6 Pt 2):H2157–68, 1996. http://ajpheart.physiology.org/content/270/6/H2157.long.

[107] Zeng J, Laurita K. R, Rosenbaum D. S, and Rudy Y. Two components of the delayed rectifier K^+ current in ventricular myocytes of the guinea pig type. Theoretical formulation and their role in repolarization. *Circ Res*, 77(1): 140–152, 1995. doi: 10.1161/01.RES.77.1.140. http://doi.org/10.1161/01.RES.77.1.140.

[108] Nygren A, Leon L. J, and Giles W. R. Simulations of the human atrial action potential. *Phil Trans A*, 359(1783):1111–1125, 2001. doi: 10.1098/rsta.2001.0819. http://doi.org/10.1098/rsta.2001.0819.

[109] Dokos S and Lovell N. H. Parameter estimation in cardiac ionic models. *Prog Biophys Mol Bio*, 85(2–3):407–431, 2004. doi: http://dx.doi.org/10.1016/j.pbiomolbio.2004.02.002. http://www.sciencedirect.com/science/article/pii/S0079610704000306.

[110] Guo T, Abed A. A, Lovell N. H, and Dokos S. Optimisation of a generic ionic model of cardiac myocyte electrical activity. *Computational and Mathematical Methods in Medicine*, 2013:1–20, 2013. doi: 10.1155/2013/706195. http://doi.org/10.1155/2013/706195.

[111] Bot C. T, Kherlopian A. R, Ortega F. A, Christini D. J, and Krogh-Madsen T. Rapid genetic algorithm optimization of a mouse computational model: Benefits for anthropomorphization of neonatal mouse cardiomyocytes. *Front Physiol*, 421(3), 2012. doi: 10.3389/fphys.2012.00421. http://doi.org/10.3389/fphys.2012.00421.

[112] Groenendaal W, Ortega F. A, Kherlopian A. R, Zygmunt A. C, Krogh-Madsen T, and Christini D. J. Cell-specific cardiac electrophysiology models. *PLOS Comput Bio*, 11(4), 2015. doi: 10.1371/journal.pcbi.1004242. http://doi.org/10.1371/journal.pcbi.1004242.

[113] Kaur J, Nygren A, and Vigmond E. J. Fitting membrane resistance along with action potential shape in cardiac myocytes improves convergence: Application of a multi-objective parallel genetic algorithm. *PLOS ONE*, 9(9): 1–10, 09 2014. doi: 10.1371/journal.pone.0107984. http://dx.doi.org/10.1371/journal.pone.0107984.

[114] Syed Z, Vigmond E, Nattel S, and Leon L. Atrial cell action potential parameter fitting using genetic algorithms. *Med Biol Eng Comput*, 43(5): 561–571, 2005. doi: 10.1007/BF02351029. http://dx.doi.org/10.1007/BF02351029.

[115] Rodríguez J. F, Renaud J. E, and Watson L. T. Trust region augmented lagrangian methods for sequential response surface approximation and optimization. *J Mech Design*, 120(1):58–66, 1998. doi: 10.1115/1.2826677. http://dx.doi.org/10.1115/1.2826677.

[116] Corsi C, Cortesi M, Callisesi G, De Bie J, Napolitano C, Santoro A, Mortara D, and Severi S. Noninvasive quantification of blood potassium concentration from ECG in hemodialysis patients. *Sci Rep*, 7:42492, 2017. doi: 10.1038/srep42492. http://www.ncbi.nlm.nih.gov/pmc/articles/PMC5309791/.

[117] Box G. E. P, Hunter J. S, and G H. W. *Statistics for Experimenters: Design, Innovation, and Discovery*. Wiley Interscience, $2^n d$ edition, 2005.

[118] Livshitz L and Rudy Y. Uniqueness and stability of action potential models during rest, pacing, and conduction using problem-solving environment. *Bio J*, 97:1265–1276, 2009. doi: 10.1016/j.bpj.2009.05.062. http://dx.doi.org/10.1016/j.bpj.2009.05.062.

[119] Dutta S, Mincholé A, Quinn T. A, and Rodríguez B. Electrophysiological properties of computational human ventricular cell action potential models under acute ischemic conditions. *Prog Biophys Mol Bio*, 2017. doi: 10.1016/j.pbiomolbio.2017.02.007. http://www.sciencedirect.com/science/article/pii/S0079610716300918.

[120] Carro J, Rodríguez J, Laguna P, and Pueyo E. A human ventricular cell model for investigation of cardiac arrhythmias under hyperkalaemic conditions. *Philos T Roy Soc A*, 369(1954):4205–4232, 2011. doi: 10.1098/rsta.2011.0127. http://doi.org/10.1098/rsta.2011.0127.

[121] Carro J, Rodríguez-Matas J. F, Monasterio V, and Pueyo E. Limitations in electrophysiological model development and validation caused by differences between simulations and experimental protocols. *Prog Biophys Mol Bio*, 2016. doi: 10.1016/j.pbiomolbio.2016.11.006. http://www.sciencedirect.com/science/article/pii/S007961071630013X.

[122] Yao A, Spitzer K. W, Ito N, Zaniboni M, Lorell B. H, and Barry W. H. The restriction of diffusion of cations at the external surface of cardiac myocytes varies between species. *Cell Calcium*, 22(6):431–438, 1997. doi: https://doi.org/10.1016/S0143-4160(97)90070-1. http://www.sciencedirect.com/science/article/pii/S0143416097900701.

[123] Alan F, Matteo F, Ronald W, and Stefano S. Computational analysis of the human sinus node action potential: model development and effects of mutations. *J Physiol*, 595(7):2365–2396, 2017. doi: 10.1113/JP273259. https://physoc.onlinelibrary.wiley.com/doi/abs/10.1113/JP273259.

[124] Sobie E. A. Parameter sensitivity analysis in electrophysiological models using multivariable regression. *Buophys J*, 96(4):1264–1274, 2009. doi: 10.1016/j.bpj.2008.10.056. http://doi.org/10.1016/j.bpj.2008.10.056.

[125] Wamsley J, Rodriguez J. F, Mirams G. R, Burrage K, Efimov I. R, and Rodriguez B. mRNA Expression Levels in Failing Human Hearts Predict Cellular Electrophysiological Remodeling: A Population-Based Simulation Study. *PLOS ONE*, 8(2):e56359, 2013. doi: 10.1371/journal.pone.0056359. http://doi.org/10.1371/journal.pone.0056359.

[126] Drouin E, Lande G, and Charpentier F. Amiodarone reduces transmural heterogeneity of repolarization in the human heart. *J Am Coll Cardiol*, 32(4):1063–1067, 1998. doi: https://doi.org/10.1016/S0735-1097(98)00330-1. http://www.sciencedirect.com/science/article/pii/S0735109798003301.

[127] Noble D, Garny A, and Noble P. J. How the Hodgkin-Huxley equations inspired the Cardiac Physiome Project. *J Physiol*, 590(Pt 11):2613–2628, 2012. doi: 10.1113/jphysiol.2011.224238.

[128] Csercsik D, Hangos K. M, and Szederkényi G. Identifiability analysis and parameter estimation of a single Hodgkin-Huxley type voltage dependent ion channel under voltage step measurement conditions. *Neurocomputing*, 77(1):178–188, 2012. doi: 10.1016/j.neucom.2011.09.006. http://doi.org/10.1016/j.neucom.2011.09.006.

[129] Lee J, Smaill B, and Smith N. Hodgkin-Huxley type ion channel characterization: An improved method of voltage clamp experiment parameter estimation. *J Theor Biol*, 242(1):123–134, 2006. doi: 10.1016/j.jtbi.2006.02.006. http://doi.org/10.1016/j.jtbi.2006.02.006.

[130] Wang G. J and Beaumont J. Parameter estimation of the Hodgkin–Huxley gating model: An inversion procedure. *Siam J Appl Math*, 64(4):1249–1267, 2004. doi: 10.1137/S0036139902419826. http://doi.org/10.1137/S0036139902419826.

[131] Cherry E. M and Fenton F. H. A tale of two dogs: analyzing two models of canine ventricular electrophysiology. *Am J Physiol Heart Circ Physiol*, 292(1):H43–H55, 2007. doi: 10.1152/ajpheart.00955.2006. http://doi.org/10.1152/ajpheart.00955.2006.

[132] Pathmanathan P, Shotwell M. S, Gavaghan D. J, Cordeiro J. M, and Gray R. A. Uncertainty quantification of fast sodium current steady-state inactivation for multi-scale models of cardiac electrophysiology. *Prog Biophys Mol Bio*, 117(1):4–18, 2015. doi: 10.1016/j.pbiomolbio.2015.01.008. http://dx.doi.org/10.1016/j.pbiomolbio.2015.01.008.

[133] Shotwell M. S and Gray R. A. Estimability analysis and optimal design in dynamic multi-scale models of cardiac electrophysiology. *J Agr Biol Envir St*, 21(2):261–276, 2016. doi: 10.1007/s13253-016-0244-7. http://doi.org/10.1007/s13253-016-0244-7.

[134] Li G. R and Nattel S. Properties of human atrial I_{Ca} at physiological temperatures and relevance to action potential. *Am J Physiol Heart Circ Physiol*, 272(1):H227–H235, 1997. http://ajpheart.physiology.org/content/272/1/H227.

[135] Magyar J, Szentandrássy N, Bányász T, Fülöp L, Varró A, and Nánási P. P. Effects of thymol on calcium and potassium currents in canine and human ventricular cardiomyocytes. *Brit J Pharmacol*, 136(2):330–338, 2002. doi: 10.1038/sj.bjp.0704718. http://doi.org/10.1038/sj.bjp.0704718.

[136] Monasterio V, Carro J, and Pueyo E. Repolarization alternans in human ventricular hyperkalaemic tissue: dependence on current stimulation. In *XXXII Congreso Anual de la Sociedad Española de Ingeniería Biomédica, Barcelona*, pages 1–4, 2014. ISBN 9788461724468.

[137] Gögelein H, Brüggemann A, Gerlach U, Brendel J, and Busch A. E. Inhibition of IKs channels by HMR 1556. *N-S Arc Pharmacol*, 362(6):480–488, 2000. doi: 10.1007/s002100000284. https://doi.org/10.1007/s002100000284.

[138] Cordeiro J. M, Spitzer K. W, and Giles W. R. Repolarizing K+ currents in rabbit heart Purkinje cells. *J Physiol*, 508(3):811–823, 1998. ISSN 1469-7793. doi: 10.1111/j.1469-7793.1998.811bp.x. http://dx.doi.org/10.1111/j.1469-7793.1998.811bp.x.

[139] Thomsen M. B, Volders P. G. A, Stengl M, Späatjens R. L. H. M. G, Beekman J. D. M, Bischoff U, Kall M. A, Frederiksen K, Matz J, and Vos M. A. Electrophysiological safety of sertindole in dogs with normal and remodeled hearts. *J Pharm Exp Th*, 307(2):776–784, 2003. doi: 10.1124/jpet.103.052753. http://jpet.aspetjournals.org/content/307/2/776.

[140] Warren M, Guha P. K, Berenfeld O, Zaitsev A, Anumonwo J. M, Dhamoon A. S, Bagwe S, Taffet S. M, and Jalife J. Blockade of the inward rectifying potassium current terminates ventricular fibrillation in the guinea pig heart. *J Cardiovasc Electr*, 14(6):621–631, 2003. ISSN 1540-8167. doi: 10.1046/j.1540-8167.2003.03006.x. http://dx.doi.org/10.1046/j.1540-8167.2003.03006.x.

The development and validation of a computational electrophysiological model is a complex process associated with a number of difficulties. Two main issues are: i) the limited amount of experimental data the model can be based; ii) the way in which information is extracted from experiments and used to build the models. Based on the increase in computational power, new strategies to reduce the number of hypothesis and/or assumptions when building an electrophysiological model were considered. In particular, the application of an optimization algorithm together with the simulation of *in silico* simulation of experimental protocols, helped to find a model that better represents the experimental results.

This thesis highlighted the benefits of using *in silico* simulations of experimental protocols to evaluate all those possibilities, as long as *in silico* simulations replicate as closely as possible the conditions of the experiments against which the simulated data is compared.

Instituto Universitario de Investigación
de Ingeniería de Aragón
Universidad Zaragoza